Droplet Impact and Solidification on Solid Surfaces in the Presence of Stagnation Air Flow

MORTEZA MOHAMMADI

A Thesis

in

the Department

of

Mechanical and Industrial Engineering

Presented in Partial Fulfillment of the Requirements
for the Degree of Doctor of Philosophy (Ph.D.)
in Mechanical Engineering Department
at Concordia University
Montreal, Quebec, Canada

June 2016

Abstract

Droplet Impact and Solidification on Solid Surfaces in the Presence of Stagnation Air Flow.
Morteza Mohammadi, Ph.D.
Concordia University, 2016

Understanding the fundamentals of ice accretion on surfaces can help in proposing solutions to reduce or prevent ice accumulation on aircraft components and power lines. The main way in which ice forms on a surface is the solidification of supercooled droplets upon impacting on the surface. On an aircraft wing, ice accumulation can easily change the flow pattern, which could result in an increase in drag force. This research investigates the use of superhydrophobic coatings (surfaces with contact angles larger than 150°) to counteract icing (anti-icing) as a result of their extremely low surface energy. The main goal of this study is to assess the performance of superhydrophobic surfaces in the presence of stagnation flow to mimic flight conditions (e.g. droplet impinging on the leading edge of an aircraft's wing). A wide range of droplet impact velocities and stagnation flows in splashing and non-splashing regimes (at high and low Weber numbers) were carried out on surfaces with various wettabilities. The results were analyzed in order to highlight the advantages of using superhydrophobic coatings. Free stream air velocity were varied from 0 to 10 m/s with a temperature which was controlled from room temperature at $20\,^{\circ}\mathrm{C}$ down to $-30\,^{\circ}\mathrm{C}$.

It was observed that while the presence of stagnation flow on hydrophilic (i.e. aluminum substrate) results in thin film formation for droplets with Weber numbers more than 220 upon impact in room temperature condition, instantaneous freezing at the maximum spreading diameter was observed in low temperature condition where air and substrate temperature was below the $-20\,^{\circ}\mathrm{C}$. Same phenomenon was observed for hydrophobic substrate at aforementioned temperature. On the other hand, striking phenomenon was observed for superhydrophobic surface when stagnation air flow

is present. Although it was expected droplet contact time to be increased by imposing stagnation air flow on an impacting droplet it was reduced as a function of droplet Weber number. This was referred to the presence of full slip condition rather than partial one where the spreading droplet moves on thin layer of air. Consequently, it promotes droplet ligament detachment through Kelvin-Helmholtz instability mechanism. While in low temperature condition above temperature of heterogeneous ice nucleation (i.e. -24 ℃)[1] supercooled water droplet contact time is reduced up to 30% to that of still air cases, droplet solidified diameter was increased up to 2 folds for air velocity up to 10 m/s compare to the still air condition at temperatures as low as -30 ℃. These results were compared with a new predictive model of droplet impact behavior on the superhydrophobic substrate.

New universal predictive model of droplet impact dynamics on the superhydrophobic surface was developed based on the concept of mass-spring model[2] which was validated against experimental results. In the new model, viscosity effect was considered through adding a dashpot term in mass-spring model. In addition, the effect of stagnation flow was also integrated to the model through classical Homann flow approach.[3] For non-isothermal condition, the effect of phase change (i.e. solidification) on droplet wetting dynamics was coupled to the model through classical nucleation theory. The universal model was compared against experimental results in room and low temperature conditions (i.e. supercooled condition) for model's validation.

Acknowledgements

Table of contents

LIST OF FIGURES

xiii

LIST OF TABLES

NOMENCLATURE

U_{cl}	Contact line velocity
f_H	Hofmann function
d_r	Receding diameter
d_a	Advancing diameter
D	Initial droplet size
g	Gravitation acceleration
V_c	Characteristic velocity of repulsion
k^{-1}	Droplet capillary length
R	Initial droplet radius
P	Pressure inside liquid drop
V	Impacting velocity of liquid drop
C_l	Speed of sounds in liquid drop
C_g	Speed of sounds in gas
V_s	Spreading velocity
t	Time
t^*	Dimensionless time
P_{atm}	Atmospheric pressure

M_g	Molecular weight of gas
k_B	Boltzmann constant
T_g	Gas temperature
$h_{lamella}$	Thickness of spread drop
D_{max}	Maximum spreading diameter
k	function of freezing line velocity
$C_{p,l}$	Specific heat of liquid drop
T_m	Melting point temperature of frozen water drop
T_s	Substrate temperature
$H_{f,l}$	Latent heat of fusion
k_g	Thermal conductivity of gas
k_w	Thermal conductivity of water
$r\,(t)$	Radius of hemispherical ice cap formed on substrate
$J(t)$	Heterogeneous ice nucleation rate as a function of time
K	Kinetic rate
U	Freezing-front velocity
t_c	Total droplet contact time
$f\left(T_{interface}\right)$	Interface temperature function
C	Function describing rate of freezing front
A_{g-w}	Gas-water interfacial area
A_{s-w}	Solid-water interfacial area

A_{s-l}	Solid-liquid interfacial area
$f_{(\theta_{wI})}$	Geometrical factor
$\Delta G_{Het}(T, \theta_{wI})$	Heterogeneous ice nucleation
T_w	Water temperature
T_s	Substrate temperature
T_g	Gas temperature
h_{pa}	Average roughness of pillar on substrate
H_v	Latent heat of vaporization
h_g	Convective heat transfer coefficient
R_a	Average roughness
R_q	Root mean square roughness
l	Height of sessile drop
l_c	Characteristic length
V_r	Radial velocity of stagnation air flow
V_z	Normal velocity of stagnation air flow
a	A constant describing growth of radial velocity of air flow
m_o	Mass of liquid water drop
C_{dl}	Damping coefficient of drop
w_o	Natural frequency
W_o	Humidity ratio
S_{air}	A function describing air shear stress
r_{max}	Maximum radius of spread drop

V_g	Gas velocity
F_{vis}	Viscous force of spread drop
W_{dis}	Dissipation energy
V_{rec}	Receding velocity of an impacting drop
V_{radial}	Radial velocity of an impacting drop at recoiling stage
$F_{s@interface}$	Air shear force at spread drop interface
N_i	Number of particle at homogenous mixture
N_s	Number of particle at solid phase
N_l	Number of particle at liquid phase
S	Entropy of system
$T_{Interface}$	Interface temperature
ΔG_v	Volumetric thermodynamic driving force
ΔG_r	Gibbs free surface energy for ice nuclei at radius of r
$\Delta G_{c,Homo}$	Homogeneous ice nucleation energy barrier based on Gibbs free surface energy
$V_{n,r}$	Volume of ice nuclei located on substrate
A_{WI}	Surface area of ice nuclei contacting with water
A_{SI}	Substrate-ice area
$\Delta G_{Het}(\theta_{wI})$	Heterogeneous ice nucleation as a function of water-ice contact angle
h	Planck constant
$\Delta F_{diff}(T)$	Diffusion activation energy
n	Number density of water molecules at the ice-water interface
D	Water diffusivity
E	Fitting parameter for finding water diffusivity

T_R	Fitting parameter for finding water diffusivity
T_{pa}	Temperature at post-air domain of rough substrate
S_{pa}	Variable defined for reducing order of ODE in post-air domain.
S_w	Variable defined for reducing order of ODE in water domain.
C_{pa}	Integral constant at post-air domain
a_{pa}	Integral constant at post-air domain
C_w	Integral constant at water domain
a_w	Integral constant at water domain
T_d	Droplet temperature
T_{sub}	Substrate temperature
$T_{w-interface}$	Water temperature at interface
$T_{g-w,interface}$	Gas-liquid interface temperature
$T_{s-l,interface}$	Solid-liquid interface temperature
$\dot{Q}_{evaporation}$	Evaporative mass transfer rate
$\dot{Q}_{g-convection}$	Convective heat transfer rate
$\dot{Q}_{w-conduction}$	Conductive heat transfer rate
$\dot{m}_{eva}$	Mass evaporation rate
$\dot{m}_{f,eva}$	Mass flux
ρ_{s-aw}	Density of saturated air at water interface
T_{oi}	Average temperature between water and surrounding gas temperature
c_{pwa}	Specific heat of water vapor for supercooled droplet
P_{vo}	Vapor pressure at gas-water interface

P_{vi}	Vapor pressure in the air
V_{air}	Average value of radial velocity in viscous layer
W_o	Humidity ratio of water vapor at interface of water
P_{vo}	Water vapor pressure at water interface
T_o	Surface temperature of water at interface
$U_{g,jet}$	Gas jet velocity of stagnation flow
U_{air}	Air jet velocity of stagnation flow
$c_{p,g}$	Specific heat of impinging gas
c_{p-ice}	Specific heat of ice
$C_{p,v}$	Specific heat of water-vapor
k_{ice}	Thermal conductivity of ice
$\hat{t}$	Characteristic time
b	Adjusting parameter describing freezing events at spread water
F_{Drag}	Drag force

Greek Symbols

θ_d	Dynamic contact angle
θ_e	Equilibrium contact angle
θ_{rec}	Receding contact angle
θ_{adv}	Advancing contact angle
θ_{hes}	Contact angle hysteresis
γ	Surface tension

Υ	Adiabatic constant of surrounding gas
ρ	Density
ρ_l	Density of liquid drop
ρ_g	Density of gas
ν	Kinematic viscosity
τ_l	Surface tension stress
ζ	Spread factor
φ_s	Solidification parameter
ε	Effusivity function, $\varepsilon = \sqrt{\rho k c_p}$
$\emptyset$	Ratio of surface wet area to total surface area
γ_{WI}	Surface tension of water-ice
γ_{SW}	Surface tension of substrate-water
γ_{SI}	Surface tension of substrate-ice
γ_{IG}	Surface tension of ice-gas
θ_{WI}	Contact angle of water-ice
θ_{IG}	Contact angle of ice-water
θ_{WG}	Contact angle of water-gas (i.e. apparent contact angle)
α_w	Thermal diffusivity of water drop
α_{ice}	Thermal diffusivity of ice
ξ	Evaporation rate constant
η	Similarity variable
τ_{rz}	Shear stress at droplet spread area

α	Adjusting parameter
Γ	Damping ratio
τ	Time constant
μ_w	Dynamic viscosity of water
μ_{air}	Dynamic viscosity of air
μ_g	Dynamic viscosity of gas
μ_i	Chemical potential of particle i_{th}
μ_s	Chemical potential of solid particle
μ_l	Chemical potential of liquid particle
γ_o	Surface tension without formation of ice nuclei
$\lambda(t)$	Surface tension variation as a function of time
$\gamma(\lambda)$	Variation of surface tension through ice nucleation
δ_w	Boundary layer thickness of spread water
δ_{air}	Boundary layer thickness of air
α_{pa}	Thermal diffusivity of post-air domain of rough surface
θ_{pa}	Temperature difference of post air domain with liquid drop
η_{pa}	Post-air domain similarity variable
θ_w	Temperature difference of water domain with liquid drop
η_w	Water domain similarity variable
δ_h	Heat penetration length
φ	Viscous dissipation function

Dimensionless Numbers

Ca — Capillary number $(= \frac{\mu U_{cl}}{\gamma})$

We — Weber number $(= \frac{\rho V^2 D}{\gamma})$

Re — Reynolds number $(= \frac{\rho V D}{\mu})$

K — Splashing number$(= \sqrt{We\sqrt{Re}})$

Ste — Stefan number$(= \frac{C_{p,l}(T_m - T_s)}{H_{f,l}})$

Pr — Prandtl number $(= \frac{\nu}{\alpha_w})$

Pe — Peclet number $(= \frac{VD}{\alpha_w})$

S_c — Splashing threshold number $(= 2.85 Ca^{0.5}(\frac{p}{P_{atm}})^{0.42})$

P_s — Dimensionless number defining drop wetting dynamics on super hydrophobic surfaces $(= We/Re^{0.8})$

s^* — Dimensionless growth rate of freezing front $(= \sqrt{2t^* \frac{Ste}{Pe}})$

t^* — Dimensionless time $(= \frac{Vt}{D})$

R — Dimensionless spreading droplet radius $(= \frac{r}{r_{max}})$

B — Spalding number $(= \frac{C_{p,v}(T_g - T_d)}{H_v})$

C_D — Drag force coefficient

Subscripts

w — Water

s — Substrate

pa — Post-air domain

rz	Associated with r-z plane
g	Gas
l	Liquid
WI	Water-ice
SW	Substrate-water
SI	Substrate-ice
IG	Ice-gas
WG	Water-gas
i	Initial condition
max	Maximum

Chapter 1

Introduction

Investigation of droplet impact behavior on solid surfaces has been progressively developed by experimental, numerical and theoretical studies since the study of Worthington.[4] Indeed, understanding the physics governing the droplet impact on wet and dry solid surfaces has plenty of applications in industries ranging from thermal spray, fuel injection in combustion chamber, ink jet printing, electrical transmission power lines and aerospace. In thermal spray processes, molten particles are accelerated through high temperature gas jet then impacting on the substrate forming a deposit.[5] Therefore, molten droplet impact condition (i.e. droplet impact velocity, droplet temperature and size) substantially determines microstructure of coating.

In terms of problems related to electrical transmission power lines, the effect of water droplet impacting on solid metal surfaces can be highlighted. It results in sever ice accretion in cold natural condition. In fact, accumulated ice results in power outage or even disruption, as it was observed in January 1998 in Canada.[6] Consequently, various anti-icing and de-icing methods have been-used in power lines through advanced technologies (i.e. low adhesion ice surfaces and development of interface sciences). Supercooled droplet impact on solid surfaces is also problematic for aerospace industries (i.e. aircraft wings and engine nacelle). At realistic inflight icing condition which mostly occurs during take off and landing time at altitudes between 9000 to

20000 ft, aircraft is faced impact of supercooled water droplet located on upper troposphere and cirrus clouds.[7] Increased accumulated ice due to the impact of supercooled water droplet on aircraft exterior will change aerodynamic characteristics of wings which results in an increased drag force. Therefore, understanding wetting and freezing behavior of supercooled water is systematically important for ice formation retardation purposes.

To this end, it should be highlighted that droplet wetting behavior in natural condition whether in freezing temperature or not is influenced by incoming air flow. In fact, the effect of stagnation flow on droplet wetting dynamics can mimic realistic occurrence of water droplet (room temperature or super-cooled droplet) impacting on leading edge of an aircraft. In the current study, various experimental analysis of the room temperature and supercooled water droplet impacting on various solid surfaces with different wettabilities accompanied with stagnation air flow are presented. Surfaces with various wettabilities were used to investigate the effect of stagnation air flow on spreading and recoiling behavior of an impacting water droplet in splashing and non-splashing regime which is highlighted in subsequent sections.

1.1 Surface wettability

Wettability of a surface is characterized by static surface contact angle where equilibrium condition is satisfied. Equilibrium condition is related to triple point characteristic (i.e. solid/liquid/gas contact point). Practically, every surface has a distinct adhesive force when liquid droplet is rested on it. It means that a surface with larger adhesive force results in larger wetting area. This phenomenon is well-defined by balancing of surface tension forces at triple phase line, which is defined by Young's equation[8], as illustrated in equation (1.1). Forces acting on a sessile droplet are illustrated in figure (1.1).
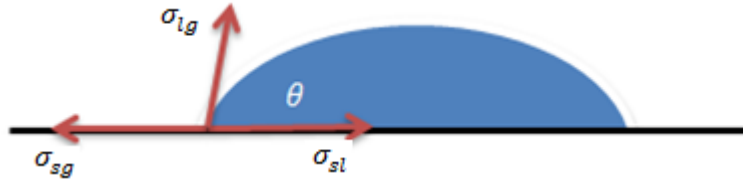
Figure 1.1: Balance of forces at contact line.

$$\cos\theta = \frac{\gamma_{sg} - \gamma_{sl}}{\gamma_{lg}} \tag{1.1}$$

In fact, if substrate has a contact angle below 5° is referred as a superhydrophilic surfaces [9,10] (e.g. Nepenthes pitcher plant[11]). In these surfaces, balance of forces between gravity, capillarity and viscosity results in equilibrium contact angle as low as 5° or even smaller. In fact, in this regime of droplet impact condition, capillary force plays not an important role and droplet hardly faces retraction phase when it is reached to the maximum wetting diameter. Same phenomenology is observed for hydrophilic surface having contact angle below 90° (e.g. aluminum substrate). However, when contact angle is larger than 90°, droplet impact condition might be systematically different which is related to kinetic energy of an impacting droplet referred as a hydrophobic surfaces. If triple phase point contact angle become larger than 150° it is defined as a superhydrophobic surface.[12] Having strong capillary force, droplet bouncing is observed even for gently deposited droplet on super-hydrophobic surfaces.[13], as demonstrated in figure (1.2).
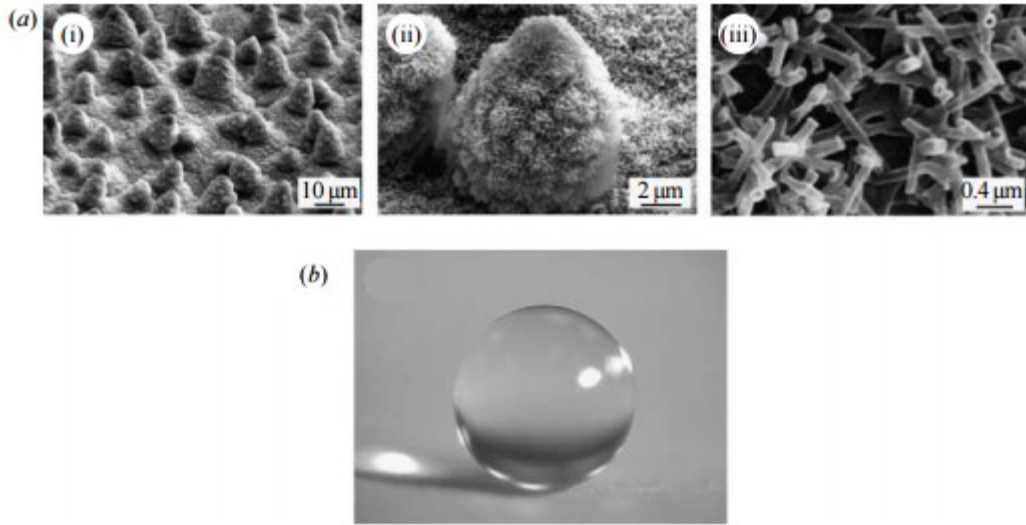
Figure 1.2: Effect of entrapped air on the generation of super mobile surfaces called superhydrophobic substrate. a) SEM images of lotus leaf and b) water droplet sitting on a superhydrophobic Lotus leaf.[14]

In terms of defining surface mobility, the difference between advancing and receding contact angle is required to be used which is called contact angle hysteresis. In fact, contact angle hysteresis is attributed to the surface morphology namely surface roughness and chemical heterogeneity.[8] Typically, very small contact angle hysteresis indicates surface water mobility. Superhydrophobic surfaces have shown great water repellency and mobility where static contact angle is larger than 150° and hysteresis contact angle is below 10°.[15] Measurement of these angles are carried out mostly by two methods. The first method is expanding and retraction where a A very narrow needle is inserted inside of sessile droplet and consequently by adding or getting a small amount of liquid advancing and receding contact angle is measured. Another method of measuring contact angle hysteresis is the so-called tilting method. Sessile droplet's incipient motion on an inclined surface is recorded by high speed camera for measuring advancing and receding contact angles.[16] It has been highlighted that surface wettability has a direct effect on the contact line velocity which can be represented by the capillary number.[20]

When a droplet is gently deposited on a surface droplet spreading phase is not dominated by inertia force but it is affected by capillary-viscous force. In general, effect of gravity is neglected if droplet Bond number is small. Therefore, the most important dimensionless number describing this phase is capillary number (i.e. $Ca = \frac{\mu U_{cl}}{\gamma}$) where U_{cl} is contact line velocity. It should be highlighted that this contact line velocity is also a function of surface wettability. Several works[17,18] were carried out to relate the dependency of contact angle to contact line velocity. By changing surface wettability, contact line velocity is also changed which eventually alters droplet dynamics behavior. This issue was analyzed by Hofmann[19], as illustrated in equation (1.2).

$$f_H = \arccos\left\{1 - 2\tanh\left[\left[5.16\left[\frac{x}{1+1.31x^{0.99}}\right]^{0.706}\right]\right]\right\} \tag{1.2}$$

Hofmann plotted advancing apparent contact angle versus capillary number when droplet impact velocity was very small and just capillarity and viscosity forces define the spreading behavior. Later on, Kistler[20] used a novel correlation which calculates dynamic contact angle based on the relation between static contact angle and capillary number by using Hofmann empirical function, as illustrated in equation (1.3).

$$\theta_d = [Ca + f_H^{-1}(\theta_e)] \tag{1.3}$$

Equation (1.3) is widely used in numerical simulations.[20] It was claimed that due to the nature of surfaces, which are not ideally smooth, advancing or receding contact angle is replaced with static contact angle, illustrated in equation (1.3), which depends on the direction of contact line velocity vectors.[20] In the following, spreading and recoiling behavior of an impacting water droplet in isothermal condition on surfaces with various wettabilities are presented.

1.2 Isothermal droplet impact dynamics

Since the first study of droplet impact about 140 years ago tremendous efforts have been allotted to characterize the dynamics of droplet in order to understand some important parameters like wetting area and residual time of an impacting water droplet on substrate. To do this, different experimental, theoretical, numerical studies were carried out to analyze hydrodynamics of droplet in details. When a droplet impacts on the surface three distinct behaviors can be observed namely spreading, splashing and rebounding, as shown in figure (1.3).. Every aspect of droplet dynamics mentioned above is strongly related to different parameters like droplet liquid properties and surface morphology. The governing parameters for the impact of isothermal droplets are droplet's diameter D, impact velocity V, static contact angle θ_e, contact angle hysteresis θ_{hys}, density ρ, surface tension γ, dynamic viscosity μ and gravitational acceleration g.[21] In wetting phenomenon, three important dimensionless numbers namely Weber (We = $\frac{\rho V^2 D}{\gamma}$), Reynolds (Re = $\frac{\rho V D}{\mu}$) and Ohnesorge number (Oh = $\frac{\mu}{\sqrt{\rho \gamma D}}$) are involved. However, having two aforementioned dimensionless numbers are necessary for describing dynamics of an impacting water droplet.

Normal impacts of liquid droplet on solid surfaces results in various outcomes. It might be gently deposited on the substrate, spread on substrate reaching to the flattened disk or even accompany with some fragmentation and receding break up or completely rebound from substrate, as illustrated in figure (1.3). In the following section, as a first step, phenomenology of liquid droplet impacting on solid surfaces are presented.
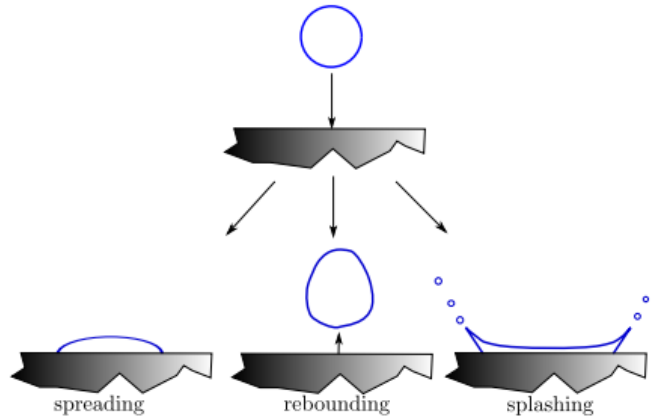
Figure 1.3: Liquid droplet impact behavior on solid surfaces, spreading, rebounding, and splashing.[22]

1.2.1 Droplet spreading and recoiling

Outcome of droplet impact on solid surfaces can be varied by increasing droplet inertia force. Inertia dominated droplet impacting on solid surfaces results in the formation of spread lamella which is expanded rapidly. Therefore, droplet ligament is extended until viscous and capillary forces overcome inertia force where droplet reaches to the maximum wetting diameter. At the maximum spreading diameter (i.e. maximum wetting diameter) droplet gets a flattened disk shape then retracting to the equilibrium state like a truncated sphere or completely wet the surface or even bounces from the substrate. It should be highlighted that for moderate inertia droplet impact condition surface contact angle is the most important parameter describing the outcome of droplet impact behavior. It is worth mentioning here that if inertia force increases ligament extension is increased so that some break up might occur during spreading (prompt splashing) or recoiling phase (receding break up). Phenomenology of aforementioned scenarios are explained in subsequent sections.

Reviewing relevant studies show that droplet impact phenomena on solid surfaces were extensively elaborated by means of numerical[23,24], theoretical[25] and experimental[22,26-28] which

most of them are focused on wettable solid surfaces. Analyses of droplet impact behavior on superhydrophobic surfaces were quite elaborated recently which is described in detail in subsequent sections.

One of the fundamental works of an impacting droplet on solid surfaces at different temperatures was carried out by Chandra and Advision.[26] Low surface tension liquid droplet (e.g. n-heptane) having 1.5 mm diameter was impacted on dry and wet solid surfaces. It was observed that spreading rate of droplet at early stage of impact condition remains unaffected by surface temperature and it is quite similar to both dry and wet surfaces. Furthermore, high resolution images showed that single bubble was formed at impingement location. It was asserted that the population of bubble are increased by increasing surface temperature. The higher surface temperature the larger rate of bubble formation. However, the overall shape of liquid droplet is not influenced by these accumulated bubbles at the early stage of the droplet impact (i.e. less than 0.8 ms). Similar study was carried out by Dam and clerk[29] showed that bubble forms at the early stage of impact condition and it is dependent to the droplet impact velocity. It was mentioned that the main reason of bubble formation is due to the air entrapment underneath of an impacting water droplet and substrate. Furthermore, the size of bubble is affected by droplet Weber number (i.e. the higher Weber number the smaller formed bubble) but it is unaffected by surface wettability. However, effect of different liquid droplet properties (i.e. surface tension, viscosity, density, droplet sizes and impact velocities) along with experimenting various target substrates having different roughness's were elaborated in detail by Rioboo et al.[28]

Temporal spreading diameter of an impacting liquid droplet with different properties (i.e. droplet sizes which varied from 0.15 mm to 3.5 mm, different liquid viscosities and surface tensions and velocities (i.e. from 0.78 m/s to 4.1 m/s) on different target substrates ranging from

superhydrophilic surfaces (i.e. advancing contact angle as low as 10º) to superhydrophobic surfaces (e.g. advancing contact angle up to 162º) was experimentally observed by Rioboo et al.[28] Different influential parameters were used to find a correlation between surface wettability with two important dimensionless numbers namely Weber and Reynolds. It was shown that different phases are involved during impact process. Kinematic phase in which dimensionless spreading diameter increases with square root of dimensionless time, $t^{*0.5}$, spreading phase is initiated which all aforementioned parameters play important roles on it. Finally, at relaxation phase, capillary and viscous forces determine the final form of the droplet equilibrium diameter. In the following, phenomenology of droplet impact dynamics on low wettable surfaces is presented.

Sufficiently high inertia droplet (i.e. above 0.1 m/s for millimeter size water droplet) impacting on low wettable surfaces (i.e. superhydrophobic surfaces) results in complete bouncing due to the weak effect of liquid-substrate adhesive force. Richard and Quere[30] studied effects of droplet impact velocities ranging from almost below the 0.1 to 0.5 m/s on the droplet coefficient of restitution (i.e. ratio of droplet rebounding velocity to the droplet impact velocity). While coefficient of restitution was observed to be around 0.9, it was reduced where droplet impact velocity became close to the critical velocity of repulsion on superhydrophobic surfaces. By increasing droplet impact velocity, viscous dissipation becomes dominant. It was highlighted that two sources of viscous dissipation are presents. One source of viscous dissipation is related to liquid droplet viscosity. However, it was claimed that where droplet deformation is small (i.e. small droplet impact velocity) viscosity effect is neglected, as it was observed by doubling droplet viscosity by experiment of water-glycerol solution.[30] It was not seen any reduction on coefficient of restitution. On the other hand, another source of viscous dissipation is related to the presence of surface roughness which is emerged on the surface contact angle hysteresis. Coefficient of

9

restitution was reduced about 0.8 where contact angle hysteresis was increased up to 30º but having same static contact angle as high as 160º.[30]

It was asserted that for a surface having small contact angle hysteresis viscous dissipation could be neglected for an impacting droplet where formation of spreading contact line is not present.[13] Therefore, droplet dynamics (e.g. droplet contact time) obeys behavior of an oscillatory of mass-spring system defined by Okumura et al.[13]. Scaling arguments was used to determine contact time of an impacting droplet in very low and moderate droplet impact velocity. It was highlighted that for small droplet impact velocity (e.g. 0.09 m/s) droplet deformation is small and the effect of viscosity is negligible. Therefore, model of mass-spring is well accounted for an impacting droplet. In fact, contact time of liquid droplet can be obtained based on the results of harmonic mass-spring solution.[13] Furthermore, velocity characteristic of the droplet repulsion on the superhydrophobic surface was also derived based on the definition of water droplet capillary length, as demonstrated in equation (1.4). In this equation, k^{-1}, is the capillary length of water droplet defined by equation (1.5).

$$V_c = (gR^3k^2)^{1/2} \tag{1.4}$$

$$k^{-1} = \sqrt{\frac{\gamma}{\rho g}} \tag{1.5}$$

On the other hand, by increasing droplet impact velocity, large droplet deformation is occurred and model of the linear mass-spring is no longer valid. In this phase droplet contact time is independent of the impact velocity and just vary with droplet size, $(R^{\frac{3}{2}})$. Effect of the viscous dissipation due to the formation of contact line cannot be ignored anymore.[13]

Droplet contact time is an important parameter in the wetting behavior of an impacting droplet on the superhydrophobic surface. Indeed, reduction of the droplet contact time have plenty of applications in industries. Lower solid-liquid interaction might be resulted in ice-free surfaces in cold environmental conditions. It was reported that droplet contact time can be reduced by increasing receding contact angle[31] or by switching recoiling dynamics behavior from axisymmetric retraction to unaxisymmetric one[32] up to about 50% (based on inertia-capillary time scale[33] (i.e. $(\rho D^3/8\sigma)^{1/2}$) through droplet break up and finally by pancake bouncing mechanism which rectification of capillary energy upward dramatically reduces droplet contact time up to 4 folds to conventional one.[34] Recently, it was highlighted that droplet contact time in splashing regime is also reduced where stagnation flow is present. [35] Although aforementioned techniques were used to reduce droplet adhesion force against surfaces by minimization of droplet contact time or by imposing shear force of air flow promoting droplet shedding[36,37] the effect of stagnation air flow on an impacting water droplet in non-splashing-transitional regime (i.e. non-splashing to splashing regime) and finally violent splashing regime was not observed yet which is profoundly elaborated in chapter 4. To this end, in the following, the most well-known predictive models of maximum spreading diameter ranging from hydrophilic to superhydrophobic surfaces are presented.

Variety of studies presented different models of the predictive maximum spreading diameters based on energies involved during impact process.[38,39] Furthermore, Attane et al.[40] derived unsteady predictive model of maximum spreading diameter based on the transient involving energies. Here, for brevity, a well-known energy based model proposed by Passandideh-Fard et al.[41], based on the balance of all energies before and after impacts, is presented. Near wall boundary layer thickness was used for proper prediction of maximum spreading diameter instead of

thickness of splat which overestimates the maximum spreading diameter. Furthermore, the effect of surface wettability was also considered in the model which provides a suitable floor for wider comparison with surfaces having different wettabilities. Typically, where Weber and Reynolds numbers are high enough, the predicted maximum spreading values agree well with experimental results. This model is presented in equation (1.6) which is defined based on the advancing dynamic contact angle during spreading phase.

$$\zeta_{max} = \frac{D_{max}}{D} = \sqrt{\frac{We+12}{3(1-cos\theta_{adv})+4\frac{We}{\sqrt{Re}}}} \qquad (1.6)$$

The second model is based on the direct usage of continuity and momentum equations. In this analytical hydrodynamic model, proposed by Roisman[42], the effect of rim edge on the maximum spreading diameter also considered. Velocity distribution in viscous region was derived based on the analytical self-similar solutions which satisfy Navier-Stocks equation. Finally, based on the some experimental evidences a semi-empirical engineering correlation was proposed to predict the maximum spreading diameter, as shown in equation (1.7).

$$D_{max} \approx 0.87Re^{\frac{1}{5}} - 0.4Re^{\frac{2}{5}}We^{-\frac{1}{2}} \qquad (1.7)$$

In this correlation effect of the surface wettability was not considered. It was highlighted that if Weber and Reynolds numbers are high enough the maximum wetting diameter is independent of surface wettability.[43] Both hydrodynamic and energy based model are used for comparison of experimental data on hydrophilic and hydrophobic surfaces. However, for superhydrophobic surfaces one additional scaling law analysis proposed by Clanet et al.[44] is also used for proper evaluation. In scaling law analysis, it was claimed that P_s factor (i.e. $We/Re^{0.8}$) determines the dynamics of wetting. For an impacting droplet with P_s <1, the maximum wetting diameter is just influenced by the capillary force and it is independent of the viscosity and can be approximated by

D_{max}/D=0.9$We^{0.25}$ but for P_s >1 dynamics of droplet is followed by the viscous force and represented by D_{max}/D=0.9$Re^{0.2}$.

1.2.2 Droplet splashing

Splashing occurs when pressure rise inside of liquid droplet exceeds the surface tension force which results in liquid droplet breaks up at the impact point where surface energy is small.[45,46] Indeed, formed shock wage at the impact point of very high velocity liquid droplet results in liquid droplet compressibility which produces dramatic pressure distribution at the droplet impact point. Recent study by Yoon and Demosthenous[47] revealed that pressure distribution is varied by presence of entrapped air where droplet contacted on substrates. This phenomenon was investigated through numerical simulation and experimental observation. Both numerical and experimental results proved that displaced air from falling water droplet acquires momentum from impacting droplet which results in generation of vortex motion right above the solid-liquid interfacial area. It was claimed that splashing phenomenon happens when formed spread lamella is drawn along this accelerated air. Furthermore, produced perturbation during spreading phase, propagates radially and it is fundamental source of the instability which results in the formation of fingers at the rim periphery of spreading droplet.[47] This generated instability is a function of surrounding gas pressure and it is dramatically reduced by gas pressure reduction.[48]

Although previously studies reveals that surface roughness and droplet liquid properties are important parameters for prediction of splashing phenomenon the effect of surrounding air pressure on behavior of splashing is explained in the following.[48] In fact, splashing phenomenon is related to the droplet size, droplet impact velocity, surface tension and viscosity of a liquid

droplet which is correlated with three dimensionless numbers namely, Weber and Reynolds numbers and also dependent dimensionless number K defined by equation (1.8).[49]

$$K = \sqrt{We\sqrt{Re}} \qquad (1.8)$$

Liu et al.[48] presented a correlation of splashing threshold based on the previously accepted dimensionless numbers namely Weber and Reynolds numbers and ambient air pressure which was supported by the theory of Kelvin-Helmholtz (K-H) instability. Experiment of Liu et al.[48] involved impacts of 1.7 mm water droplet with different impact velocities from 1 to 5 m/s on the smooth plexiglass substrate having small roughness (0.8μm) on different substrate angles from horizontal to 45°. In order to observe the effect of air pressure on the splashing phenomenon, a chamber was designed in order to control the surrounding gas pressure from 0.2 to 6 atm. Previous experiments showed that a rise in the internal pressure of liquid droplet might produce droplet splashing which is a function of liquid droplet surface tension. Although previously pressure distribution defined by water hammer pressure, shown in equation (1.9) [50], was related to liquid properties (i.e. droplet density, velocity and speed of sound in the liquid droplet), a modified form of pressure distribution at the droplet impact point was defined by Xu et al.[51] which is a function of surrounding gas density and speed of sound in the gas instead of liquid droplet. This model is shown in equation (1.10).

$$P = \rho_l V C_l \qquad (1.9)$$

$$P \sim \rho_g V_s C_g \qquad (1.10)$$

Equation (1.10) is based on the spreading velocity (i.e. V_s) of an impacting water droplet and density and speed of sound in the gas. The relation of droplet impact velocity and spreading velocity can be expressed by equation (1.11).[48]

$$V_S = \sqrt{\frac{DV}{4t}}$$ (1.11)

Based on the ideal gas law and definition of speed of sound, pressure rise inside of droplet during impact condition can be expressed by equation (1.12) defined by Xu et al.[51] where Υ is the adiabatic constant of surrounding gas, M_g, is the Molecular weight of gas, V, is the droplet impact velocity, k_B is the Boltzmann constant and T_g, is the surrounding gas temperature.

$$P = \frac{P_{atm}M_g}{k_BT} \cdot \sqrt{\frac{DV}{4t}} \cdot \sqrt{\frac{\Upsilon k_B T_g}{M_g}}$$ (1.12)

If pressure shown in equation (1.12) exceeds the amount of generated surface tension stress, produced by thin layer of spreading droplet, splashing is occurred. Surface tension stress can be expressed by equation (1.13) where γ, and ν are surface tension and kinematic viscosity of liquid droplet.

$$\tau_l = \frac{\gamma}{h_{lamella}} = \frac{\gamma}{\sqrt{\nu t}}$$ (1.13)

In fact, splashing phenomenon is the competition of two aforementioned stresses. Although pressure inside of droplet generates instability the surface tension stress stabilizes propagated pressure.[51] It was claimed that splashing phenomenon is initiated if ratio of gas-pressure stress to surface tension stress, defined by equation (1.14), exceeds the value up to 0.45.

$$\frac{P}{\tau_l} \sim \frac{\frac{P_{atm}M_g}{k_BT} \cdot \sqrt{\frac{DV}{4t}} \cdot \sqrt{\frac{\Upsilon k_B T_g}{M_g}}}{\frac{\gamma}{\sqrt{\nu t}}} = P_{atm} \cdot \sqrt{\Upsilon M_g} \sqrt{\frac{DV}{4k_B T_g}} \frac{\sqrt{\nu}}{\gamma}$$ (1.14)

Therefore, the final form of predictive empirical correlation of splashing thresholds, in terms of capillary number (i.e. *We/Re*) and surrounding gas pressure is demonstrated by equation (1.15).

$$S_c = 2.85Ca^{0.5}(\frac{p}{p_{atm}})^{0.42} > 1 \tag{1.15}$$

Which provides more comprehensive criterion compare to the previously defined predictive splashing threshold (i.e. $\sqrt{Ca} > 0.35$).[52]

Effect of two distinct mechanisms of splashing namely corona and prompt splashing was elaborated through interplay role of the roughness and surrounding pressure.[53] For smooth surfaces surrounding pressure defines corona splashing. The higher the ambient pressure the larger the edge of lifted ligament of spreading droplet due to the accelerated air upon droplet impact point. It was found that if surrounding pressure becomes lower than critical pressure (34 kpa) corona splashing is completely eliminated. On the other hand, for rough surfaces, mechanism of splashing is dramatically changed by increasing surface roughness. Prompt splashing presents where small droplet is detached from the thin advancing spread contact line. In order to eliminate the effect of surrounding air pressure, which produces coronal splashing, very low ambient air pressure far below the defined critical pressure was used for proper evaluation of prompt splashing.

 A single ethanol droplet (3.4 mm) impacted on the substrate with velocity up to 4.3 m/s. Surrounding pressure was reduced down to 17kp to just evaluates the effect of different surface roughness (e.g. from 3μm to 78 μm) on the prompt splashing mechanism. While for smooth surface it was not observed any splashing occurrence, prompt splashing appeared for the lowest surface roughness (5 μm) at the early stage of impact. However, it was stabilized with the help of surface tension stress at the later time. Nevertheless, by increasing roughness of surface, prompt splashing inevitably presents during entire spreading process. It was concluded that where droplet impacts on the substrate having small surface roughness corona splashing controls the droplet

ejection from lifted droplet ligaments while for very rough substrates prompt splashing governs shattering of tiny droplets during spreading phase.[53]

1.3 Non-isothermal droplet impact

Liquid droplet phase change is initiated by impacting undercooled droplet on the cold substrate. Respecting hydrodynamic analysis with or without solidification, abundant theoretical[54], experimental[65] and numerical[55,56] studies were carried out. In fact, combination of heat transfer knowledge along with phase change mechanism (i.e. solidification) are necessary for prediction of droplet pinning on cold substrates. In the following sub-sections, relevant studies regarding theoretical and experimental investigations of an impacting droplet with solidification are discussed.

1.3.1 Analytical models

Abundant effort had been allotted regarding droplet spreading characterization in the non-isothermal condition by analytical and experimental methods. However, numerical technique was also used where capturing moving solid-liquid phase (i.e. freezing line) is possible which were mostly carried out for molten metals. On the other hand, solid-liquid interface capturing for supercooled water droplet in the still air needs a substantial develop on the conventional techniques namely VOF or level-set methods. Where cold air flow is also present it becomes much more complicated problem. Therefore, the current research is focused on the analytical and experimental studies. Most of analytical models of droplet solidifications are related to the effect of molten metal droplet impacting on a substrate.[57,58] The pioneer of these works was Madejeski.[58] The combination of experimental and analytical study showed that the maximum spread factor of splat is a function of three dimensionless numbers namely Reynolds, Weber, Peclet and parameter of K

which is a function of freezing line velocity, derived from solution of the Stefan problem. By proposing some approximations, the maximum spread factor of the splat is demonstrated by equation (1.16).

$$\xi_{max} = 1.5344k^{-0.395} \tag{1.16}$$

In the model of Madejeski, It was assumed that thickness of the spreading lamella just varies with time and not space and droplet gets a cylindrical shape at the maximum spreading diameter. It was claimed that the agreement between experimental data and analytical model was relatively good if constant freezing velocity derived from the solution of Stefan problem is taken into account. Later on, some modification on freezing velocity was carried out to satisfy boundary condition at the upper part of splat in order to show a better agreement with experimental results.[59]

Another predictive model of maximum spreading diameter with consideration of phase change is presented by Passandideh-Fard et al.[57] This model, which is based on the balance of energies, incorporates another term of viscous dissipation along with conventional term in hydrodynamics model. It was assumed that all of kinetic energy is lost in the solidified ice layer thickness. Therefore, the final form of the aforementioned model is demonstrated by equation (1.17).

$$\zeta_{max} = \frac{D_{max}}{D} = \sqrt{\frac{We+12}{\frac{3}{8}Wes^*+3(1-cos\theta_{adv})+4\frac{We}{\sqrt{Re}}}} \tag{1.17}$$

In deriving equation (1.17), it was assumed that heat conduction is one dimensional, the substrate is isothermal, the thermal contact resistance is negligible and the stefan number is small, as well. Therefore, s^* is increased with dimesnioless time shown by equation (1.18).[60]

$$s^* = \sqrt{2t^* \frac{Ste}{Pe}} \tag{1.18}$$

Where s^* is dimensionless growth rate of freezing front which follows Stefan problem soultion. Dimensionless Stefan number, which is the ratio of sensible heat to the latent heat, $Ste = \frac{C_{p,l}(T_m - T_s)}{H_{f,l}}$, is directly related to the degree of subcooling (i.e. difference between substrate temperature and melting point temperature of liquid droplet, $(T_m - T_s)$). It was shown that if square root of Stefan to Prandtl numbers becomes much smaller than one (i.e. $\sqrt{\frac{Ste}{Pr}} \ll 1$) the effect of solidified ice layer on the maximum spreading diameter is negligible. Similar study was carried out by Aziz and Chandra[61] based on the another model of dimensionless ice growth which was derived from an approximate analytical solution.[62] It was assumed that conduction heat transfer is 1D, there is not any thermal contact resistance at the solid-liquid interface, reduction in droplet temperature across the solidified layer is negligible and the substrate was considered as a semi-infinite surface and thermal properties of substrates are constant. Therefore, dimensionless ice growth was presented as a function of Stefan number ($Ste = \frac{C_{p,l}(T_m - T_s)}{H_{f,l}}$), Peclet number ($Pe = VD/\alpha_w$), and effusivity function $\varepsilon^2 = k\rho C_p$, as demonstrated in equation (1.19). Which k, ρ and C_p are thermal conductivity, density and specific heat, respectively.

$$S^* = \frac{2}{\sqrt{\pi}} Ste \sqrt{\frac{t^* \varepsilon^2_{substrate}}{Pe \, \varepsilon^2_{drop}}} \qquad (1.19)$$

Therefore, by substitution of equation (1.19) in (1.17), final predictive model of the maximum spreading diameter accompanied with phase change is shown by equation (1.20).

$$\zeta_{max} = \frac{D_{max}}{D} = \sqrt{\frac{We + 12}{WeSte\sqrt{\frac{3\varepsilon^2_{substrate}}{2\pi Pe \varepsilon^2_{drop}}} + 3(1 - \cos\theta_{adv}) + 4\frac{We}{\sqrt{Re}}}} \qquad (1.20)$$

In this model it was claimed that if solidification parameter, φ, controlled by Stefan number, Prandtl number ($Pr = \nu/\alpha_w$) and droplet/substrate properties becomes below the unity the effect of solidified ice layer on the maximum spreading diameter is negligible, as demonstrated in equation (1.21).

$$\varphi = \frac{Ste}{\sqrt{Pr}}\sqrt{\frac{\varepsilon^2_{substrate}}{\varepsilon^2_{drop}}} < 1 \qquad\qquad (1.21)$$

However, both predictive models of the maximum spreading diameter accompanied with phase change slightly overestimates the maximum spread factor as compared with measured experimental results because of the fact that thermal contact resistance were not taken into account in the aforementioned models. After discussion regarding models of the maximum spreading diameter for molten metal liquids, some analytical studies regarding the metastable supercooled water droplet impacting on the cold solid surfaces are presented.

Although some studies theoretically found temperature distribution of the formed ice based on solution of transient conduction equation [63,64] ,to the best of our knowledge, there is not any predictive model of maximum spreading diameter for metastable supercooled water droplet except model of Bahadur et al.[2] which was developed recently.

Analytical predictive model of supercooled water droplet repulsion or pinning on superhydrophobic surfaces was carried out by Bahadur et al.[2] through combination of classical nucleation theory and droplet wetting dynamics. This model was derived based on the three assumptions. First, droplet pinning is happened at the recoiling stage and the effect of phase change during spreading phase and consequently on the maximum spreading diameter is negligible. This assumption was also experimentally observed by robust study of Mischenko et al.[65] Secondly, it

was assumed that droplet is spread on the superhydrophobic substrate as a mass-spring model which formerly showed by Okumura et al.[13] Finally, it was shown that superhydrophobicity break down is initiated by the growth of hemispherical ice cap underneath of an impacting water droplet and substrate. An innovative technique was used to show this effect on droplet wetting dynamics equation. Based on the Cassie-Baxter model, apparent contact angle was integrated to the surface topography where ice layer is present through definition of wet surface to the total surface area, defined as a $\emptyset$ ratio, as demonstrated in equation (1.22).

$$cos\theta = -1 + 2\emptyset \qquad (1.22)$$

Based on the classical nucleation theory, nucleation rate multiplied with freezing front ice cap propagation rate was coupled to the equation (1.22) through variation of $\emptyset$ ratio, as shown in equation (1.23). In fact, where substrate temperature is cold enough for formation of ice nuclei, apparent contact angle of water-substrate is reduced due to the increase of $\emptyset$ ratio (see equation (1.22)). Consequently, superhydrophobicity break down might happen during retraction phase.

$$\emptyset(t) = 2\pi\emptyset_o \int_0^t J(t)[r(t)]^2 dt \qquad (1.23)$$

In equation (1.23) $J(t)$ and $r(t)$ are heterogeneous ice nucleation rate and radius of hemispherical ice cap formed on the substrate, respectively. Final form of the dimensionless predictive model of droplet repulsion or pinning on a superhydrophobic surface is demonstrated by equation (1.24). Theoretical value of (C) is defined as a multiplication of kinetic rate of ice nucleation (K), and freezing-front velocity (U)[66], shown in equation (1.25). t_c is the droplet total contact time. Approximated function of the interface temperature is defined by equation (1.26).[65]

$$\frac{d^2R}{dt^2} + [1 - C\phi_o t_c^2 \exp(f(T_{interface}))] R = 0 \qquad (1.24)$$

21

$$C = \pi K U^2. \tag{1.25}$$

$$f(T_{interface}) \approx \frac{-T_m^2}{\left(\left(T_m - T_{(s-l)interface}\right)^2 T_{(s-l)interface}\right)} \tag{1.26}$$

As shown in equation (1.26), solid-liquid interface temperature becomes very important parameter. Indeed, nucleation rate, demonstrated in equations (1.27) and (1.28) are dramatically changed by this parameter. Therefore, appropriate prediction of this value is vital for proper calculation of ice nucleation rate shown by equation (1.27).

$$J(T) = K(T) A_{s-l} exp\left(\frac{-\Delta G_{Het}(T, \theta_{wI})}{k_B T_{(s-l)interface}}\right) \tag{1.27}$$

$$\Delta G_{Het}(T, \theta_{wI}) = \frac{T_m^2 16\pi \gamma_{wI}^3}{3H_f^2 (T_m - T_{(s-l)interface})^2} f_{(\theta_{wI})} \tag{1.28}$$

In equation (1.27) and (1.28), $J(T)$, $K(T)$, A_{s-l}, T_m, $T_{(s-l)interface}$, H_f, γ_{wI}, $f_{(\theta_{wI})}$, $\Delta G_{Het}(T, \theta_{wI})$ and k_B are nucleation rate, kinetic prefactor, solid-liquid interfacial area, melting temperature of frozen water, solid-liquid interface temperature, latent heat of fusion, water-ice surface tension, geometrical factor, Gibbs free surface energy based on the heterogeneous ice nucleation and Boltzmann constant. More detailed information regarding different types of ice nucleation mechanisms are presented in chapter 3.

Maitra et al.[67] showed interface temperature of an impacting water droplet on cold substrate can be approximated by equation (1.29) which is derived based on the concept of contacting two semi-infinite surfaces.

$$T_{(s-l)interface} = \left(\frac{\varepsilon_w T_w + \varepsilon_s T_s}{\varepsilon_w + \varepsilon_s}\right) \tag{1.29}$$

In equation (1.29), ε_w and ε_s are effusivity of water and surfaces, respectively. It is defined by equation (1.30).

$$\varepsilon = (\rho C_p k)^{0.5} \tag{1.30}$$

Where $\rho, C_p,$ and k represent density, specific heat and thermal conductivity, respectively. However, in the real occurrence of an impacting supercooled water droplet, interface temperature is subjected to the transient variation of droplet to substrate temperature which is not included in Maitra's model. Bahadur et al.[2] defined water-substrate interface temperature based on the solution of transient heat conduction from droplet to substrate. In this model effect of the thermal air resistance was also considered. Final form of the transient solid-liquid interface temperature derived by Bahadur et al.[2] is demonstrated in equation (1.31).

$$T_{(s-l)interface}(h, t_c) = T_{drop} + [(T_{substrate} - T_{drop})] \frac{erfc\left(\frac{h_{pa}}{2\sqrt{\alpha_{pa}t_c}}\right)}{erfc\left(\frac{h_w}{2\sqrt{\alpha_w t_c}}\right)} \tag{1.31}$$

Which h, α_w, t_c are height of pillar for textured superhydrophobic surface, thermal diffusivity of supercooled water droplet and total contact time of an impacting supercooled droplet on substrate, respectively. The subscript pa denotes pillar-air domain for textured superhydrophobic surfaces. Although equation (1.31) provides transient behavior of solid-liquid interface temperature but it underestimates (i.e. lower temperature than substrate) interface temperature at initial condition. Indeed, equation (1.31) needs modifications which are described in detail in chapter 3.

In spite of the fact that predictive model of the solid-liquid interface temperature is vital for appropriately defining heterogeneous ice nucleation rate in the still air, however, in the presence of cold air flow another thermodynamically preferable nucleation is also present which is defined

as a homogeneous ice nucleation. Jung et al.[36] showed that in unsaturated cold environmental condition, due to the presence of forced convective heat transfer and evaporation cooling, gas-liquid interface temperature becomes even lower than surrounding gas. Under quasi steady-state condition and balancing of energies for an evaporating sessile droplet local temperature difference between gas and supercooled water droplet is determined by equation (1.32).

$$\Delta T = T_g - T_w \approx -\frac{\Delta H_v \xi \rho_w}{MR} \frac{1}{h_g + k_w/l} \tag{1.32}$$

In equation (1.32), T_w denotes gas-liquid interface temperature and T_g, ΔH_v, ξ, ρ_w, M, R, h_g, k_w, l are the gas temperature, the enthalpy of vaporization, the evaporation rate constant, the supercooled water droplet density, the molecular weight, the radius of droplet, the convective heat transfer coefficient, the thermal conductivity and height of sessile supercooled water droplet, respectively.

Equation (1.32) provides concrete information regarding variation of ice nucleation rate based on gas properties (i.e. gas temperature, velocity and humidity) for a sessile droplet. However, it does not provide a relation for an impacting supercooled water droplet on the substrate. In fact, the effect of maximum spreading diameter, which results in larger both solid-liquid and gas-liquid interfacial area, was not considered in this model. These requirements must be taken into account for appropriately prediction of ice nucleation rate. After discussion regarding theoretical studies, recent experimental studies regarding droplet impact with solidifications are elaborated in the following topic.

1.3.2 Experimental studies

In terms of reviewing experimental works, abundant studies have been reported which all of them can be analyzed though combination of classical nucleation theory and heat transfer mechanisms. Evaluation of the heterogeneous ice growth inside of a supercooled water droplet, which is due to the solid-liquid interaction, was investigated by various studies.[2,36,65] Definition of the thermodynamic driving forces and Gibbs free energy were used to address critical condition of ice nuclei formation on a solid surface. However, in the cold environmental condition both the effect of heterogeneous and homogeneous ice nucleation are present, as water droplet exposed to both cold substrate and airflow (i.e. homogeneous nucleation). Previous evaluation of nucleation phenomena are limited to the effect of cold substrate and just few publications considered the effect of cold atmosphere on nucleation rate.[36,68]

Sassen et al.[68] showed that only homogeneous ice nucleation can describe the freezing behavior of the tremendously supercooled droplet whose temperature can be reached to as low as -35 ºC. It was also highlighted that the presence of formed ice-crystal on solid-liquid surface (i.e. heterogeneous nucleation) can promote ice growth inside of the supercooled water droplet while in homogeneous ice nucleation, due to the lack of ice nuclei (i.e. there is not solid-liquid interface), there would be a large delay on ice nucleation initiation.

An experimental study of homogeneous ice nucleation mechanism for free fall freezing droplet was carried out by Stephan et al.[69] In this study, by using depolarization technique for discrimination of phases, different nucleation rates of falling droplet were characterized based on the releasing height and the temperature of droplet. It was highlighted that homogeneous ice nucleation is initiated at very low temperature (-37 ºC) while heterogeneous temperature can

happen at higher temperatures (e.g. -8 °C). Indeed, it was claimed that such a large difference between two types of nucleation mechanisms can be referred to the nucleation agents which can be a cold substrate. However, more comprehensive elaboration of different types of nucleation mechanism was carried out by Sastry.[70] It was asserted that homogeneous ice nucleation can happen in wave clouds even at higher aforementioned temperature (i.e. -37 °C). The difference between laboratories measured temperature of homogeneous ice nucleation and realistic scenario in clouds is justified by the presence of evaporation mechanism. Nucleation mechanism can be altered when critical ice nuclei are located inside of supercooled droplet but close to the droplet gas-liquid interface. It was demonstrated that due to the evaporation of such a supercooled droplet in clouds ice nuclei eventually is contacted with droplet interface which results in rapid growth of crystallization. This type of nucleation, which is common in wavy clouds, called "contact-nucleation inside-out" produced by evaporation cooling due to blowing of cold airflow.[70]

Effect of the cold air flow on homogeneous ice nucleation of a sessile supercooled water droplet experimentally and theoretically elaborated by Jung et al.[36] This study was concerned about evaporation cooling of water droplet located on cold environment condition with thermal equilibrium state (i.e. temperature of droplet, substrate and atmosphere were as cold as -15 °C). Due to the fact that evaporation cooling is a dependent function respect to humidity, various relative humidities ranging from 30 to 100% were considered. Supercooled evaporation rate was experimentally determined on a controllable experimental condition. It was observed that preferred nucleation is highly related to the amount of Gibbs free surface energy. In fact, gas-liquid interface temperature, which was explained in previous section, is a determining parameter for explaining nucleation mechanism which is a function of cold air velocity and humidity. In unsaturated condition (i.e. low humidity) for average air velocities up to 2 m/s, accounted for velocity variation

in boundary layer, preferable ice nucleation mechanism was observed to be homogeneous one. However, where evaporation rate becomes insignificant in the saturated condition (there is not any evaporation where relative humidity is 100%) gas-liquid temperature reduction was not observed and thermodynamically preferable nucleation becomes heterogeneous one. Furthermore, when humidity is increased both liquid and substrate becomes more wet (i.e. frost formation) and chance of pinning is dramatically increased. Therefore, stronger shear force is needed to droplet being roll-off on the substrate which is directly correlated with contact angle hysteresis.[71,72]

Study of frost formation on superhydrophobic surfaces was carried out by Varanasi et al.[71] It was shown that heterogeneous ice nucleation is one of the main reasons of reducing static contact angle of sessile water droplet on the cold substrate originated from either desublimation or condensation. In case of the supersaturated condition, frost formation is initiated without any preference in location. It means that both Wenzel ice (inside of pillar and sideways of pillar) and Cassie ice (i.e. at the top of pillar) can be formed which results in a significant decrease in water-substrate contact angle. Consequently, by decreasing contact angle, wetting area are increased which results in higher heat transfer cooling rate which finally leads to the superhydrophobicity breakdown. Ice cap is rapidly developed where humidity is present. This phenomenon was validated by environmental scanning electron microscopy (ESEM) of formed frost on substrate's pillar. A droplet having small impact velocity close to 0.7 m/s impacted on both room and low temperature condition on a superhydrophobic surface. It was shown that frost formation can change wettability of surfaces converting superhydrophobic to hydrophilic surface.[73]

Evaluation of droplet impact behavior on solid surfaces with different wettabilities whether in room and low temperature condition was carried out by Alizadeh et al.[74] Wide range of droplet sizes from 1.6 to 3.4 mm with impact velocities ranging from 1.5 to 2.3 m/s impacted on solid

surfaces with wide range of static contact angles ranging from 44º to 149º highlighting different wettabilities from hydrophilic to superhydrophobic surfaces. Subsequent wetting dynamics and phase transition was observed using combination of high speed imaging and IR thermography. Droplet temperature was measured based on the IR thermometry, as water droplet is considered as an opaque object for IR camera. Temperature measurements of an impacted water droplet on various solid surfaces showed a rapid increase of temperature from supercooling condition (i.e. below zero) up to 0 ºC. This rapid rise in temperature is an indication of freezing initiation highlighting that latent heat of fusion is liberated at this stage. Due to the rapid jump in temperature, viscosity of impacting droplet vary dramatically causing droplet wetting dynamics to be affected by this variation.[75,76]

Viscous water droplet (i.e. supercooled water) impacting on superhydrophobic surfaces has gained abundant attention in the recent studies. Large number of parameters ranging from droplet size, droplet temperature, droplet impact velocity and surface morphology are involved in the characterization of droplet wetting dynamics. Khedir at al.[77] investigated results of a rather small droplet impact velocity (i.e. 0.54 m/s) at warm and supercooled condition impacted on a substrate maintained at temperatures as low as -10 ºC. In this study the effect of internally increased viscous dissipation was analyzed through measurement of coefficient of restitution. It was shown that in the range of Weber numbers from 5.2 to 5.7 and Reynolds numbers from 200 to 700 maximum spreading diameter and droplet contact times remained unaffected by an increase in viscosity up to 2.7 times to that of room temperature water droplet. In fact, it was claimed that for millimeters size water droplet impacting on the nano pillars rough surface the effect of contact angle hysteresis becomes negligible for Weber numbers smaller than 120.[78] On the other hand, measured values of coefficient of restitution showed a decrease up to 23% to that of room temperature droplet.[77]

Similar study was carried out by Maitra et al.[67] where 2.6 mm water droplet at room temperature

condition having two different Weber numbers namely 66 and 100 impacted on undercooled micro

and nano textured superhydrophobic surfaces maintained at temperature as low as -30 $^{\circ}$C. It was

observed that droplet contact time is slightly increased at Weber numbers up to 100 (i.e. higher

impact velocity of 1.7 compare to 1.4 m/s). It was claimed that an increase in droplet contact time

is related to locally near wall water droplet viscosity jump. In the light of fact that thermal diffusion

length of water droplet with small time scale (i.e. droplet contact time) is in the order of

micrometer, it was asserted that the near wall viscosity is increased up to 5 times at substrate

temperatures as low as -30 $^{\circ}$C. This increase in viscosity results in droplet meniscus penetration

(still it is partial penetration at the aforementioned range of droplet impact velocity) which

dissipates energy at contact line causing reduction in droplet receding velocity. Indeed, reduction

in droplet receding velocity is a principle reason of an increase in droplet contact time.[67]

Recently, the effect of viscous supercooled water droplet impacting on the cold substrate was

experimentally evaluated by Maitra et al.[79] A chamber was designed to provide an environmentally

cold surrounding gas condition at temperature as low as -17 $^{\circ}$C. Supercooled water droplet with

different sizes ranging from 1.9<D<2.4 mm having different impact velocities ranging from 0.77

<V<4 m/s corresponding to a wide range of Weber and Reynolds numbers (i.e. 20 <We<400,

500<Re<7500) impacted on a textured superhydrophobic surface with low contact angle hysteresis

(i.e. around 10°). Due to the fact that frost formation can change the surface wettability, as it was

highlighted before, experiments were only carried out in zero relative humidity condition. It was

claimed that due to the rapid increase of viscosity, droplet wetting dynamics can be fundamentally

changed. Two important parameters namely, droplet contact time and dimensionalized maximum

spreading diameter were evaluated in this study. It was claimed that droplet contact time was

increased up to two folds to that of room temperature due to the viscosity jump which increases the chance of pinning through phase transition.

Previous studies showed the importance of increased viscosity of supercooled water droplet which changes droplet coefficient of restitution, droplet maximum spreading diameter or droplet contact time by decreasing receding velocity arises from droplet partial penetration into rough substrates.[67,79] An increases in viscosity changes droplet contact angle hysteresis which might promote chance of droplet pinning/freezing on surfaces. Therefore, various studies correlated water repellency to icephobicity by contact angle hysteresis instead of static contact angle.

Zheng et al.[80] investigated impact of supercooled water droplets on functionalized carbon nano tube superhydrophobic surface. It was highlighted that the combination of both static contact angle and very low contact angle hysteresis are essential for water/ice repellency. They examined icephobicity of substrates cooled down as low as -8 $^\circ$C exposed to impact of supercooled water droplet having the same temperature. Droplet impact velocity was quite small corresponding Weber number up to 8 (droplet radius was 1.3 mm having impact velocity up to 0.7 m/s). It was highlighted that complete water repellency is achieved for superhydrophobic substrate while droplet remains attached and frozen on the aluminum substrate due to large contact angle hysteresis.

Norvorsky et al.[81] investigated variation of droplet contact angle hysteresis based on the energy dissipation defined by surface topography (i.e. pillars height and pitches). It was shown that energy dissipation during wetting and dewetting phases are related to the viscous dissipation within bulk of droplet and contact line. Therefore, energy barrier corresponding Cassie transition to Wenzel is correlated to surface characteristics (i.e. pillars height and pitches). This energy barrier can be

related to work of adhesion which is the product of surface tension of water to the contact angle hysteresis.[82]

Icephobicity of different solid surfaces ranging from hydrophilic to superhydrophobic surfaces exposed to supercooled water droplet was experimentally carried out by Wang et al.[83] Supercooled water droplet injected in the fabricated climate chamber (i.e. icing wind tunnel) with temperature maintained as low as -6 °C. These supercooled water droplets impacted on solid surfaces up to 10 minute (it can be inferred from the paper that Weber number was in the range of 40 to 70). The results clearly showed the strong repellency of superhydrophobic surfaces in comparison with other surfaces. Droplet roles over surfaces due to the low contact angle hysteresis.

Surface water repellency can be incorporated with receding contact angle. However, finding relation between water repellency and icephobicity of surfaces was experimentally carried out by Meuer et al.[84] it was shown that surface wettability and icephobicity can be integrated through linear relationship of $(1+\cos\theta_{rec})$. It was claimed that strength of ice adhesion, which can be correlated by imposing air shear force, is reduced up to 4.2 folds where bare steel substrate coated with chemical material having low surface energy.[85] However, in all aforementioned studies, the effect of incoming air flow was not considered either in room or low temperature conditions. In fact in most scenario of realistic droplet impingement on surfaces effect of the incoming air flow is present which is profoundly elaborated in the current study.

1.4 Objectives

The effect of stagnation airflow can completely change wetting and phase change mechanism of an impacting water droplet which has not been addressed yet. The resulting shear and normal forces of air flow on either room or low temperature conditions (i.e. supercooled water droplet) on

31

various solid substrates can significantly change droplet wetting dynamics. In the current study, a combination of various experimental methods along with a proposed theoretical model is used to meet the following objectives.

- To investigate phenomenology of spreading and recoiling phases of an impacting water droplet having low and high droplet impact velocity (i.e. impacted at critical velocity of non-splashing to splashing regime, Weber numbers from 30 to around 220) on hydrophilic, hydrophobic, and superhydrophobic surfaces accompanied with airflow (air velocity varies from 0 to 10 m/s) at room temperature condition.

- To understand wetting behavior of an impacting supercooled water droplet on various solid surfaces maintained at low temperature (i.e. below and above critical temperature of heterogeneous ice nucleation,-24 °C for bouncing droplet[1]) condition ranging from -10 °C to -30 °C.

- To investigate the net effect of air flow on an impacting water droplet for given Weber and Reynolds numbers.

- To develop a predictive model of droplet impact on the superhydrophobic surface with and without air flow in room and low temperature conditions by significant advancing knowledge of adding viscosity term and integration of air flow using classical Homann approach on droplet wetting dynamics model. Furthermore, solidification phenomena are taken into consideration using classical nucleation theory.

1.5 Thesis outline

After reviewing relevant studies regarding phenomenology of isothermal and non-isothermal droplet impact on solid surfaces in chapter 1, the experimental methodology along with detailed explanation of the experimental setup are presented in chapter 2. This chapter is divided into two

sections. At the first step, generation of isothermal stagnation flow along with mechanism of releasing droplet at stagnation point is profoundly explained. In the next step, producing supercooled water droplets accompanied with cold air flow at various velocities are also presented. Chapter 3 describes the proposed theoretical methodology. In this chapter previously defined mass-spring model[2] is developed based on consideration of viscous force where droplet impacts on superhydrophobic substrates. Furthermore, the effect of stagnation air flow is integrated to the developed model through classical Homann flow approach[3]. Additionally, the aforementioned model is further modified by consideration of heat transfer and phase change by classical nucleation theory for non-isothermal droplet impact condition.

Chapter 4 covers the results of the isothermal and non-isothermal water droplet impacting on various solid surfaces with different wettabilities ranging from hydrophilic to superhydrophobic surfaces. Elaboration of incoming air flow on an impacting isothermal and non-isothermal water droplet was carried out by scaling force analysis. Furthermore, droplet impact behavior on near superhydrophobic and coated superhydrophobic surfaces were analyzed based on the definition of pressure and shear domain droplet impact condition. In addition to that, the developed predictive model of droplet repulsion or pinning on superhydrophobic surfaces, which was presented in chapter 3, is compared against experimental results. Chapter 5 involves the summary and conclusions of the current research followed by useful recommendations for future works.

Chapter 2

Experimental methodology

The focus of this chapter is to present the details of experimental test setup along with substrate surface properties. The first stage is related to the influence of surface wettability on droplet dynamics behavior. Therefore, different substrates with wettabilities ranging from hydrophilic to superhydrophobic were utilized. These substrates were characterized by laser confocal microscopy technique. In the current research, experimental methodology is also divided into two distinct sections namely isothermal and non-isothermal water droplet impact conditions. Aforementioned droplet impact conditions are accompanied with room and low temperature stagnation air flow. In order to produce stagnation air flow a device which is termed here droplet accelerator was designed and built to provide controllable air velocities ranging from 0 (i.e. still air) to 10 m/s. This setup is also used in low temperature condition. Analysis of droplet wetting dynamics is carried out through the usage of image processing technique. Finally, test matrix of droplet impact at room and low temperature condition are presented which covers a wide variety of experimental test conditions.

2.1 Substrate properties

Experiments were conducted on different substrates namely polished aluminum as a hydrophilic surface, Teflon as a hydrophobic surface, sanded Teflon, which was only used in the isothermal condition due to the lack of durability, as a near superhydrophobic surface and superhydrophobic surface coated with WX2100. Aluminum and Teflon surfaces were purchased from McMaster Carr, USA (Aluminum 6061, mirror like-finish and Teflon made with virgin Teflon® PTFE resins). Sanded Teflon was made with 320 grit sandpaper which was uniformly rubbed on Teflon sheets. Finally, superhydrophobic surfaces were produced using WX2100 spray on polished aluminum which is commercially available by Cytonix (Maryland, USA).

Regarding the surface morphology, a laser confocal microscopy (VK-X200, Keyence, Japan) was carried out to capture surface topography of different surfaces, as demonstrated in figure (2.1). Two important parameters are extracted. First, average and root mean square roughness of all surfaces and surface area ratio of wet surface to base area (i.e. $\emptyset$ ratio). These information are important to obtain when knowing solid-liquid interface temperature, which is further discussed in chapter 3.
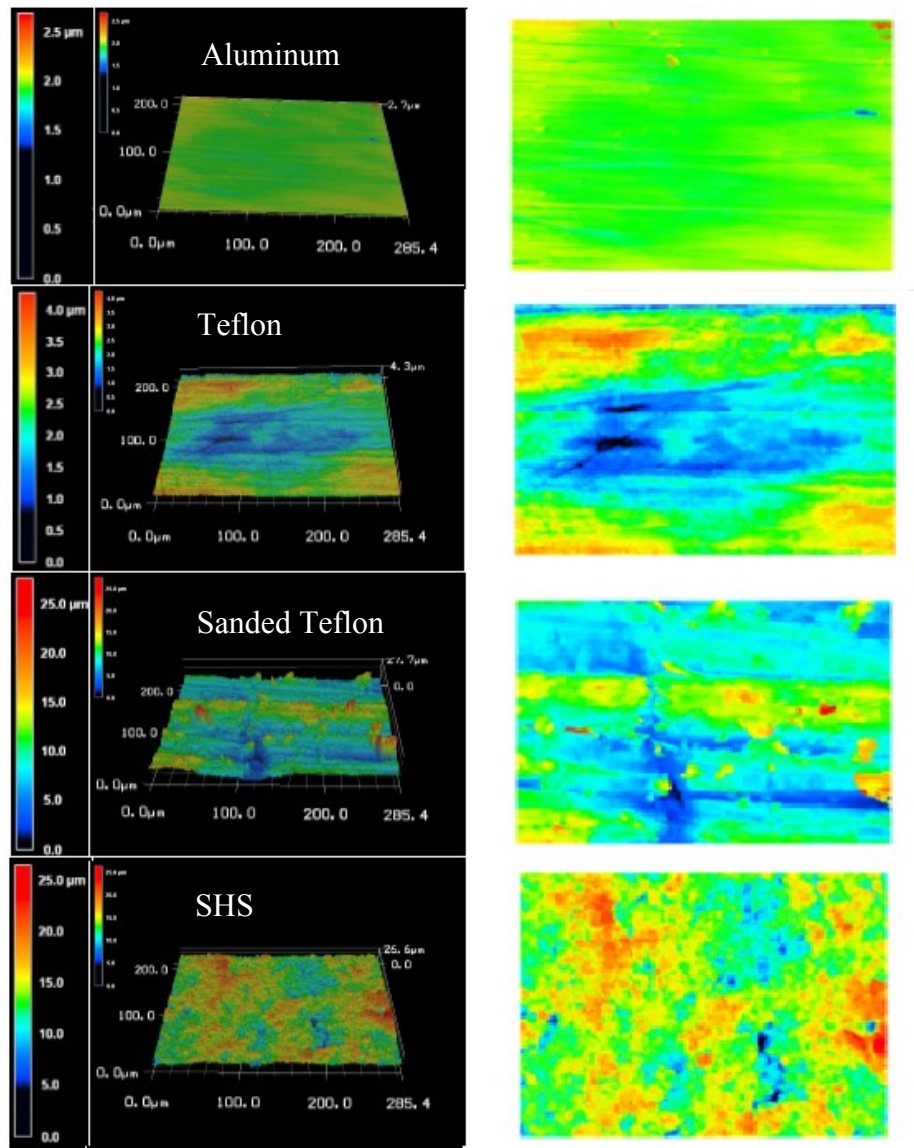
Figure 2.1: Laser confocal microscopy analysis of the different solid surfaces. Left column) angle view, right column) top view.

Wetting characterizations of all target surfaces were carried out by measuring static contact angle, advancing and receding contact angles of sessile droplet. Expansion method was used for the aluminum substrate, while tilting method was used for the other substrates, respectively. Small movement of droplet was monitored using high speed imaging photography. When droplet proceeds to moving, advancing and receding contact angles were measured. The contact angle hysteresis is deduced from the difference between these two angles, which represents the surface

mobility. As illustrated in table (2.1), four surfaces with almost comparable differences in wettabilities (i.e. $90^o < \theta_{adv} < 160^o, 50^o < \theta_{rec} < 150^o$ and $6^o < \theta_{hes} < 40^o$) were served in the current study to illustrate the effect of surface wettability on droplet dynamics behavior where room and low temperature stagnation flow is present. Detailed information of surface characterization is demonstrated in table (2.1).

Table 2.1: Characteristics of various substrates: equilibrium (θ_e), advancing (θ_{adv}), receding (θ_{rec}), and hysteresis (θ_{hys}) contact angles, as well as surface average roughness (R_a), surface root mean square (R_q) and surface area ratio (Ø ratio).

Surface	State	θ_e (°)	θ_{adv} (°)	θ_{rec} (°)	$\theta_{hes} = \theta_{adv} - \theta_{rec}$ (°)	$R_a (\mu m)$	$R_q (\mu m)$	Ø ratio
Aluminum	smooth	70° ± 3°	90° ± 4°	50° ± 4°	40° ± 4°	0.04±0.02	0.05±0.02	0.9 ± 0.05
Teflon	smooth	95° ± 3°	110° ± 4°	80° ± 4°	30° ± 4°	0.44±0.04	0.54±0.04	0.3 ± 0.05
Teflon320	Wenzel	135° ± 3°	150° ± 3°	110° ± 3°	40° ± 3°	2.19±0.15	2.83±0.15	0.1± 0.05
WX2100 (SHS)	Cassie	155° ± 2°	158° ± 2°	152° ± 2°	6° ± 2°	1.89±0.08	2.46±0.08	0.4 ± 0.05

In table (2.1), standard deviation of the contact angles are based on at least 10 experiments for each substrate. In addition, for the sanded Teflon and coated superhydrophobic substrates each of the 10 experiments were also carried out for 3 similarly produced samples. Following, detailed elaboration on the experimental test setup in isothermal condition is presented.

2.2 Experimental setup - isothermal condition

In this part, experiments were conducted at room temperature, pressure and humidity conditions (i.e. relative humidity was 25%). The novelty of this study is related to the presence of airflow (i.e. stagnation flow) toward an impacting water droplet. In order to generate stagnation

flow, a multi-component device named droplet accelerator was added to the typical set up of the droplet generator in the still air. This set up is illustrated in figure (2.2).
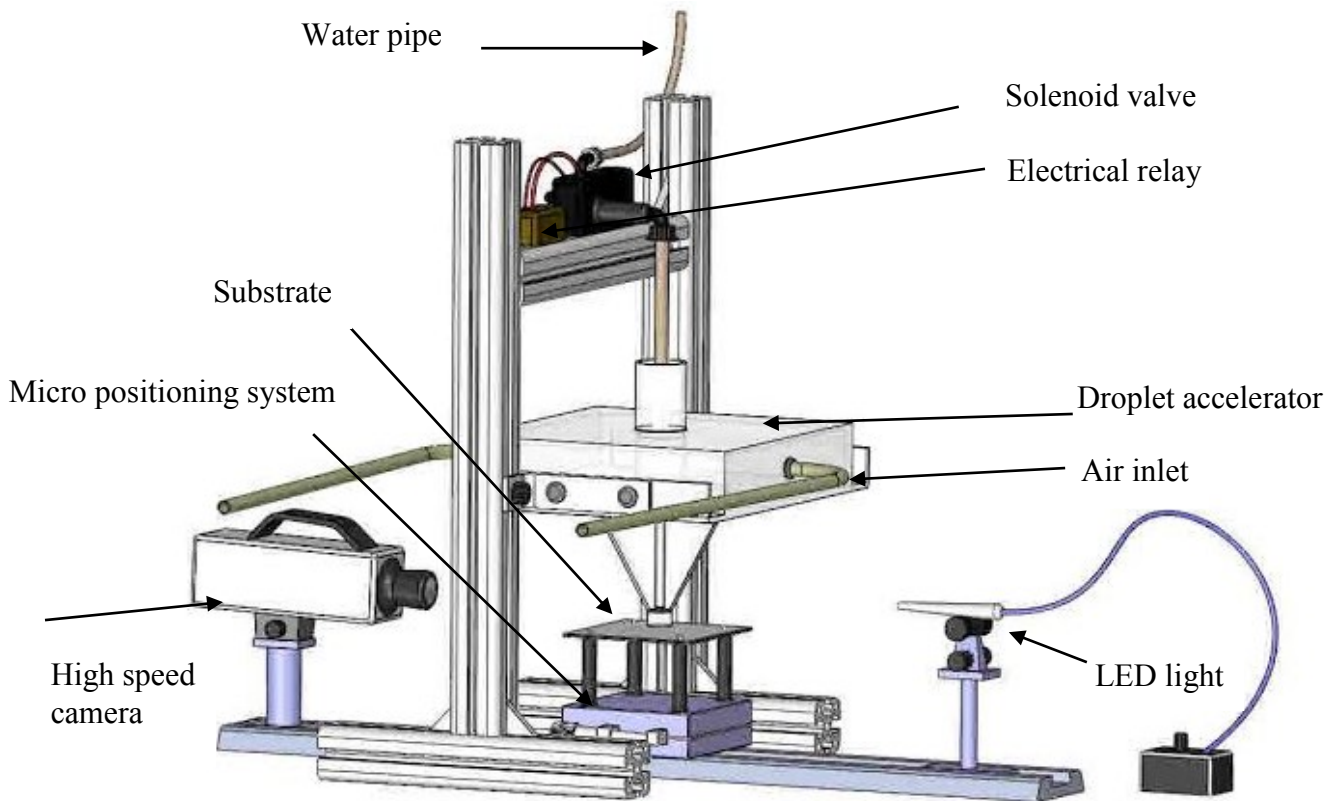
Figure 2.2: Schematic of the experimental test set up at room temperature condition.

In this device, two air intakes were used to provide which can conduct airflow at various air speeds. Air velocity was measured using Dwyer Pitot tube (MS-351-LCD) at the outlet of the droplet accelerator. However, characterization of the airflow at nozzle outlet was performed using detailed numerical simulation [see appendix B]. Schematic of the droplet accelerator along with the associated accessories are illustrated in figure (2.3).
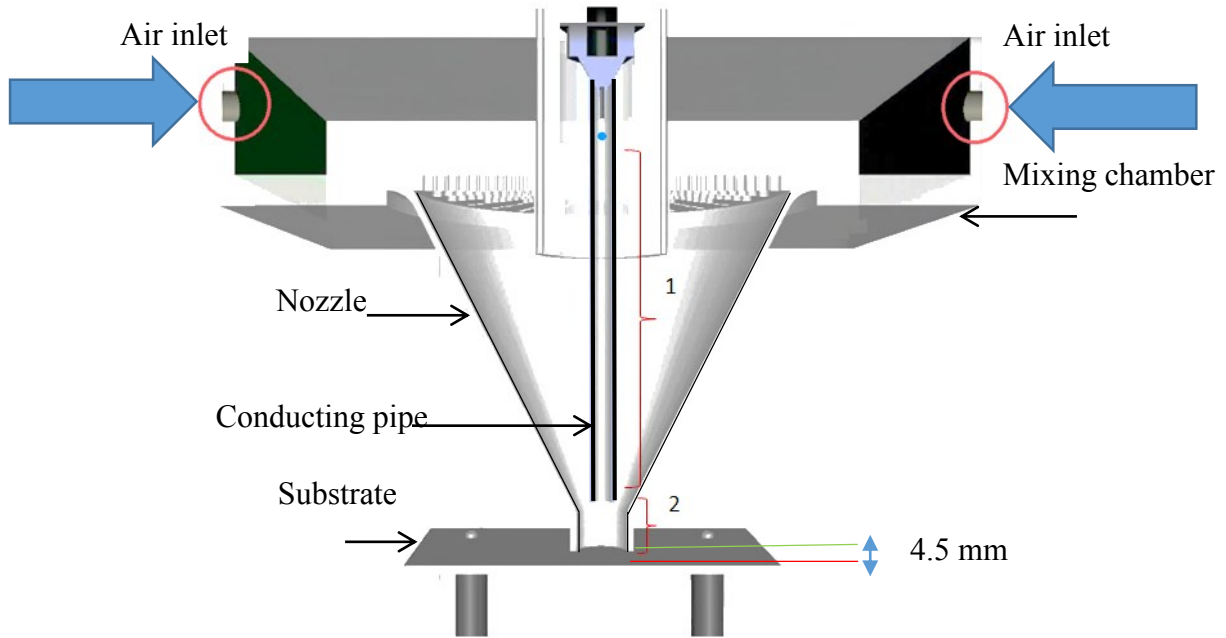
Figure 2.3: Schematic of the droplet accelerator.

The height between nozzle exit and substrate was kept fixed about 4.5 ±0.1 mm. Further decreases in the height results in droplet accelerator malfunctionality. It should be highlighted that droplet impact velocity is followed by gravity and not aerodynamic force. Releasing droplet in completely stagnation point is almost impossible if droplet exposes to air far from nozzle exit (e.g. middle of nozzle). Any small deformation either on droplet shape or droplet deviation from stagnation point results in non-repeatable experimental results. The following, three important parameters are required to be taken into considerations.

First, the shape of droplet moving through co-flow is highly related to the air velocity. Droplet shape at impact point should have a similar shape to that of still air (i.e. spherical shape). Secondly, impact velocity with and without airflow is required to be similar in order to have the same Weber and Reynolds numbers which are two important dimensionless numbers where predicting maximum spreading diameter is a matter of interest. Finally, droplet needs to be impacted at the stagnation point which makes the current experiment very challenging. By utilizing a conducting

pipe, as illustrated in figure (2.3), droplet impacts in the stagnation point. If the falling droplet is slightly deviated from the stagnation point it will touch the conducting pipe which results in having irregular droplet shape. Therefore, many carefully challenging experiments were performed to achieve handful number of cases in which droplets are almost spherical, impacting at the stagnation point and have the same impact velocity with and without air flow. Schematic of stagnation flow is demonstrated in figure (2.4).
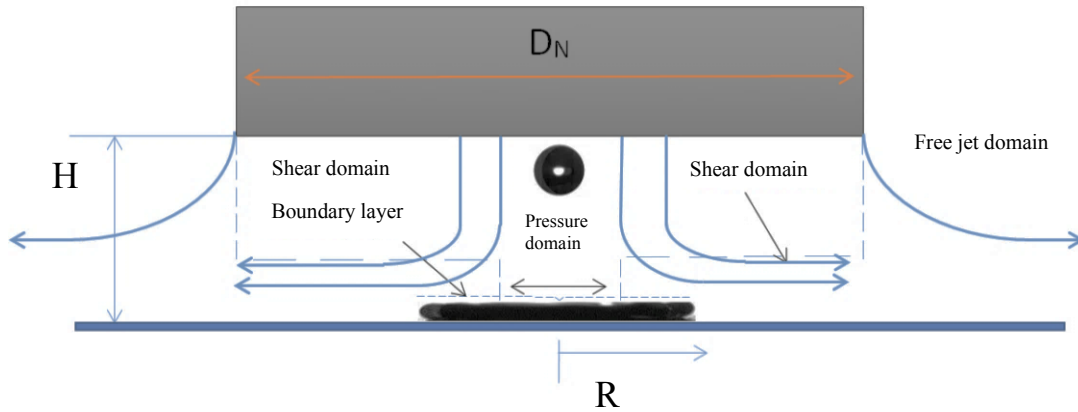
Figure 2.4: Schematic of stagnation flow and corresponding shear and pressure domains.

As highlighted in the above paragraph, the current study is focused on observing the net effect of the air flow on an impacting water droplet having similar impact velocity to that of still air condition. To do this, a small clear cellulose (Butyrate) tube, 3/8" OD, 1/4" ID is provided which is connected to the droplet generator system. As demonstrated in figure (2.3), pipe's length was chosen based on the distance from location of the needle to almost 1 mm above the entrance of the nozzle throat. Based on the numerical simulation [see appendix B], droplet is exposed to the air flow close to the substrate. The associated drag force causing an extra acceleration of droplet from the nozzle exit to substrate (i.e. 4.5 mm, drop size 2.6 mm) is negligible [see appendix A]. In the following, the mechanism of producing single water droplet is elaborated.

As illustrated in figure (2.2), droplet is produced from tip of the needle which is connected to a copper tube filled with pressurized water. Flow is driven by a pressurized water tank at pressures maintained between 20 psi to 50 psi and controlled by a normally closed solenoid valve (Ascovalve, USA). In order to control functionality of the solenoid valve a solid state relay (OMEGA engineering, USA) 12 VDC is connected to the waveform function generator. By triggering the function generator (Keysight 33220A 20MHz waveform generator, USA), working on the burst and pulse mode of the transmitting waves, electrical circuit between the function generator, relay, and the solenoid valve is closed which allows solenoid valve to be opened. Furthermore, at the same time, function generator sends another signal to the high speed camera to start recording. It means that by synchronization of the high speed camera with solenoid valve, it is possible to capture wetting phenomenon of an impacting water droplet on different solid surfaces.

Droplet wetting dynamics behavior is imaged using a high-speed camera. Imaging equipment used in the current study include a Photron SA1.1 (Photron, California, USA) high speed camera, a LED light and a high magnification zoom macro lens (Nikon AF.S Micro nikkor lens with focal length of 105 mm). Spatial resolution was 19-21 μm for 1 pixel. Different recording rates were used to trace impact behavior of the water droplet. For aluminum and Teflon substrates recording rate were 2000 and 10000 frames per second while for SHS recording rate was only 10000 frames per second. For measuring droplet contact time on SHS recording rate cannot not be less than 9000 fps.[86], as associated errors regarding contact time measurement are required to be minimal. Furthermore, different exposure time (i.e. shutter speed) namely 3 μs and 5.33 μs with appropriate back lighting produced by LED light were used in order to define clear interface of an impacting water droplet on different target substrates.

Detailed explanation of the LED light and fiber optics are presented in the following. KL 2500 LED (SCHOTT 24VAC, USA) light has been used to provide excellent illumination as a bright and white light source. It has a LCD display showing intensity of emitted light from 0 to100. Maximum illumination power was 1000 lumens. KL 2500 LED SCHOTT has a light guide with internal diameter of 9 mm which can be connected to a flexible optical LED fiber bundle. Having high quality glass optical fibers (PURAVIS® SCHOTT) which has a 4 μm diameter per beam, it is possible to easily conduct light to a desirable direction for better illumination. Finally, all of the mentioned parts of the visualization are installed on a breadboard work station optical bench (THOR LABS, USA). This optical bench has an active self-damping from vertical and horizontal vibration provides a suitable floor for precise recording. For instance, a superhydrophobic surface has a small contact angle hysteresis. It means that droplet start sliding on it with just few angles from horizontal line (i.e. 5°). Therefore, measuring important parameters of sessile droplet (e.g. static contact angle) can be carried out on the aforementioned optical bench. In the following, detailed explanation on non-isothermal test condition is presented.

2.3 Experimental test setup – non- isothermal condition

Supercooled water droplet impacting on cold solid substrates in the presence of cold air flow requires a complex experimental test setup. Similar substrates were used in low temperature condition except sanded Teflon sample which was excluded due to the lack of durability/repeatability under cold conditions. Information regarding substrate properties, can be found in the previous section, as demonstrated in table (2.1).

Experiments were conducted in low temperature condition ranging from -10 down to -30 ℃ with almost negligible relative humidity (i.e. 0.1%). The novelty of this part is related to the presence of cold airflow (i.e. stagnation flow) toward impacting a supercooled water droplet. Experimental

set up of producing cold air flow along with generation of the supercooled water droplet is demonstrated in figure (2.5). Large volume flow rate of dry room temperature air is cooled down by an immediate cooling through an in-house designed heat exchanger. Single-pass counter flow heat exchanger, which works with liquid nitrogen (Les Gaz Spéciaux Megs, Montreal, Canada), was designed to generate very cold air flow at the exit pipe of the heat exchanger. It is worth mentioning that latent heat of vaporization of liquid nitrogen is 200 kJ/kg. It has a melting point temperature of up to -196 $^{\circ}$C which make it possible to generate cold air flow as low as -80 $^{\circ}$C at 30 cfm air flow rate. Therefore, a simple calculation shows an interesting cooling power up to 1.4 kW. Heat exchanger design was based on the usage of small amount of liquid nitrogen which is transferred by a cryogenic transfer flex hose (internal diameter of 0.5 inch and 36 inch long (Les Gaz Spéciaux Megs, Montreal, Canada)) from liquid nitrogen vessel.

Heat exchanger is a Styrofoam box (Les Gaz Spéciaux Megs, Montreal, Canada) with external dimensions of 19.5" length, 16.5" width, 15" height. Internal dimensions are 17.5" length, 14.5" width and 13" height. Helical copper pipe with a length of 50 ft and external diameter of 0.5" is also used as a dry air passage inside the heat exchanger. Small thermal conductivity of the Styrofoam chamber (i.e. 0.033 W/m.K) makes it an ideal insulation for heat exchanger when it works with liquid nitrogen. At the top part of the heat exchanger, one pipe with external diameter of 10 cm is connected and completely sealed with Aluminum foil tape (General Purpose, 2" wide and 004" thick, McMaster-Carr, USA) which acts as an exhaust pipe. To this end, exhaust pipe is connected to the laboratory fume for safety precautions. Therefore, by this mechanism, it is possible to have a cold air as low as almost -80 $^{\circ}$C. This cold air pipe is connected to the one of air intake of the droplet accelerator, as schematically shown in figure (2.6).
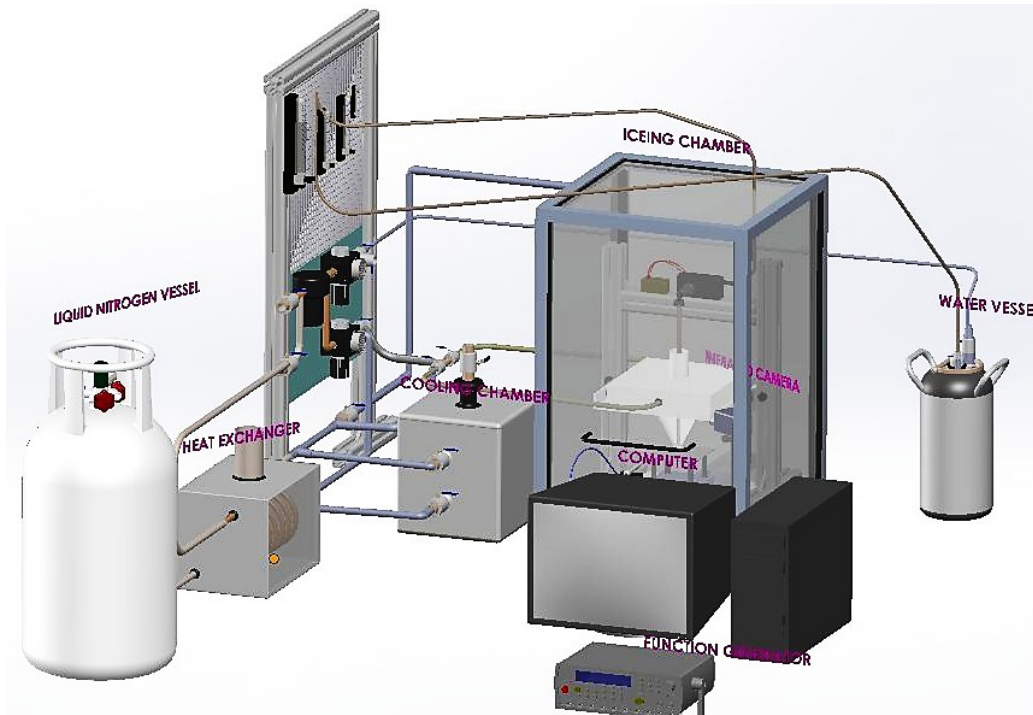
Figure 2.5: Schematic of experimental set up for generation of cold stagnation flow.

In order to generate cold stagnation flow, similar droplet accelerator to that of room temperature one was added to the typical set up of the droplet generator in the still air. Droplet accelerator provides cold co-flow at various air speeds and temperatures. Air temperature can be controlled through mixing of controllable flow rate of the room and low temperature air at the mixing chamber of the droplet accelerator. Schematic of the droplet accelerator along with associated accessories in order to produce cold air flow is illustrated in figure (2.6).
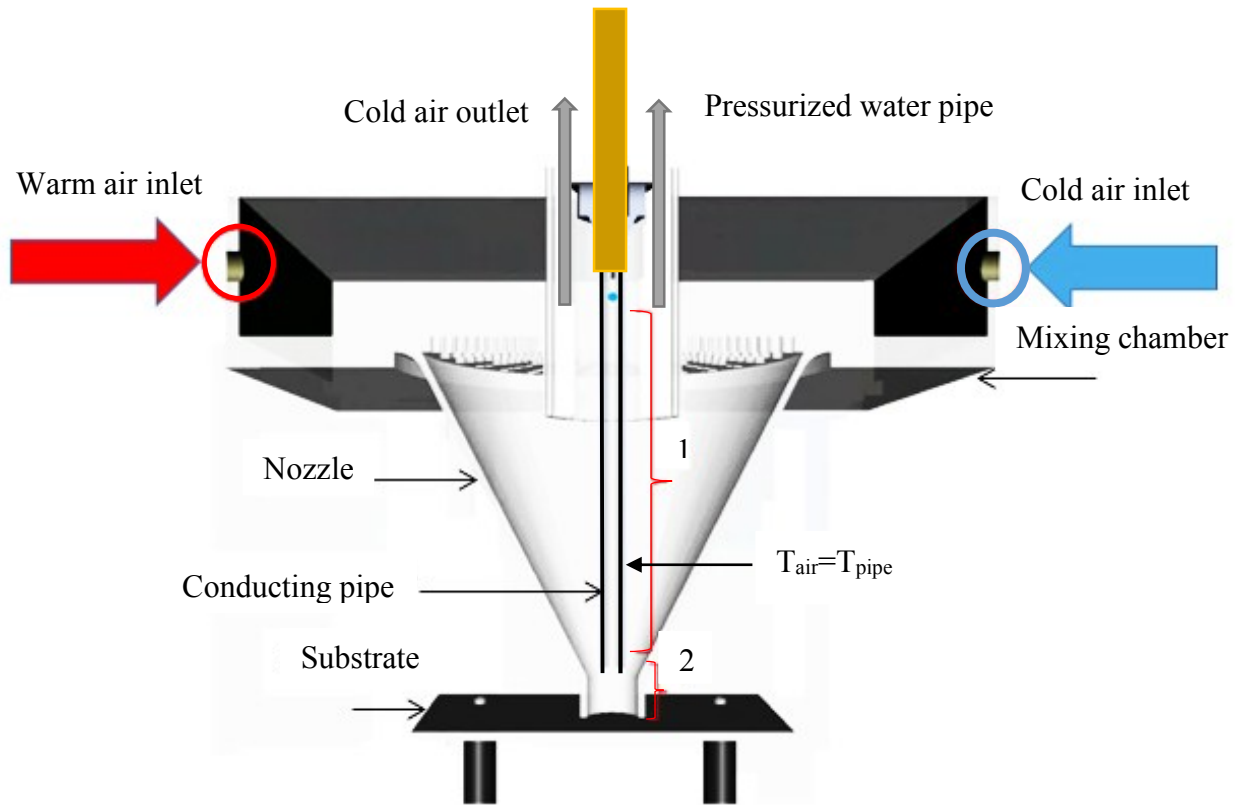
Figure 2.6: Schematic of droplet accelerator in low temperature condition.

As presented in figure (2.5), three different branches of the cold air flow are required. One branch

of the cold air flow is used to be mixed with room temperature air at controllable flow rate in the

mixing chamber of the droplet accelerator. Cold air flow rate is controlled by a brass ball valves

(McMaster-Carr, USA). Temperature measurements at internal part of the nozzle showed a

uniform and constant temperature at the nozzle throat which demonstrates an effective mixing

through mixing chamber of the droplet accelerator. Second cold air line is used for cooling of the

icing chamber. Temperature was kept as low as -1 °C in order to pressurized water inside of the

icing chamber not to be solidified. Droplet generation set up and its accessories, as demonstrated

in figure (2.5) (i.e. droplet accelerator, supports, solenoid valve, electrical relay, guide rail of high

speed camera, infrared camera) are inserted inside of the icing chamber. The icing chamber has a

dimension of 90 cm height, 55 cm length and 45 cm width and it is made of five optically clear

cast acrylic Plexiglas sheets (McMaster-Carr, USA). Finally, the third cold air pipeline is connected to a chamber, which is called primary cooling chamber. This chamber was designed in order to cool down target substrates in a comparable lower time required in the icing chamber. Reaching to a specific temperature in the primary cooling chamber is accomplished by the same methodology to that of mixing chamber of the droplet accelerator. After generation of the cold air flow, producing metastable supercooled water droplet is an important stage in the current study which is described in the following paragraph.

Mechanism of producing supercooled water droplet is based on the forced convection heat transfer between copper pressurized water pipe and cold air flow exhausting from droplet accelerator, as illustrated in figure (2.6). Measurement of water droplet temperature from almost specific period of time released from tip of needle, shows different droplet temperatures exposed to different air temperatures. Based on the assumption of laminar flow over pressurized water pipe, convective heat transfer coefficient will not vary significantly (e.g. 0.2% increase) with air temperature ranging from -10 down to -30 ℃, but it is a strong function of air speed (e.g. almost 50% increases from 4 m/s to 10 m/s). Therefore, it can be deducted that cooling time is increased for smaller air velocity due to lower Nusselt number and convective heat transfer coefficient.

It is worth mentioning that measuring surface temperature of different substrates and supercooled water droplet has been carried out by non-intrusive IR thermography method.[74] Due to the fact that aluminum substrate is very shiny, spectral reflectivity is high enough showing a misleading temperature. Therefore, aluminum substrate was covered by a very thin black conductive thermal tape (i.e. 0.008 inch thickness). This method has been used for two other surfaces. However, reflectivity of Teflon and superhydrophobic surfaces are much less than polished mirror like aluminum.

46

The IR thermometry has been used in the current study to measure surface temperature of solid surfaces and supercooled water droplets.[74] In this study A320 IR camera (FLIR, USA) and ThermoVision ExaminIR® software has been used in order to monitor surface temperature of the target substrates and supercooled water droplet. For measuring surface and air temperature a rather wide field of view is needed. In this case, 200 mm/75° lens with spatial resolution of 0.24 mm for 1 pixel is used to monitor surface temperature of the solid substrate. IR camera can provide surface temperature distribution of water droplet whether in room and supercooled conditions. In IR thermography method, water droplet is considered as an opaque object.[74] Calibration of IR camera was carried out by choosing emissivity factor of 0.96 to 0.97. Due to the fact that measurement of the surface temperature of water droplet needs finer spatial resolution, therefore 10 mm/90° lens with spatial resolution of 0.1 mm for 1 pixel has been used. Recording rate in all cases were 9 frames per seconds. It is worth mentioning that in well-insulated condition surface temperature at stagnation domain is similar to gas temperature, as demonstrated in figure (2.7).
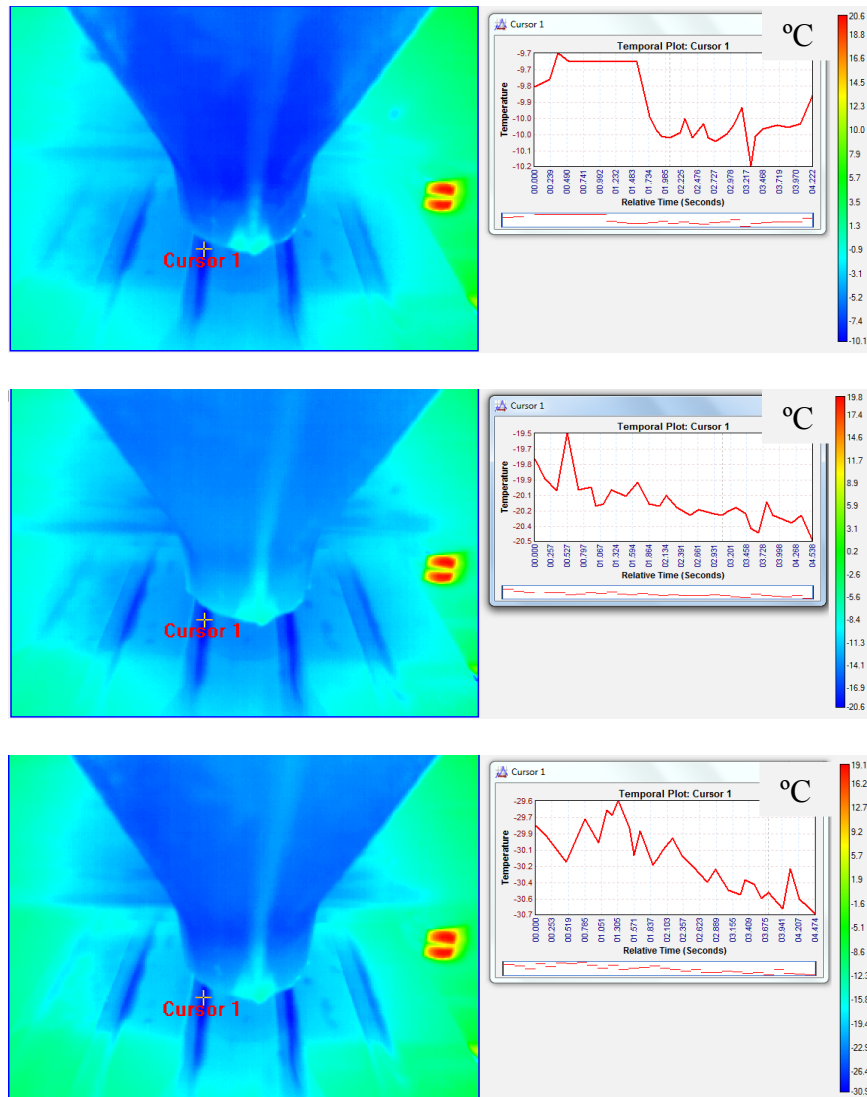
Figure 2.7: Surface temperature measurement using IR thermography in the low temperature condition.

During experiment, icing chamber should be closed and opened frequently which makes a large temperature gradient between gas and atmospheric temperature inside the icing chamber. Therefore, the assumption of thermal balance is no longer valid. However, gas temperature can be monitored by measuring surface temperature of an opaque small droplet conducting pipe which is inserted inside of the nozzle. A very small hole on the top part of nozzle's wall was made to capture surface temperature of the pipe. Flow rate was slightly increased to compensate the escaped

airflow. The created small hole is far away from main convergent part of the nozzle. Therefore, air profile at the nozzle outlet was not affected, as the outlet velocity was measured by Pitot tube. Small pipe is an opaque object and it is long enough to reach to end of the nozzle throat. In this case, the assumption of thermal equilibrium between surrounding gas and small pipe is valid, as it was monitored by IR camera. It was not observed any temperature gradient between the internal wall of the nozzle and small pipe surface.

Method of producing water droplet is similar to what was elaborated in the previous section which is based on the usage of pressurized water tank and synchronized solenoid valve with high speed camera. However, it is worth mentioning that the functionality of solenoid valve is completely limited in cold air condition. Therefore, an appropriate insulation is used to prevent gate clogging of the solenoid valve in low temperature conditions. As demonstrated in figure (2.5), solenoid valve is almost in direct exposure to the cold air flow ranging from -10 $^{\circ}$C down to -30 $^{\circ}$C from top part of the droplet accelerator. Without appropriate insulation it is faced clogging and experiment should be reinitialized. In order to prevent any potential freezing of water in solenoid vale gates, two methods have been used. At first step, an ultra-thin heat sheet 28 VAC was used (rectangle shape, McMasterCarr, USA) with a maximum 30 watts power usage which was installed behind the supporting ridge (see figure (2.5) to warm it up in a discontinuous way. Secondly, combinations of two insulation are used to store added heat within solenoid valve and its support. Cork/Synthetic Rubber Pipe Wrap, 1/8" thick along with a clear polyethylene bubble wrap (McMaster-Carr, USA), which both of them have a small thermal conductivity, (0.1 (*W/mK*) and 0.02 (*W/mK*) for rubber and air, respectively) are covered completely around thermal thin heat sheet and solenoid valves. Experimental observations showed a continuous operation of the

solenoid valve during 1 hour operation without any malfunctionality. Therefore, it is possible to produce repeatable supercooled water droplet accompanied with various cold air flow.

While many important parameters are involved in the wetting dynamics of an impacting water droplet namely different velocities and different droplet sizes, in this study only one impact velocity and droplet size were taken into account due to the extremely challenging experimental test conditions. On the other hand, different air velocities with different temperatures were used to investigate the effect of stagnation air flow on the supercooled water droplet spreading and retraction behavior. Supercooled water droplet wetting dynamics were imaged by high speed imaging technique and processed according to the methodology explained below

2.4 Image processing and error analysis

Quantitative evaluation of recorded images were carried out by image processing software, IMAGEJ.[87] As illustrated in figure (2.8), sequential recorded images were imported to this software and then threshold of desired area was precisely initiated. At the final stage, converting threshold images to binary images were implemented. By using threshold of 50%-60% which depends on the image contrast (i.e. the contrast between droplet and background of recorded images), it is possible to precisely measure droplet spreading edge. Due to the binary conversion, slight errors may arise from the edge detection. As illustrated in figure (2.9), comparison of different threshold percentages show that the associated error regarding boundary detection is increased up to almost 2 times for 20% threshold to that of 60% one. It was not seen any significant difference for higher threshold percentage. The associated error in this case is just about 2.3 pixels (1 pixel is about 19-21μm).
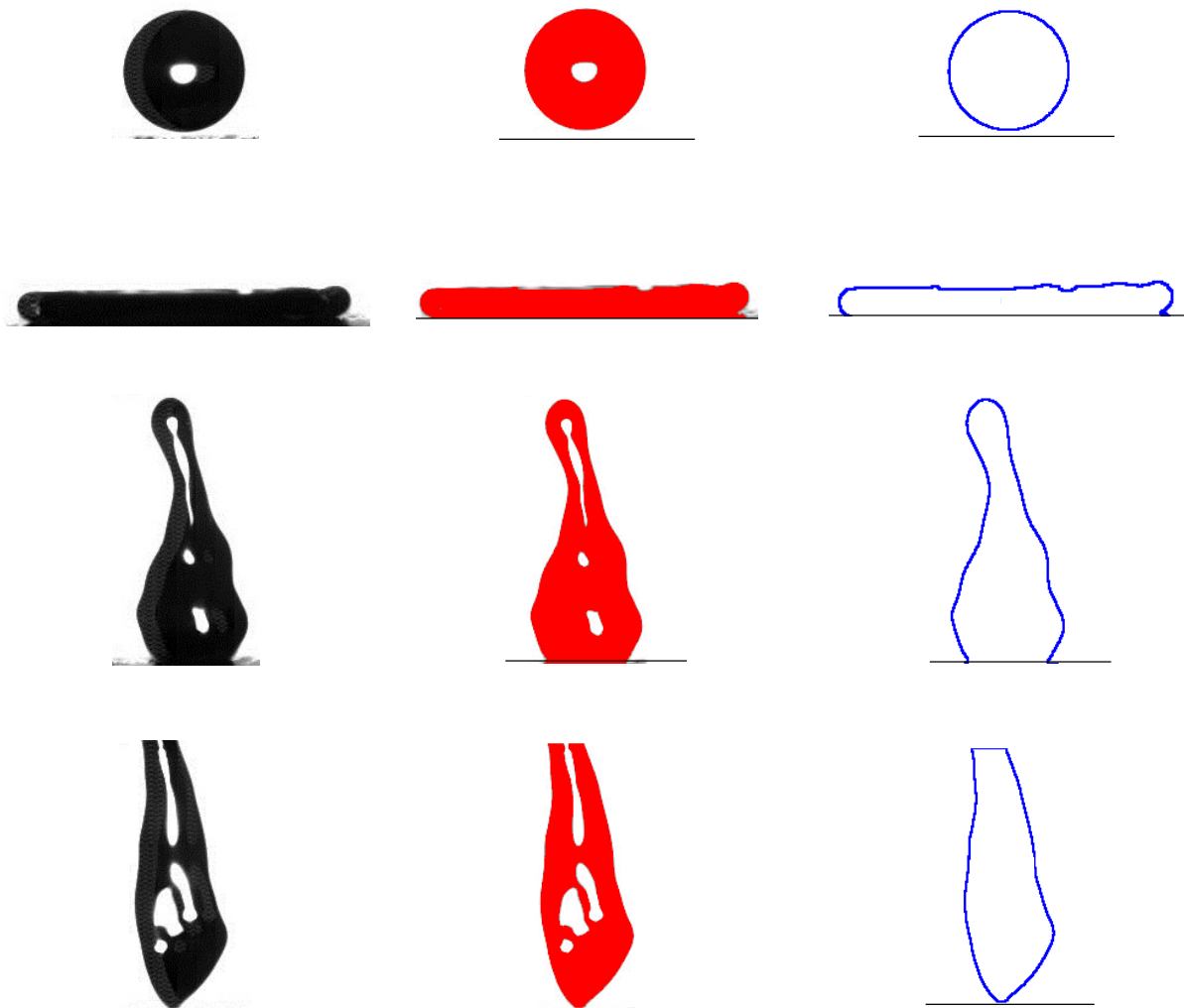
Figure 2.8: Method of tracking droplet boundary by choosing appropriate threshold intensity.

(a) Raw image   (b) 20% threshold   (c) 60% threshold
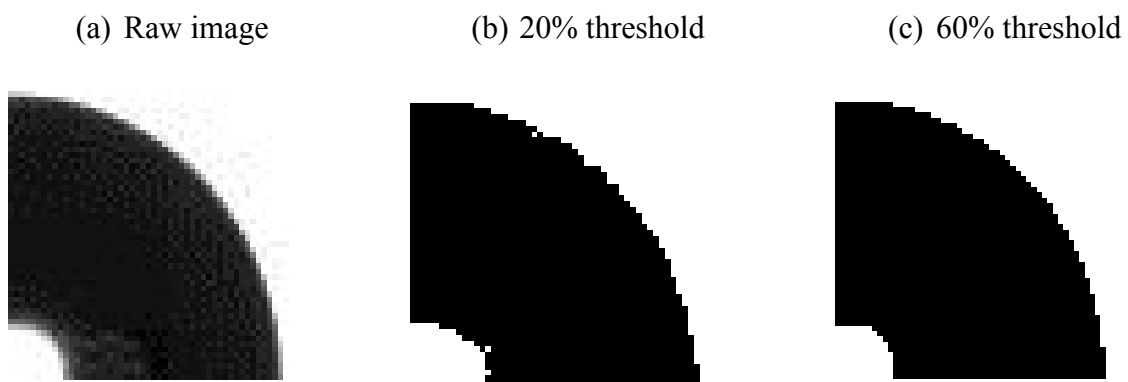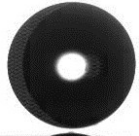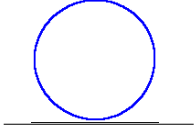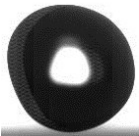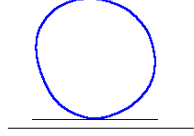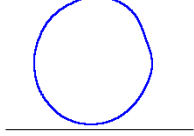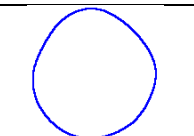
Figure 2.9: Associated errors related to binary conversion for boundary capturing.

When droplet is exposed to air flow it might be faced some sort of deformation which is related to droplet size and relative velocity between air and moving droplet. The maximum air speed used in the current study was based on the assumption of negligible droplet deformation of free falling droplet exposed to gas flow. The dimensionless number describing this phenomenon is relative Weber number, $\frac{\rho_{air} (U_g - U_D)^2 D}{\gamma_{lv}}$, which is defined based on the density of gas which is air in the present experiment (ρ_{air}), relative velocity of impinging water droplet and air jet velocity, ($U_g - U_D$), water droplet size D, and surface tension of water droplet (γ_{lv}). The largest relative Weber number is calculated based on air jet velocity up to 10 m/s. Droplet diameter is assumed to be constant during free falling as effect of evaporation on droplet size during free falling in the current study (i.e. 0.15 m height) is negligible (within1 % of initial droplet size).[88] Calculation of relative Weber number shows that it becomes close to the recommended values (i.e. 3) having almost spherical droplet shape.[89] Considering air and droplet impact velocity are 10 m/s and 1.2 m/s, respectively, the relative Weber number becomes up to 3.3 for water droplet size as large as 2.6 mm. Therefore, deformation of water droplet is almost negligible during short air exposure time up to 5.5 ms [see appendix B] and droplet remains almost spherical. In order to show that droplet deformation is negligible droplet's sphericity is analyzed through image processing technique. Quantitative evaluation of droplet sphericity which is moving through air upon impact condition is performed by image processing analysis, as illustrated in table (2.2). Analysis of the roundness of moving droplet before impacting on different substrates showed an insignificant droplet deformation exposed to air flow with velocities up to 10 m/s. Up to 7% deviation from a perfect sphere was observed for the worst case scenario. . Indeed, this small deviation did not have a significant effect on wetting dynamics of an impinging water droplet, as it was confirmed by measuring maximum spreading diameter to that of the still air case. Quantitative evaluation of the

deformed droplet with higher air velocity (i.e. 15 m/s and 20 m/s) shows that maximum spreading diameter is affected by droplet deformation where droplet aspect ratio becomes larger than 1.2. Furthermore, droplet falling height was chosen to be high enough in order to eliminate the effect of the droplet shape oscillation.

Table 2.2: Aspect ratio analysis of falling droplets deformed due to the airflow.

Air velocity (m/s)	Raw images	Traced Interface boundary	Image processing information
Still air (i.e. 0 m/s)			Aspect ratio: 1.016 Round: 0.984
10 m/s			Aspect ratio: 1.074 Round: 0.931
10 m/s			Aspect ratio: 1.09 Round: 0.927
10 m/s			Aspect ratio: 1.064 Round: 0.939

In addition to what was mentioned regarding some potential source of experimental errors (i.e. droplet oscillation, droplet deformation due to the imposed air flow, variation of incoming air velocity, errors due to the binary conversion and droplet and substrates temperature measurement) inhomogeneity of coated surfaces could increase errors. However, performing abundant droplet impact experiments on various substrates with similar surface characteristics, it was not seen any significant deviation in experimental measurements. For instance, for 20 cautiously coated superhydrophobic surfaces, same wetting behavior in terms of advancing and receding dynamic contact angles and maximum spreading diameter were observed. Therefore, the associated errors

regarding the usage of different substrates are assumed to be negligible. Furthermore, temperature variation could change water-substrate contact angle through condensation mechanism for rough substrates and frost formation due to the environmental humidity. However, due to the usage of extremely low humidity air (i.e. 0.1%) the effect of condensation and frost formation is completely eliminated. In addition, to this variation of both surface tension and density of supercooled water droplet are very small (i.e. 4% and 0.1%, respectively) to alter advancing and receding contact angles.

2.5 Test matrix of droplet impact on solid surfaces

2.5.1 Isothermal condition

Room temperature water droplet impact experiments on various solid surfaces have been carried out with various droplet sizes, impact velocities along with various incoming air velocities comprising wide range of droplet Weber and Reynolds numbers with and without air flow. As described in section (2.2), droplet impact velocity with and without airflow is similar. Therefore, it is possible to investigate the net effect of air flow on the droplet wetting dynamics, as droplet Weber and Reynolds numbers remain unaffected when air flow is present. For room temperature condition, test matrix is illustrated in table (2.3).

Table 2.1: Test matrix of droplet impact experiments at the room temperature condition for aluminum, Teflon and sanded Teflon substrates. Standard deviation is related to the at least five cases for small droplet sizes (i.e. 1.65 and 2 mm) and ten different experimental tests for the largest one (i.e. 2.6 mm).

Droplet diameter (mm)	1.65 (±0.07)	2 (±0.05)	2.6 (±0.04)
Droplet impact velocity (m/s)	1.2, (±0.02)	1.2, (±0.02)	1.2, 1.6 ,2, 2.5 (±0.01)
Air velocity (m/s)	0, 4, 7, 10 (±0.5)	0, 4, 7, 10 (±0.5)	0, 4, 7 ,10 (±0.5)

Table 2.2: Test matrix of droplet impact at room temperature for superhydrophobic substrate. Standard deviation is related to the at least five cases for small droplet sizes (i.e. 1.65 and 2 mm) and ten different experimental tests for the largest one (i.e. 2.6 m).

Droplet diameter (mm)	1.65 (±0.07)	2 (±0.05)	2.6 (±0.04)	2.3 (±0.05)
Droplet impact velocity (m/s)	1.2, (±0.02)	1.2, (±0.02)	1.2, 1.6 ,2, 2.5 (±0.01)	2.7, 3.2, 3.7 (±0.02)
Air velocity (m/s)	0, 4, 7, 10 (±0.5)	0, 4, 7, 10 (±0.5)	0, 4, 7 ,10 (±0.5)	0, 10 (±0.5)

It is worth mentioning that 10 and 6 number of acceptable experiments (i.e. droplets aspect ratio were below the 1.08 to that of still air for all scenarios where air flow is present) were performed for every imposed air velocity (i.e. 0, 4, 7, 10 m/s) on the largest (i.e. 2.6 mm) and small droplet sizes (i.e. 1.65 and 2 mm), respectively. Standard deviation highlighted in table (2.3) and (2.4) is based on mean values obtained from various numbers of runs. In the following, effect of the viscosity on droplet dynamics behavior is presented.

As it will be discussed in chapter 3, one theoretical model of droplet wetting dynamics on superhydrophobic surfaces is presented which is based on adding new viscous term on previously defined mass-spring model[2]. This new viscous term is experimentally determined by performing water-glycerol solution droplet impact experiments at various viscosities, as illustrated in table (2.5). Detailed information regarding obtaining viscosity term of an impacting water droplet on the superhydrophobic surface will be discussed in chapter 3.

Table 2.3: Test matrix of water-glycerol solution droplet impact experiments at room temperature condition having various viscosities.

Droplet diameter (mm)	1.65 (±0.08)	2 (±0.05)	2.6 (±0.04)
Droplet impact velocity (m/s)	1.6 (±0.02)	1.6 (±0.02)	1.6 (±0.01)
Water-glycerol viscosity (mPa.s)	1, 1.9, 2.5	1, 1.9, 2.5	1, 1.9, 2, 2.2, 2.5, 3, 3.5, 4.5, 5.5

2.5.2 Non-isothermal condition

Supercooled water droplet impact experiments on various solid surfaces are carried out with different air velocities and temperatures. In this section, text matrix of low temperature conditions are presented. Standard deviation, illustrated in table (2.6), for droplet and substrate temperatures are related to spatial resolution of IR camera which mean value of colorful pixels are used for temperature evaluation.

Table 2.4: Test matrix of droplet impact in low temperature condition, Droplet size and impact velocity are 2.6 mm and 1.6 m/s, respectively.

Droplet temperature (°C)	20 (±1)	-2 (±1)	-3.5 (±1)	-5.5 (±1)
Air and substrate temperature (°C)	20 (±1.5)	-10 (±1.5)	-20 (±1.5)	-30 (±1.5)
Air velocity (m/s)	0, 7, 10 (±0.5)	0, 7, 10 (±0.5)	0, 7 ,10 (±0.5)	0, 7 ,10 (±0.5)

To this end, physical properties of room and supercooled water droplet along with water-glycerol solution with various viscosity are presented in table (2.7). In fact mimicking wetting dynamics of viscous supercooled water droplet on solid surfaces especially superhydrophobic surfaces are carried out by that of water-glycerol solution. This topic is profoundly elaborated in chapter 3.

Table 2.5: Physical property of water-glycerol solution at various viscosities along with room and supercooled water drops at various temperatures.[90,91,92,93,]

% weight of Glycerol in water	Density of water-glycerol solution (kg/m³)	Dynamic viscosity Of water-glycerol solution (mPas)/supercooled water viscosity	Surface tension Of water-glycerol solution (mN/m)	Density of water at different temperature (kg/m³)	Surface tension of water at different temperature (mN/m)
0	998.2	1.002/ water@ 20 °C	72.8	998.2/ water@ 20 °C	72.8/ water@ 20 °C
22.3	1052.8	1.93 / water@-2 °C	70.8	999.7/ water@-2 °C	76.01/ water@-2 °C
23.8	1056.7	2.04 /water@ -3.5 °C	70.7	999.5/ water@ -3.5 °C	76.2/ water@ -3.5 °C
26	1062.4	2.205/water@ -5.5 °C	70.5	999.1/ water@ -5.5 °C	76.47/ water@ -5.5 °C
30	1072.7	2.5/water @ -8.5 °C	70.3	998.6/ water @ -8.5 °C	77.02/ water @ -8.5 °C
34.1	1083.6	3/water @ -13 °C	70	997.3/ water @ -13 °C	77.8/ water @ -13 °C
38.2	1094.5	3.5/water @ -16 °C	69.7	996.1/water @ -16 °C	78.5/water @ -16 °C
43.4	1108.5	4.5/water @ -20.6 °C	69.3	993.1/water @ -20.6 °C	79.27/water @ -20.6 °C
47.8	1120.4	5.5/water @ -24.3 °C	68.7	990.6/ water @ -24.3 °C	79.8/ water @ -24.3 °C

Chapter 3

Theoretical methodology

The focus of this chapter is on the theoretical description of stagnation air flow and its effect on wetting behavior of an impacting isothermal and non-isothermal water droplet on superhydrophobic surfaces. Characterization of the stagnation air flow is carried out based on the classical Homann flow approach.[3] Derivation of the resultant shear force of incoming air flow is performed by solving the principle equations (i.e. continuity and momentum equations). Consequently, some important information namely radial velocity, resultant shear and normal forces and thickness of the boundary layer on spreading droplet are obtained. The next stage is related to the coupling of stagnation flow on droplet wetting behavior.

Droplet wetting behavior on the superhydrophobic surface accompanied with air flow is evaluated by presenting new transient model of droplet spreading diameter on the superhydrophobic surface in room temperature condition. This model is based on the modification of previously defined mass-spring model[2] by adding a viscous term to account the viscous dissipation of a spreading droplet. Consequently, the predicted maximum spreading diameter and droplet contact time can be obtained from this model which are validated against the experimental results (shown in chapter 4). Aforementioned model is further developed to be used in non-isothermal condition where the effect of phase change is present.

Phase change mechanism is elaborated through the classical nucleation theory based on the definition of Gibbs free surface. When Gibbs energy is minimized, thermodynamic system is forced to stabilize the system through phase change mechanism. For water droplet which is gradually cooled down below the triple phase point at 1 atm (i.e. 0 $^{\circ}$C) it is possible to have a metastable liquid phase. This phenomenon can be explained on differences in chemical potential of a system defined as a thermodynamic driving force. Here, derivation of thermodynamic driving force of a system through thermodynamic relations, which is integrated directly to the Gibbs free surface energy equation, is presented. Indeed, thermodynamic driving force is directly related to the solid-liquid or gas-liquid interface temperature which is used for calculation of ice nucleation rate.

Ice nucleation rate is a function of Gibbs free surface energy which is strongly influenced by solid-liquid and gas-liquid interface temperatures. Therefore, two models of transient solid-liquid and gas-liquid interface temperature for different solid surfaces are derived. The model of solid-liquid interface temperature is derived based on the solution of two transient conduction equations within droplet and rough substrate. Furthermore, the model of gas-liquid interface temperature is derived based on the balance of all involved energies in the quasi-steady condition.

Finally, the predictive model of droplet wetting dynamics on superhydrophobic surfaces is used for further modification based on the classical nucleation theory. In fact, this equation is a predictive model of droplet repulsion or pinning on the superhydrophobic surface when cold air flow is present. In the following, detailed explanation regarding a modification on the model of droplet wetting dynamics on superhydrophobic surfaces is presented.

3.1 Droplet wetting dynamics on superhydrophobic substrate

The governing equation for droplet spreading and retracting on a solid surface having low surface energy (i.e. superhydrophobic surface) can be described by balancing of all forces at the contact line, as demonstrated in figure (3.1). Bahadur et al.[2] presented the dynamics of spreading and retraction of an impacting droplet in still air based on mass-spring analogy, as demonstrated in equation (3.1).
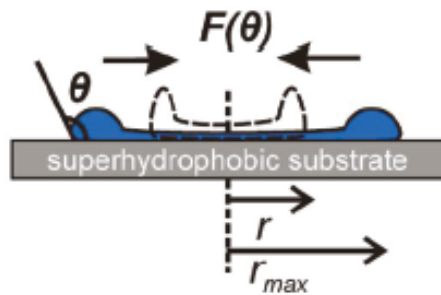
Figure 3.1: Spreading and retraction of water droplet on a superhydrophobic surface based on the mass-spring model. [2]

$$m_o \ddot{r} + 2\pi\gamma r(1 - cos\theta) = 0 \qquad (3.1)$$

It is important to mention that the model of mass-spring is valid where droplet deformation is much smaller than the radius of initial droplet where there is neither contact line formation nor jetting phenomenon. In this regime, coefficient of restitution is higher than 0.9 highlighting negligible effect of viscosity. However, for large enough droplet impact velocity where the formation of droplet contact line is present, nonlinear mass-spring model defines the spreading and recoiling of an impacting droplet and the effect of viscosity needs to be taken in to account.[13]

The current study investigates droplet wetting dynamics on a superhydrophobic surface where impact velocity is sufficiently high so that rim formation is happened. At this regime of impact velocity two scenarios are occurred. Firstly, droplet contact time becomes independent of the droplet impact velocity. Linear mass-spreading model is no longer valid due to fact that spreading

contact line is formed.[13] Secondly, due to the generation of spreading lamella, the assumption of Eulerian flow is not valid and the effect of viscosity either internal or contact line are required to be considered in equation (3.1). Therefore, general form of droplet wetting dynamics on the superhydrophobic surface is shown in equation (3.2).

$$m_o\ddot{r} + C_{vis}\dot{r} + 2\pi\gamma r(1 - cos\theta) = 0 \qquad\qquad (3.2)$$

As shown in equation (3.2), mass-spring model is modified by the assumption of adding a dashpot term in equation (3.1) to account for effect of liquid viscosity on the droplet wetting dynamics. Droplet spreading and retraction phases on the superhydrophobic surface are affected by liquid droplet viscosity which can change wetting behavior (e.g. maximum spreading diameter). Clanet et al.[44] performed a scaling law analysis of viscous droplet impacts on superhydrophobic surfaces. Results showed that P_s factor (i.e. $We/Re^{0.8}$) determines the dynamics of wetting. For an impacting droplet with P_s <1, maximum wetting diameter is just influenced by the capillary force and it is independent of the viscosity and can be approximated by $D_{max}/D=0.9We^{0.25}$. While for P_s >1, droplet dynamics is governed by the viscous force and the maximum spreading diameter is represented by $D_{max}/D=0.9Re^{0.2}$. However, recent study of the high viscous water droplet impacting on superhydrophobic surfaces showed that by increasing water droplet viscosity up to 4 folds, which shows P_s < 0.6, maximum spreading diameter was reduced up to 25% for high impact velocity (i.e. 3 m/s) while it was reduced up to about 8% for low inertia water droplet impact condition (i.e. 1.3 m/s).

Therefore, it is highly appreciated to define a universal model of the droplet impact on the superhydrophobic surface which effect of the viscosity variation is taken in to account. In order to find the damping coefficient of an impacting droplet, equation (3.2) needs to be solved.

Consequently, damping coefficient (i.e. C_{vis}) can be obtained by appropriate curve fitting (i.e. by solving equation (3.2)) to that of experimental results.

In order to solve ordinary differential equation of (3.2), two initial conditions are required. Initial conditions are obtained from the nature of droplet impact behavior. Although definition of the mass-spring model was presented by Clanet et al.[44] and formulated by Bahadur at al.[2], the importance of presenting appropriate initial conditions for solving and simulation of transient droplet spreading and retraction behavior were not taken into considerations. First initial condition comes from the fact that the radius of spreading droplet is zero upon droplet impact (i.e. for t=0, r=0). Second boundary condition is related to the conversion of the kinetic energy of an incoming droplet upon impact to radial direction. Therefore, the challenging issue is related to the correlation of the droplet impact velocity to radial velocity.

As illustrated in the study of Vadillo,[94] temporal droplet spreading factor is represented by droplet size, droplet velocity and time, as indicated in equation (3.3) where t^* is defined by $\frac{tV}{D}$. First derivation of the equation (3.4) results in the correlation of the droplet impact velocity to the radial velocity, as shown in equations (3.5) and (3.6). One adjusting parameter is used to define this semi-empirical correlation as a general relation for all scenarios of the droplet impact experiments. In the current study, assumption of the formed spread rim at 0.5 ms, which is experimentally observed, results in having adjusting parameter up to 1.56 for a water droplet size of 2.6 mm having impact velocities up to 1.2 m/s at room temperature condition. The sensitivity analysis has been taken in to accounts in order to evaluate the results to small variation in aforementioned numerical adjusting parameter. Therefore, this adjusting parameter is used for all scenarios of the droplet impact conditions (i.e. different droplet sizes and droplet impact velocities).

$$\frac{d(t)}{D} = 2\alpha\sqrt{t^*} \tag{3.3}$$

$$\frac{1}{D}\frac{d(d(t))}{dt} = \frac{1}{2}2\alpha\frac{V}{D}\left(\frac{tV}{D}\right)^{-\frac{1}{2}}$$ (3.4)

$$\dot{r} = \alpha V\left(\frac{tV}{D}\right)^{-\frac{1}{2}} \quad or \quad \dot{r} = \frac{\alpha V}{\sqrt{\frac{tV}{D}}}$$ (3.5)

$$\alpha = 1.56$$ (3.6)

The equation (3.6) is needed to be further discussed. As demonstrated in equation (3.5), radial velocity singularity arises at time equal to zero. On the other hand, based on the experimental observation, rim formation happens slightly after finishing kinetic phase which is in the order of few micro seconds. Hocking et al.[95] proposed that slip boundary condition is present which is due to the surface roughness. In addition to that, recent study showed that interfacial creation process happens very fast and approximated cut-off length is defined for definition of the slip velocity at the stagnation point.[96] Therefore, it is physically accepted that equation (3.5) to be used just after finishing kinematic phase.

Equation (3.2) can be rearranged appropriately, as shown in equation (3.7), and can be solved numerically by two initial condition demonstrated in equations (3.8) and (3.9).

$$\ddot{r} + \frac{C_{vis}}{m_o}\dot{r} + \frac{2\pi\gamma r(1-\cos\theta)}{m_o} = 0$$ (3.7)

$$r = 0 \ @ \ t = 0$$ (3.8)

$$\dot{r} = \frac{1.56\,V}{\sqrt{\frac{tV}{D}}} \ @ \ t = 0.5\,ms$$ (3.9)

Equation (3.7) is a homogenous second order ODE having constant coefficient defined by equation (3.10). Therefore, general solution of above equation (3.10) can be represented by equation (3.11).

$$a\ddot{y} + b\dot{y} + cy = 0$$ (3.10)

$$r(t) = c_1\exp(\alpha t)\cos(\beta t) + c_2\exp(\alpha t)\sin(\beta t)$$ (3.11)

Where c_1, c_2 can be found by applying initial conditions. In equation (3.11) α, β are defined by equation (3.12).

$$\alpha = \frac{-b}{2a}, \beta = \frac{\sqrt{(4ac-b^2)}}{2a} \qquad (3.12)$$

Therefore, coefficient of C_{vis} is extracted by the appropriate curve fitting on the transient solution of the droplet spreading diameter with that of experimental data, as presented in figure (3.2). It is important to highlight that in any damping system, dashpot term reduces oscillation of an oscillatory system. System oscillation is directly related to the dashpot viscous liquid property. Therefore, it can be deducted that when droplet impact velocity is high enough for formation of spread rim, viscosity effect cannot be neglected and harmonic solution of mass-spring equation [2] is not relevant to the real scenario of the droplet impact dynamics. Indeed, temporal spreading diameter on the superhydrophobic surface resembles an under-damped oscillatory system (i.e. damping ratio varies from 0 to 1) with continuous reduction on the amplitude as a function of time. At any mass-spring-dashpot system; vibrational equation is shown by equation (3.13). Natural frequency and damping ratio of the aforementioned equations are demonstrated by equation (3.14).

$$\ddot{r} + \frac{C_{vis}}{m_o}\dot{r} + \frac{k}{m_o}r = 0 \qquad (3.13)$$

$$\omega_o = \sqrt{\frac{k}{m_o}}, \Gamma = \frac{C_{vis}}{2\sqrt{m_o k}} \qquad (3.14)$$

Therefore, the ratio of $\frac{C_{vis}}{m_o} = 2\,\Gamma\,\omega_o$, which is an important parameter, can be obtained by comparison of various experimental data and numerical solution of mass-spring-dashpot equation. Based on the numerical simulation, illustrated in figure (3.2), the corresponding $\frac{C_{vis}}{m_o}$ is 381±0.1. In fact, this ratio is considered as a constant value for all distilled water droplet sizes used in the current study. In chapter 4, comparison of experimental results with aforementioned new model and previous studies are carried out. As it was highlighted in chapter 1, droplet contact time is not

a function of droplet impact velocity. Therefore, new presented model is compared against experimental data having different impact velocities ranging from 0.8 to 1.6 m/s, as illustrated in figure (3.3). It shows that the new model appropriately predicts both maximum spreading diameter and droplet contact time. This topic is elaborated in detail in chapter 4.
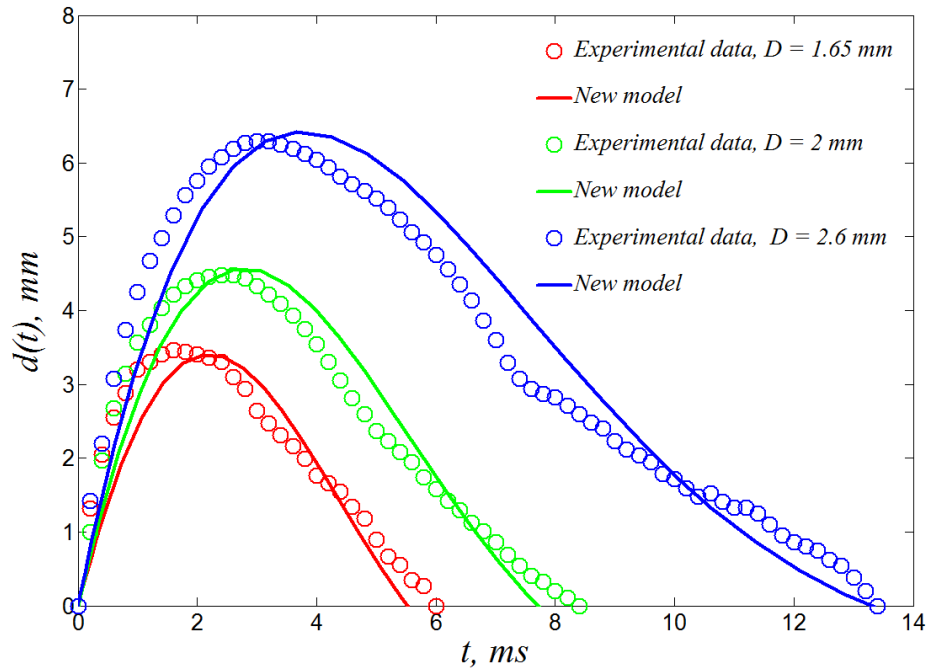
Figure 3.2: Transient solution of droplet wetting dynamics equation with MATLAB ODE 45 toolbox (using 4th order Runge-Kutta method). Droplet impact velocity is 1.2 m/s.
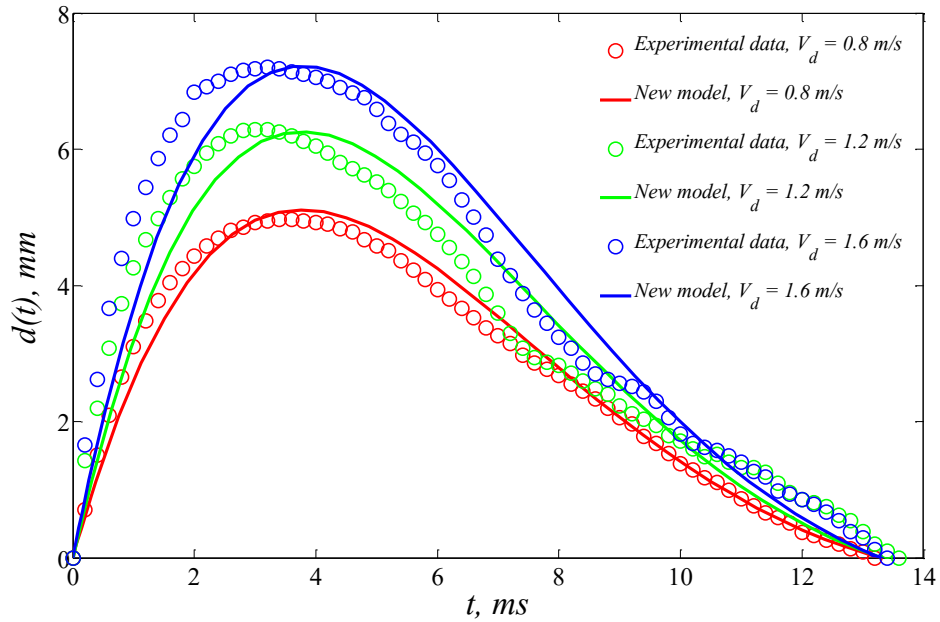
Figure 3.3: Comparison of experimental data and new presented model at various droplet impact velocities. Droplet size is 2.6 mm.

In order to widen the effect of water droplet viscosity in the aforementioned new model (i.e. coefficient of damping, C_{vis}), experimentation of wide variety of water-glycerol solution droplet impact on the superhydrophobic surface were carried out. In fact, an increase in droplet viscosity can mimic viscosity of supercooled water droplet at different temperatures. As illustrated in figure (3.4), contact time of an impacting droplet on superhydrophobic surface is slightly increased by increasing water-glycerol solution viscosity which is not exactly followed by linear behavior.
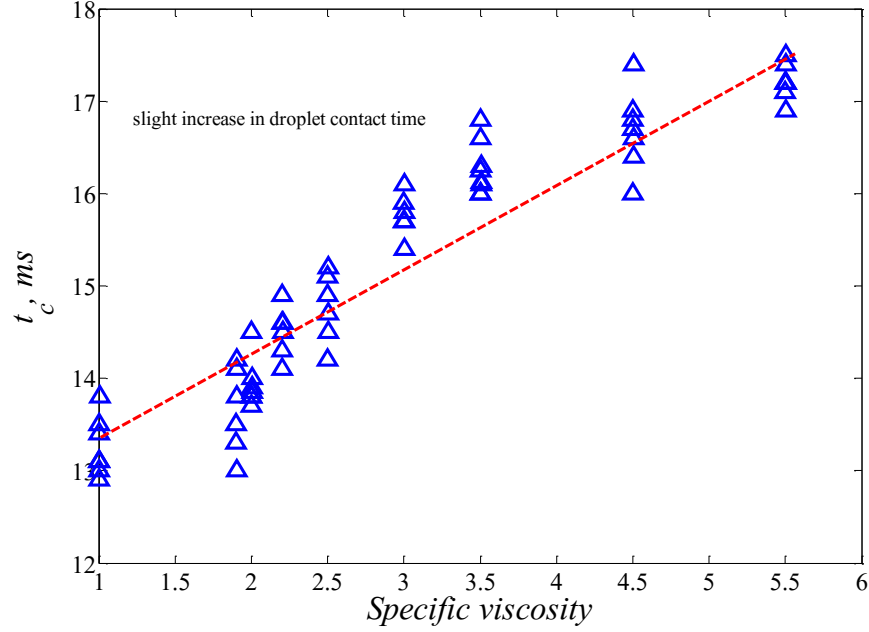
Figure 3.4: Variation of the contact time of an impacting viscous water droplet against specific viscosity. Droplet size and impact velocity are 2.6 mm and 1.6 m/s, respectively.

By using appropriate damping coefficient into droplet wetting dynamic equation (i.e. equation (3.2)) a power-law correlation is obtained, as illustrated in figure (3.5). This behavior was also observed for experiment of different droplet sizes ranging from 1.65 to 2.6 mm having specific viscosity up to 2.5.

It is worth mentioning that this correlation is only valid for impact velocities below the critical velocity of meniscus impalement. Indeed, when dynamic pressure of water droplet overcomes air compression strength, droplet full meniscus penetration is occurred and droplet contact time significantly increases which is out of scope of the current model. For the entire experiments carried out in the present study no water impalement was observed for droplet impact velocity up to 1.6 m/s. Therefore, the final form of the damping coefficient for large viscous droplet impacting on the superhydrophobic surface is showed by equation (3.15).

$$C_{vis} = 0.0103\mu^{0.1579} \tag{3.15}$$

$$C_{vis} = 0.0103\mu^{0.1579}$$
$$R^2 = 0.9289$$
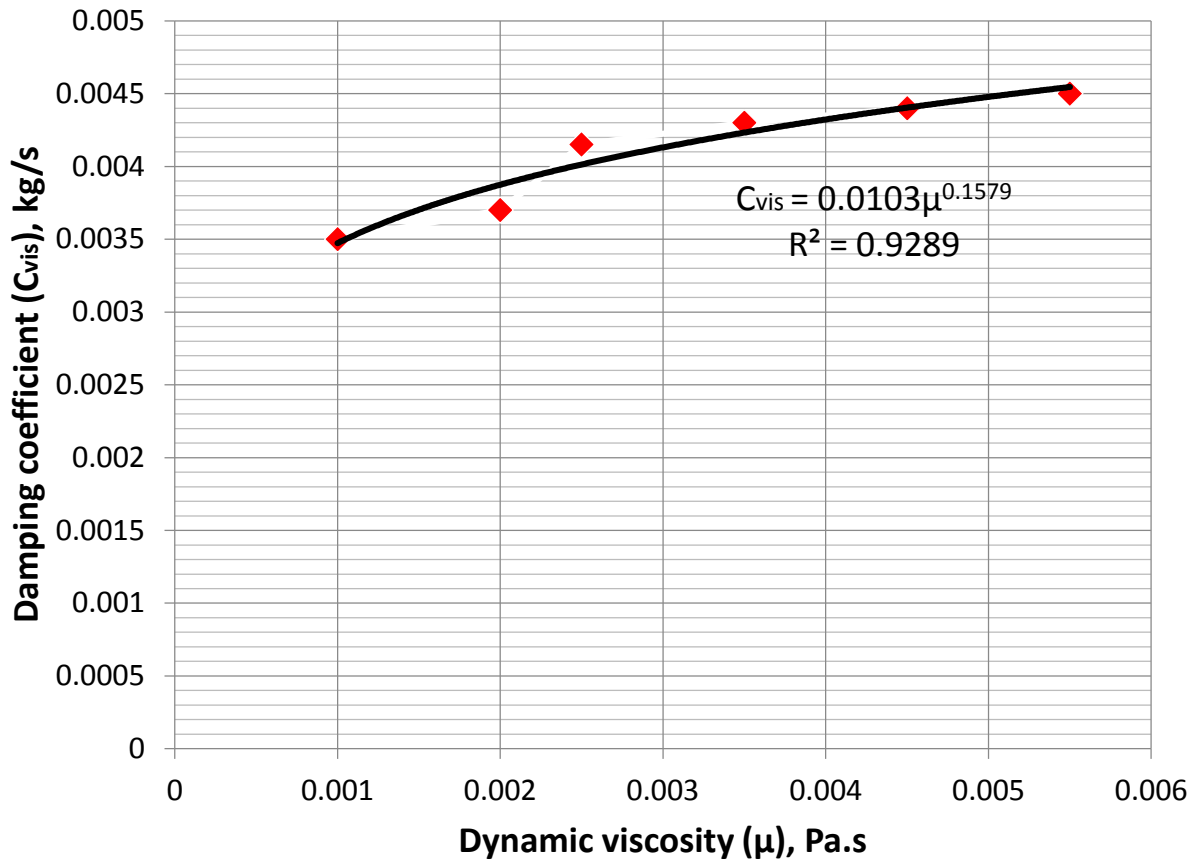
Figure 3.5: Variation of damping coefficient of viscous droplet as a function of dynamic viscosity on the superhydrophobic surface.

Dynamics of water droplet impacting on the superhydrophobic surface might be influenced by the effect of incoming air flow which is present in the most real scenarios of droplet/solid interaction (e.g. aerospace industries; where the effect of stagnation flow on an impinging droplet at the leading edge of aircraft' wing is present). In the following, the effect of stagnation air flow is profoundly elaborated.

3.2 Effect of stagnation airflow on droplet impact dynamics, classical Homann flow approach

In many practical applications, dynamics of an impacting water droplet on the superhydrophobic surface is affected by incoming air flow. Stagnation air flow can change droplet

spreading and recoiling behaviors by imposing the resultant air shear and normal forces acting on the spreading droplet.Understanding the mechanism of imposing air shear and normal forces was carried out by analysis of the classical Homann flow approach.[3] The air jet leaving the outlet of the droplet accelerator generates a stagnation flow on the substrate which rapidly transforms to an axisymmetric radially outward flow, as illustrated in figure (3.6(b)).
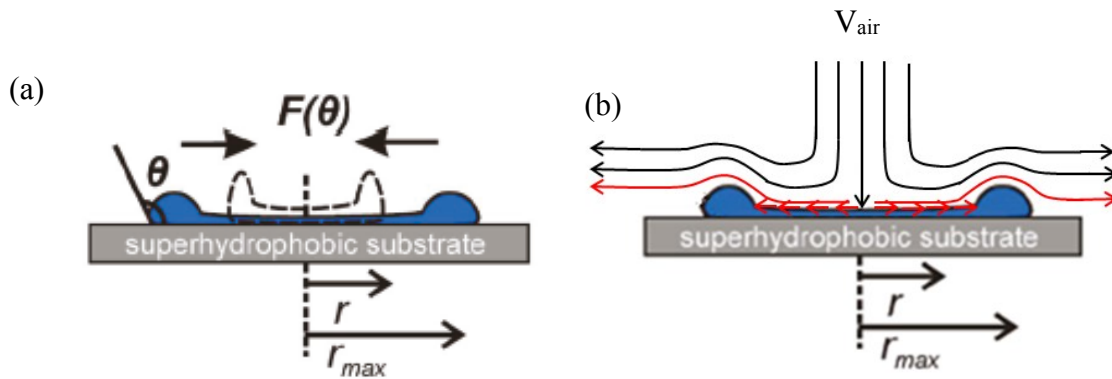
Figure 3.6: a) Droplet dynamics on the superhydrophobic substrate in still air, b) effect of the stagnation air flow on droplet impact behavior on the superhydrophobic substrate.

The following assumptions, similar to Homann flow analysis (see figure (3.7)), were made in simplifying the Navier-Stokes equation.

- The flow is 2D axisymmetric.

- The flow is in a steady state condition.

- Postulated velocity profile is just for stagnation zone.

- Incompressible flow field.

Using continuity and momentum equations, it is possible to find the shear force imposed on the air-water interface along with boundary layer thickness of the stagnation flow.
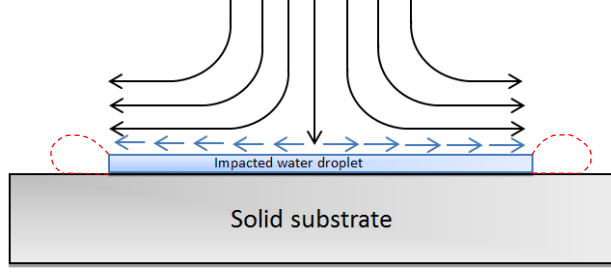
Figure 3.7: Schematic of stagnation air flow on solid substrate, classical Homann flow.

Continuity equation

$$\frac{\partial V_r}{\partial r} + \frac{\partial V_z}{\partial z} + \frac{V_r}{r} = 0 \tag{3.16}$$

r-momentum equation

$$\left[V_r \frac{\partial V_r}{\partial r} + V_z \frac{\partial V_r}{\partial z} \right] = -\frac{\partial P}{\partial r} + \upsilon \left[\frac{1}{r} \frac{\partial V_r}{\partial r} + \frac{\partial^2 V_r}{\partial z^2} - \frac{V_r}{r^2} \right] \tag{3.17}$$

Where, V_r and V_z are velocities in the r and z directions. In order to solve equation (3.14), pressure

distribution is derived by solving potential flow, which is assumed to be far from the impacting

water droplet. Using the similarity analysis, $\eta = z\sqrt{\frac{2a}{\upsilon}}$, velocity components, satisfying the

continuity equation, can be expressed by equations (3.18) and (3.19).

$$V_r = arf'(\eta) \tag{3.18}$$

$$V_z = -\sqrt{2a\upsilon}\, f(\eta) \tag{3.19}$$

Substituting the velocity components in the r-momentum equation leads to the following nonlinear

ODE:

$$f'^2 - 2ff'' = 1 + 2f''' \tag{3.20}$$

This equation needs three boundary conditions defined by equation (3.21).

$$f(0) = f'(0)=0,\ f'(\infty) = 1 \tag{3.21}$$

The first and second boundary conditions highlight the fact that V_r and V_z are zero at stagnation

point (i.e. no-slip boundary condition). The third boundary condition comes from the fact that

outside the boundary layer (i.e. for $z \xrightarrow{yields} \infty, \eta \xrightarrow{yields} \infty$), $V_r = ar$. By substituting V_r in equation (3.18), $f'(\infty)$ becomes as equal as 1.

By solving equation (3.20) numerically, with MATLAB ODE 45 toolbox (using 4th order Runge-Kutta method), the velocity components which are essential for finding shear and normal forces are obtained. Variation of the radial velocity component in the viscous region is illustrated in figure (3.8).
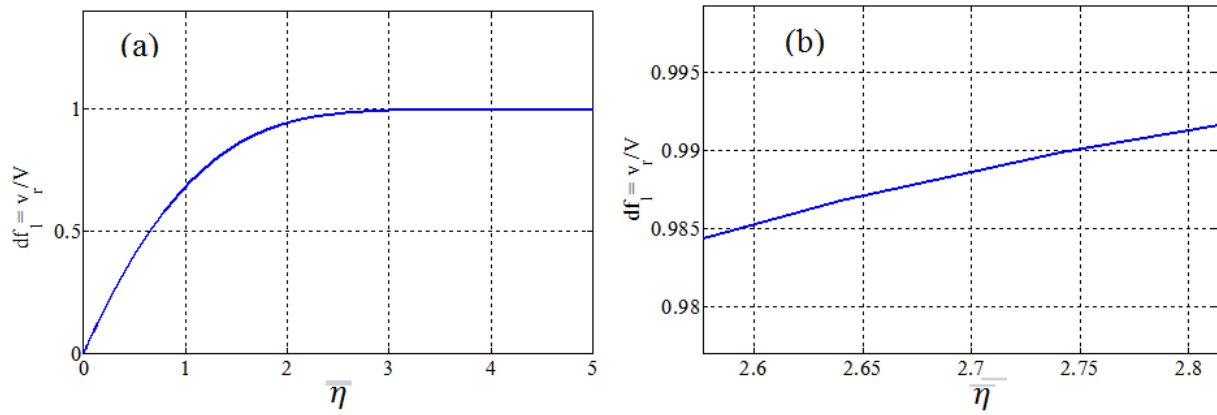
Figure 3.8: Variation of radial velocity in viscous region, b) showing definition of boundary layer thicknesses in the viscous region.

After finding variation of $f'(\eta)$, velocity components can be found. Therefore, the imposed shear force of air flow on the liquid-droplet interface is determined by equation (3.22).

$$\tau_{rz(z=0)} = \mu(\frac{\partial V_r}{\partial z} + \frac{\partial V_z}{\partial r}) \tag{3.22}$$

As it was mentioned earlier, the coefficient of a is obtained from numerical simulation of impinging air flow (see appendix B). For finding boundary layer thickness, it is needed to define a radial length scale, as radial velocity varies radially. The maximum spreading diameter for an impacting droplet on aluminum, Teflon and superhydrophobic surfaces at room temperature condition for Weber number up to 90 (i.e. non-splashing regime) are 8.6 mm, 8.4 mm and 7.2 mm,

respectively. Therefore, the corresponding coefficient of a for 10 m/s impinging air velocity becomes around 1700 (1/s) for aforementioned length scales.

As demonstrated in figure (3.8(b)), the corresponding η which defines the thickness of the boundary layer is 2.75. Therefore, using air properties at room temperature condition, the boundary layer thicknesses is approximated around 0.18 mm. The above information are used where force analysis of an impacting droplet on the solid surface is taken into account.

Having derived velocity components in the viscous region, the resultant air shear force, which varies radially, is coupled with the droplet wetting dynamics model. Indeed, this new external force of air flow inserted on the droplet wetting equation can change droplet spreading and recoiling behavior. Variation of the radial velocity in the viscous region was obtained from numerical simulation of boundary layer equation, presented in equation (3.20). Based on the numerical simulation results, air shear stress and force can be obtained through equations (3.23) and (3.24). In fact, the shear force term is simply eliminated once evaluation of droplet impact in the still air is taken into consideration. Therefore, the modified droplet wetting dynamics, demonstrated in equation (3.25), is numerically solved with the same aforementioned initial conditions.

$$\tau_{rz(z=0)} = \mu \times 0.9a\sqrt{\frac{2a}{\nu}}\,r = S_{air}r \tag{3.23}$$

$$F_{rz(z=0)} = \int_0^{2\pi}\int_0^r \mu \times 0.9a\sqrt{\frac{2a}{\nu}}\,r \times r\,dr\,d\theta = 2\pi S_{air}\frac{r^3}{3} \tag{3.24}$$

$$m_0\ddot{r} + C_{vis}\dot{r} + 2\pi\gamma(1 - cos\theta)r + 2\pi S_{air}\frac{r^3}{3} = 0 \tag{3.25}$$

As illustrated in figure (3.9), the effect of stagnation air flow, at maximum air velocity up to 10 m/s, has an observable effect on the spreading and retraction phase of an impacting water droplet. It slightly increases the maximum spreading diameter and droplet contact time. Furthermore, radial

velocity is varied as a function of distance from the stagnation point (i.e. r). Therefore, larger spreading diameter of an impacting water droplet is exposed to the larger resultant shear force of incoming air flow. On the other hand, for smaller spreading diameter (i.e. smaller droplet size or smaller droplet impact velocity) the effect of imposed air shear force is minimal, as it was confirmed by numerical solution of equation (3.25) demonstrated in figure (3.10). It is worth stressing that droplet rim formation is directly related to the droplet impact velocity. Therefore, limitation of not choosing higher droplet impact velocity arises from fragmentation phenomenon. Indeed, the presented model is valid for moderate droplet impact velocity in non-fragmentation regime.
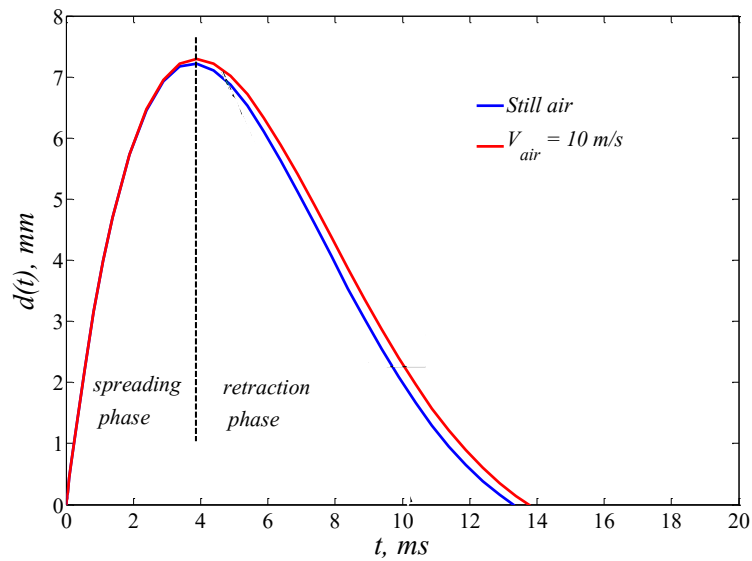
Figure 3.9: Effect of the stagnation air flow on wetting behavior of an impacting water droplet on the superhydrophobic surface. Droplet size and impact velocity are 2.6 mm and 1.6 m/s, respectively.
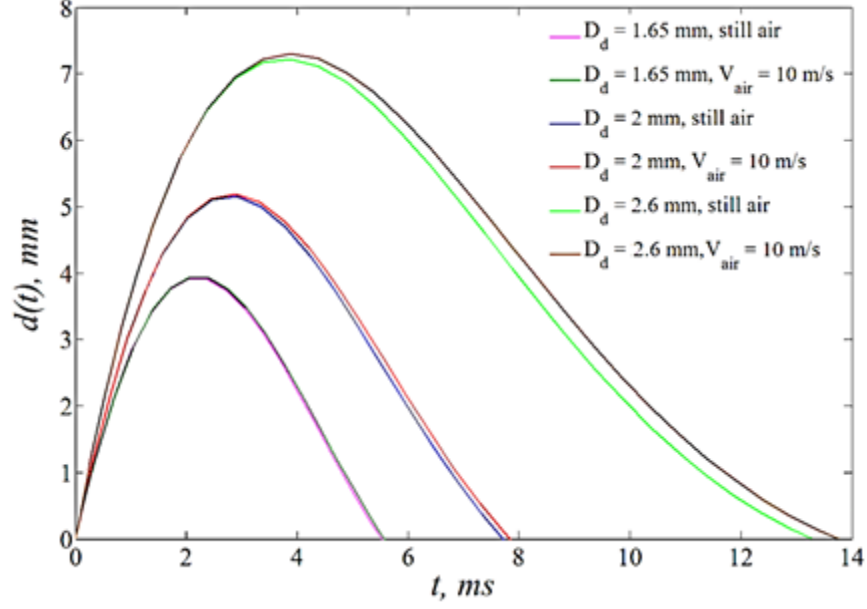
Figure 3.10: Effect of the maximum wetting diameter on the behavior of an impacting water droplet on the superhydrophobic surface accompanied with air flow.

As illustrated in figure (3.9), droplet maximum spreading diameter is slightly increased due to the presence of stagnation air flow. Although the aforementioned increase is small but it can change droplet wetting behavior from non-splashing to splashing regime where severe instability (i.e. Rayleigh instability) is formed at the rim periphery. This topic is elaborated in detail in chapter 4.

To this end, equation (3.25) is presented in a dimensionless form by defining $r = r_{max}R$ and $t_c = t^*\tau$, which t_c and τ are total time and time constant, respectively. Therefore, the final dimensionless form of the droplet wetting dynamics exposed to air flow is demonstrated by equation (3.26). τ (i.e. time constant) is shown in equation (3.27).

$$\frac{d^2R}{dt^{*2}} + \frac{C_{vis}}{4\pi\tau\gamma}\frac{dR}{dt^*} + \frac{1}{2}(1-cos\theta)R + \frac{D^2 S_{air} We^{0.5}}{24\gamma}R^3 = 0 \qquad (3.26)$$

$$\tau = \sqrt{\frac{m_0}{4\pi\gamma}} \qquad (3.27)$$

This model is validated against the experimental results at various droplet sizes, droplet impact velocities and viscosities which are presented in chapter 4. Furthermore, equation (3.26) is used

for further modifications when phase change (i.e. solidification) happens and the effect of ice nucleation mechanisms are coupled with the aforementioned equation. Detailed information regarding phase change (i.e. solidification) is presented in the following section.

3.3 Non-isothermal droplet impact dynamics with phase change

Understanding phase change mechanism is a crucial issue for many industrial applications ranging from wind turbine, electrical transmission power line and aerospace industries. In fact, solidification is a first order phase change which involves the concept of metastability and nucleation mechanism.[97] In temperature below the freezing point (i.e. 0 ℃ at 1 atm for water) solid phase becomes more stable phase compare to liquid one, as demonstrated in figure (3.11). Therefore, ice-water system is transformed from metastable condition to stable one by energy minimization. There are situations that metastability condition can be maintained if energy required for phase transition is not provided. Therefore, it is possible to have a water liquid below the freezing point. This liquid is called supercooled water. As illustrated in figure (3.12), freezing point of the water droplet can be changed by variation of the water pressure.[98] Therefore, by increasing pressure, triple phase point temperature for water liquid is reduced, as well. For instance, if pressure increases up to 4 bar, the triple phase point temperature will become around -4 ℃.
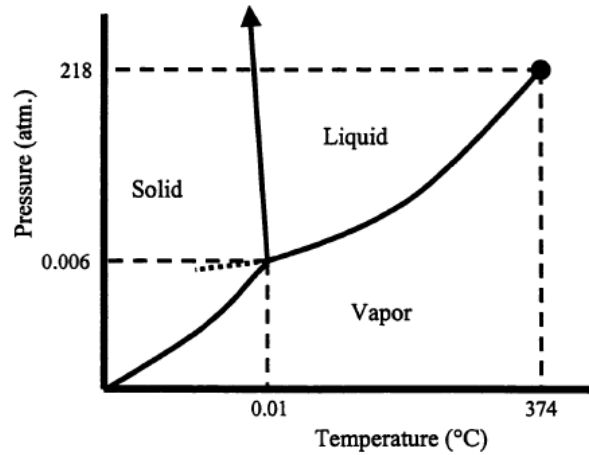
Figure 3.11: Phase diagram for H2O. [97]
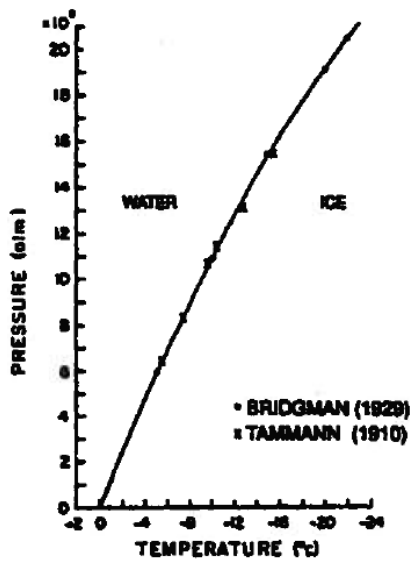
Figure 3.12: The melting curve for frozen water. [98]

3.3.1 Gibbs energy and ice nucleation rate

In general, phase change happens when heat generated or absorbed in a system. In fact, by variation of temperature, pressure and composition of a thermodynamic system (i.e. chemical

76

potential), it is possible to predict phase change phenomenon. Therefore, analysis of phase change is carried out based on the definition of thermodynamic potential namely Gibbs energy.

$$G = G(P, T, N_1, N_2, \dots, N_i) \tag{3.28}$$

For a homogeneous mixture, Gibbs energy is presented by the equation (3.26) which is derived based on the thermodynamic relationships.[99]

$$dG = VdP - SdT + \sum_i \mu_i dN_i \tag{3.29}$$

Where G, V, S and N are Gibbs energy, volume, entropy and particles number in a thermodynamically closed system. Furthermore, μ_i is defined as chemical potential of the system which is demonstrated in equation (3.30).

$$\mu_i = \left(\frac{\partial G}{\partial N_i}\right)_{P,T,N_j} \tag{3.30}$$

When a thermodynamic system is maintained at constant temperature and pressure, variation of Gibbs energy is presented by the production of chemical potential of system to the number of particles. For a binary system, which only solid and liquid phase are present, it is demonstrated by equation (3.31). [100]

$$dG = \mu_s dN_s + \mu_l dN_l \tag{3.31}$$

In a binary system total number of particles are constant (i.e. $N = N_s + N_l$). Therefore, equation (3.31) can be rearranged based on differences in chemical potentials, as shown in equation (3.32).

$$dG = (\mu_s - \mu_l)dN_s \tag{3.32}$$

By expanding chemical potential, $\mu(T, P)$, at constant temperature and knowing that variation of chemical potential versus temperature at contact pressure is defined with entropy of a system $,S = -\left(\frac{\partial \mu}{\partial T}\right)_p$, volumetric thermodynamic driving force is related to the entropy of a system demonstrated by equation (3.33).

$$\Delta G_v = \Delta\mu = -(S_s - S_l)\Delta T = H_{f,l}\frac{\Delta T}{T_m} \quad = H_{f,l}\frac{(T_m - T_{Interface})}{T_m} \tag{3.33}$$

Where, T_m and $H_{f,l}$ are melting point temperature of supercooled water droplet at 1 atm (i.e. 273.2 K) and latent heat of fusion, respectively. Indeed, the difference between chemical potential of ice nuclei and supercooled liquid results in a thermodynamic driving force towards solid phase where thermodynamic systems tries to minimize its energy by converting metastability condition to stable one.

Ice-water interface phase energy is defined based on the total amount of energy required for phase transformation within volume of water droplet (i.e. volume free energy driving force) and through surface area (i.e. surface energy retarding force). Therefore, for spherical ice nuclei, Gibbs free surface energy is shown by equation (3.34)

$$\Delta G_{(r,T)} = -\frac{4}{3}\pi r^3 \Delta G_v + 4\pi r^2 \gamma \tag{3.34}$$

Number of ice nuclei (embryos) existed at any time can be statistically represented by Boltzmann function which describes distribution of ice nuclei at any time.[101] However, number of ice nuclei at specific size (i.e. critical size) is a function of Gibbs free surface energy. Therefore, number of ice nuclei formation events at the critical size of embryos per unit area and time is demonstrated by equation (3.35), which is called ice nucleation rate.[102]

$$J(T) = K(T)A_{s-l}exp\left(\frac{-\Delta G_{(r,T)}}{k_B T}\right) \tag{3.35}$$

In the above formula, $K(T), A_{s-l}, \Delta G$ and k_B are kinematic rate prefactor describing diffusive flux of water molecules across the ice surface, interfacial area of water-substrate, Gibbs free surface energy regarding the formation of critical ice nuclei and Boltzmann constant.

The first term in the nucleation rate equation (e.g. (3.35)) is related to kinematic rate prefactor presented in equation (3.36). Indeed, the kinetic prefactor, $K(T)$, is combined with diffusion activation energy of a water molecule in order to cross the water-ice interface.[103]

$$K(T) = \frac{k_B T}{h} exp \left(\frac{-\Delta F_{diff}(T)}{k_B T} \right) n \qquad (3.36)$$

Where $T, h, \Delta F_{diff}$ and n are the absolute temperature, the Planck constant, the diffusion activation energy of a water molecule in order to cross the water-ice embryo and number of density of water molecules at the ice-water interface, respectively. n, is approximated about, $n \approx 10^{19} \ m^{-2}$.[103]

Therefore, kinetic prefactor combined with various parameters can be directly expressed based on aforementioned parameters and constants. However, for small variation of temperature in the supercooled water droplet (in the current research is -5 °C) kinematic prefactor is approximated to be a constant value (i.e. $10^{24} \ m^{-2} s^{-1}$).[2] In the following, two different types of ice nucleation mechanism which requires different amount of Gibbs free surface energy are presented. They are defined as homogeneous and heterogeneous ice nucleation mechanisms which are explained in detail in the following subsection.

3.3.2 Homogeneous ice nucleation

Classical nucleation theory (CNT) assumes that statistical fluctuations of embryos of ice nuclei molecules are the main reason of ice propagation through metastable supercooled water droplet.[101] Furthermore, surface energy barrier amount of each embryo is as equal as to that of macroscopic ice-water interface.[101] Energy required for system stabilization through phase change is related to entropy of ice-water molecules which results in producing volumetric thermodynamic driving force shown in equation (3.34).

As demonstrated in equation (3.34), for very small ice nuclei, volumetric thermodynamic driving force (i.e. negative sign in the equation) becomes smaller than surface retarding force (i.e. positive sign in the equation) maintaining metastability condition and ice-water interface will not be formed. However, as it passes the critical size of ice nuclei, defined by r^*, thermodynamic driving force for phase change becomes dominant compared to that of surface retarding force. Therefore, ice nuclei propagates through entire system forming macroscopic ice-water interface. Schematic of variation of Gibbs free surface energy varying by ice-nuclei radius is presented in figure (3.13).
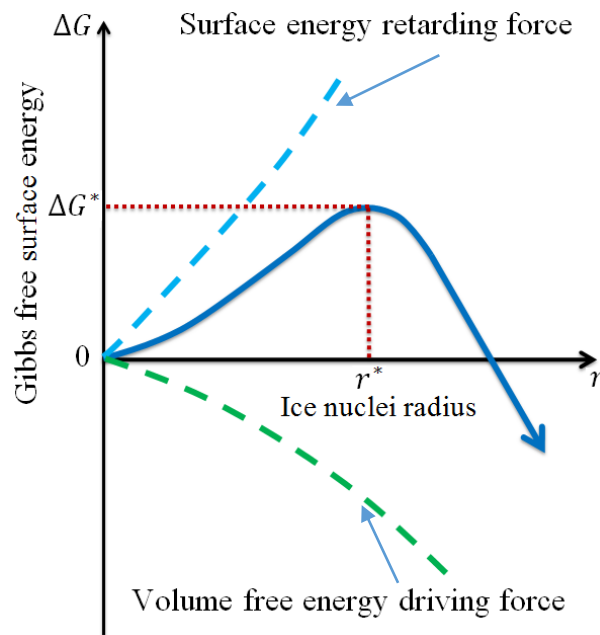
Figure 3.13: Variation of Gibbs free surface energy as a function of ice nuclei radius (adapted from L.A Tarshis, Solidification).[101]

As illustrated in figure (3.13), the maximum Gibbs free surface energy at the corresponding critical ice embryos defines whether crystallization process happens or not. In fact, ice embryos might produce during metastability condition but it is shrunken if it becomes smaller than critical size of stable ice nuclei. Furthermore, by derivation of equation (3.34) respect to the ice nuclei radius, critical size of the ice nuclei is represented by the equation (3.37) which is a function of ice-water surface tension at specified temperature over volumetric thermodynamics driving force.

$$\frac{d\Delta G_{(r,T)}}{dr} = 0, \ r^* = \frac{2\gamma_{wI}}{\Delta G_v} \tag{3.37}$$

By inserting above critical size of ice nuclei in equation (3.35), the maximum amount of energy required for stable ice propagation is defined by equation (3.38). In fact, the presented formula is well-known as a homogeneous ice nucleation mechanism.

$$\Delta G_{c,Homo} = \frac{16\pi\gamma_{wI}^3}{3\Delta G_v^2} \tag{3.38}$$

3.3.3 Heterogeneous ice nucleation

In many practical freezing conditions the effect of external agent (i.e. solid substrate) results in a faster minimization of Gibbs free surface energy at temperature above critical temperature of homogeneous ice nucleation [i.e. -37 ᵒC], as it was observed through various experimental observations.[65,79,104] In order to highlight this difference, ice-water surface tension force, where the bulk of ice particle contacts with substrate, is presented by balance of forces at the triple phase line, as demonstrated in figure (3.14). Water-ice surface tension can be presented by surface tension of substrate-water and substrate-ice, as demonstrated in equation (3.39).
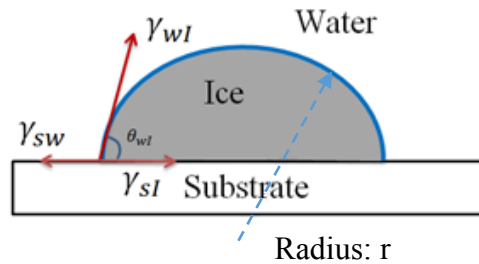
Figure 3.14: Forces acting on an ice nuclei in a supercooled water located on the solid substrate.

$$\gamma_{sw} = \gamma_{wI} \cos\theta_{wI} + \gamma_{sI} \tag{3.39}$$

Therefore, Gibbs free surface energy where an external agent is present (i.e. substrate) is demonstrated by equation (3.40), which has a new term in comparison with equation (3.34).

$$\Delta G\ (\theta_{wI}) = -V_r\Delta G_v + A_{wI}\gamma_{wI} + A_{sI}(\gamma_{sI} - \gamma_{sw}) \tag{3.40}$$

It is worth stressing that Gibbs free surface energy is also a function of the surface roughness which changes the amount of energy barrier required for phase change. However, recent studies have shown that where average roughness of the substrate is one order of magnitude larger than the critical size of ice nuclei Gibbs free surface energy can be presented only with ice-water contact angle.[102]

In the next step, volume of ice, surface area of ice-water and ice-substrate interfacial area can be defined through equations (3.41-3.43). Volume of ice nuclei located on the substrate is represented as a function of r, as demonstrated in equation (3.41).[97]

$$V_{i,r} = (2 + cos\theta_{wI})(1 - cos\theta_{wI})^2 \frac{\pi r^3}{3} \tag{3.41}$$

Surface are of ice nuclei is also presented as a function of r, defined by equation (3.42).

$$A_{wI} = (2 - 2cos\theta_{wI})\pi r^2 \tag{3.42}$$

Furthermore, substrate-ice area is shown by equation (3.43).

$$A_{sI} = \pi(rsin\theta_{wl})^2 \tag{3.43}$$

Substitution of all above equations in to the equation (3.40) and doing mathematical manipulations, the following equations (i.e. (3.44) and (3.45)) are given.

$$\Delta G\ (\theta_{wI}) = -\frac{4\pi}{3}r^3\Delta G_v f_{(\theta_{wI})} + 4\pi r^2\gamma_{wI}f_{(\theta_{wI})} \tag{3.44}$$

$$\Delta G\ (\theta_{wI}) = (-\frac{4\pi}{3}r^3\Delta G_v + 4\pi r^2\gamma_{wI})f_{(\theta_{wI})} \tag{3.45}$$

Where, $f_{(\theta_{wI})}$, is a geometrical factor defined by equation (3.46).

$$f_{(\theta_{wI})} = \left[\frac{(2+cos\theta_{wI})(1-cos\theta_{wI})^2}{4}\right] \tag{3.46}$$

Now it becomes clear that Gibbs free surface energy in the case of heterogeneous ice nucleation is weaker than that of homogeneous nucleation one which is due to the presence of geometrical value

of $f_{(\theta_{wI})}$, as illustrated in equation (3.46). Geometrical factor vary from 0 corresponding to extreme superhydrophilicity, to 1 regarding extreme superhydrophobicity, as illustrated in figure (3.15).

$$\Delta G_{Het}(\theta_{wI}) = \Delta G_{Homo}(\theta_{wI})f_{(\theta_{wI})} \qquad (3.47)$$
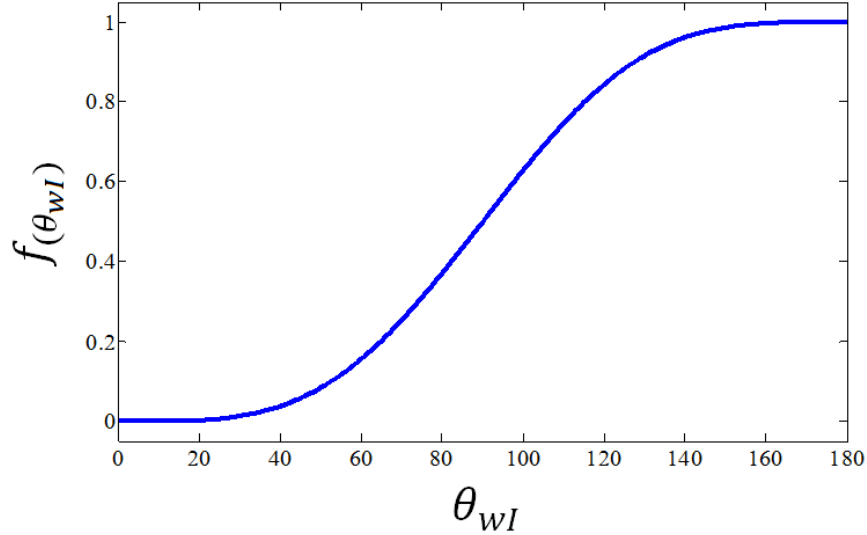
Figure 3.15: Variation of the geometrical factor as a function of water-ice surface contact angle on the planar surface.

As illustrated in figure (3.15), energy barrier for initiation of the phase change for heterogeneous ice nucleation mechanism becomes as equal as homogeneous one for extremely low wettable surfaces (i.e. a superhydrophobic surface with a contact angle near 180°). Therefore, superhydrophobic surfaces can be used as an excellent candidate for anti-icing purposes due to the associated large geometrical value which increases the amount of the energy barrier required for the phase change. Previous studies showed that in the extreme supercooling condition homogeneous ice nucleation occurs at temperature as low as -37 °C.[70] Recent study showed that heterogeneous ice nucleation for the bouncing droplet can be postponed significantly if droplet maintained above -24 °C which is almost close to that of homogeneous nucleation temperature.[1] The difference in the temperature arises from the fact that contact angle of superhydrophobic

surfaces is defined above 150° and not exactly in the extreme low wettability condition (i.e. contact angle up to 180°).[105]

The remaining issue is related to the correlation of the water-ice contact angle to apparent contact angle of the sessile droplet on the substrate. In fact, as discussed above, Gibbs energy barrier is defined with water-ice contact angle which cannot be simply measured by experimental apparatus. Therefore, equation (3.48) is used to relate water-ice contact angle to the apparent contact angle of sessile droplet.[102]

$$\gamma_{Ig}cos\theta_{Ig} = \gamma_{wg}cos\theta_{wg} + \gamma_{wI}cos\theta_{wI} \qquad (3.48)$$

It was experimentally observed that the contact angle of ice-gas on a substrate is equal to that of water-gas for freezing droplets. (i.e. $\theta_{Ig} = \theta_{wg}$).[102] Therefore, equation (3.49) is used for calculation of the geometrical factor. In equation (3.46), θ_{wg}, is the apparent contact angle of the sessile water droplet on the substrate.

$$cos\theta_{wI} = \frac{\gamma_{Ig}-\gamma_{wg}}{\gamma_{wI}}cos\theta_{wg} \qquad (3.49)$$

3.4 Solid-liquid interface temperature

In this section, a model for the transient conduction heat transfer from droplet to cold substrate is presented. Similar approach by Bahadur et al.[2] has been used for finding transient interface temperature and temperature distribution within spread droplet on different solid surfaces ranging from hydrophilic to superhydrophobic substrates. By using confocal image microscopy technique which provides the information regarding surface morphology (e.g. average roughness and ratio of wet to base area, Ø ratio,), it is possible to define semi post-air domain similar to that of textured surfaces. Therefore, previous predictive model of interface temperature for textured superhydrophobic surfaces can be modified accordingly to account for the spray on coated

superhydrophobic surfaces. Additionally, the proposed model of Bahadur et al.[2] needs to be further discussed as the predicted interface temperature contradicts with physical state being colder than that of substrate at the initial condition. Therefore, another derivation of the transient conduction equation was carried out to predict the interface temperature. Transient conduction equation was solved for each domain. The first domain involves substrate and semi post-air geometry and the second one is the droplet, as demonstrated in figure (3.16), which is similar to that of Bahadur et al.[2]

It is worth mentioning that convection boundary condition (i.e. airflow effect) at the top of spread droplet was not considered for solving transient heat condition equations. In fact, the penetrated heat length, [67] $\delta_h \approx (\alpha_w t_c)^{\frac{1}{2}}$, during spreading and retraction time for SHS, which is about 14 ms, is 42 μm. Furthermore, for aluminum and Teflon substrates spreading and retraction time is up to 100 ms. Therefore, heat penetration length becomes 112 μm which is almost 5 folds smaller than the thickness of splat. Therefore, the effect of the convective heat transfer due to the cold air flow on the interface of spread droplet can be neglected. In the following, analytical predictive model of solid-liquid interface temperature is presented.
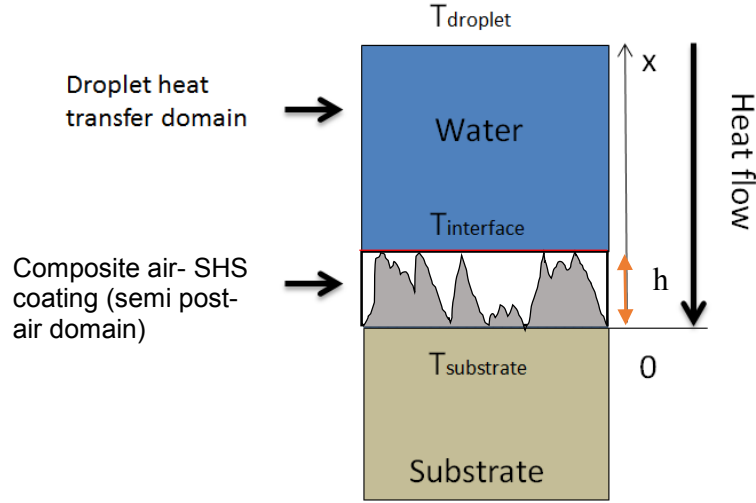
Figure 3.16: Schematic of two domains involved in the model of transient heat conduction for finding interface temperature. Effect of air thermal resistance is modeled in the average thermal diffusivity of semi post-air domain.

Transient heat conduction equations for domains illustrated in figure (3.16) are demonstrated by equations (3.50) and (3.51).

$$\frac{\partial T_{pa}(x,t_c)}{\partial t_c} = \alpha_{pa} \frac{\partial^2 T_{pa}(x,t_c)}{\partial x^2} \text{ , for region between } 0 < x < h. \qquad (3.50)$$

$$\frac{\partial T_w(x,t_c)}{\partial t_c} = \alpha_w \frac{\partial^2 T_w(x,t_c)}{\partial x^2}, \quad \text{for region between } x > h. \qquad (3.51)$$

In the above equations, T_{pa}, is temperature of semi post-air domain and T_w is water temperature, h is average roughness of surface and t_c is the total contact time of liquid droplet on the surface. α_{pa} and α_w are thermal diffusivity of semi post-air domain and water, respectively, as presented by Bahadur et al.[2]

The boundary and initial conditions for each domain are presented below. Indeed, two boundaries and one initial condition are needed for each domain.

Boundary and initial conditions for semi post-air domain are like following:

First boundary condition: $T_{pa}(0,t) = T_{substrate}$, $x = 0$ \qquad (3.52)

Second boundary condition: $T_{pa}(h, t) = T_w(h, t)$, $x = h$ (3.53)

First initial condition: $T_{pa}(x < h, 0) = T_{substrate}$, $t = 0$ (3.54)

Boundary and initial conditions for water domain are like following:

First boundary condition: $T_w(h, t) = T_{pa}(h, t)$, $x = h$ (3.55)

Second boundary condition: $T_w(\infty, t) = T_{droplet}$, $x = infinity$ (3.56)

First initial condition: $T_w(x > h, 0) = T_{droplet}$, $t = 0$ (3.57)

By applying boundary and initial conditions [see appendix (C) for more detail], the final form of the solid-liquid interface temperature is shown by equation (3.58).

$$T_{w-interface}(h, t_c) = T_{drop} + [(T_{sub} - T_d)] erfc \left(\frac{h_{pa}}{2\sqrt{\alpha_{pa} t_c}} \right)$$ (3.58)

Furthermore, transient temperature distribution within water droplet is also demonstrated in equation (3.59).

$$T_w(x_w, t_c) = T_{drop} + [(T_{sub} - T_d)] \frac{erfc\left(\frac{h_{pa}}{2\sqrt{\alpha_{pa} t_c}}\right)}{erfc\left(\frac{h_w}{2\sqrt{\alpha_w t_c}}\right)} . erfc \left(\frac{x_w > h}{2\sqrt{\alpha_w t_c}} \right)$$ (3.59)

It is worth mentioning that the complementary error function is a reducing function which becomes equal to 1 when $\eta = \frac{x_w > h}{2\sqrt{\alpha_w t_c}} \to 0$. However, the height of semi post-air domain at interface line, which has a small length scale compare to the thickness of spread droplet (i.e. average roughness length scale), is not exactly zero which leads to the complementary error function becomes smaller than 1. Neglecting this term causes a significant physical conflict in terms of temperature value which becomes even colder than substrate temperature totally contradicted with initial and boundary conditions.

Form equation (3.58) it is possible to find the interface temperature of an impacting supercooled water droplet on different solid surfaces. As illustrated in figure (3.17), aluminum substrate shows

a faster convergence to substrate temperature in comparison with Teflon and superhydrophobic surfaces due to the small average roughness (see table (2.1)) and higher thermal diffusivity of semi post-air domain. Furthermore, from equation (3.59) temperature distribution within the water droplet can be obtained, as demonstrated in figure (3.18).
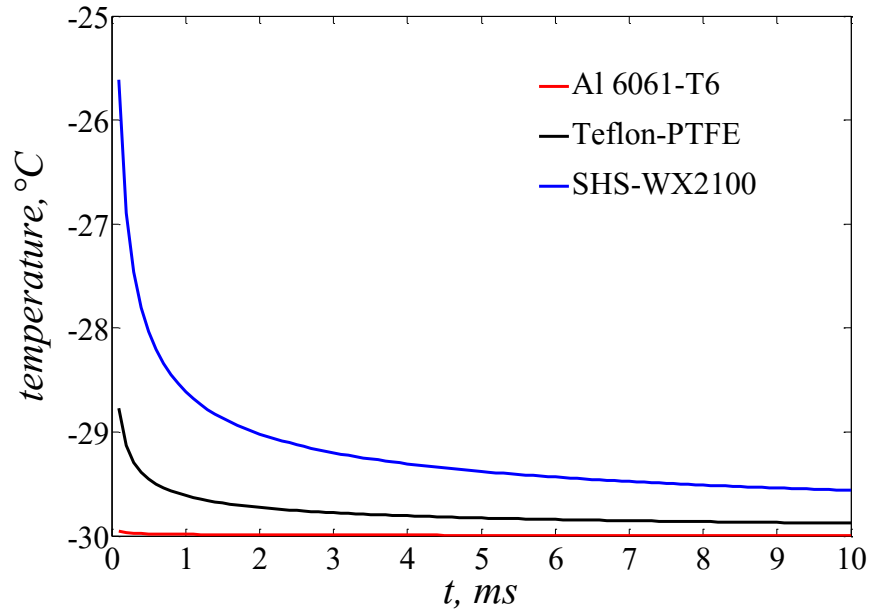
Figure 3.17: Transient interface temperature of an impacting supercooled water droplet on solid surfaces. Droplet and substrate temperatures are -5.5 and -30 ⁰C, respectively.
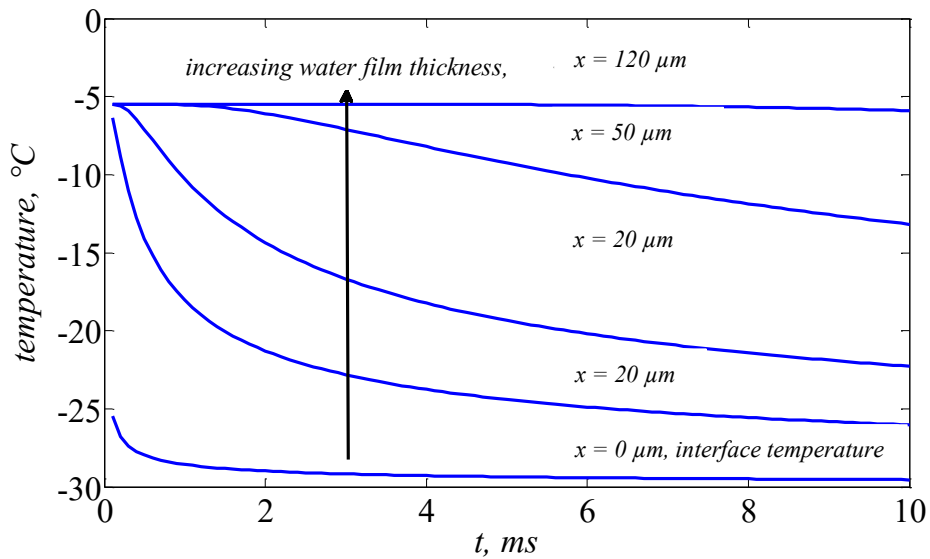
Figure 3.18: Transient temperature distribution of an impacting supercooled water droplet on cold superhydrophobic surface. Droplet and substrate temperatures are -5.5 and -30 ⁰C, respectively.

3.5 Gas-liquid interface temperature

In this section, a model for quasi-steady heat transfer from droplet to cold gas is presented. It was confirmed that supercooled water droplet in an unsaturated gas flow is faced evaporation cooling which further reduces the supercooled water droplet interface temperature.[36] Evaporation rate of water droplet is varied when air velocity and humidity are present. Therefore, for pure diffusive condition (i.e. still air), evaporation rate is minimal. In fact, by increasing the air velocity, the interface temperature reduction becomes larger to that of still air which significantly promotes the effect of homogeneous ice nucleation mechanism rather than heterogeneous nucleation one. In the current study, which investigates the effect of stagnation air flow on an impacting supercooled water droplet, evaporation rate assumed to be uniform at all location of an impacting droplet at the maximum spreading diameter. Indeed, this is a conservative assumption by slightly overestimating the evaporation cooling rate due to the fact that radial velocity (see figure (3.19), which promotes the evaporation rate, is varied radially.
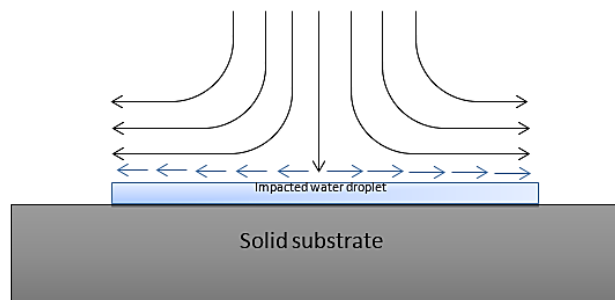
Figure 3.19: Schematic of an impacting water droplet at maximum spreading diameter accompanied with stagnation flow.

In the following, the temperature difference at the gas–liquid interface is estimated for an impacting supercooled water droplet on various solid surfaces (i.e. aluminum, Teflon and superhydrophobic surfaces) at the maximum spreading diameter where various air velocities and

different humidity ratios are present. In fact, the effect of homogeneous ice nucleation becomes more dominant for larger interfacial area (i.e. maximum spreading diameter) which the most probable crystallization process at gas-liquid interface is occurred at this time. As discussed before, the radial velocity, $V_r = arf'(\eta)$, is a an important parameter for evaluation of evaporation cooling rate. Therefore, radial velocity variation in the boundary layer thickness is taken into consideration. Based on the derived equation of viscous air flow (i.e. Homann flow approach) an average value of $f'(\eta)$ (i.e. 0.7) was chosen to account the effect of boundary layer on the radial air velocity. Assuming quasi steady condition, evaporation rate can be obtained by balancing all the involved energies,[36] as demonstrated in equation (3.60). Due to the presence of air flow, forced convective heat transfer is present. Furthermore, heat flow is transferred from the droplet to substrate by conduction mechanism.

$$\dot{Q}_{evaporation} = \dot{Q}_{g-convection} + \dot{Q}_{w-conduction} \tag{3.60}$$

In equation (3.60), it is need to incorporate solid-liquid interface temperature at the maximum spreading diameter (i.e. 3 ms) in equation (3.60). In fact, in such a small period of time (i.e. 3 ms) interface temperature rapidly changes from droplet to substrate temperature, as illustrated in figure (3.20). In the following, the detailed derivation of gas-liquid interface temperature undergoes evaporation cooling is presented.
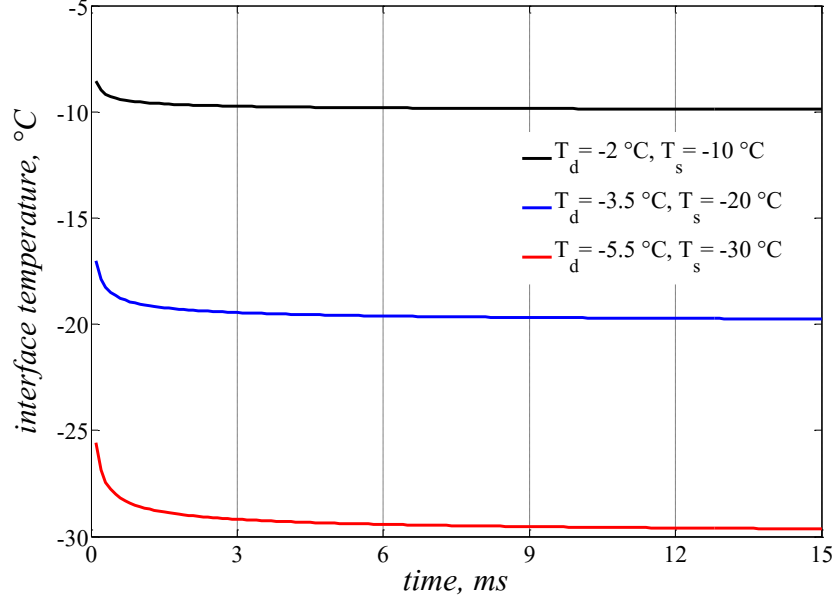
Figure 3.20: Variation of solid-liquid interface of impacting supercooled water droplet on superhydrophobic surface at different temperatures.

Heat rate of the aforementioned terms in equation (3.60) is expressed like the following equations.

$$\dot{Q}_{evaporation} = \Delta H_v \dot{m}_{eva} \tag{3.61}$$

$$\dot{Q}_{g-convection} = h_g A_{g-w}(T_g - T_w) \tag{3.62}$$

$$\dot{Q}_{w-conduction} = \frac{k_w A_{s-w}(T_{s-l,interface} - T_w)}{h_{lamella}} \tag{3.63}$$

Therefore, substituting equation (3.61), (3.62) and (3.63) into equation (3.60) results in equation (3.64).

$$\Delta H_v \dot{m}_{eva} = h_g A_{g-w}(T_g - T_w) + \frac{k_w A_{s-w}(T_{s-l,interface} - T_w)}{h_{lamella}} \tag{3.64}$$

Where evaporation rate per area is demonstrated by equation (3.65).

$$\dot{m}_{f,eva} = \frac{\dot{m}_{eva}}{A_{g-w}} \tag{3.65}$$

Rate of evaporation per area (i.e. mass flux) is approximated by equation (3.66).[106]

$$\dot{m}_{f,eva} \approx [0.0093/\rho_{s-aw}c_{pwa} + 6.7 \times 10^{-6} \, V_{air}] \frac{(P_{vo} - P_{vi})}{T_{oi}} \tag{3.66}$$

91

Where, $T_{oi} = (T_d + T_g)/2$, is the average surface temperature of water and ambient gas. c_{pwa}, P_{vo} and P_{vi} are specific heat of water vapor for supercooled droplet ($c_{pwa} = 1858 \ j/(kg.K)$), vapor pressure at gas-water interface and vapor pressure in the air, respectively.

At maximum spreading diameter thickness of the spreading lamella is defined based on the mass conservation of an impacting droplet before and after impact condition at the maximum spreading diameter. Therefore, the thickness of spreading lamella at the maximum spreading diameter is represented by equation (3.67).

$$h_{lamella} = \frac{2D^3}{3D_{max}^2} \qquad\qquad (3.67)$$

On the other hand, at the maximum spreading diameter, which spreading droplet gets cylindrical flattened shape, interfacial area of liquid-gas (i.e. A_{g-w}) and solid-liquid (i.e. A_{s-w}) is approximated with circular area at the maximum spreading diameter. Therefore, assuming lateral surface of spread droplet is negligible ($h_{lamella}$ is small), solid-liquid and gas-liquid interfacial area becomes equal (i.e. $A_{g-w} = A_{s-w}$). Therefore, equation (3.64) is rewritten as equation (3.68).

$$\frac{4\Delta H_v \dot{m}_{eva}}{\pi D_{max}^2} = h_g(T_g - T_{g-w,interface}) + \frac{k_w(T_{s-l,interface} - T_{g-w,interface})}{h_{lamella}} \qquad\qquad (3.68)$$

Therefore, by simple manipulation and knowing that maximum spreading diameter can be replaced with theoretical models (see appendix C for more detail) predictive model of gas-liquid interface temperature accompanied by evaporation cooling is shown by equation (3.69).

$$T_{g-w,interface} = (h_g T_g + 1.5 \ \frac{k_w D_{max}^2 T_{s-w,interface}}{D^3} - \Delta H_v \dot{m}_{f,eva})/ (h_g + 1.5 \ \frac{k_w D_{max}^2}{D^3}) \quad (3.69)$$

As demonstrated in equation (3.69), solid-water interface temperature is an important parameter for finding gas-water interface temperature. It demonstrates that solid-water interface temperature will not be as cold as substrate temperature, as demonstrated in figure (3.20). If substrate

92

temperature considered in the equation (3.69) gas-liquid interface would be slightly overestimated which results in inappropriate calculation of ice nucleation rate, as illustrated in figure (3.21). After deriving predictive model of gas-liquid interface temperature, incorporating the rate of homogeneous ice nucleation on droplet wetting dynamics is elaborated as follows.

Effect of the homogeneous ice nucleation mechanism can be incorporated to the wetting dynamics of an impacting supercooled water droplet by changes in the surface tension of the droplet. After the formation of ice nuclei on spreading droplet interface, surface tension of supercooled water droplet is substituted with ice-water mixture. Surface tension of ice-water is almost three folds smaller than that of liquid state. Therefore, by increasing the exposure time of airflow on spreading droplet, a significant reduction in retraction capillary force (i.e. $\pi \gamma D_{max}(1 - cos\theta_{rec})$ is occurred. In the following section, this topic is profoundly elaborated.
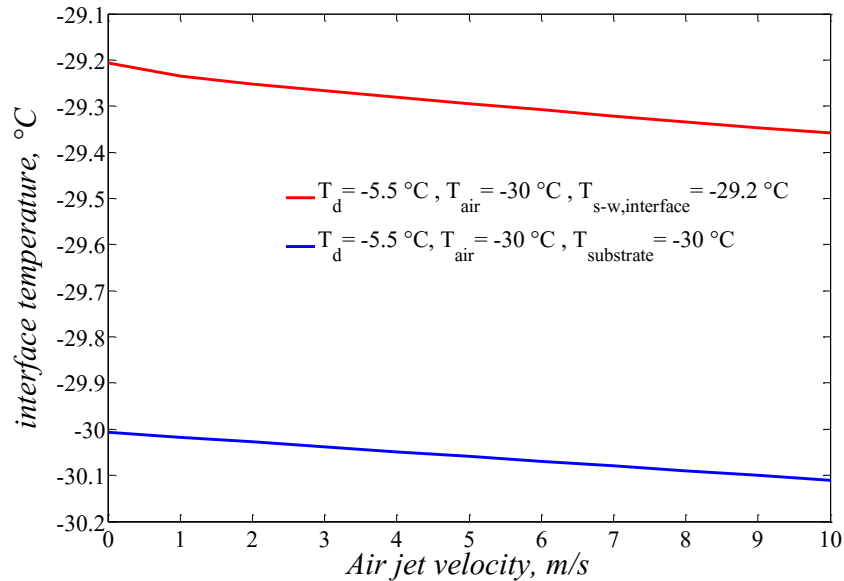
Figure 3.21: Variation of gas-liquid interface of impacting supercooled water droplet on the superhydrophobic surface at different air jet velocities at the maximum spreading diameter.

93

3.6 Integrated model of droplet wetting dynamics with ice nucleation theory

As described in the previous sections, a universal model of droplet impact behavior on a superhydrophobic surface was presented based on the modified mass-spring-dashpot system. The effect of incoming air flow (i.e. stagnation flow) was inserted to the droplet wetting dynamics through classical Homann flow approach. The final dimensionless form of droplet wetting dynamics on a superhydrophobic surface with high mobility (i.e. low contact angle hysteresis) combined with the effect of air flow is shown in equation (3.26) represented in equation (3.70).

$$\frac{d^2 R}{dt^{*2}} + \frac{C_{vis}}{4\pi\tau\gamma}\frac{dR}{dt^*} + \frac{1}{2}(1 - cos\theta)R + \frac{D^2 S_{air} We^{0.5}}{24\gamma}R^3 = 0 \qquad (3.70)$$

Which τ is time constant defined by equation (3.27).

The next important step is related to non-isothermal condition where phase change phenomenon is present. Bahadur et al.[2] used an innovative method of coupling heterogeneous ice nucleation on wetting dynamics of a supercooled water droplet by changing in the contact angle of water-substrate. It was proved that when ice growth rate becomes dominant surface superhydrophobicity break down happens at a temperature below the critical temperature of heterogeneous ice nucleation for the bouncing droplet (i.e. -24 ºC). This superhydrophobicity breakdown arises from the fact that the formed ice nuclei changes the contact angle of water-substrate which converts superhydrophobic surface to the hydrophilic one. By consideration of variation of contact angle with temperature [2], the final form of the droplet wetting dynamics considering the effect of both stagnation air flow and heterogeneous ice nucleation is demonstrated by equation (3.71).

$$\frac{d^2 R}{dt^{*2}} + \frac{C_{vis}}{4\pi\tau\gamma}\frac{dR}{dt^*} + \left[1 - C\phi_o t_c^2 \exp\big(f\big(T_{interface}\big)\big)\right]R + \frac{D^2 S_{air} We^{0.5}}{24\gamma}R^3 = 0 \qquad (3.71)$$

Where C_{vis}, C, t_c are empirical viscosity, empirical and theoretical term regarding ice propagation in supercooled water [65] and total contact time of an impacting droplet, respectively. Furthermore,

ϕ_o, which is defined as a ratio of wet area to base area of substrate, can be extracted from confocal laser microscopy technique. Additionally, the function $f(T_{interface})$ is approximated by equation (3.72).[65] More detailed information regarding integration of heterogeneous ice nucleation mechanism on the droplet wetting dynamics can be found in appendix C.

$$f(T_{interface}) \approx \frac{-T_m^2}{((T_m - T_{s-l})^2 T_{s-l})} \tag{3.72}$$

In the following, methodology of coupling the effect of homogeneous ice nucleation (i.e. to the effect of air flow) on droplet wetting dynamics is presented.

As discussed in the above paragraph, the effect of heterogeneous ice nucleation is coupled with droplet wetting dynamics through variation of water-substrate contact angle. On the other hand, under practical condition of droplet impact on a cold substrate the effect of cold air flow is also present which might change droplet wetting dynamics behavior. Therefore, expectation of having both homogeneous and heterogeneous ice nucleation is rational. As presented in equation (3.71), heterogeneous ice nucleation can be coupled with the droplet hydrodynamics model through contact angle reduction. In fact, the effect of contact angle reduction on the droplet wetting dynamics is emerged by reducing retraction capillary force, $\pi \gamma_{wg} D_{max} (1 - cos\theta_{rec})$. By growth of ice nuclei, receding contact angle becomes lower than the recommended value for a surface being considered as a superhydrophobic substrate (i.e. below 150°). Aforementioned capillary force can be even further reduced by the reducing amount of surface tension where air flow is present (i.e. the effect of homogeneous ice nucleation).

Homogeneous ice nucleation is also integrated with droplet wetting dynamics through variation of surface tension. Cold air flow induces homogeneous ice nucleation by evaporation cooling mechanism as ice nuclei cluster finally locates at the gas-liquid interface due to the evaporation of water which results in reduction on Gibbs free surface energy promoting crystallization process.

In fact, the associated Gibbs energy barrier becomes even lower than that of heterogeneous ice nucleation by gas-liquid interface temperature reduction. Consequently, ice nuclei propagates through the spread droplet which results in having mixture of ice-water at the interface of supercooled water droplet.

Mixture of ice-water has a surface tension almost 3.5 [e.g. 20 mN/m]^2 folds lower than water droplet at room temperature [e.g. 73 mN/m]. Therefore, during retraction phase, surface tension is reduced which further decreases the retraction capillary force, $\pi \gamma_{wl} D_{max}(1 - cos\theta_{rec})$,. Here, a method of coupling homogeneous ice nucleation to droplet wetting dynamics model is implemented based on the variation of surface tension. Changes in the supercooled water surface tension due to the growth of ice nuclei can be represented by equation (3.73).[2]

$$\lambda(t) = 2\pi \int_0^{t_c} J(t)\, r(t)^2 dt \qquad (3.73)$$

Where, $\lambda(t)$, is time dependent surface tension function, $J(t)$ is homogeneous ice nucleation rate based on the gas-liquid interface temperature and $r(t)$ is ice cap radius. More detailed information regarding the correlation between ice cap radius to the surface and droplet properties can be found in appendix C. Variation of surface tension through ice nucleation mechanism is shown by equation (3.74).

$$\gamma(\lambda) = \gamma_o - \frac{\partial \gamma}{\partial \lambda}\lambda(t) \qquad (3.74)$$

Which γ_o is surface tension of supercooled water at the specific temperature without formation of ice nuclei at the gas-liquid interface. Therefore, equation (3.74) is rewritten as demonstrated in equation (3.75). In this equation, $b = 0.015$, is an adjusting parameter used for all scenarios of supercooled water droplets impacting on cold substrates.

$$\gamma(\lambda) = \gamma_o - b\lambda(t) \qquad (3.75)$$

Using the same methodology presented for variation of water-substrate contact angle,[2] variation of surface tension versus temperature can be demonstrated by equation (3.76). In equation (3.76) C, t_c and $f(T_{interface})$ are empirical and theoretical terms regarding ice propagation in supercooled water droplet,[65] total contact time and temperature function, respectively. Function $f(T_{interface})$ is approximated by equation (3.77).[65]

$$\lambda(t) = Ct_c^2 \exp(f(T_{interface})] \tag{3.76}$$

$$f(T_{interface}) \approx \frac{-T_m^2}{((T_m - T_{g-l})^2 T_{g-l})} \tag{3.77}$$

In order to couple the effect of homogeneous ice nucleation through variation of surface tension on droplet wetting dynamics model, primary non-dimensionless form of the aforementioned equation is used, as presented in equation (3.78).

$$m_o \frac{d^2r}{dt^2} + 2\pi\gamma(1 - cos\theta)r = 0 \tag{3.78}$$

In equation (3.78), temporal water surface tension is inserted to the droplet wetting dynamics' model, as given in equation (3.79).

$$m_o \frac{d^2r}{dt^2} + 2\pi r(\gamma_o - b\lambda)(1 - cos\theta) = 0 \tag{3.79}$$

By defining $R = \frac{r}{r_{max}}$ and $t^* = \frac{t_c}{\tau}$ which, τ, is a time constant shown by equation (3.27). Dimensionless form of equation (3.79) is presented in equation (3.80).

$$\frac{d^2R}{dt^{*2}} + (1 - b\frac{\lambda}{\gamma_o})\frac{1}{2}(1 - cos\theta)R = 0 \tag{3.80}$$

Therefore, the final dimensionless form of droplet wetting dynamics considering the effect of both homogeneous and heterogeneous ice nucleation is shown in equations (3.81). In fact, the effect of homogeneous and heterogeneous ice nucleation can be clearly observed in equation (3.81) through variation of surface tension and water-substrate contact angle, respectively.

$$\frac{d^2R}{dt^{*2}} + \left(1 - b\frac{\lambda}{\gamma_o}\right)\left[1 - C\phi_o t_c^2 \exp\left(f\left(T_{interface}\right)\right)\right]R = 0 \tag{3.81}$$

The final form of the droplet wetting dynamics' model accompanied with airflow at different velocities and temperatures is demonstrated in equation (3.82). Indeed, the effect of both viscous term and stagnation air flow alter wetting dynamics behavior, as it was discussed in previous section. The proposed predictive model of droplet wetting dynamics can facilitate the evaluation of wetting dynamics of an impacting supercooled water droplet accompanied with phase change phenomenon.

$$\frac{d^2R}{dt^{*2}} + \frac{C_{vis}}{4\pi\tau\gamma}\frac{dR}{dt^*} + \left(1 - b\frac{\lambda}{\gamma_o}\right)\left[1 - C\phi_o t_c^2 \exp\left(f\left(T_{interface}\right)\right)\right]R + \frac{D^2 S_{air} We^{0.5}}{24\gamma}R^3 = 0 \tag{3.82}$$

Equation (3.82) is solved numerically with MATLAB ODE45 using the following initial conditions:

$$\frac{dR}{dt} = 0 \text{ @ } t = 0$$

$$R = 1 \text{ @ } t = 0$$

Numerical results of equation (3.82) are presented in chapter 4 which are compared against the experimental results of supercooled water droplet.

Chapter 4

Results and discussion

In this chapter the results of isothermal and non-isothermal water droplet impacting on surfaces with various wettabilities are presented. First, the results of room temperature stagnation air flow on hydrophilic, hydrophobic, near superhydrophobic and coated superhydrophobic surfaces are presented. In fact, phenomenology of the stagnation air flow on an impacting water droplet is carried out by definition of the pressure and shear domain air flow which is discussed in detail in the current chapter. Furthermore, predictive transient model of the maximum spreading diameter on superhydrophobic surfaces is also validated against experimental results.

Consequently, thermal transport analysis of an impacting supercooled water droplet on a cold substrate is presented. Experimental results are presented in three distinct sections. For hydrophilic and hydrophobic surfaces the concept of the pinning/freezing at the maximum spreading diameter is presented which can be directly related to the droplet and substrate temperatures. On the other hand, for the superhydrophobic surface, critical temperature of pinning/freezing, where superhydrophobicity breakdown is occurred, can be found through various experiments in the low temperature conditions. Furthermore, the effect of stagnation air flow in the low temperature condition on the droplet wetting behavior is provided. It facilitates repellency of an impacting droplet through contact time reduction where substrate temperature is above the temperature of

heterogeneous ice nucleation for the bouncing droplet (i.e. -24 ºC). On the other hand, it has an adverse effect for temperatures below the critical one (i.e. -24 ºC). Finally, these results are compared against predictive model of ice formation in low temperature conditions described in chapter 3.

4.1 Isothermal droplet exposed to air flow

In this part, experimental investigation of air flow effect on an impacting water droplet was carried out on four surfaces with different wettabilities ranging from hydrophilic to superhydrophobic surfaces. Air velocity was varied from still air to 10 m/s. The maximum air velocity was chosen to satisfy the assumption of negligible droplet deformation moving through air flow which was explained in detail in chapter 2.

4.1.1 Hydrophilic and hydrophobic surfaces

The effect of stagnation air flow on an impacting water droplet on hydrophilic (i.e. aluminum) and hydrophobic (i.e. Teflon) substrates are investigated using scaling analysis of forces acting on the spreading droplet. In figures (4.1) and (4.2) sequential images of an impacting water droplet on aluminum substrates are illustrated. As shown in figure (4.1), the spread ligament is faced retraction delay where air velocity is present. However, non-recoiling phase of an impacting water droplet at Weber number around 220 was observed for air velocity up to 10 m/s, as demonstrated in figure (4.2). This phenomenon is related to the competition of capillary and viscosity forces against resultant shear and normal forces of incoming stagnation air flow which is described in the following.
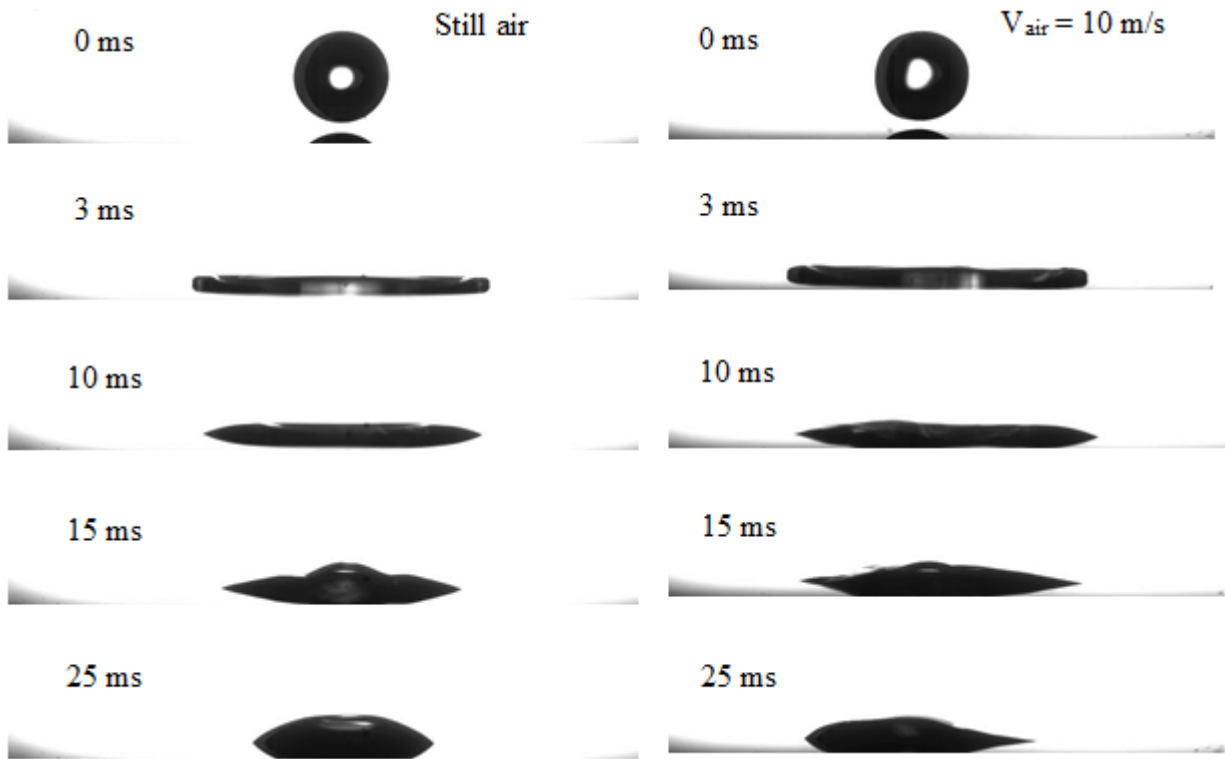
Figure 4.1: Sequential images of an impacting water droplet on the aluminum substrate in still air and air velocity of 10 m/s. Droplet size and impact velocity are 2.6 mm and 1.6 m/s, respectively.
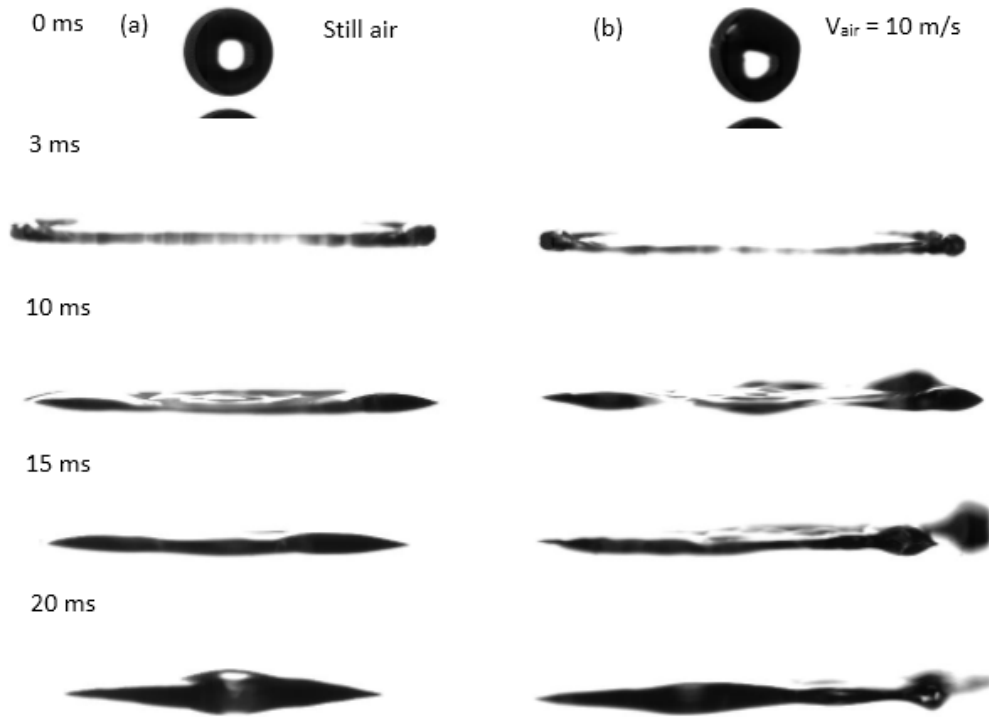
Figure 4.2: Sequential images of an impacting water droplet on the aluminum substrate in the still air and air velocity of 10 m/s. Droplet size and impact velocity are 2.6 mm and 2.5 m/s, respectively.

For an impacting water droplet, the capillary force during the recoiling phase can be defined by dynamic receding contact angle in an arbitrary length of the spreading lamella. Maximum capillary force attained at the corresponding maximum spreading diameter is expressed by, $\pi \gamma D_{max}(1 - cos\theta_{rec})$ and viscous force is defined by $F_{vis} \approx \mu \frac{\partial V_r}{\partial z} A \approx \mu_w \frac{V_{rec}}{4\delta_w} \pi D_{max}^2$,[79] which δ_w is boundary layer thickness of the spread water droplet.[41] Velocity components of stagnation air flow in the viscous region are $V_r = arf'(\eta)$, $V_z = -\sqrt{2a\upsilon} f(\eta)$ and $\eta = z\sqrt{\frac{2a}{\upsilon}}$ is similarity variable used to solve nonlinear ODE based on geometrical value of a. Coefficient of a is determined by the numerical simulation of air flow and becomes around 1700 1/s for air jet velocity up to 10 m/s (see appendix B and C).

Resultant shear stress on an impacting water droplet is obtained by $\tau_{rz(z=0)} = \mu \left(\frac{\partial V_r}{\partial z} + \frac{\partial V_z}{\partial r} \right)$.

Therefore, by scaling analysis, resultant air shear force at the liquid-gas interface is defined $F_{s@interface} \approx \mu_{air} \left(\frac{ar}{\delta_{air}} \right) \pi r^2$ or at the maximum spreading diameter can be written like $F_{s@interface} \approx \mu_{air} \left(\frac{aD_{max}}{8\delta_{air}} \right) \pi D_{max}^2$, where δ_{air} is the boundary layer thickness of the stagnation air flow on the interface of spread droplet. Boundary layer thickness of air is almost two times larger than that of liquid water droplet (i.e. 0.18 mm for air flow compare to 0.08 mm for water droplet), as it was discussed in chapter 3. Wetting area of an impacting water droplet (solid-liquid) is similar to that of liquid-gas interfacial area. Therefore, the remaining influential parameters are recoiling velocity of water droplet and radial velocity of air flow.

Quantitative evaluation of temporal spreading diameter, as demonstrated in figure (4.3), shows that receding velocity ($V_{rec} = 2V_{d,radial}$) of an impacting water droplet on the polished aluminum in the still air is around 0.15 m/s at the early stage of retraction phase (i.e. less than 15 ms) for droplet impact velocity up to 1.6 m/s. On the other hand, radial velocity of air flow at the maximum spreading diameter for a droplet having impact velocity up to 1.6 m/s reaches about 6 m/s for the stagnation air jet velocity up to 10 m/s.
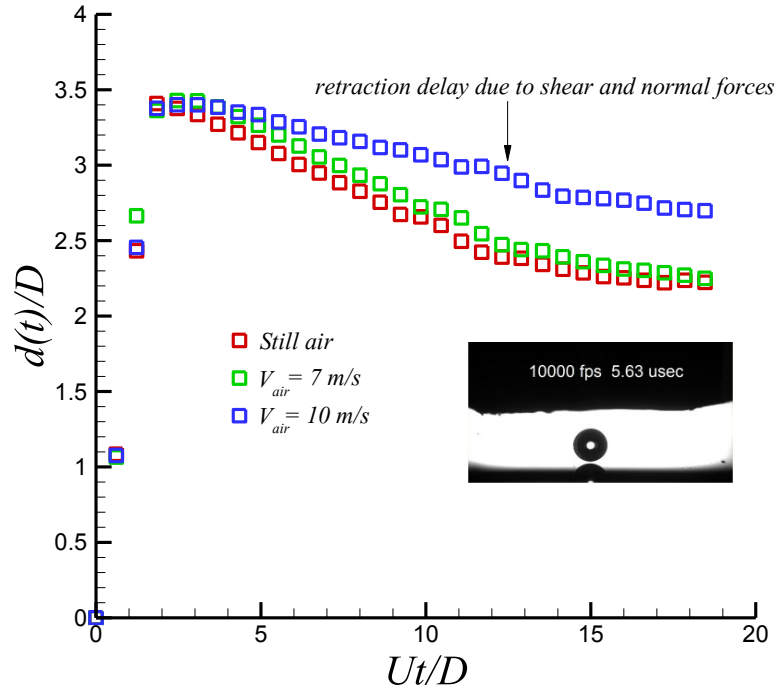
Figure 4.3: Temporal evolution of an impacting water droplet on the aluminum substrate. Droplet size and impact velocity are 2.6 mm and 1.6 m/s, respectively. It faced different air speeds from 0 to 10 m/s.

Although radial velocity of air flow is one order of magnitude larger than recoiling velocity of impacting water droplet, the dynamic viscosity of water at room temperature is 1.002e-3 which is also one order of magnitude larger than air which is 1.85e-5 at the same temperature. Evaluation of dynamic viscosity ratio multiply to velocity and thickness of boundary layer ratios, $(\frac{\delta_{air}\mu_w V_{rec}}{2\delta_w \mu_{air} V_{radial}})$, shows the value about 1.55. It clearly highlights the effect of resultant shear force of air flow on an impacting water droplet. In other words at the recoiling phase, for producing retraction delay or complete non-recoiling phase, the resultant air shear force competes with two source of forces. First, viscous dissipation due to the contact line viscosity and second one is related to the capillary force (i.e. $\pi \gamma D_{max}(1 - cos\theta_{rec})$) trying to return spread droplet to the equilibrium state. As demonstrated in figure (4.3), by increasing air velocity retraction delay appears which reduces the recoiling velocity up to 55% at 16 ms (corresponding dimensionless time around 10).

Same phenomena were observed in figure (4.4) for Teflon substrate which can be described with the same scaling force methodology as mentioned for the aluminum substrate.
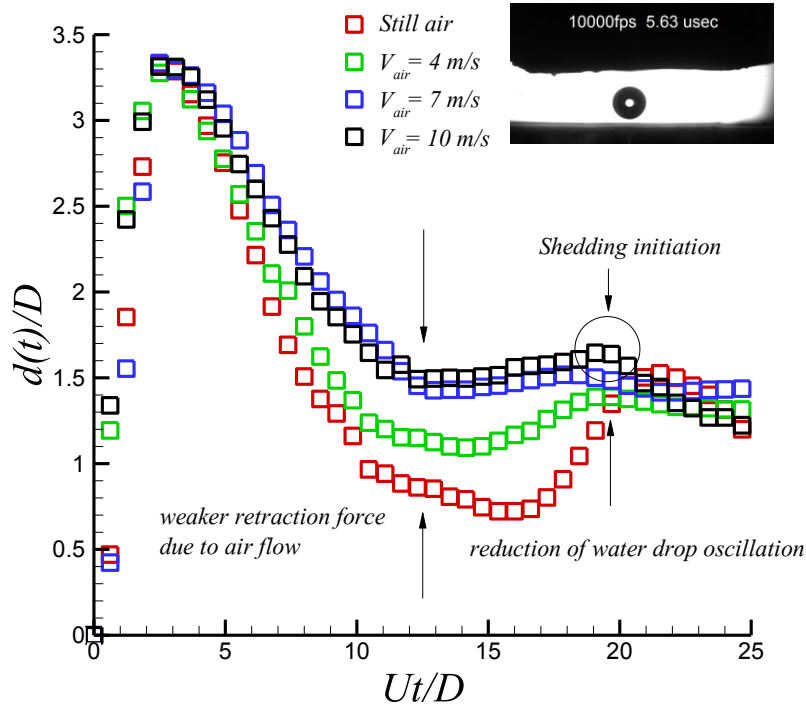
Figure 4.4: Temporal evolution of an impacting water droplet on the Teflon substrate. Droplet size and impact velocity are 2.6 mm and 1.6 m/s, respectively. It faced different air speeds from 0 to 10 m/s.

Figure (4.4) shows that spreading diameter at recoiling phase faced retraction delay which results in having wetting diameter up to 26% larger than that of still air case at 16 ms (corresponding dimensionless time is around 10). Comparing retraction delay of Teflon substrate to that of aluminum substrate shows a clear difference between droplet wetting behavior on hydrophilic and hydrophobic substrates where air flow is present. It can be argued that surface with low wettability has a higher retraction capillary force arises from higher dynamics receding contact angle. Referring to the capillary force, $\pi \gamma D_{max}(1 - cos\theta_{rec})$, dynamic receding contact angle, as demonstrated in figure (4.5), of Teflon substrate during recoiling phase is higher than of aluminum substrate $(\theta_{Tef,drec} = 70^o, \theta_{Al,drec} = 35^o)$ resulting in a higher retraction force. Therefore,

resultants shear forces cannot produce non-recoiling phase similar to aluminum substrate for droplet impact velocity up to 2.5 m/s.
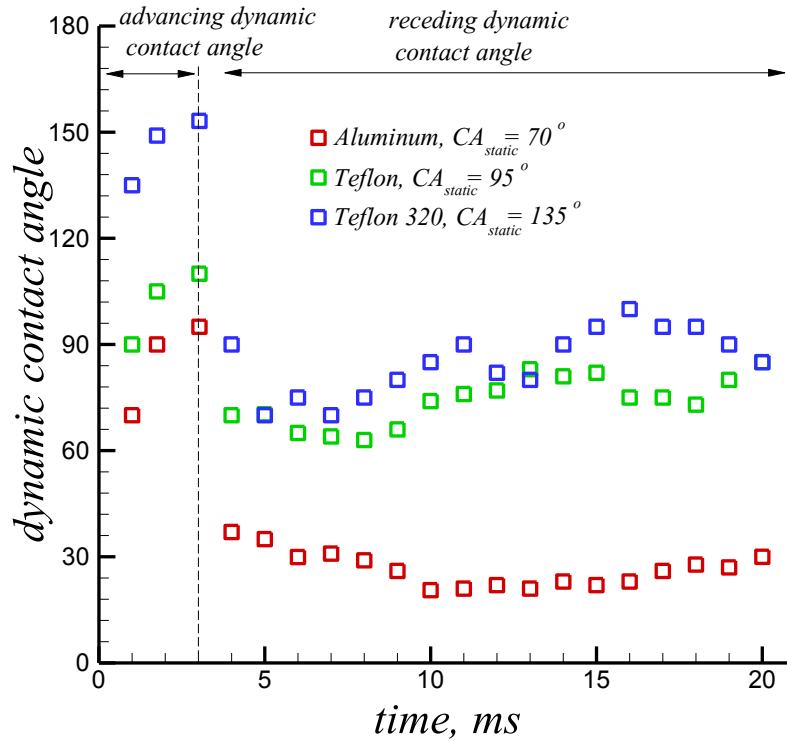
Figure 4.5: Variation of dynamic contact angle during spreading and receding phases of an impacting water droplet on different solid surfaces.

Effect of stagnation flow on an impacting water droplet can be better illustrated by imposing various maximum wetting diameters in the stagnation flow region. Therefore, various droplet sizes (see appendix D) and droplet impact velocities have been used for better clarification of influential incoming air flow. As demonstrated in figure (4.6), various droplet impact velocities ranging from 1.2 m/s to 2.5 m/s having droplet sizes up to 2.6 mm have been used to demonstrate the effect of maximum spreading diameter on the droplet wetting behavior on aluminum substrate where air flow is present. The corresponding Weber and Reynolds numbers are 50 to 220 and 3120 to 6500, respectively.
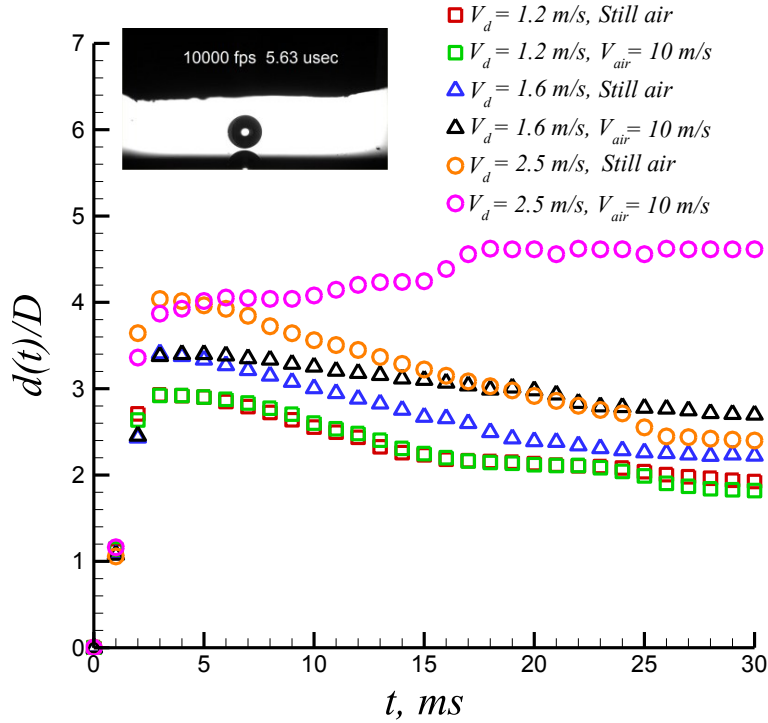
Figure 4.6: Temporal evolution of an impacting water droplet on the aluminum substrate at various droplet impact velocities ranging from 1.2 to 2.5 m/s. Droplet diameter is 2.6 mm and the corresponding Weber and Reynolds numbers from around 50 to 220 and 3120 to 6500, respectively.

As illustrated in figure (4.6), recoiling velocity at the early stage of droplet retraction phase is almost remains almost constant. Therefore, referring to the aforementioned force scaling analysis, dynamic viscosity ratio multiply to the velocity and thickness of boundary layer ratio $(\frac{\delta_{air}\mu_w V_{rec}}{2\delta_w \mu_{air} V_{radial}})$ becomes smaller where droplet impact velocity is increased. In fact, the numerator is almost constant while the denominator is a function of maximum spreading diameter. The higher wetting diameter, the larger radial velocity of air flow (i.e. V_{radial}). Radial velocity becomes almost as equal as incoming air jet velocity (i.e. 10 m/s) at the maximum spreading diameter around 10.5-10.8 mm. The boundary layer thickness o ($\delta_w = \frac{2D}{\sqrt{Re}}$)[41] is 0.065 mm for water droplet having droplet impact velocities up to 2.5 m/s and 2.6 mm droplet size corresponding Reynolds

number up to 6500. However, this value for air flow ($\delta_{air} = \eta = z\sqrt{\frac{2a}{v}}$) gets the aforementioned

value (i.e. 0.18 mm) as air jet velocity remains constant (i.e. 10 m/s). Therefore, value of the

aforementioned ratio (i.e. ($\frac{\delta_{air}\mu_w V_{rec}}{2\delta_w\mu_{air}V_{radial}}$)) becomes 1.15 showing a very good agreement with that

of the experimental results.

Effect of stagnation airflow under high inertia droplet impact condition (i.e. V_d= 2.5 m/s) on Teflon

substrate can be elaborated by the aforementioned force scaling law analysis. Such a high inertia

water droplet impact results in a large maximum spreading diameter about 10.3 to 10.6 mm which

is almost identical to that of aluminum substrate (i.e. 10.5-10.8 mm). However, behavior of

retraction phase is fundamentally different due to stronger capillary force of the spread water

droplet on Teflon substrate which results in having recoiling phase while airflow is present (see

appendix D). In the following, detailed explanation regarding behavior of droplet impact on a near

superhydrophobic surface accompanied with air flow is presented.

4.1.2 Near superhydrophobic surface

As it was explained in section (4.1.1), dynamic receding contact angle has an observable

effect on the retraction behavior of an impacting water droplet. Indeed, it becomes clear that the

higher receding contact angle results in faster droplet retraction where it is exposed to the air flow

compared to that of hydrophilic surface. However, the effect of contact angle hysteresis on wetting

dynamics of an impacting water droplet where air flow is present has not been elaborated yet.

Therefore, a special surface is used which has an intermediate characteristic to other surfaces.

Sanded Teflon substrate, which is called here near superhydrophobic surface, has a static contact

angle close to the superhydrophobic surfaces (i.e. 135°). Its receding dynamic contact angle is

similar to the Teflon substrate (i.e. 70°) but having contact angle hysteresis close to that of

aluminum surface (i.e. 40º), as demonstrated in figure (4.5). Having large contact angle hysteresis should result in severe viscous dissipation of spreading droplet when airflow is present. Therefore, wetting analysis is carried out based on the contact angle hysteresis. In order to highlight the importance of the contact angle hysteresis on droplet wetting behavior, droplet impact area is divided into two distinct regions namely pressure and shear domains.

Pressure domain is referred to a region having low radial air velocity. Numerical simulation of stagnation air flow regarding experimental test set up shows that stagnation domain has an almost 1 mm diameter (see appendix B). Radial velocity in the aforementioned area is below than 2% of incoming air jet velocity. Furthermore, numerical simulation shows that radial velocity is not well developed at region as large as 3.5 mm. Therefore, wetting dynamics of an impacting water droplet in the aforementioned diameter (i.e. 3.5 mm) can be referred as a pressure domain droplet impact condition. On the other hand, for moderately high inertia water droplet, the maximum spreading diameter is at least 2 folds larger than pressure domain diameter (i.e. 7 mm). Therefore, radial velocity component of incoming air flow is well developed in that area. In the current study, for droplet Weber number larger than 50, (i.e. experiments were conducted in a wide range of droplet Weber numbers from 30 to 220) wetting dynamics of an impacting water droplet is refereed as a shear domain droplet impact condition. In the following, experimentation of pressure domain droplet impact condition is presented (i.e. for droplet Weber numbers below 50). Figure (4.7) shows the sequential images of droplet impact in the pressure on sanded Teflon substrate, different droplet sizes ranging from 1.65 to 2.6 mm having impact velocity up to 1.2 m/s which results in droplet Weber numbers from 30 to 50. As illustrated in figure 4.7(a), for the smallest droplet size (i.e. 1.65 mm) droplet reaches the maximum spreading diameter at 2 ms. Droplet recoiling phase is initiated just after finishing the relaxation phase. Due to the relatively strong capillary force,

retraction phase ends at 10 ms. However, because of meniscus full penetration [79] partial impalement occurs while the majority of impacted water droplet is bounced off the substrate. Similar behavior was observed for higher weber numbers in still air cases. On the other hand, where stagnation flow is present, droplet wetting behavior is completely changed.

Small pinned droplet
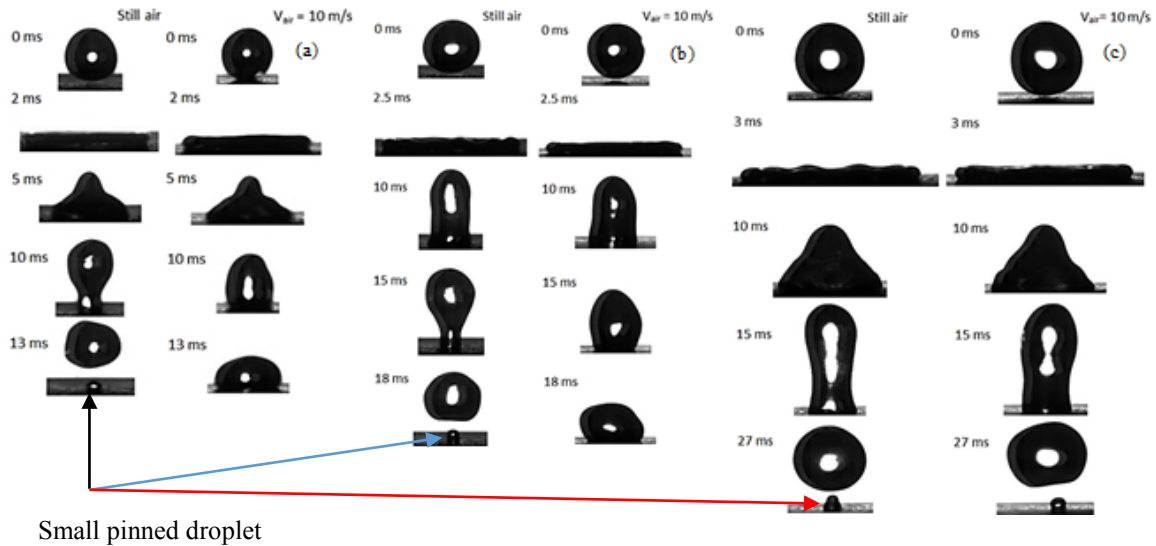
Figure 4.7: Sequential images of water droplets at low Weber numbers impacting on pressure domain of incoming stagnation air flow with a velocity of 10 m/s. a) Droplet size = 1.65 mm, b) droplet size = 2 mm, c) droplet size = 2.6 mm.

By imposing stagnation air flow on small droplet sizes (i.e. 1.65 and 2 mm) systematic changes were observed. Surface repellency was completely limited due to the air dynamic pressure at pressure domain impact condition. Surface wetting area is dramatically increased up to 4.5 folds at the time of repulsion, as illustrated in quantitative analysis of the maximum spreading diameter in figure (4.8). In spite of the fact that air flow has an observable effect on small droplet sizes, no difference was observed for the largest water droplet size (i.e. 2.6 mm) impacting at the pressure domain. Indeed, the difference arises from the different momentum exchanged between incoming air flow and the bounced water droplet. Larger water droplet size has a larger upward momentum which results in the complete detachment from the substrate. This phenomenon can be better

clarified by the quantitative analysis of the temporal height of an impacting water droplet. As illustrated in figure (4.9), for the small droplet size (i.e. 1.65 mm), the maximum droplets' height is almost decreased up to 30% due to the incoming air flow but no difference was observed for the largest droplet size which imprints the influence of the stagnation air flow on the variation of surface wettability.
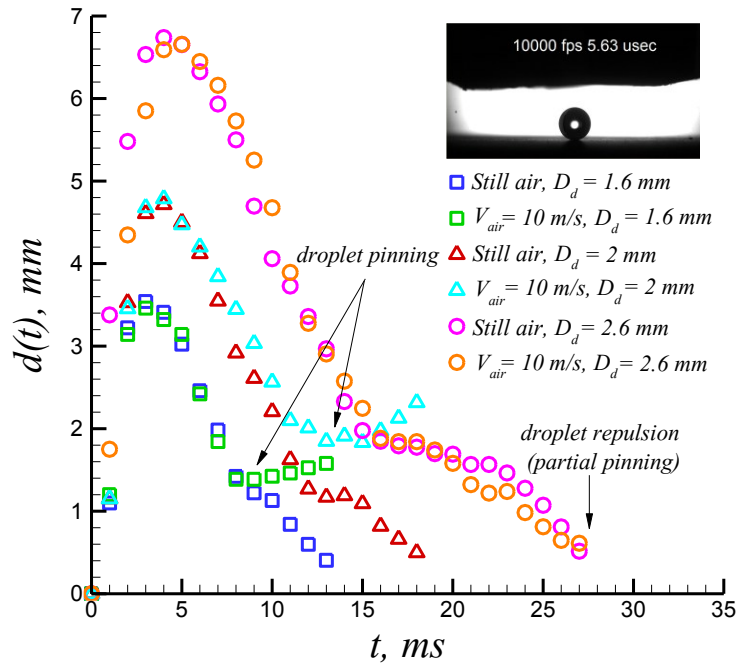
Figure 4.8: Temporal spreading diameter of an impacting water droplet at different sizes from 1.65 to 2.6 mm on the sanded Teflon substrate in still air and with air velocity of 10 m/s. Droplet impact velocity is 1.2 m/s.
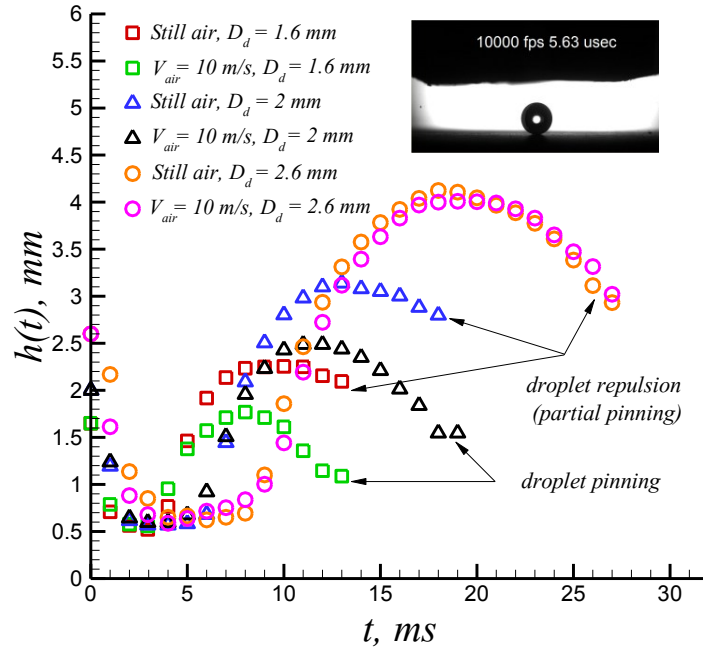
Figure 4.9: Temporal height analysis of an impacting water droplet at different sizes from 1.65 to 2.6 mm on the sanded Teflon substrate in still air and with air velocity of 10 m/s. Droplet impact velocity is 1.2 m/s.

Effect of shear domain stagnation air flow on an impacting water droplet is evaluated by increasing droplet impact velocity up to 1.6 m/s for droplet sizes up to 2.6 mm. Quantitative analysis of both droplet temporal spreading diameter and height are demonstrated in figure (4.10). In this case droplet height is affected due to the presence of air dynamic pressure up to 35% but having large receding capillary force results in droplet bouncing from the substrate. In fact, the resultant shear force of incoming air flow on spread water droplet which is not sufficiently developed preventing droplet repulsion on the sanded Teflon substrate. Therefore, it is appreciated to find the critical droplet impact velocity where droplet repulsion is limited.
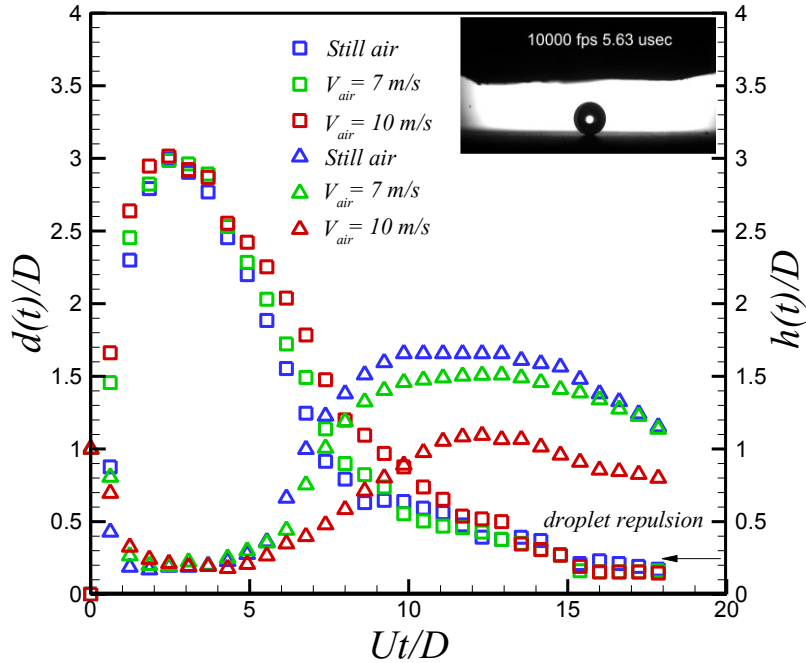
Figure 4.10: Temporal spreading diameter and height of an impacting water droplet on sanded Teflon substrate with various air velocities from 0 to 10 m/s. Droplet size and impact velocity are 2.6 mm and 1.6 m/s, respectively.

Figure (4.11) shows sequential images of an impacting water droplet on the sanded Teflon substrate with and without air flow. Droplet impact velocity is increased up to 2 m/s with corresponding Weber and Reynolds numbers up to around 140 and 5200, respectively. Although wetting behavior of impacting droplet in the still air is similar to previous cases droplet wetting behavior where air flow is present is substantially changed. Droplet is spreaded large enough to be exposed to high regime of air shear force. Therefore, with same methodology described in section (4.1.1) recoiling velocity is faced reverse velocity gradient at air-liquid interface. Furthermore, rough nature of sanded Teflon substrate results in having large contact angle hysteresis which increases viscous dissipation through droplet wetting contact line. Consequently, receding velocity of an impacting water droplet with Weber number up to around 140 becomes zero at 20 ms and surface repellency is completely eliminated.

114
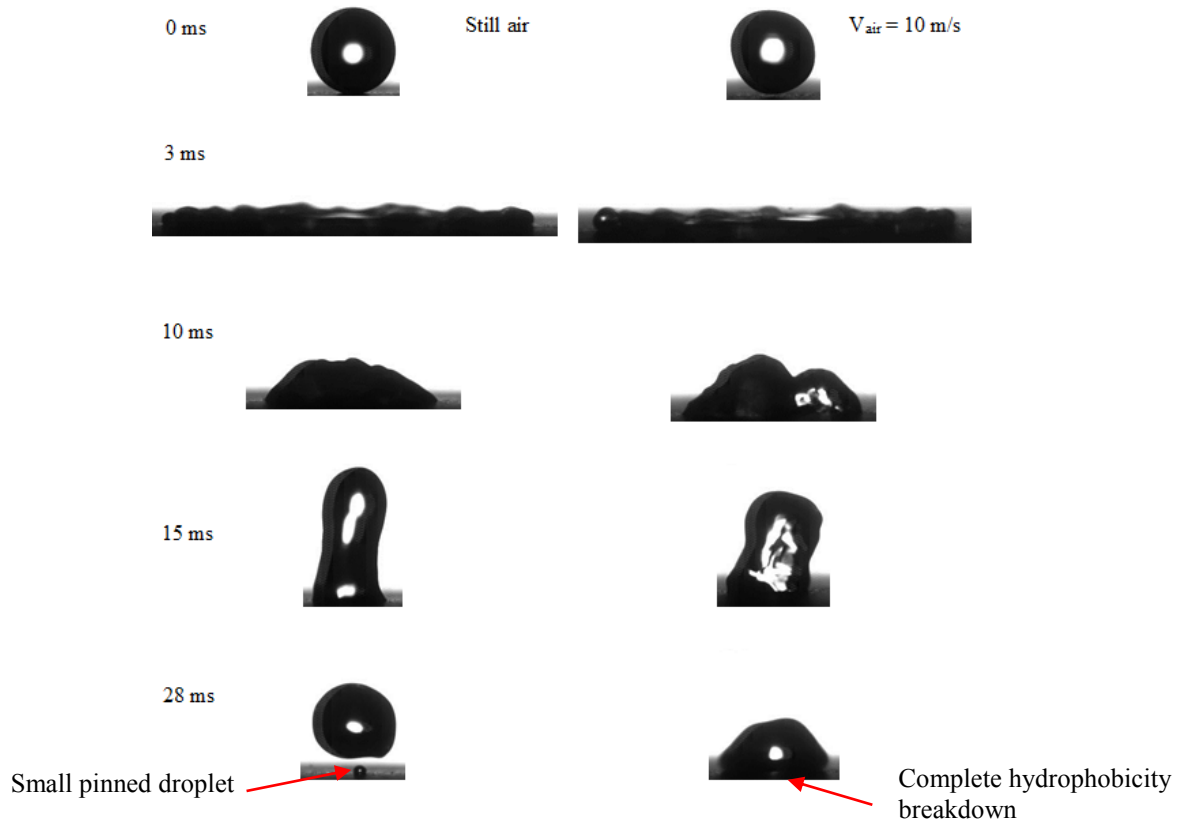
Figure 4.11: Sequential images of high inertia water droplet impacting on the sanded Teflon substrate. Droplet Weber and Reynolds numbers are around 140 and 5200, respectively. Droplet size and droplet impact velocity are 2.6 mm and 2 m/s, respectively.

Quantitative temporal analysis of the droplet spreading diameter and height of aforementioned condition is illustrated in figure (4.12). Droplet wetting diameter is increased up to 6.5 folds to that of still air at 28 ms. This result highlights the importance of shear domain droplet impact condition on substrates having large contact angle hysteresis.

Further increase in the droplet impact velocity results in droplet receding break up (i.e. splashing regime) on the sanded Teflon substrate which results in significant decrease in the receding velocity. Indeed, as demonstrated in figure (4.13), recoiling droplet is pinned on the substrate and repellency break down happens. Same phenomenon was occurred where air flow was imposed on the spread droplet but it produces further retraction delay because of the presence of stagnation air flow.
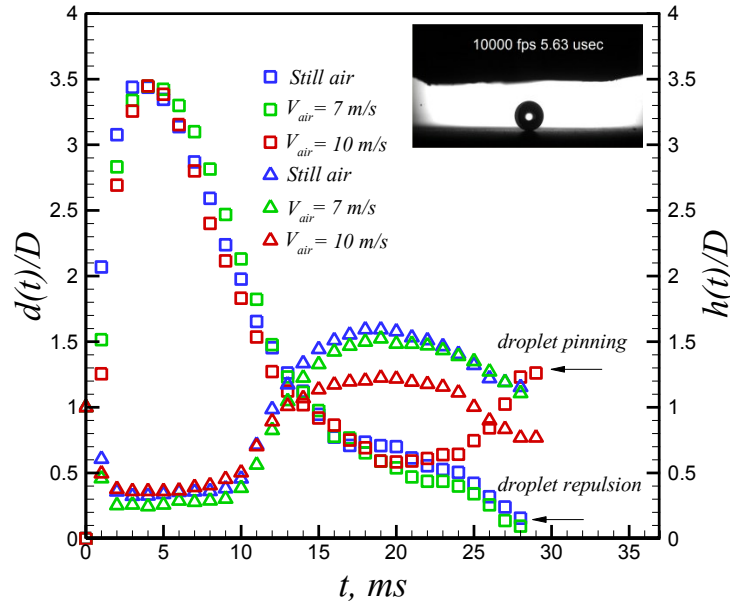
Figure 4.12: Temporal analysis of the spreading diameter and height of high inertia water droplet impacting on the sanded Teflon substrate. Droplet size and impact velocity are 2.6 mm and 2 m/s, respectively.
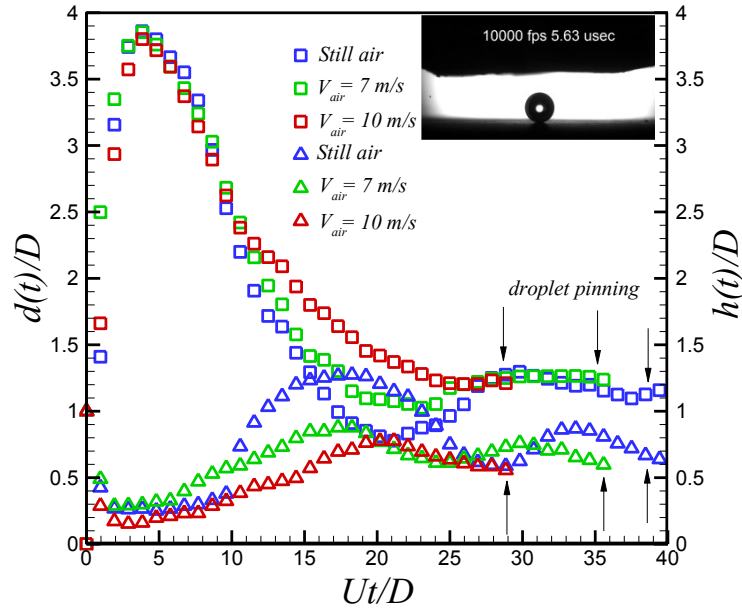
Figure 4.13: Temporal analysis of the spreading diameter and height of high inertia water droplet impacting on the sanded Teflon substrate. Droplet size and impact velocity are 2.6 mm and 2.5 m/s, respectively.

4.1.3 Superhydrophobic surface

Wetting behavior of an impacting water droplet on the superhydrophobic surface is evaluated in the current section. In fact, due to the large receding contact angle (i.e. around 150º) which results in strong receding capillary force, droplet wetting behavior on superhydrophobic surfaces is completely different. Therefore, a wide range of droplet sizes and impact velocities, corresponding Weber numbers from 30 to 450[107] are used to quantitatively describe the effect of incoming air flow on an impacting water droplet on a superhydrophobic surface. As explained in section (4.1.2), wetting area of an impacting water droplet is divided into pressure and shear domains. This terminology is used again for complete and comprehensive explanation of droplet dynamics on the superhydrophobic surface.

Figure (4.14) shows sequential images of an impacting water droplet on a superhydrophobic surface in the pressure domain impact condition. Droplet size and impact velocity are 2.6 mm and 1.2 m/s, respectively. The corresponding Weber and Reynolds numbers are around 50 and 3120, respectively. In this regime of droplet impact velocity it was not seen any instabilities at rim periphery. Therefore, it is referred as a completely non-splashing regime. Droplet spreading phase is similar to the other surfaces. The droplet reaches the maximum spreading diameter at 3 ms and starts recoiling with relatively smaller relaxation time up to 0.3 ms. Due to the strong receding capillary force originated from large receding contact angle, droplet jet formation is initiated at 7 ms. Droplet is detached from the surface at 13.3 ms in still air condition. On the other hand, in the presence of air flow jetting phenomenon is systematically suppressed by the incoming air flow at 9 ms and droplet detachment time (i.e. droplet contact time) is reduced up to 15% for air velocity up to 10 m/s.
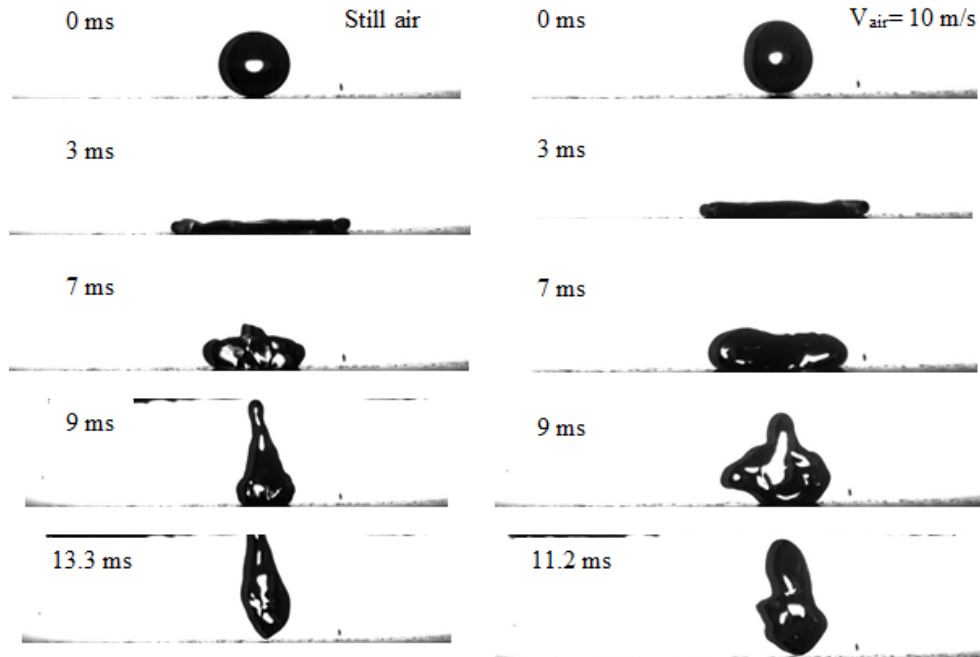
Figure 4.14: Sequential images of water droplet impacting on a superhydrophobic surface. Droplet size and droplet impact velocity are 2.6 mm and 1.2 m/s, respectively. The corresponding Weber and Reynolds numbers are around 50 and 3120, respectively.

In order to profoundly understand the physics behind the reduction on the droplet contact time, droplet impact experiments at different droplet sizes and impact velocities were performed. It covers a wide range of Weber number ranging from 30 to 90 as a complete non splashing regime. Furthermore, droplet Weber number around 140 was used which shows a transitional regime of non-splashing to splashing, as small droplet detached from the spread lamella at the maximum spreading diameter. In addition to that, high inertia water droplet impact condition which demonstrates violent splashing (i.e. Weber numbers from 220 to 450) has been used to investigate the effect of stagnation air flow on droplet wetting behavior.

Low Weber number droplet impact experiments ranging from 30 to 50, which referred as pressure domain droplet impact conditions, were carried out to understand the wetting behavior of an impacting water droplet on superhydrophobic surfaces. As demonstrated in figure (4.14), droplet detachment time was slightly reduced where droplet impact velocity is sufficiently high reaching

to the border of pressure domain area (i.e. We = 50). However, for smaller Weber numbers ranging from 30 to 40 (i.e. smaller maximum spreading diameter) droplet wetting dynamics was not shown a significant difference neither in spreading nor in recoiling phase. Droplet contact time remains almost constant in the low Weber number droplet impact experiments with and without the air flow. In the next step, droplet Weber number is increased in order to quantitatively evaluate the effect of shear domain stagnation air flow on the droplet impact behavior on the superhydrophobic substrate.

Figure (4.15) shows the sequential images of an impacting water droplet on the superhydrophobic substrate. Droplet diameter, impact velocity, Weber and Reynolds numbers are 2.6 mm, 1.6 m/s, 90, 4160, respectively. Droplet impact velocity was intentionally chosen to be in the critical regime of non-splashing but accompanied with sever instability at the rim periphery. Repeatable droplet impact experiments show that droplet reaches to the maximum spreading diameter without any fragmentation and break up. Combining acceleration Rayleigh–Taylor instability (R-T instability) with effective shear driven Kelvin–Helmholtz instability (K-H instability) results in finger formation at this stage but not snap–off. After this phase, droplet starts pulling back edges with strong capillary force compared to that of aluminum and Teflon substrates. In fact, large dynamic receding contact angle is the main reason of rapid recoiling phase, $\pi \gamma D_{max}(1 - cos\theta_{rec})$.

Analysis of dynamic receding contact angle shows that it remains above 145° during the entire recoiling phase. Droplet reaches to the maximum spreading diameter at 3 ms with and without the air flow. Droplet starts recoiling just after finishing relaxing time up to 0.5 ms for still air case. On the other hand, where air velocity is increased, relaxation time or time at the maximum spreading

119

diameter is increased up to 1.5 ms with a slight increase in the maximum spreading diameter, as illustrated in figure (4.15).

Droplet reaches to the maximum spreading diameter with the aforementioned instabilities similar to that of still air case. However, in the presence of air flow the formed fingers at spread rim periphery encounter the large shear and normal force of incoming air flow. Consequently, droplet starts recoiling with increased relaxing time about 3 times larger than that of still air case. This fingered shape droplet are susceptible to being snap off where air velocity is increased. As shown in figure (4.15), droplet capillary force cannot merge fingered shape droplet. Consequently, the imposed shear and normal forces of incoming airflow on an impacting water droplet result in spread lamella break up at 6.5 ms, as shown in figure (4.16).

Quantitative evaluation of temporal spreading diameter, demonstrated in figure (4.16), shows successive droplet break up at 6.5 ms. Droplet spreading lamella lifts up from surface at 5.8 ms which results in a faster decrease in the wetting diameter. After this time, it faces the same break up. More detailed information regarding pressure effect of incoming airflow can be found in appendix D.
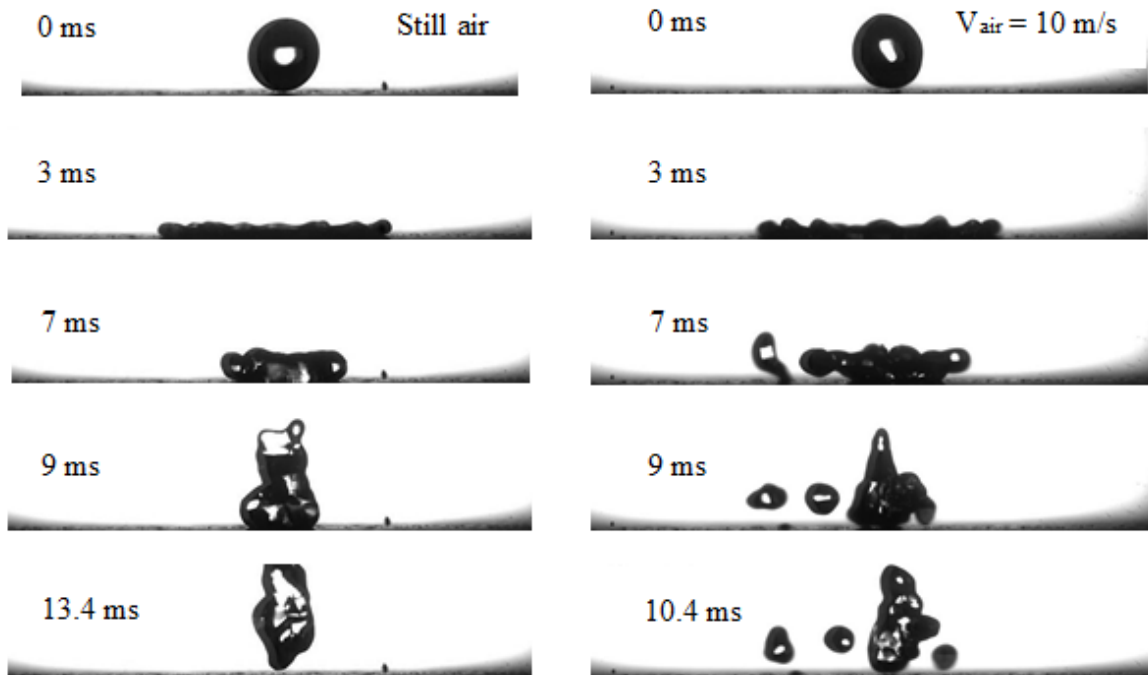
Figure 4.15: Sequential images of water droplet impacting on the superhydrophobic substrate in still air and air velocity of 10 m/s. Droplet size and impact velocity are 2.6 mm and 1.6 m/s, respectively.
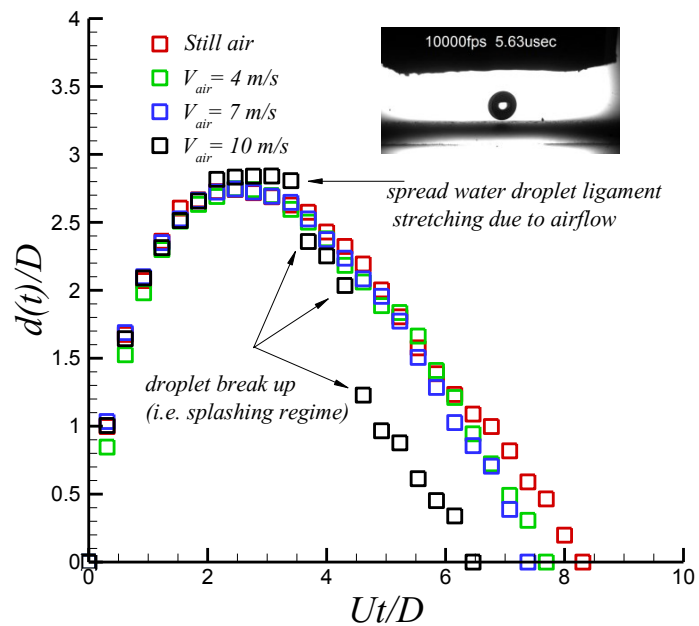
Figure 4.16: Temporal evolution of an impacting water droplet on the superhydrophobic substrate. Droplet size and impact velocity are 2.6 mm and 1.6 m/s, respectively. It is accompanied to different air velocities from 0 to 10 m/s.

More effective shear domain droplet impact experiment can be accomplished by increasing droplet impact velocity up to 2 m/s (Droplet Weber and Reynolds numbers are around 140 and 5200, respectively). In this regime, which is referred as a transitional regime between non-splashing to splashing, droplet contact time is reduced up to 35% (see appendix D for more detail).

In figure (4.17), variation of droplet contact time as a function of incoming air jet velcoity for all aformanetioned case senarioes are illustrated. As shown, droplet contact time is decreased where air velocity is increased in both non-splashing and splashing regimes. The same senario was also happened for high velocity droplet impact condition with Weber numbers up to 450 (i.e. violent splashing).[108] This reduction in the droplet contact time is also increased by increasing droplet impact velocities. Therefore, it can be deducted that larger maximum spreading diameter which is extended in the shear domain stgnation flow prones to detache from substrate in the comparable lower time to that of still air case. Therefore, it is rational to demonstrate this reduction as a fuction of droplet Weber number. Indeed, it is directly related to the droplet maximum spreading diameter through the correlation proposed by Clanet et al.[44] As demonstrated in figure (4.18), droplet contact time is decreased by increasing droplet Weber number. In the following, the proposed mechanism of droplet contact time reduction is presented.
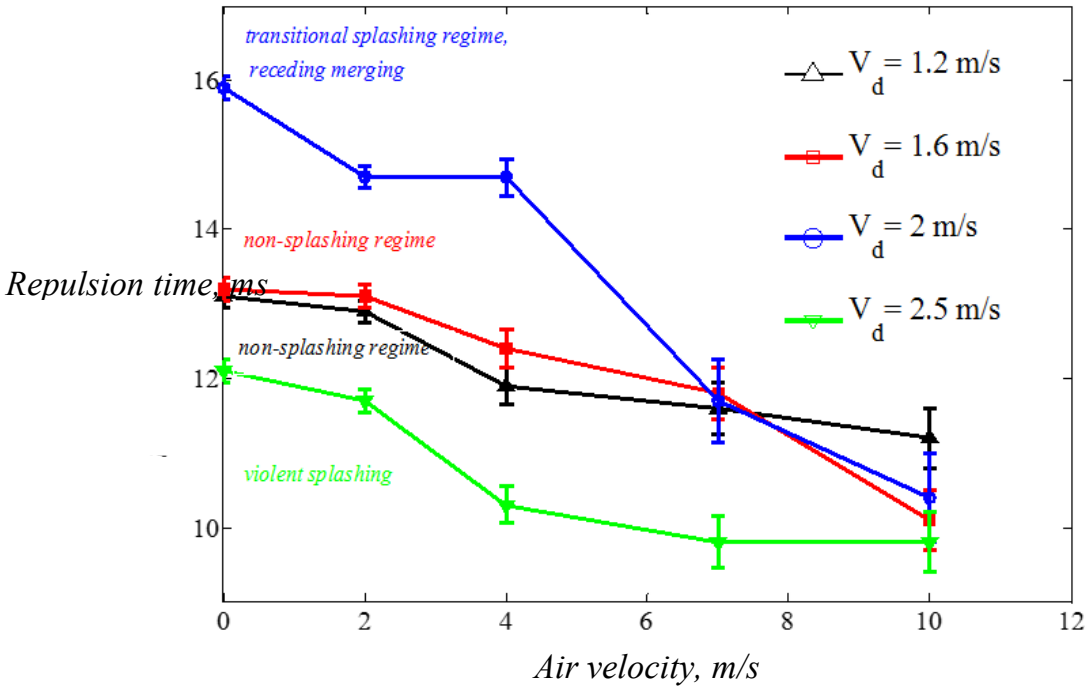
Figure 4.17: Variation of droplet contact time against stagnant air jet velocity for various droplet impact velocities from non-splashing to violent splashing regimes.

Recent study of droplet impact on dry ice showed that there is a rapid generation of gas vapor formed beneath of an impacting droplet on the surface.[109] This formed vapor provides a compressed layer of gas on which the spreading droplet moves over rather than on the surface. This phenomenon results in imposing full slip condition rather than partial one which makes a slight increase in the maximum spreading diameter. Full slip condition promotes capillary force by elimination the viscous dissipation through contact line leads achieving complete repellency like superhydrophobic surfaces. Similar results were also observed for droplet impact on surfaces maintained in Liedenfrost temperature. Droplet contact time was reduced about 14% due to the generation of vapor film underneath an impacting water droplet and substrate leads changing partial slip to full slip condition.[110]

123

It can be deducted that stagnation flow results in two striking phenomena. First, dynamic pressure of air flow converts to static pressure at the stagnant point which increases surface capillary pressure. In fact, summation of air dynamic pressure along with surface capillary pressure confronts droplet dynamic pressure. On the other hand, extra pressure build up increases superhydrophobicity of surface. However, 15-35 % reduction in droplet contact time is not only related to an increase in entrapped air pressure but also is justified with the presence of thin moving layer of air underneath the impacting water droplet on superhydrophobic surface. By increasing incoming air velocity, the thin air layer gets more acceleration in the viscous region helps reducing droplet contact time by two mechanisms.

Firstly, the formed rim of droplet contacts with the thin layer of air which has already been accelerated promotes slightly larger droplet spreading without significant viscous dissipation compared to the still air case. In fact, near wall boundary layer is not similar to the still air case. Secondly, and the most important one, K-H instability is increased by increasing air speeds on solid-air-liquid interface which results in more unstable spread ligament. In fact, when droplet impact velocity is increased, droplet will move on faster accelerated thin film producing more unstable spread droplet. Contribution of both increased entrapped air pressure and generation of full slip boundary condition instead of partial one combined with the presence of K-H instability results in faster detachment of water droplet in the recoiling phase.
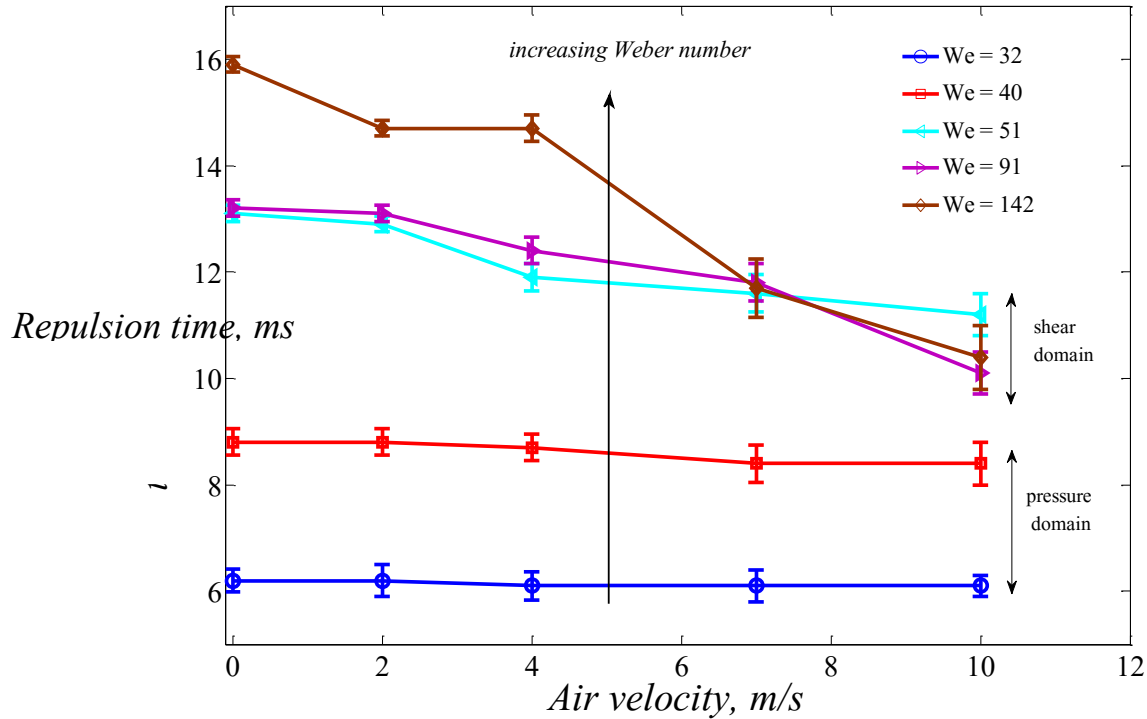
Figure 4.18: Variation of droplet contact time exposed to various air velocities from 0 to 10 m/s as a function droplet Weber number.

Having explained droplet impact behavior on superhydrophobic surfaces with and without air flow, the proposed new transient predictive model of droplet spreading diameter (see chapter 3) are compared against the experimental results on the superhydrophobic surface for model's validation. Comparison of experimental data with various droplet sizes and impact velocities are presented in figure (4.19). Droplet sizes ranging from 1.65 to 2.6 mm with impact velocities up to 1.2 m/s were used for evaluation of new transient model of droplet spreading diameter. As shown, the presented model predicts very well both maximum spreading diameter and droplet contact time. For the maximum spreading diameter, an excellent agreement with the mean value deviation up to 1.5% was observed. On the other hand, the mean value deviation of droplet contact time was up to 11% for the smallest droplet size (i.e. 1.65 mm) while it was reduced up to 9% for 2 mm water droplet size. This slight deviation in droplet contact time can be related to the nature of three

dimensional recoiling behavior (i.e. the presence of both R-T and K-H instabilities, and surface roughness). A detailed comparison of maximum spreading diameter with different predictive models is presented in the last part of the current section. Here, the comparison of droplet contact time with new presented model is carried out.
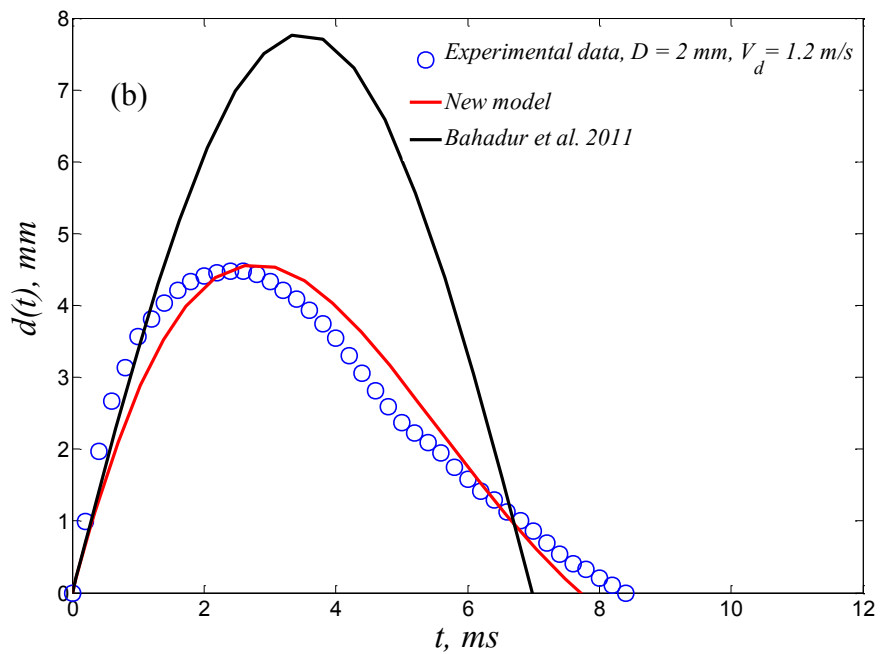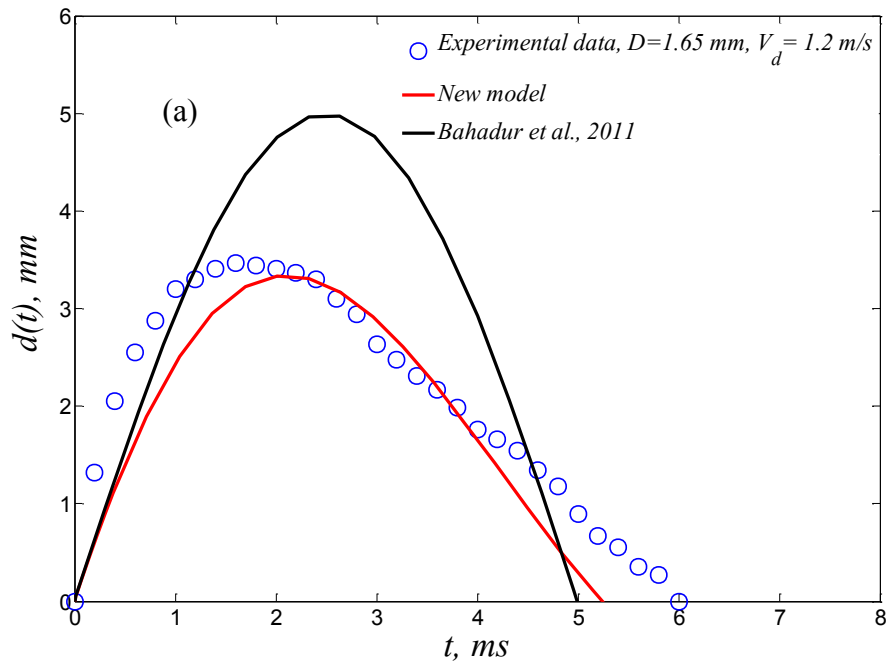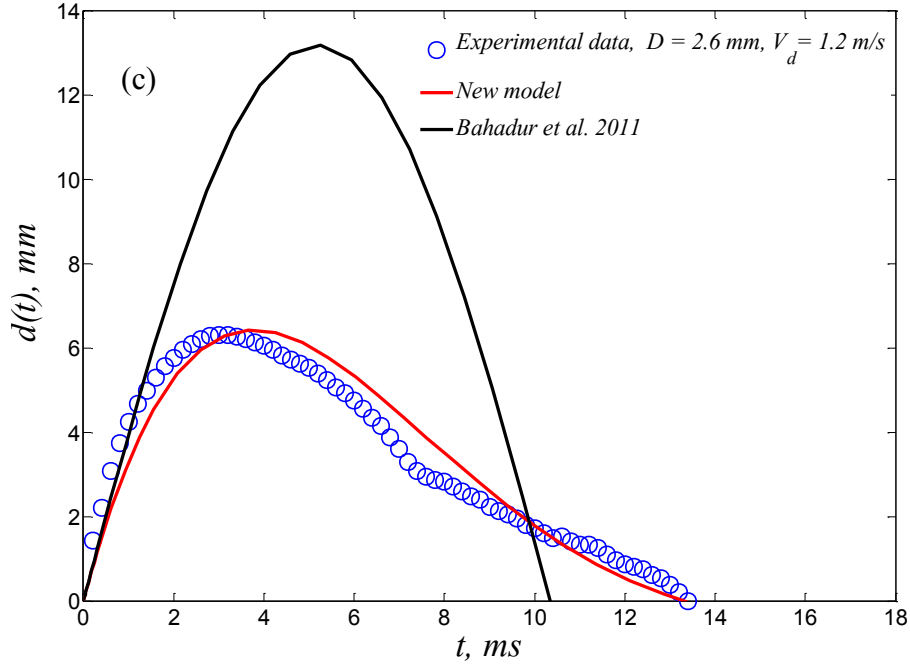
Figure 4.19: Comparison of experimental data with new presented model. Droplet sizes are 1.65 mm (a) 2 mm (b) and 2.6 mm (c). Droplet impact velocity is 1.2 m/s.

As highlighted by Clanet et al.[33] droplet contact time is not a function of droplet impact velocity on superhydrophobic surfaces. Therefore, comparisons of the aforementioned model with various droplet impact velocities are appreciated. Three impact velocities ranging from 0.8 m/s to 1.6 m/s in the non-fragmentation regime (i.e. non-splashing regime) were used for proper evaluation of transient behavior of droplet spreading diameter. As demonstrated in figure (4.20), droplet contact time is not a function of the droplet impact velocity when it is sufficiently larger than the critical velocity of droplet repulsion (i.e. $V_c = (gR^3k^2)^{1/2}$, Which k^{-1} is capillary length of water droplet, $k^{-1} = \sqrt{\gamma/\rho g}$) and vary with $R^{2/3}$.[13] As shown in figure (4.20), an excellent agreement with the experimental data was observed while previously defined mass-spring model substantially overestimated the maximum spreading up to 1.5 and 2 folds for the smallest and largest droplet sizes combined with observable underestimation of the droplet contact time.

127
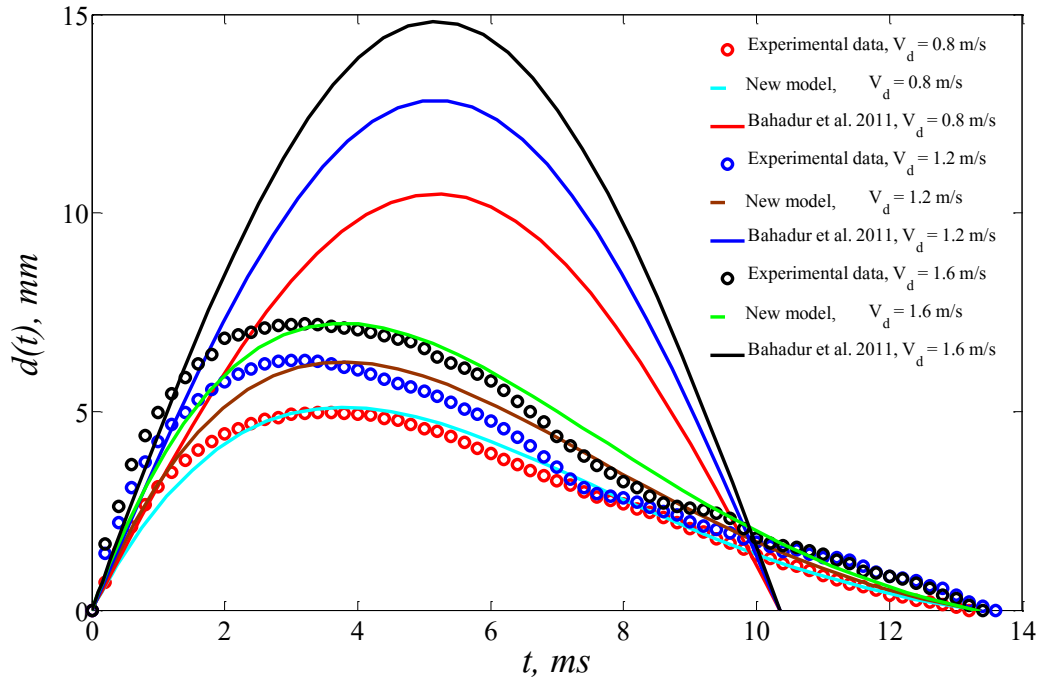
Figure 4.20: Comparison of experimental data with the new model. Droplet sizes are 1.65 mm (a) 2 mm (b) and 2.6 mm (c). Droplet impact velocity is 1.2 m/s.

Comparison of non-splashing regime of water droplet impact on the superhydrophobic surface has been carried out with three previously defined predictive models of maximum spreading diameter along with the new proposed model. In figure (4.21), comparison of two predictive models namely energy based model and hydrodynamic analytical model with the experimental results are presented. Droplet Weber number was up to 90 for water droplet and water-glycerol droplet solution having various specific viscosities up to 5.5. As illustrated in figure (4.21), for water droplet impact condition the mean value deviations for energy based model is up to 8% but it becomes relatively large up to 23% for analytical hydrodynamic model. However, by increasing droplet viscosity the mean value deviations is slightly decreased. For moderate specific viscosity within 2 to 3.5 energy based model predict very well the maximum spreading diameter with the mean value deviation between 0.5% and 4.5%. On the other hand, it becomes as high as 14% and 10% for analytical hydrodynamic models, respectively. The mean value deviation for the highest

viscous droplet (i.e. specific viscosity of 5.5) becomes 8.6% and 5% for energy based and analytical hydrodynamics model, respectively.
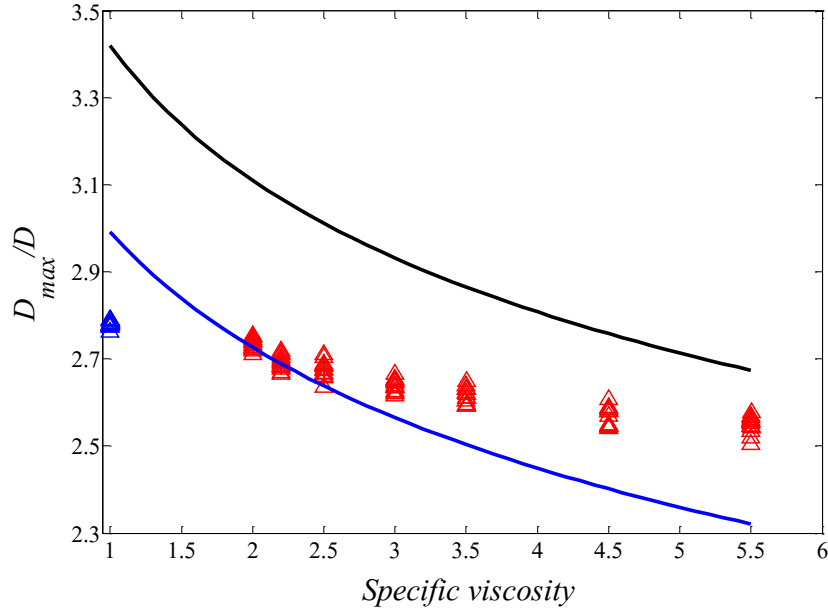
Figure 4.21: Comparison of energy based model (blue line) and analytical hydrodynamic model (dark line) with water and water-glycerol solution (blue and red triangles) droplet impact experiments. Droplet size and impact velocity are 2.6 mm and 1.6 m/s, respectively.

As illustrated in figure (4.21), the mean value deviations for both energy based model and analytical hydrodynamic model become relatively large, especially for the analytical hydrodynamics model. Therefore, the maximum spreading diameter of an impacting water droplet on superhydrophobic surfaces cannot be compared well to the aforementioned models. Consequently, the correlation of Clanet et al.[44] based on the scaling law analysis is used for comparison with the experimental data. Figure (4.22) illustrates the variation of dimensionless spreading diameter against dimensionless Weber number for distilled water and viscous water-glycerol solution having specific viscosity up to 2.5. As shown in figure (4.22), scaling law (dark line) predicts very well the maximum spreading diameter of distilled water droplet with the mean

value deviation up to 0.4% in the range of droplet Weber number from 60 to 90 (i.e. non-splashing regime). Furthermore, comparison of new presented model defined in equation (3.23) is also carried out with the experimental data. As demonstrated in figure (4.22), the proposed model (green square) compares very well with distilled water experimental data with almost negligible mean value deviation (up to 0.2%). On the other hand, for the viscous water-glycerol solution, having specific viscosity up to 2.5, the overestimated mean value deviation of scaling law for the highest droplet Weber number (i.e. 90) becomes about 3.5%. Similar deviations but with underestimated value were observed for the new model.
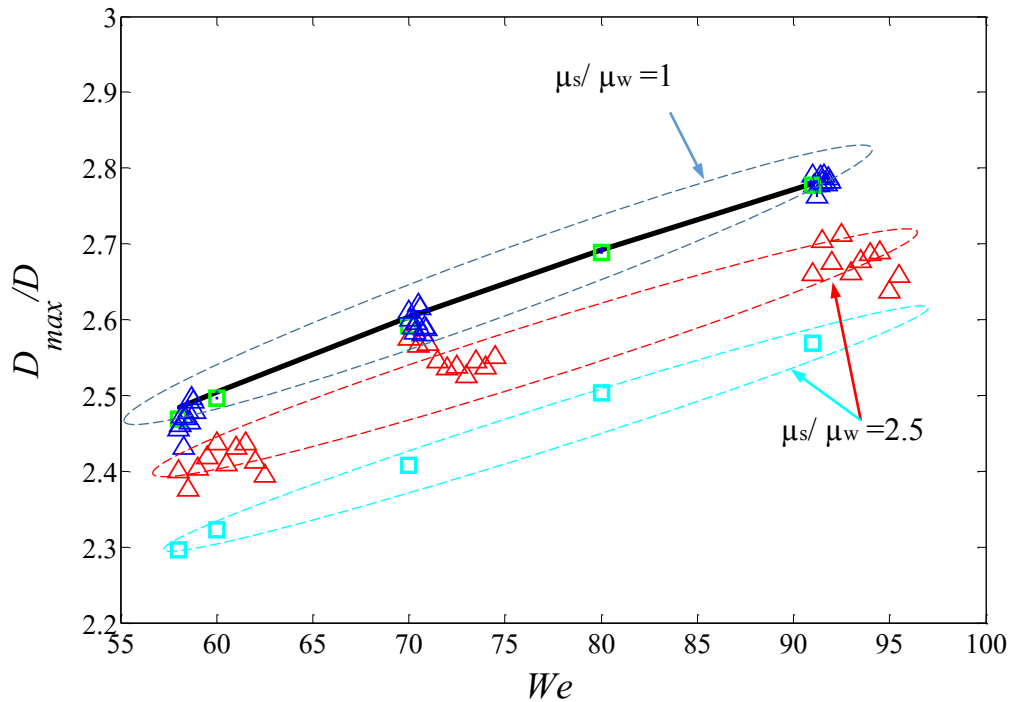
Figure 4.22: Variation of dimensionless spreading factor versus droplet Weber number for distilled water and water-glycerol solution (blue and red triangles) compared with the scaling law analysis correlation (dark line) and new presented model (green and sky-blue squares).

In order to suitably compare the maximum spreading diameter of an impacting viscous water droplet various weight ratio of water-glycerol solution, as described in chapter 2, were used. The results are used in order to validate the new model. As illustrated in figure (4.23), droplet Weber

130

numbers were not changed significantly when water-glycerol solution is used. Droplet Weber number was remained constant about 95 (i.e. 90-105, due to the very small variation in liquid droplet surface tension and density values, see chapter 2), but specific viscosity is increased up to 5.5 folds. As illustrated in figure (4.23), the predictive values obtained by the scaling law, significantly overestimates the maximum spreading diameter with the mean value deviations up to 9.5% while the new proposed model's means value deviations agree well up to 5.5% deviation. Therefore, the new model can be considered as a robust predictive model for the viscous droplet impact on the superhydrophobic surfaces, especially for P_s factor (i.e. $We/Re^{0.8}$) below 1. As it will be discussed in the following section, wetting dynamics of a supercooled water droplet, which is faced an increase in viscosity up to 5.5 folds at -24 °C, can be well evaluated by this new model compared to the former predictive model (i.e the correlation based on the scaling law analysis) which has shown relatively large deviation against the experimental results of viscous water droplet impact condition.
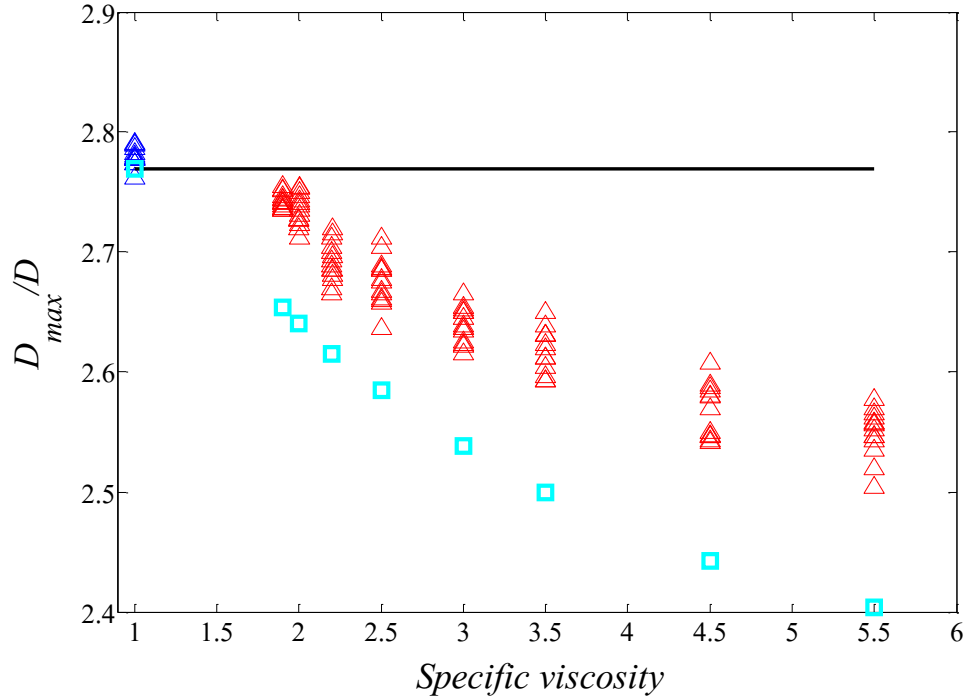
Figure 4.23: Variation of dimensionless spreading factor for droplet Weber number around 90. For distilled water (blue triangle) and water-glycerol solution (red triangle) compared with the correlation based on the scaling law analysis (dark line) and new presented model (sky-blue square). Droplet size and impact velocity are 2.6 mm and 1.6 m/s, respectively.

4.2 Non-isothermal droplet impact dynamics

Ice formation mechanism of an impacting supercooled water droplet on a cold substrate, where phase change is instantaneously initiated upon impact, can be explained by incorporating wetting dynamics, thermal transport and classical nucleation theory based on the Gibbs free surface energy, as presented by Mishchenko et al.[65] in still air condition. In the current study, detailed explanation of an impacting supercooled water droplet accompanied with cold airflow at the low temperature condition is presented. One of the most important parameter is the maximum wetting or maximum spreading diameter. It was experimentally[36] demonstrated that the maximum spreading diameter on the cold substrate is substantially influenced by the variation of viscosity of

132

an impacting droplet. An increase in the viscous force due to the droplet temperature reduction is led to a reduction on the maximum spreading diameter which is explained here in detail.

Viscous dissipation[111] is represented by the incorporating viscosity, impact velocity and thickness of boundary layer.[41] Lowering both substrate and water droplet temperature can increase viscosity up to 8 times for the extreme degree of subcooling of water droplet down to -30 $^{\circ}$C.[76] Therefore, it is clear that it has an effect on the maximum spreading diameter. In the following, wetting behavior of a supercooled water droplet impacting on the different solid surfaces with wettability ranging from hydrophilic to superhydrophobic is discussed.

Experiments were performed on the low temperature condition ranging from -10 down to -30 $^{\circ}$C which is exposed to the dry air having extreme low relative humidity as low as 0.1% in order to prevent any surface frost formation. The water droplet degree of supercooling is dependent on the stagnation air flow temperature. The effect of stagnation air flow on an impinging supercooled water droplet is profoundly elaborated through various analyses.

4.2.1 Thermal transport analysis of supercooled droplet exposed to airflow

In order to properly investigate the wetting dynamics of an impacting supercooled water droplet in the presence of cold stagnation flow, thermal analysis of falling droplet is carried out in the extreme cold condition (i.e. -30 $^{\circ}$C with air velocity up to 10 m/s) to illustrate temperature distribution on the supercooled droplet. Two important dimensionless numbers namely Biot and Fourier have been used for the evaluation of droplet temperature distribution. Analysis of moving droplet through air is divided in to two domains, as illustrated in figure (4.24(a)).
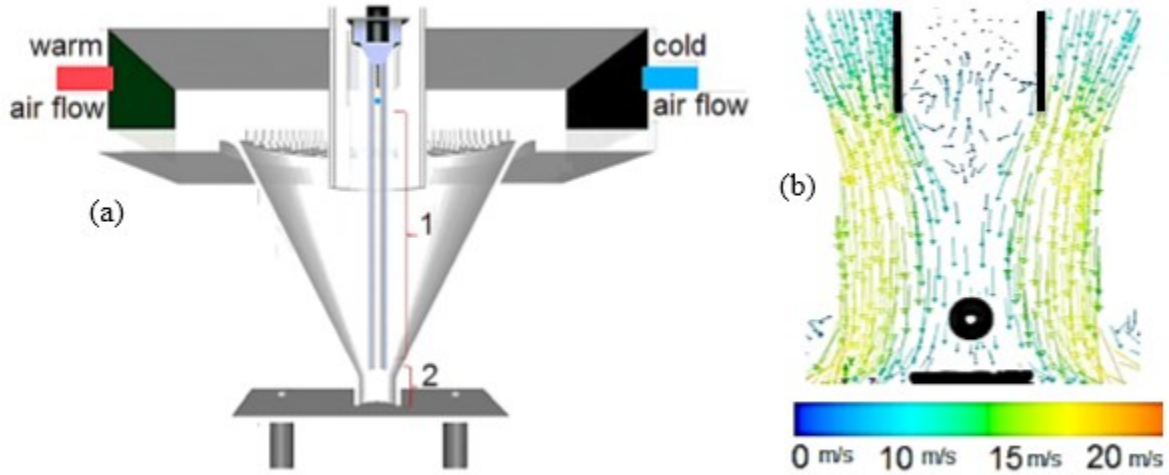
Figure 4.24: a) Schematic of producing stagnation cold flow, b) imposed air velocity on moving droplet through cold air flow.

Calculation of Biot number based on the droplet terminal velocity justifies the assumption of the uniform temperature distribution with in the droplet, as it was less than the critical Biot number in domain 1. (i.e. 0.08 < 0.1). Indeed, this value is even smaller than 0.08 as droplet velocity in domain 1 is varied from 0 to almost terminal velocity.

$$Bi = \frac{h_g l_c}{k_d} = \frac{h_g D}{6k_d} \qquad (4.1)$$

For both domains 1 and 2, Biot number is calculated based on the forced convective heat transfer coefficient as illustrated in equations (4.2) to (4.6).

$$Re = \frac{\rho_g D(U_g - U_d)}{\mu_g} \qquad (4.2)$$

$$Pr = \frac{\mu_g c_{p,g}}{k_g} \qquad (4.3)$$

$$Spalding\ number = B = \frac{C_{p,v}(T_g - T_d)}{H_f} \qquad (4.4)$$

$$Nu = \left(2 + 0.6Re^{\frac{1}{2}}Pr^{\frac{1}{3}}\right)(1+B)^{-0.7} \qquad (4.5)$$

$$h_g = \frac{Nu.k_g}{D} \qquad (4.6)$$

Where, k_g , is the thermal conductivity of cold air at -30 °C. Nusselt number, *Nu,* is presented by the modified Ranz-Marshall correlation for liquid droplet.[112] Property of air at wide range of temperature from 20 °C to -30 °C is illustrated in table (4.1).[113,114]

Table 4.1: Dry air properties at different temperature

Temperature (k)	Density (kg/m³)	Dynamic viscosity (10^{-6} Pa.s)	Thermal conductivity (10^{-3} W/m.K)	Specific heat (J/kg.K)	Thermal diffusivity (10^{-6} m²/s)
240	1.47	15.54	21.45	1005.5	14.49
250	1.41	16.06	22.26	1005.4	15.67
260	1.35	16.57	23.05	1005.5	16.87
290	1.21	18.05	25.38	1006.0	20.72

Analysis of Biot number in domain 2 showed that it is larger than the critical Biot number (i.e. 0.1) and becomes as large as 0.17 due to the larger convective heat transfer coefficient. On the other hand, calculation of another important dimensionless number, Fourier number ($\tau = \frac{4\alpha_w t}{D^2}$), shows very small value up to 0.00045. it demonstrates that only the interface of liquid water droplet is affected by the incoming cold air flow. Therefore, for proper evaluation of the droplet wetting dynamic, heat penetration length is calculated. Calculation of heat penetration lengths[67], $\delta_h \approx (\alpha_w t_c)^{\frac{1}{2}}$, shows heat penetrated length value up to 0.1 mm ($\alpha_w = 0.13\ e - 6 \left(\frac{m^2}{s}\right)$ and $t_c \approx 85$ ms). It is evident that interface temperature of an impacting supercooled water droplet becomes as cold as -30 °C. Consequently, there is a viscosity jump up to 8 and 3.6 folds higher than those of room temperature and water droplet temperature at -5.5 °C, respectively. Therefore, viscous dissipation should be represented by the combination of internal bulk of an impacting supercooled water and that of interface one. Similar methodology was used for thermal transport analysis of substrates where air flow is present. More detailed information is provided in appendix E. In the

following, detailed elaboration on the supercooled droplet wetting dynamics on hydrophilic and hydrophobic substrates are presented.

4.2.2 Hydrophilic and hydrophobic substrates

The experimental results of supercooled water droplet impacting on aluminum (i.e. hydrophilic) and Teflon (hydrophobic) substrates exposed to cold air flow are presented. Figure (4.25), shows the sequential images of the supercooled water droplet impacting on the polished aluminum substrate in cold atmospheric condition with different air speeds. When droplet impact condition is no longer isothermal, phase change might happen based on the difference between droplet and target substrate temperatures. There are two important dimensionless numbers which are Stefan and Prandtl numbers describing phase change phenomenon. In the current study, the aforementioned dimensionless numbers are frequently used. Therefore, for supercooled water droplet maintained at -2 °C Stefan, Prandtl numbers are 0.128, 14.83, respectively. In the following, wetting behavior of an impacting supercooled water droplet on the aluminum substrate is explained.
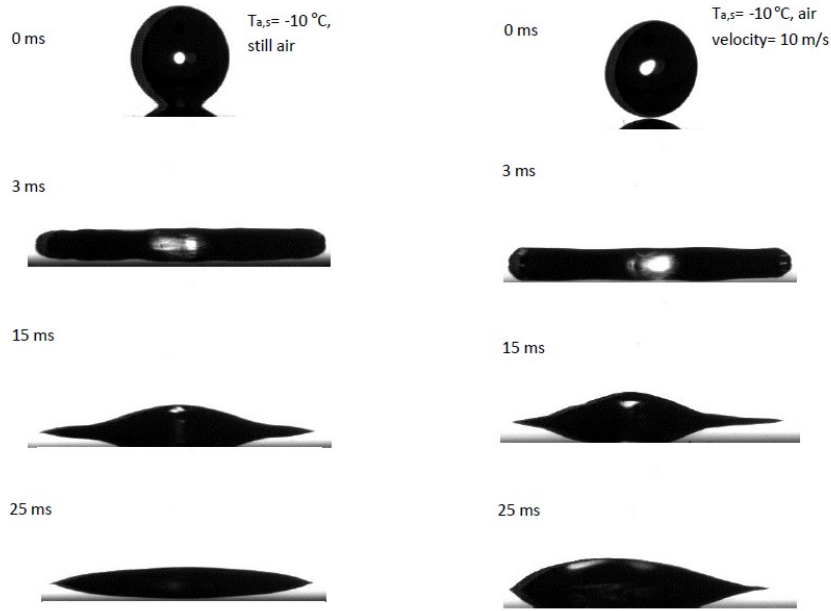
Figure 4.25: Sequential images of supercooled water droplet with and without air flow on the aluminum substrate. Droplet size and impact velocity are 2.6 mm and 1.6 m/s, respectively.

As illustrated in figure (4.25), the droplet before impact was spherical and it was on the metastable supercooled condition. After the impact, deformation of droplet is initiated by rapid conversion of energies. Pressure is rapidly increased at the droplet stagnant point allows the formation of lamella on the substrate. This phase is very fast (nano to few micro second) and it is independent of liquid viscosity.[115] Following this phase, droplet spreading is governed by the viscosity of impacting droplet. The droplet gradually gets a cylindrical flattened shape after central part of water droplet becomes as thin as the spread lamella. Droplet reaches to the maximum spreading diameter after 3 ms of initial impact where kinetic energy of the spreading droplet is depleted. Droplet remains at the maximum diameter about 0.5 ms until surface tension force pulls back two edges of droplet initiating recoiling stage.

Recoiling phase of an impacting water droplet on hydrophilic surfaces governed by surface tension and viscous forces yielding equilibrium contact line and angle. It is worth mentioning that increasing in viscosity of an impacting supercooled water droplet causes retraction force to be

decreased. In fact, contact line friction is increased which results in more viscous dissipation energy.[116] Consequently, receding velocity is affected by an increase in the contact line friction which inevitably increases the droplet relaxation time (i.e. time at the maximum spreading diameter). The mean value temperature of an impacting supercooled water droplet is -2 $^{\circ}$C. Consequently, water droplet viscosity is increased up to 1.9 times compared to the room temperature condition. Therefore, receding velocity is affected by the resultant excessive viscous force. More detailed information of this phenomenon is presented by the quantitative analysis of the recorded images.

Dimensionless spreading factor versus dimensionless time is illustrated in figure (4.26). Increasing relaxing phase time, rapidly increases the heat transfer cooling rate between the droplet and substrate. Large interfacial area of spreading droplet results in a significant decrease in receding velocity in comparison with the room temperature condition. However, it is clear that at the maximum spreading diameter there is not any instantaneous freezing (i.e. no retraction, pinning). This phenomenon can be more elaborated through classical ice nucleation theory combined with the knowledge of solid-liquid interface temperature explained in chapter 3.
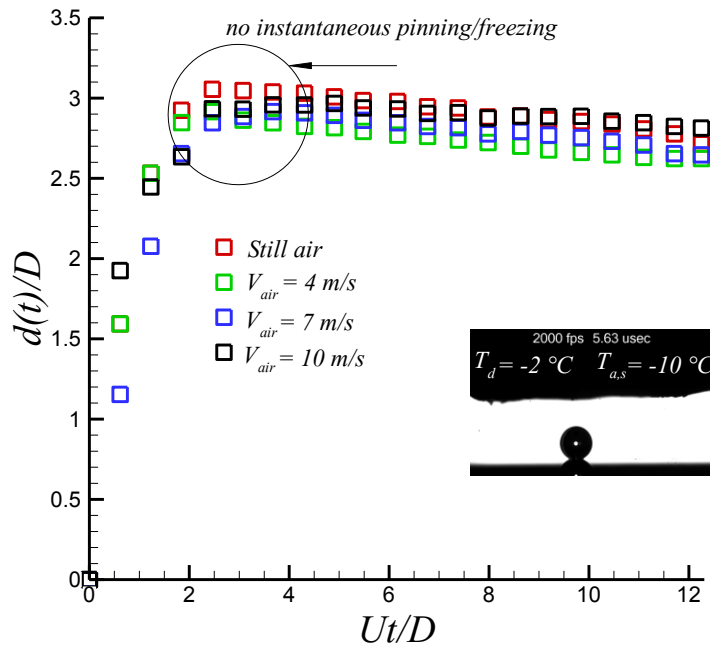
Figure 4.26: Temporal evolution of an impacting supercooled water droplet on the aluminum substrate exposed to cold air at various velocities. Droplet size and impact velocities are 2.6 mm and 1.6 m/s, respectively.

Interface temperature of an impacting supercooled water droplet on the aluminum substrate becomes rapidly close to the substrate temperature due to the high thermal diffusivity of the aluminum and nano scale roughness of polished aluminum surface, as illustrated in figure (3.17). For the substrate maintained at a temperature of -10 ℃ , due to the both liberation of latent heat of fusion and molecular diffusivity [74], there is a sufficient freezing delay time after droplet reaches to the maximum spreading diameter which results in retraction initiation. However, After 25 ms, the retraction force becomes almost zero signaling that heterogeneous ice nucleation between impacting supercooled water droplet and substrate results in droplet pinning to the substrate. In the following, the effect of cold air flow on the supercooled water droplet impact behavior is discussed.

Although the effect of stagnation air flow on an impacting supercooled water droplet results in producing shear force at the gas-liquid interface, it does not show an observable difference as it compares to the still air case. In fact, strong solidification process at solid-liquid interface (i.e. heterogeneous ice nucleation) along with gas-liquid crystallization (i.e. homogeneous ice nucleation) causes droplet spreading behavior remains unaffected by the presence of air flow. Similar results were also found for other scenario of impact condition (i.e. -3.5 and -5.5 °C supercooled water droplet). More detailed information is presented in appendix F.

Figure (4.27), demonstrates the effect of surface and droplet temperature on the wetting dynamics of an impacting supercooled water droplet on the aluminum substrate. The change in the maximum spreading diameter is related to an increase in droplet viscosity which results in a decrease in the maximum spreading diameter compared to the room temperature condition. Here, droplet impact phenomenon is described in terms of all involved energies during impact. As highlighted in the study of Chandra and Avedisian,[111] dissipation energy is increased when viscosity is changed, $W_{dis} = \varphi V t_c$, where W_{dis}, φ, V, t_c are dissipation energy, viscous dissipation function, $\varphi \approx \mu \left(\frac{U}{L}\right)^2$ (L: thickness of the boundary layer for the spread droplet), volume of droplet and characteristic time of spreading which is defined as $8D/3U$ by Passandideh-Fard et al.[41] There are different viscous boundary layer thicknesses which results in different viscous dissipation rate. The thickness of boundary layer is increased by increasing kinematic viscosity (Reynolds number is decreased) signaling that dissipation rate should be decreased. However, competition between an increase in the fluid viscosity (μ) and increase in the boundary layer thickness of the spreading droplet results in an increase in the rate of viscous dissipation. It is clear that if dissipation energy increases the maximum spreading diameter decreases, as demonstrated in figure (4.27).
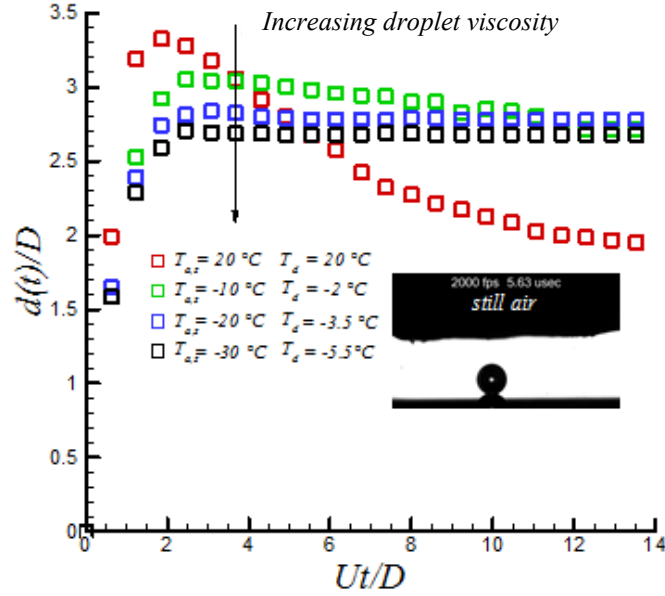
Figure 4.27: Temporal evolution of impacting water droplet on aluminum substrate at wide range of droplet temperatures from 20 ºC down to -5.5 ºC. Droplet impact velocity is 1.6 m/s.

In order to show that reduction in the maximum spreading diameter is only related to the viscosity jump in liquid droplet and not crystallization process, the following discussion is beneficial. Evaluation of the maximum spreading diameter, when phase change is present was carried out by the model of Passandideh-Fard et al.[117] This model which is based on the balance of energy considers another term of the viscous dissipation along with conventional term presented in the hydrodynamics model. It was assumed that all of the kinetic energy is lost in the solidified ice layer thickness. The final form of this model is presented in equation (4.7):

$$\zeta_{max} = \frac{D_{max}}{D} = \sqrt{\frac{We+12}{\frac{3}{8}Wes^*+3(1-cos\theta_{adv})+4\frac{We}{\sqrt{Re}}}} \qquad (4.7)$$

Where, $s^* = \sqrt{2t^*\frac{Ste}{Pe}}$ is the dimensionless growth rate of freezing front which follows Stefan problem soultion. Dimensionless Stefan number, which is the ratio of sensible heat to latent heat $\frac{C_{p,l}(T_m-T_s)}{H_{f,l}}$, is directly related to the degree of subcooling (i.e. difference between substrate

141

temperature and melting point temperature of water droplet, $(T_m - T_s)$. Furthermore, latent heat of fusion of supercooled water from -2 °C to -5.5 °C is a weak function of temperature at the range of current study. Therefore, it is clear that the Stefan number is increased by temperature difference between impacting droplet and substrate which becomes about 0.4 for the lowest temperature condition (i.e. -30 °C). It was showed than when $\sqrt{\dfrac{Ste}{Pr}} \ll 1$ the effect of formed ice nuclei on the maximum spreading dimeter is negligeble.

In the current study, this ratio is about 0.154 for the lowest temperature condition stressing that wetting dynamics during spreading phase is not much affected by the phase change mechanism. Therefore, prediction of maximum spreading diameter using hydrodynamic energy balance model can be performed. After discussion regarding viscosity effect on the droplet maximum spreading diameter on the aluminum substrate, the effect of substrate and droplet temperature on an impacting supercooled water droplet on the Teflon substrate is presented.

In order to highlight the effect of an increased internal and contact line viscosity of supercooled water droplet on Teflon substrate, quantitative evaluation of temporal spreading diameter at various temperatures is illustrated in figure (4.28). While retraction force is substantialy large for the droplet having the lowest viscosity (i.e. room temperature one), droplet retraction is almost eliminated due to both increased viscosity and phase change occurrence after reaching to the maximum spreading diameter for supercooling condition. The droplet experiences instantaneous freezing after reaching to the maximum spreading where it impacts on the cold Teflon substrate maintained at temperatures as low as -30 °C. It shows 17% reduction in the maximum spreading diameter in comparison with room temperature droplet impact condition. More detailed information can be found in appendix F.
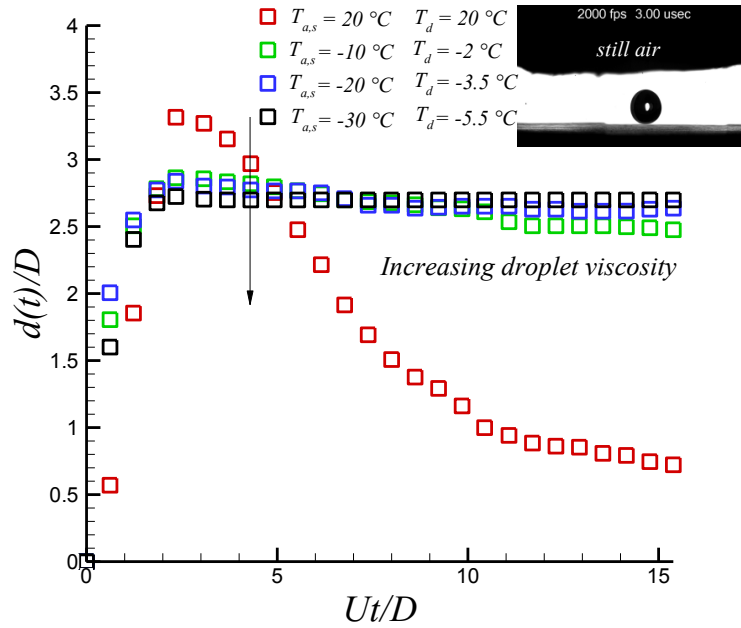
Figure 4.28: Temporal evolution of an impacting supercooled water droplet on Teflon substrate at wide range of droplet temperature from 20 ºC down to -5.5 ºC. Droplet size and impact velocity are 2.6 mm and 1.6 m/s, respectively.

4.2.3 Superhydrophobic substrate

Supercooled water droplet impacting on the superhydrophobic substrate is elaborated below. Furthermore, the effect of stagnation air flow is also investigated which can change the wetting behavior of an impacting supercooled water droplet on a superhydrophobic substrate at various temperatures. Figure (4.29), shows the sequential images of a supercooled water droplet impacting on the superhydrophobic substrate. Droplet diameter, impact velocity, Weber Reynolds, Stefan, Prandtl numbers are 2.6 mm, 1.6 m/s, 88, 2190, 0.128, 14.83, respectively. Droplet changes its sphericity after impact due to the raise in pressure at the impact point and gets the flattened cylindrical shape at 3 ms. Droplet impact velocity was chosen to be in the critical regime of non-splashing regime in order for the spreading rim to face instabilities. Combination of R-T and K-H instabilities due to the blowing air on liquid surface produces some waviness shape called fingering shape. However, the Weber number was not high enough to produce snap-off phase. The time at

the maximum spreading diameter (i.e. relaxation time) was slightly smaller than that of the case of Teflon and aluminum substrates as it was about 0.3 ms. Thereafter, due to the presence of strong capillary force which originated from high receding contact angle, $\pi\gamma D_{max}(1 - cos\theta_{rec})$, the droplet starts recoiling and gets compacted cylindrical shape accompanying jet formation in the still air case at 8 ms. However, by increasing the air jet velocity droplet bouncing and jet formation is dramatically suppressed at this time, as demonstrated in figure (4.29).

Analysis of viscous force shows that viscous dissipation is much smaller compared to the case of aluminum and Teflon substrates, $\tau_{vis} \approx \mu\frac{\partial V}{\partial y}A \approx \mu\frac{V}{h_{lamella}}\pi D_{max}^2$ (i.e. smaller maximum spreading diameter). This result highlights that viscous dissipation on the superhydrophobic substrate is smaller than those on aluminum and Teflon substrates. However, by increasing liquid water droplet viscosity up to 1.9 folds at -2 ºC compared to that of room condition, the effect of viscous dissipation becomes significant.
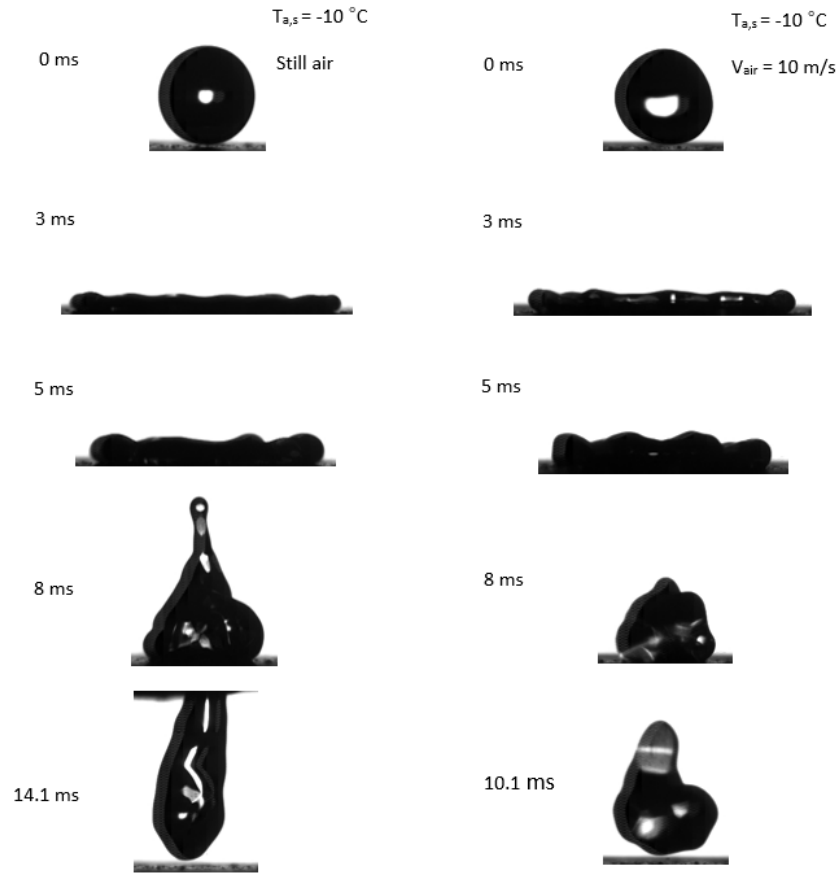
Figure 4.29: Sequential images of supercooled water droplet at a temperature of -2 ℃ impacting on superhydrophobic substrate maintained at -10 ℃.

Although bulk viscosity is increased up to around 2 folds to that of room temperature one, the droplet bounces from the substrate at 14 ms. In fact, due to the very small contact angle hysteresis (i.e. 5°±1°) and partial slip condition typically presented on the superhydrophobic surfaces[118,119] droplet repulsion was observed in the still air condition. On the other hand, quantitative analysis of supercooled water droplet behavior accompanied with different air speeds show different phenomena, as demonstrated in figure (4.30). Droplet contact time is decreased where air velocity is increased which is similar to that of room temperature case. Droplet is detached from the substrate in a considerably shorter time compared to the still air case. Contact time is reduced up to 30% with an air velocity of 10 m/s. Reduction in droplet contact time can be explained similar

to what was described in the isothermal condition. Similar phenomenon was observed where droplet and substrate temperatures were -3.5 ℃ and -20 ℃, respectively. More detailed information can be found in appendix F.
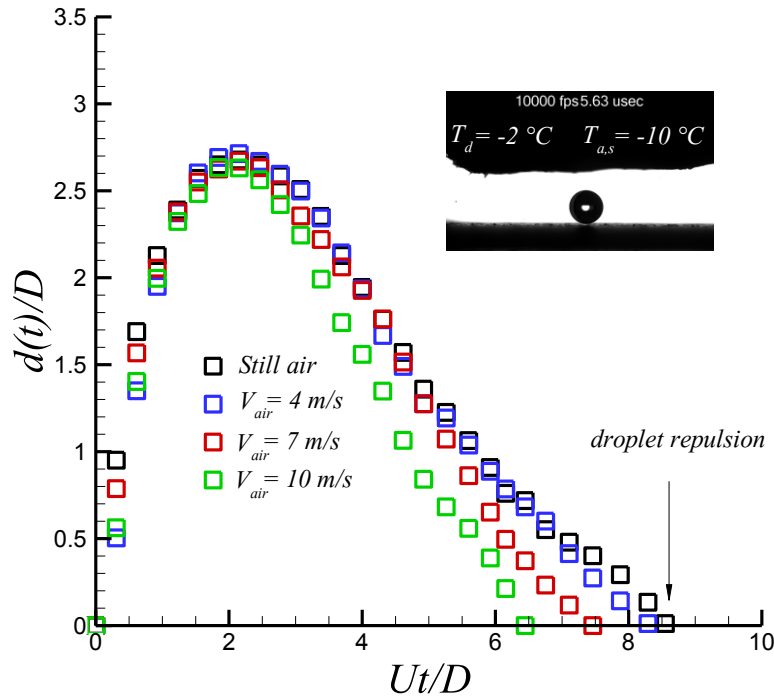
Figure 4.30: Temporal evolution of an impacting supercooled water droplet on the cold superhydrophobic substrate. Droplet and substrate temperatures are -2 and -10 ℃, respectively.

In figure (4.31), dimensionless contact time (based on the capillary-inertia time scale) versus specific viscosity for various supercooled water droplet temperatures are presented. In addition, the results of water-glycerol solution having the same viscosity as the supercooled water droplet were added to investigate the effect of increasing viscosity on the detachment time of an impacting supercooled water droplet.
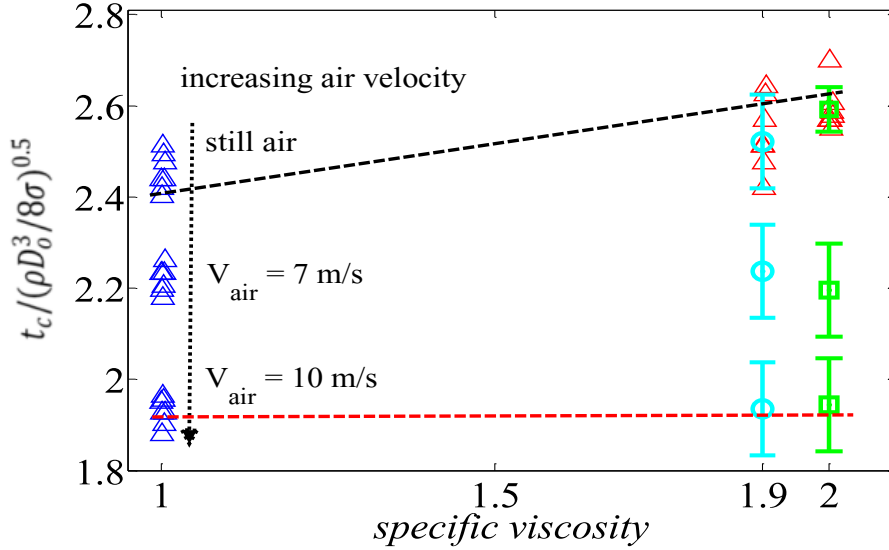
Figure 4.31: Comparison of dimensionless contact time of supercooled water droplet (i.e. Sky blue and green error bars represent supercooled water at -2 and -3.5 ºC, respectively) with water-glycerol solution (i.e. red triangle) with the same viscosity.

Figure (4.32), shows sequential images of an impacting supercooled water droplet with a temperature of -5.5 ºC on the superhydrophobic surface with substrate temperature maintained at -30 ºC. It was exposed to various air velocities ranging from 0 to 10 m/s. In this case, droplet impacts on the superhydrophobic surface having temperatures lower than the critical temperature of crystallization process for bouncing droplets (i.e. -24 ºC). Droplet rim formation starts right after 0.5 ms of initial droplet impact condition. After this time, spreading phase is governed by the viscous force while the droplet reaches the maximum spreading diameter at 3 ms. This highlights that spreading phase was unaffected by the both significant increase in internal bulk of viscosity up to 2.2 folds and contact line viscosity up to 8 folds combined with crystallization process. As shown in figure (4.32), during the spreading phase, superhydrophobicity was maintained by measuring advancing dynamic contact angle. The variation of dynamic contact angle falls within 145º to 140º (±10º) during spreading phase. The spreading phase (i.e. 3 ms) is fast enough to wetting diameter remains unaffected by the crystallization process which might reduce the maximum spreading diameter if root square ratio of Stefan/Prandtl becomes close to 1 or larger.

147
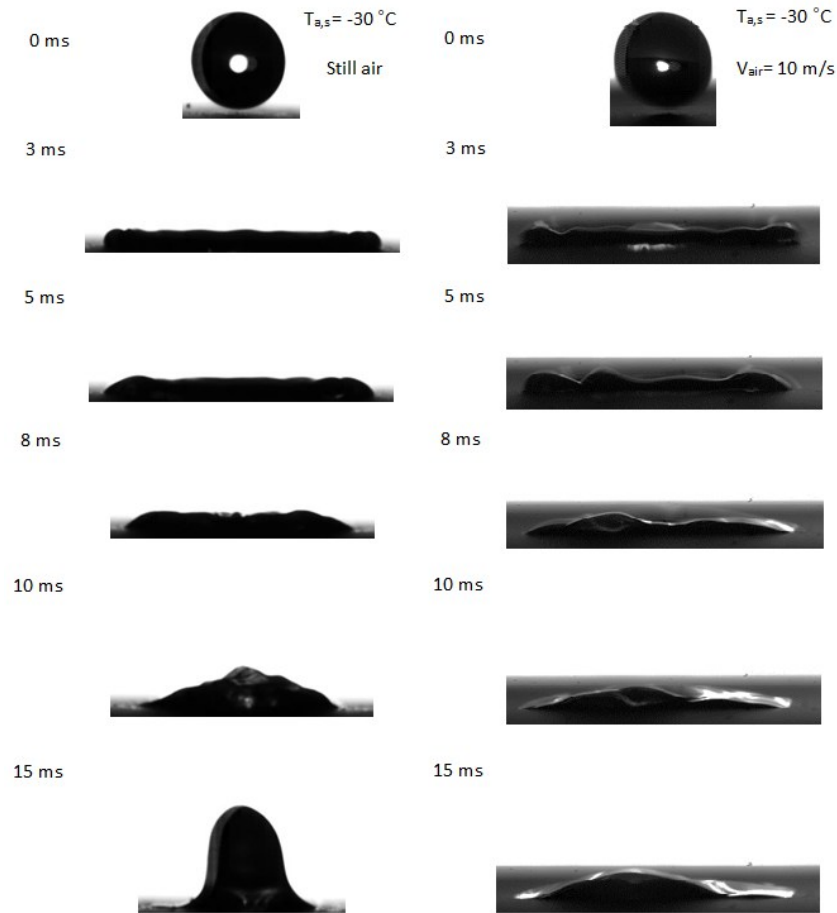
Figure 4.32: Sequential images of supercooled water droplet impacting on the superhydrophobic substrate maintained at -30 ºC.

The maximum spreading diameter was not affected by nucleation process verified by measuring both maximum spreading diameter and advancing dynamic contact angle during the spreading phase. Bahadur et al.[2] proposed a model of pinning/freezing of droplet impact on the superhydrophobic surface which relates heterogeneous ice nucleation process based on the temporal change in the contact angle of triple phase point. Combining dynamics wetting of droplet with the associated heat transfer between droplet-substrate (e.g. finding interface temperature) along with ice nucleation process, it was shown that ice nucleation mechanism becomes dominant and the chance of pinning increases where contact angle is decreased due to the growth of ice

nuclei. Consequently, this results in conversion of surface superhydrophobicity to even hydrophilicity.

As demonstrated in figure (4.32), it was not shown any variation in advancing dynamic contact angle during the spreading phase which imprint our explanation regarding no influence of crystallization process on the maximum spreading diameter. However, a striking phenomenon was observed where droplet reached to the maximum spreading diameter. The time at the maximum spreading diameter (i.e. relaxation time) was significantly increased up to 2 ms causing dramatic increase in heat transfer cooling due to the large wetting area. Faster heterogeneous nucleation rate is also prompted due to the larger interfacial area which dramatically changes the receding contact angle. As demonstrated in figure (4.32), receding contact angle systematically affected by the heterogeneous ice nucleation process which results in a complete superhydrophobicity break down at 5 ms.

Due to the combination of receding contact angle reduction and rapid increase in the viscosity specially at the contact line, (i.e. liquid water droplet molecules close to substrate with large relaxing time has a lower entropy[102] which its property is similar to the water droplet having lower temperature) significant reduction in the receding capillary force is occurred, $\pi\gamma D_{max}(1 - cos\theta_{rec})$. Consequently, receding velocity is dramatically decreased which even further increases the chance of heat transfer cooling rate and heterogeneous ice nucleation process. Quantitative analysis of droplet dynamics behavior on the superhydrophobic surface in the still air is illustrated in figure (4.33). It shows that the capillary force becomes zero corresponding no receding velocity at 11 ms.

On the other hand, when the droplet is exposed to cold air flow, droplet wetting behavior undergoes a complicated process due to the presence of evaporation cooling promoting another type of ice

nucleation process called homogeneous ice nucleation and crystallization induced nucleation from inside-out.[120] Indeed, because of the presence of evaporation cooling gas-liquid interface temperature becomes even lower than air temperature which is a function of air velocity and air humidity.[36] It was observed that where relative humidity is negligible, which is similar to the current study, the effect of evaporation cooling becomes significant and another thermodynamically preferred nucleation mechanism happens at the air-liquid interface.

The effect of homogeneous ice nucleation mechanism has an adverse effect on the wetting dynamics of an impacting supercooled water droplet by reducing the receding capillary force due to surface tension reduction, as explained in detail in chapter 3. Likewise heterogeneous ice nucleation mechanism, which its effect is correlated with a change on the apparent contact angle, the effect of homogeneous ice nucleation can be incorporated to the wetting dynamics of an impacting supercooled water droplet by variation of surface tension. Surface tension of a mixture of ice-water is about 20 mN/m^2 which shows a reduction on the water surface tension up to 3.5 folds compared to that of room temperature (i.e. 73 mN/m). Therefore, after the formation of ice nuclei on the gas-liquid interface the surface tension (or capillary force) of an impacting water droplet is altered especially at the time of maximum spreading diameter in which the droplet is exposed to the maximum evaporation cooling because of larger interfacial area. Finally, the receding capillary force experiences severe decrease originated from surface tension and apparent receding contact angle reduction, $\pi\gamma D_{max}(1 - cos\theta_{rec})$, as depicted in figure (4.33).
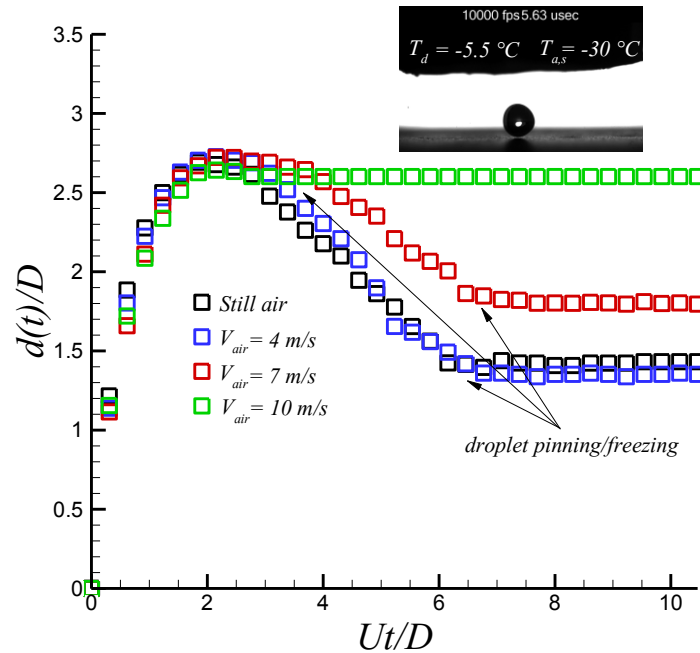
Figure 4.33: Temporal evolution of an impacting supercooled water droplet on a cold superhydrophobic substrate. Droplet and substrate temperatures are -5.5 and -30 ºC, respectively. Droplet size and impact velocity are 2.6 mm and 1.6 m/s, respectively.

As mentioned above, stagnation air flow results in interface temperature reduction by evaporation cooling mechanism which promotes the probability of homogenous ice nucleation process. It also produces shear and normal forces on the spreading droplet interface. These two forces promote further countermovement of recoiling droplet. Consequently, the relaxation time is dramatically increased which is combined with immediate reduction on the receding contact angle. The imposed continuous shear and normal forces of air flow result in further reduction in capillary force causing droplet to be pinned on the substrate right after the beginning of recoiling phase. As illustrated in figure (4.33), droplet pinning occurs at 4.5 ms which is slightly after the initiation of retraction phase. In addition to this, solidified wetting length considerably becomes larger compared to the still air case. It increases up to 2 folds at 10 m/s air velocity which highlights a significant difference on an impacting supercooled water droplet on the superhydrophobic surface where stagnation air flow is present.

Figure (4.34), shows temporal evolution of an impacting supercooled water droplet on the superhydrophobic surface at different temperatures. While the maximum spreading diameter was remained unaffected by increasing both bulk and contact line viscosity the retraction phase is significantly influenced by these aforementioned parameters. As illustrated in figure (4.34), owning to the presence of heterogeneous ice nucleation which results in consecutive reduction in the receding contact angle, superhydrophobicity break down happens at 10 ms (corresponding to dimensionless time up to 6).

Although maximum spreading diameter was not varied with increasing water and contact line viscosity, the mean value contact time was slightly changed due to the increased viscosity up to 11%. However, mimicking extreme supercooled water droplet (i.e. -24 °C) by producing solution of water-glycerol with the same viscosity to that of supercooled droplet, it is clear that maximum spreading diameter was slightly affected by an impacting viscous droplet up to 6%. In addition to that, large increase in viscosity of an impacting droplet up to 5.5 times causes the receding velocity to be affected by partial meniscus penetration through inside of surface roughness which results in an increase in droplet contact time up to 30%.[79] In the following, the aforementioned experimental results are used for validation of predictive model of droplet wetting dynamics in the low temperature condition presented in chapter 3.
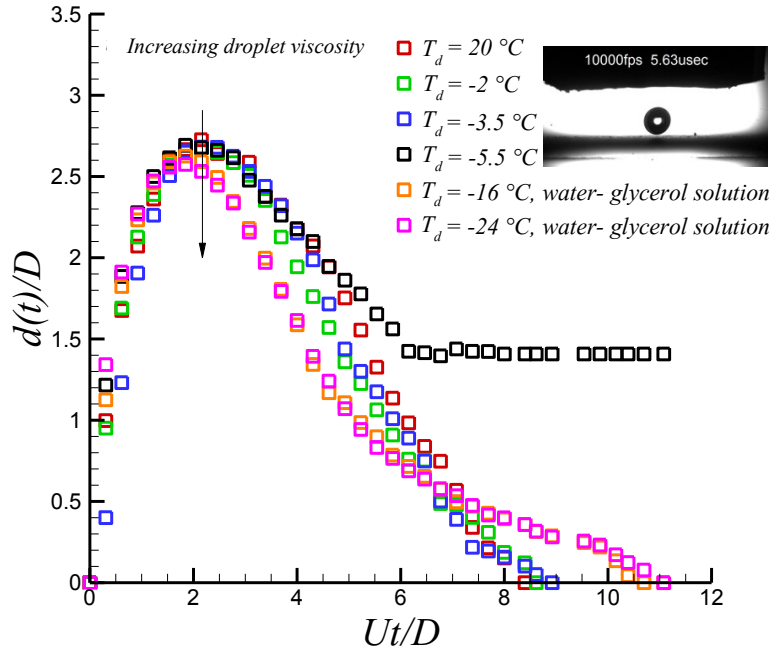
Figure 4.34: Temporal evolution of an impacting water droplet on the superhydrophobic substrate for a wide range of droplet temperatures from 20 ºC to -5.5 ºC. Droplet size and impact velocity are 2.6 mm and 1.6 m/s, respectively.

As illustrated in figure (4.35(a)), variation of transient retraction capillary force is plotted (i.e. blue line) against spreading diameter which both of them are illustrated in the normalized form. For temperatures below the critical temperature of heterogeneous ice nucleation (i.e. -24 ºC), droplet, is spread and retracted without facing crystallization process. In fact, droplet is retracted in the recoiling phase with almost constant retraction capillary force highlighting the complete bouncing from the cold substrate maintained at the temperatures as low as -10 ºC. Droplet contact time is similar to that of room temperature up to about 13 ms. It is worth mentioning that the time illustrated in figure (4.35(a)) is a dimensionless time of retraction which should be multiplied with the droplet time constant demonstrated in equation (3.25). More detailed information about new presented model can be obtained in chapter 3.
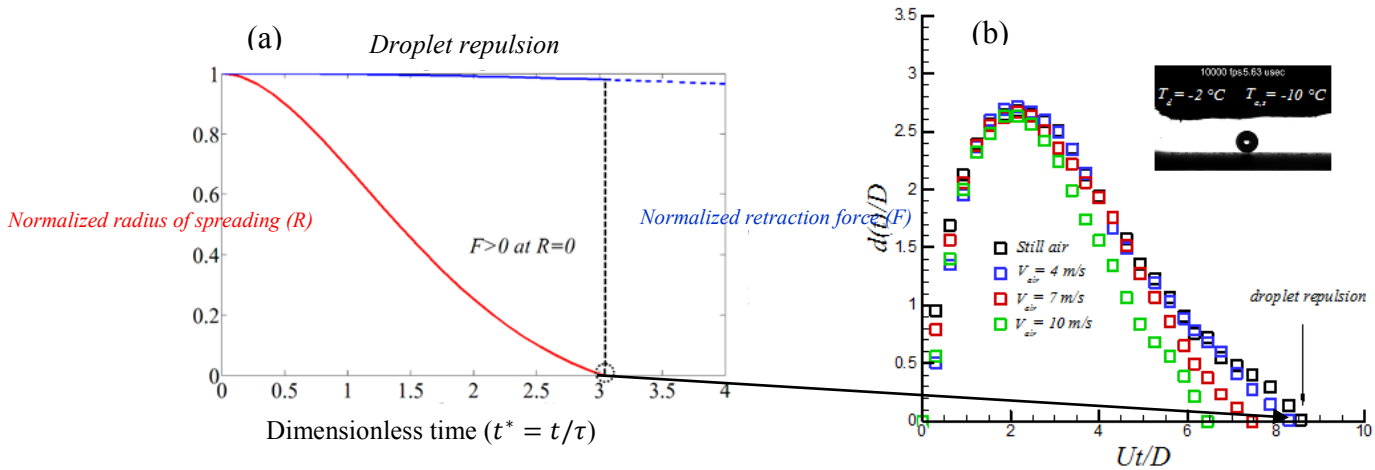
Figure 4.35: a) Temporal normalized spreading diameter plotted against retraction force. b) experimental behavior of an impacting supercooled water droplet. Droplet, substrate, air temperatures and air velocity are -2, -10, -10 °C and 10 m/s, respectively.

Similar phenomenon was observed for the supercooled water droplet impacting on the cold superhydrophobic substrate maintained at -20 °C, as demonstrated in figure (4.36 (a)) which is still above the critical temperature of heterogeneous ice nucleation. In spite of the fact that droplet completely bounces from the substrate, a slight increase in droplet contact time is observed which is almost similar to that of the experimental results. Transient retraction force is significantly reduced from maximum values at initial stage of retraction phase and becomes almost zero at the time of droplet repulsion. This result highlights that an increase in supercooled bulk water droplet viscosity up to 2 folds and around 5 folds in droplet contact line is the main reason of an increase in droplet contact time which shows a good agreement with that of experimental results. Finally, the wetting behavior of an impacting supercooled water droplet on the substrate maintained at a temperature as low as -30 °C (i.e. below the critical temperature of heterogeneous ice nucleation (i.e. -24 °C)) is presented below.

.
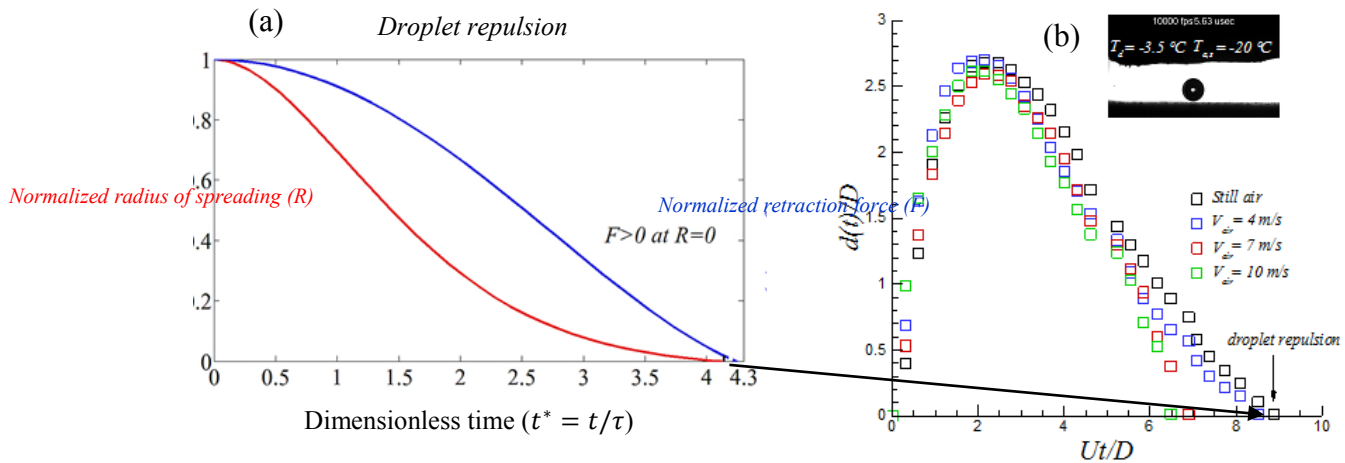
Figure 4.36: a) Temporal normalized spreading diameter plotted against retraction force. b) experimental behavior of an impacting supercooled water droplet. Droplet, substrate, air temperatures and air velocity are -3.5, -20, -20 ⁰C and 10 m/s, respectively.

Supercooled water droplet impacting on the cold substrate below the critical temperature of heterogeneous ice nucleation is faced solidification after reaching to the maximum spreading diameter. Figure (4.37(a)) illustrates the effect of heterogeneous ice nucleation mechanism on wetting dynamics of an impacting supercooled water droplet which is similar to the study of Mishchenko et al.[65]. However, the effect of viscous term was not provided in the aforementioned study which was considered in the new predictive model. In figure (4.37(a)) the effect of both resultant shear flow of incoming air flow and homogeneous ice nucleation were neglected to just consider the net effect of the heterogeneous ice nucleation mechanism on droplet wetting behavior. As shown, droplet recoiling phase is faced sever crystallization process only due to the heterogeneous ice nucleation mechanism. It shows that ice formation results in solidified diameter up to 20% of the maximum spreading diameter. On the other hand, by including the effect of air flow up to 10 m/s and by consideration of both resultant shear force of incoming airflow and also the effect of homogenous ice nucleation mechanism (i.e. due to evaporation cooling), the solidified wetting diameter is increased up to 2 folds to that of still air case. Indeed, the effect of

155

homogeneous ice nucleation where convective evaporation cooling is present results in faster crystallization process, as illustrated in figure (4.37(b)).

(a)

(b)

(c)
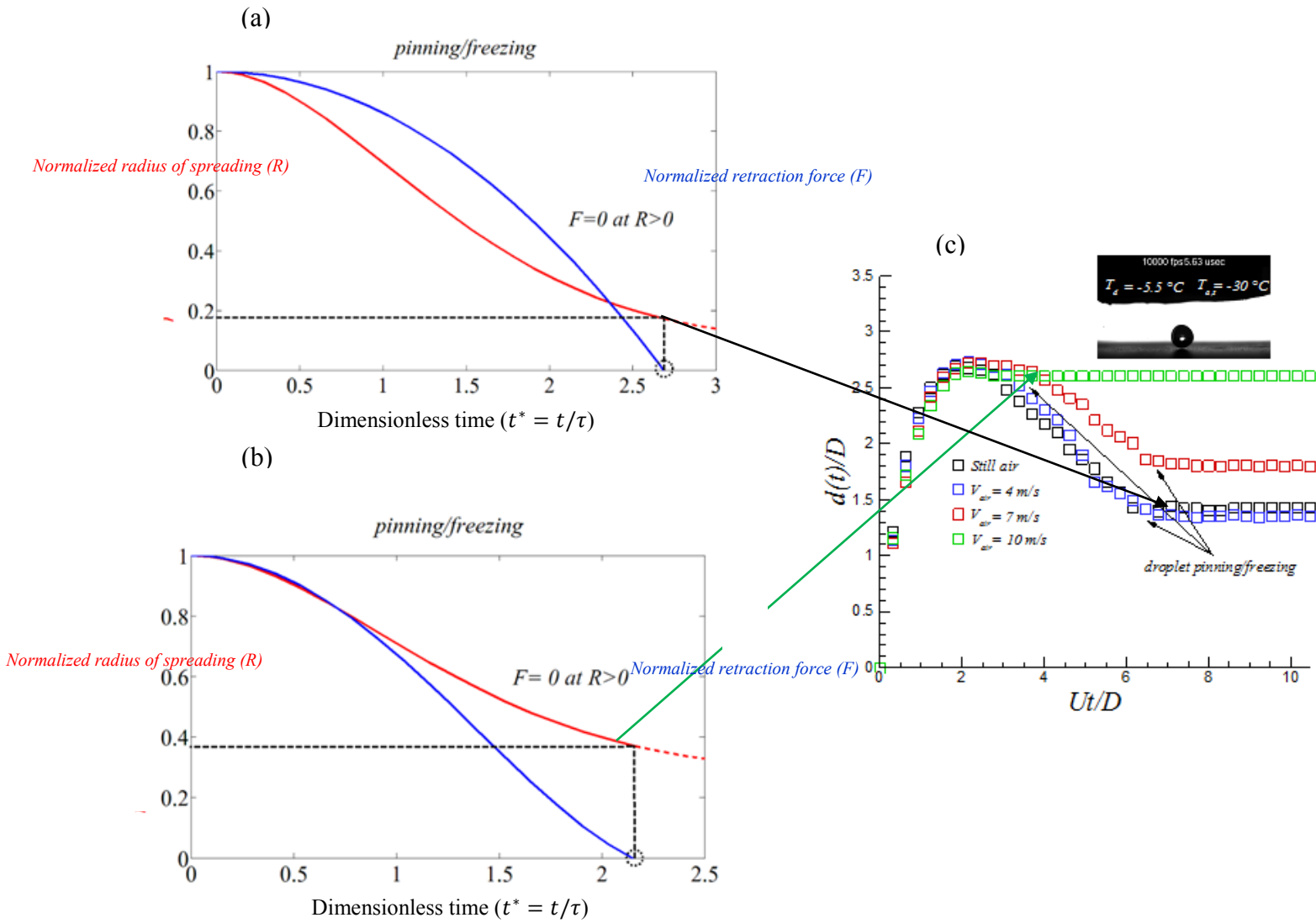
Figure 4.37: a) Temporal normalized spreading diameter plotted against retraction force without the effect of homogeneous ice nucleation b) temporal normalized spreading diameter plotted against retraction force with the effect of homogeneous ice nucleation c) experimental behavior of an impacting supercooled water droplet. Droplet, substrate, air temperatures and air velocity are -5.5, -30, -30 ºC and 10 m/s, respectively.

156

Chapter 5

Closure

Phenomenology of liquid droplet impacting on dry solid surfaces is a classical study in fluid mechanics involving a wide range of industrial applications from thermal spray, inkjet printing, electrical transmission power line and aerospace industries. In fact, knowing the physics of liquid droplet impacting on surfaces is substantially beneficial in the aforementioned fields. The most complexity of this phenomenon is related to the estimation of maximum wetting area of an impacting droplet which subsequently determines the rate of heat and mass transfer through evaporation and or solidification mechanism in non-isothermal conditions. Based on the application, interfacial area of solid-liquid (i.e. wetting area) can be increased or decreased through the knowledge of advanced material and interface science. Complexity of finding wetting interfacial area through impacting of liquid droplet stems from various involving parameters namely droplet size, droplet impact velocity, droplet temperature, viscosity and surface tension of impacting liquid droplet. In fact, all the aforementioned parameters combining with substrate properties determines the droplet wetting area (i.e. droplet spreading diameter).

Among the parameters mentioned above, the role of incoming air flow on an impacting droplet has been overlooked in the literature. In fact, studies of two subsequent stagnation flows having comparable viscosity have been completely neglected. It is mostly related to the challenging experimental methodology and theoretical analysis. Practically, many of natural droplet impact

phenomena are accompanied with air flow which can be either stagnation airflow or shear one. The interest in the study of stagnation air flow arises from the fact that maximum droplet wetting area (i.e. maximum spreading diameter) may be different to that of still air case. Furthermore, in case of non-isothermal condition (e.g. impact of supercooled water droplet on the cold substrate), stagnation flow may result in different freezing mechanisms in comparison with the still air condition.

In this thesis, in the first stage, the impact of various water droplet sizes having various impact velocities accompanied with the stagnation air flow were investigated using experimental methods. Solid surface wettabilities were varied from hydrophilic to superhydrophobic surfaces. One theoretical part was also developed which provides a predictive model of transient droplet spreading diameter on the superhydrophobic surface. This model was further developed to consider the effect of stagnation air flow using classical Homann flow approach. Additionally, in non-isothermal condition, the effect of phase change (i.e. solidification) was also considered on the aforementioned model through the classical nucleation theory. The methodology which was used in the current study and results of experimental tests in the room and low temperature conditions along with validation of the developed model are summarized in the subsequent section.

5.1 Summary and conclusion

The effect of stagnation air flow on an impacting water droplet on different solid surfaces have not been reported yet due to the challenging experimental test conditions. In chapter 2, experimental set up of producing stagnation flow was elaborated. Stagnation flow was produced using a device which was termed droplet accelerator. Various air velocities ranging from 0 (i.e. still air) to 10 m/s was produced. The limitation of imposing higher air velocity stemmed from the necessity to have spherical droplet with and without air flow based on the definition of the critical

relative Weber number below 3. Furthermore, the net effect of air flow on an impacting water droplet was evaluated by having the same droplet impact velocity with and without air flow. Using classical Homann flow approach, the resultant shear and normal forces of incoming air flow on spreading droplet were evaluated and compared with that of still air condition. It was observed that receding contact angle is an important parameter where air flow is present.

For hydrophilic surface (i.e. aluminum substrate, the receding contact angle at maximum spreading diameter is about 35°) non-recoiling phase was observed for the maximum droplet Weber number around 220 (i.e. droplet impact velocity was 2.5 m/s) accompanied with air velocities up to 10 m/s. No significant variations were observed for the Teflon substrate, as a hydrophobic surface having dynamic receding contact angle up to 70°. On the other hand, phenomenology of droplet wetting dynamic was completely affected on the sanded Teflon substrate where air flow is present. This surface was termed as a near superhydrophobic surface having static contact angle of 135° which was treated as an intermediate substrate having almost similar receding contact angle to that of Teflon substrate (i.e. 70°) and similar contact angle hysteresis to that of aluminum substrate (i.e. 40°).

It was highlighted that incoming stagnation air flow could be divided into two distinct domains namely pressure and shear domain. While for low Weber number droplet impact experiments (i.e. 30 and 40), which results in small maximum spreading diameters, wetting behavior was mostly affected by the pressure domain air flow. It was observed that within the pressure domain, partial droplet repulsion was converted to the fully droplet pinning for an air velocity of 10 m/s. However, for slightly larger droplet size (i.e. 2.6 mm corresponding Weber number of 50), phenomenology of droplet wetting dynamics was quite similar to that of still air condition. This phenomenon was clarified by increasing the droplet impact velocity.

159

An interesting phenomenon was observed when droplet impact velocity was increased to 2 m/s corresponding to droplet Weber number around 140. Indeed, droplet wetting diameter was sufficiently developed locating in the shear domain of stagnation air flow. The resultant shear force of incoming air flow showed a dominant role on the droplet wetting dynamics by producing significant reverse velocity gradient at the spreading water droplet interface. Consequently, for shear domain droplet impact condition, at the aforementioned critical droplet Weber number (i.e. 140), a complete droplet sticking was observed for the air velocity of 10 m/s. However, almost full droplet repulsion was seen in the still air condition.

Wetting dynamics of an impacting water droplet on the extremely low wettable surfaces (i.e. superhydrophobic surfaces) was substantially affected by the incoming stagnation air flow. Using the same terminology of pressure and shear domains stagnation airflow, wetting characteristics namely maximum spreading diameter and droplet contact time were investigated for a wide range of droplet Weber numbers from 30 to 450. While for the pressure domain droplet impact conditions (i.e. 30 to 50) droplet contact time was barley affected by the incoming air flow, systematic reduction in the droplet contact time was observed by increasing the droplet Weber numbers (i.e. increasing maximum spreading diameter). For droplet Weber numbers within 50 to 140, due to presence of stagnation air flow, droplet contact time was decreased. It was reduced up to 15%, 22% and 35% for droplet Weber numbers of 50, 90 and 140, respectively. This phenomenon was attributed to the presence of K-H instability at the solid-gas-liquid interface combined with transition of partial slip condition to the full slip one (i.e. contact line viscous dissipation was neglected) in the complete non-splashing regime on the superhydrophobic surface (i.e. Weber numbers from 30 to 90).

Non-isothermal wetting behavior of an impacting supercooled water droplet on hydrophilic (i.e. aluminum), hydrophobic (i.e. Teflon) and superhydrophobic substrates were carried out by the analysis of temporal spreading diameter and droplet contact time. Although for hydrophilic and hydrophobic substrates non-instantaneous pinning at the maximum spreading diameter was observed at temperature above -20 $^{\circ}$C, a complete water droplet repellency happened on superhydrophobic surface. A striking phenomenon was observed. Droplet contact time was reduced up to about 30% on the superhydrophobic substrate for air velocity up to 10 m/s compared to the still air case. Indeed, this phenomenon can be explained similar to that of room temperature condition. Nevertheless, for substrate temperatures below the critical temperature of heterogeneous ice nucleation on bouncing droplets (i.e. -24 $^{\circ}$C), instantaneous pinning (i.e. no recoiling phase) was observed for hydrophilic and hydrophobic surfaces. However, for the superhydrophobic surface, recoiling phase is subjected to the sever reduction in the receding contact angle and also surface tension which results in transition from superhydrophobicity to hydrophilicity by rapid crystallization process. Further decreases in the droplet recoiling phase was observed by imposing stagnation air flow up to 10 m/s which results in almost non-recoiling phase of the supercooled droplet impacting on the superhydrophobic surface.

Experimental results of both isothermal and non-isothermal droplet impact on the superhydrophobic substrate are used as a suitable floor in order to validate a new predictive model of transient droplet spreading diameter on the superhydrophobic substrate. dashpot

Wetting phenomenon of an impacting water droplet on the superhydrophobic substrate was also simulated through a predictive model of transient spreading diameter based on the model of mass-spring-dashpot equation. Okumura et al.[13] highlighted that for large droplet deformation on superhydrophobic surfaces the model of mass-spring is no longer linear and the effect of contact

161

line viscosity cannot be ignored anymore. Based on the previous model of the mass-spring presented by Bahadur et al.[2], an additional term of viscous force was appropriately added to the model in order to fully predict the temporal spreading diameter. The proposed model predicts very well both the maximum spreading diameter and droplet contact time. For the maximum spreading diameter an excellent agreement with the mean value deviation of 1.5% was observed while the mean value deviation of droplet contact time was up to 11% for the smallest droplet size (i.e. 1.65 mm). However, it was reduced up to 9% for 2 mm water droplet size. This slight deviation in the droplet contact time can be related to the three dimensional nature of recoiling behavior (i.e. presence of instabilities both R-T and K-H instabilities and surface roughness) of an impacting water droplet. This new model was used to be coupled with the effect of phase change mechanism (i.e. solidification) through the classical nucleation theory which is summarized in the following. Investigation of the supercooled water droplet impacting on various solid surfaces spanning from hydrophilic to superhydrophobic surfaces were carried out through combination of droplet wetting dynamics, thermal transport within droplet to substrate and the classical nucleation theory. It was previously highlighted that both ice nucleation mechanisms (i.e. heterogeneous and homogeneous ice nucleation) are defined based on the Gibbs free surface energy which is directly related to the solid-liquid (i.e. heterogeneous ice nucleation) or gas-liquid (i.e. homogeneous ice nucleation) interface temperature. Therefore, predictive analytical models of solid-liquid and gas-liquid interface temperatures were derived to be appropriately coupled with the ice nucleation rate. Consequently, the effect of phase change (i.e. solidifications) through solid-liquid or gas-liquid interaction were coupled with the aforementioned predictive model. Finally, the predictive model was validated against experimental results showing good agreements in terms of predicting the

162

critical temperature of droplet repulsion or pinning on the superhydrophobic surface. In the following the main outcome of the current study is itemized.

- Droplet wetting behavior is influenced by four different parameters in isothermal condition including pressure and shear domain stagnation air flow, the receding contact angle, contact angle hysteresis and the maximum spreading diameter. There are two more parameters in non-isothermal condition where stagnation airflow is present including substrate-water and gas-water interface temperatures.

- Regarding the effect of receding contact angle, within shear domain, droplet wetting behavior is changed in response to an increase in hydrophilicity.

- Droplet impact behavior accompanied with stagnation air flow on a surface having large contact angle hysteresis (e.g. sanded Teflon) results in less droplet mobility and more droplet pinning.

- Shear domain droplet impact condition reduces droplet contact time up to 35% by increasing droplet Weber numbers on superhydrophobic surfaces with a very small contact angle hysteresis (e.g. 5°).

- In non-isothermal condition, stagnation air flow reduces the chance of solidification on the superhydrophobic substrate by droplet contact time reduction mechanism where substrate-liquid interface temperatures are above the critical temperature of heterogeneous ice nucleation for bouncing droplets (i.e. -24 °C).[1]

- Stagnation air flow extents the solidified wetting diameter up to 2 folds compared to the still air cases where substrate-water interface temperature is below the critical temperature of heterogeneous ice nucleation (i.e. -24 °C).

- The new proposed model of transient spreading diameter in the isothermal condition predicts very well both the maximum spreading diameter and the contact time of an impacting water droplet having different viscosities on a superhydrophobic surface compared to the previous models.

- The aforementioned predictive model of transient droplet spreading diameter in non-isothermal conditions reasonably predicts the critical temperatures of pinning or repulsion on superhydrophobic surfaces. Indeed, the effect of cold air flow (i.e. both air shear force and homogeneous ice nucleation effects) were implemented to the model in order to mimic the realistic ice formation mechanism in the low temperature conditions.

5.2 Recommendations for future works

The current study is aimed at conducting experimental and analytical approaches to understand the main features of droplet impact phenomena on solid surfaces where stagnation air flow is present. The following topics are recommended to be further studied in detail which is beneficial to better understand the complex this topic, multi-phase flow.

- To capture wetting area of isothermal impacting liquid droplet having wide range of viscosities and surface tensions. Indeed, specially, varying liquid droplet surface tension might change wetting behavior where stagnation flow is present. It is worth stressing that retraction capillary force is directly related to droplet surface tension.

- To produce different profile of stagnation flow. It can be obtained by imposing different air velocities. However, the limitation of exposing higher air velocity regarding droplet deformation should be taken into account.

- A numerical simulation of two phase flow can be carried out for better understanding of gas-liquid-solid interaction. In case of non-isothermal condition the effect of phase change should be taken into account through adding energy equation on the available solver.

References

1. Eberle P, Tiwari MK, Maitra T, Poulikakos D. Rational nanostructuring of surfaces for extraordinary icephobicity. *Nanoscale*. 2014; 6(9):4874-4881.

2. Bahadur V, Mishchenko L, Hatton B, Taylor JA, Aizenberg J, Krupenkin T. Predictive model for ice formation on superhydrophobic surfaces. *Langmuir*. 2011; 27(23):14143-14150.

3. Sahoo B, Labropulu F. Steady homann flow and heat transfer of an electrically conducting second grade fluid. *Comput Math Appl*. 2012; 63(7):1244-1255.

4. Dussan E. On the spreading of liquids on solid surfaces: Static and dynamic contact lines. *Annu Rev Fluid Mech*. 1979;11(1):371-400.

5. Passandideh Fard M. Droplet impact and solidification in a thermal spray process: Droplet-substrate interactions. 1996. *PhD dissertation*.

6. Volat C, Farzaneh M, Leblond A. De-icing/anti-icing techniques for power lines: Current methods and future direction. *11th International Workshop on Atmospheric Icing of Structures*. 2005:12-16.

7. Jung S, Dorrestijn M, Raps D, Das A, Megaridis CM, Poulikakos D. Are superhydrophobic surfaces best for icephobicity? *Langmuir*. 2011; 27(6):3059-3066.

8. De Gennes P. Wetting: Statics and dynamics. *Reviews of modern physics*. 1985;57(3):827.

9. Tadanaga K, Morinaga J, Matsuda A, Minami T. Superhydrophobic-superhydrophilic micropatterning on flowerlike alumina coating film by the sol-gel method. *Chemistry of materials*. 2000;12(3):590-592.

10. Patel P, Choi CK, Meng DD. Superhydrophilic surfaces for antifogging and antifouling microfluidic devices. *Journal of the Association for Laboratory Automation*. 2010; 15(2):114-119.

11. Ueda E, Levkin PA. Emerging applications of Superhydrophilic-Superhydrophobic micropatterns. *Adv Mater*. 2013;25(9):1234-1247.

12. Feng L, Li S, Li Y, et al. Super-hydrophobic surfaces: From natural to artificial. *Adv Mater*. 2002;14(24):1857-1860.

13. Okumura K, Chevy F, Richard D, Quéré D, Clanet C. Water spring: A model for bouncing drops. *EPL (Europhysics Letters)*. 2003; 62(2):237.

14. Bhushan B, Jung YC, Koch K. Micro-, nano-and hierarchical structures for superhydrophobicity, self-cleaning and low adhesion. *Philos Trans A Math Phys Eng Sci.* 2009; 367(1894):1631-1672.

15. Li X, Reinhoudt D, Crego-Calama M. What do we need for a superhydrophobic surface? A review on the recent progress in the preparation of superhydrophobic surfaces. *Chem Soc Rev*. 2007; 36(8):1350-1368.

16. Yuan Y, Lee TR. Contact angle and wetting properties. In: Surface science techniques. *Springer*; 2013:3-34.

17. Bracke M, De Voeght F, Joos P. The kinetics of wetting: The dynamic contact angle. In: Trends in colloid and interface science III. *Springer*; 1989:142-149.

18. Jiang T, Soo-Gun O, Slattery JC. Correlation for dynamic contact angle. *J Colloid Interface Sci*. 1979; 69(1):74-77.

19. Hoffman RL. A study of the advancing interface. I. interface shape in liquid-gas systems. *J Colloid Interface Sci*. 1975; 50(2):228-241.

20. Farhangi MM, Graham PJ, Choudhury NR, Dolatabadi A. Induced detachment of coalescing droplets on superhydrophobic surfaces. *Langmuir*. 2012; 28(2):1290-1303.

21. Mohammadi M, Moghtadernejad S, Graham PJ, Dolatabadi A. Dynamic impact behavior of water droplet on a superhydrophobic surface in the presence of stagnation flow. *Journal of applied mechanics and material* 2012; 232:267-272.

22. Bolleddula DA. Droplet impact and spreading of viscous dispersions and volatile solutions. 2011.*PhD dissertation*.

23. Fukai J, Shiiba Y, Yamamoto T, et al. Wetting effects on the spreading of a liquid droplet colliding with a flat surface: Experiment and modeling. *Physics of Fluids* (1994.present). 1995;7(2):236-247.

24. Gunjal PR, Ranade VV, Chaudhari RV. Dynamics of drop impact on solid surface: Experiments and VOF simulations. *AIChE J*. 2005; 51(1):59-78.

25. Roisman IV, Berberović E, Tropea C. Inertia dominated drop collisions. I. on the universal flow in the lamella. Physics of Fluids (1994.present). 2009;21(5):052103.

26. Chandra S, Avedisian C. On the collision of a droplet with a solid surface. *Proceeding of royal society of a mathematical, physical and engineering sciences*. 1991; 432(1884):13-41.

27. Pasandideh-Fard M, Qiao Y, Chandra S, Mostaghimi J. Capillary effects during droplet impact on a solid surface. *Physics of Fluids (1994.present)*. 1996;8(3):650-659.

28. Rioboo R, Marengo M, Tropea C. Time evolution of liquid drop impact onto solid, dry surfaces. *Exp Fluids*. 2002; 33(1):112-124.

29. Van Dam DB, Le Clerc C. Experimental study of the impact of an ink-jet printed droplet on a solid substrate. *Physics of Fluids (1994.present)*. 2004; 16(9):3403-3414.

30. Richard D, Quéré D. Bouncing water drops. *EPL (Europhysics Letters)*. 2000;50(6):769.

31. Antonini C, Villa F, Bernagozzi I, Amirfazli A, Marengo M. Drop rebound after impact: The role of the receding contact angle. *Langmuir*. 2013; 29(52):16045-16050.

32. Bird JC, Dhiman R, Kwon H, Varanasi KK. Reducing the contact time of a bouncing drop. *Nature*. 2013;503(7476):385-388.

33. Richard D, Clanet C, Quéré D. Surface phenomena: Contact time of a bouncing drop. *Nature*. 2002;417(6891):811-811.

34. Liu Y, Moevius L, Xu X, Qian T, Yeomans JM, Wang Z. Pancake bouncing on superhydrophobic surfaces. *Nature Physics*. 2014.

35. Mohammadi M, Moghtadernejad S, Graham PJ, Dolatabadi A. Dynamic impact behavior of water droplet on a superhydrophobic surface in the presence of stagnation flow. *Journal of applied mechanics and material*. 2012; 232:267-272.

36. Jung S, Tiwari MK, Doan NV, Poulikakos D. Mechanism of supercooled droplet freezing on surfaces. *Nature communications*. 2012; 3:615.

37. Milne A, Amirfazli A. Drop shedding by shear flow for hydrophilic to superhydrophobic surfaces. *Langmuir*. 2009;25(24):14155-14164.

38. Ukiwe C, Kwok DY. On the maximum spreading diameter of impacting droplets on well-prepared solid surfaces. *Langmuir*. 2005;21(2):666-673.

39. Mao T, Kuhn D, Tran H. Spread and rebound of liquid droplets upon impact on flat surfaces. *AIChE J*. 1997; 43(9):2169-2179.

40. Attané P, Girard F, Morin V. An energy balance approach of the dynamics of drop impact on a solid surface. *Physics of Fluids (1994.present)*. 2007; 19(1):012101.

41. Pasandideh-Fard M, Qiao Y, Chandra S, Mostaghimi J. Capillary effects during droplet impact on a solid surface. *Physics of Fluids (1994.present)*. 1996; 8(3):650-659.

42. Roisman IV. Inertia dominated drop collisions. II. an analytical solution of the Navier–Stokes equations for a spreading viscous film. *Physics of Fluids (1994-present)*. 2009;21(5):052104.

43. Rioboo R, Marengo M, Tropea C. Time evolution of liquid drop impact onto solid, dry surfaces. *Exp Fluids*. 2002; 33(1):112-124.

44. Clanet C, Béguin C, Richard D, Quéré D. Maximal deformation of an impacting drop. *J Fluid Mech*. 2004; 517:199-208.

45. Harlow FH, Shannon JP. The splash of a liquid drop. *J Appl Phys*. 1967;38(10):3855-3866.

46. Engel OG. Waterdrop collisions with solid surfaces. *Journal of Research of the National Bureau of Standards*. 1955;54(5):281-298.

47. Yoon SS, Demosthenous B. Effects of air on splashing during a large droplet impact: Experimental and numerical investigations. *Atomization and Sprays*. 2006;16(8).

48. Liu J, Vu H, Yoon SS, Jepsen RA, Aguilar G. Splashing phenomena during liquid droplet impact. *Atomization and Sprays.* 2010;20(4).

49. Mundo C, Sommerfeld M, Tropea C. Droplet-wall collisions: Experimental studies of the deformation and breakup process. *Int J Multiphase Flow*. 1995;21(2):151-173.

50. Engel OG. Waterdrop collisions with solid surfaces. *Journal of Research of the National Bureau of Standards*. 1955;54(5):281-298.

51. Xu L, Zhang WW, Nagel SR. Drop splashing on a dry smooth surface. *Phys Rev Lett*. 2005;94(18):184505.

52. Vander Wal RL, Berger GM, Mozes SD. The splash/non-splash boundary upon a dry surface and thin fluid film. *Exp Fluids*. 2006; 40(1):53.59.

53. Xu L, Barcos L, Nagel SR. Splashing of liquids: Interplay of surface roughness with surrounding gas. *Physical Review E*. 2007; 76(6):066311.

54. Myers TG, Charpin JP. A mathematical model for atmospheric ice accretion and water flow on a cold surface. *Int J Heat Mass Transfer*. 2004; 47(25):5483-5500.

55. Pasandideh-Fard M, Chandra S, Mostaghimi J. A three-dimensional model of droplet impact and solidification. *Int J Heat Mass Transfer*. 2002;45(11):2229-2242.

56. Tabakova S, Feuillebois F. On the solidification of a supercooled liquid droplet lying on a surface. *J Colloid Interface Sci*. 2004; 272(1):225-234.

57. Pasandideh-Fard M, Bhola R, Chandra S, Mostaghimi J. Deposition of tin droplets on a steel plate: Simulations and experiments. *Int J Heat Mass Transfer*. 1998; 41(19):2929-2945.

58. Madejski J. Solidification of droplets on a cold surface. *Int J Heat Mass Transfer*. 1976;19(9):1009-1013.

59. Markworth AJ, Saunders JH. An improved velocity field for the madejski splat-quench solidification model. *Int J Heat Mass Transfer*. 1992; 35(7):1836-1837.

60. Mills AF. *Heat Transfer*. Boston MA: Irwin. 1992:183-186.

61. Aziz SD, Chandra S. Impact, recoil and splashing of molten metal droplets. *Int J Heat Mass Transfer*. 2000;43(16):2841-2857.

62. Poirier DR, Poirier E. Heat transfer fundamentals for metal casting. *The Minerals, Metals & Materials Society (TMS)*, 420 Commonwealth Dr, Warrendale, Pennsylvania 15086, USA, 1992.

63. Feuillebois F, Tabakova S, Radev S, Daru V. Entrained film of Ice–Water slurry with impinging supercooled water droplets. *Journal of Engineering Physics and Thermophysics*. 2014; 87(1):54-68.

64. Myers T, Charpin J, Thompson C. Slowly accreting ice due to supercooled water impacting on a cold surface. *Physics of Fluids (1994.present)*. 2002; 14(1):240-256.

65. Mishchenko L, Hatton B, Bahadur V, Taylor JA, Krupenkin T, Aizenberg J. Design of ice-free nanostructured surfaces based on repulsion of impacting water droplets. *ACS nano*. 2010; 4(12):7699-7707.

66. Poulikakos D. Conduction heat transfer. *Prentice Hall*; 1994.

67. Maitra T, Tiwari MK, Antonini C, et al. On the nanoengineering of superhydrophobic and impalement resistant surface textures below the freezing temperature. *Nano letters*. 2013; 14(1):172-182.

68. Sassen K, Dodd GC. Homogeneous nucleation rate for highly supercooled cirrus cloud droplets. *J Atmos Sci*. 1988; 45(8):1357-1369.

69. Wood SE, Baker MB, Swanson BD. Instrument for studies of homogeneous and heterogeneous ice nucleation in free-falling supercooled water droplets. *Rev Sci Instrum*. 2002;73(11):3988-3996.

70. Sastry S. Supercooled water: Going strong or falling apart? *Nature*. 1999;398(6727):467-469.

71. Varanasi KK, Hsu M, Bhate N, Yang W, Deng T. Spatial control in the heterogeneous nucleation of water. *Appl Phys Lett*. 2009;95(9):094101.

72. Farhadi S, Farzaneh M, Kulinich S. Anti-icing performance of superhydrophobic surfaces. *Appl Surf Sci*. 2011; 257(14):6264-6269.

73. Varanasi KK, Deng T, Smith JD, Hsu M, Bhate N. Frost formation and ice adhesion on superhydrophobic surfaces. *Appl Phys Lett*. 2010;97(23):234102.

74. Alizadeh A, Yamada M, Li R, et al. Dynamics of ice nucleation on water repellent surfaces. *Langmuir*. 2012;28(6):3180-3186.

75. Hallett J. The temperature dependence of the viscosity of supercooled water. *Proceedings of the Physical Society*. 1963;82(6):1046.

76. Biddle JW, Holten V, Sengers JV, Anisimov MA. Thermal conductivity of supercooled water. *Physical Review E*. 2013; 87(4):042302.

77. Khedir KR, Kannarpady GK, Ishihara H, et al. Temperature-dependent bouncing of super-cooled water on teflon-coated superhydrophobic tungsten nanorods. *Appl Surf Sci*. 2013; 279:76-84.

78. Tsai P, Pacheco S, Pirat C, Lefferts L, Lohse D. Drop impact upon micro-and nanostructured superhydrophobic surfaces. *Langmuir*. 2009;25(20):12293-12298.

79. Maitra T, Antonini C, Tiwari MK, et al. Supercooled water drops impacting superhydrophobic textures. *Langmuir*. 2014; 30(36):10855-10861.

80. Zheng L, Li Z, Bourdo S, et al. Exceptional superhydrophobicity and low velocity impact icephobicity of acetone-functionalized carbon nanotube films. *Langmuir*. 2011; 27(16):9936-9943.

81. Nosonovsky M, Bhushan B. Energy transitions in superhydrophobicity: Low adhesion, easy flow and bouncing. Journal of Physics: *Condensed Matter*. 2008; 20(39):395005.

82. Rioboo R, Voué M, Vaillant A, De Coninck J. Drop impact on porous superhydrophobic polymer surfaces. *Langmuir*. 2008; 24(24):14074-14077.

83. Wang F, Li C, Lv Y, Lv F, Du Y. Ice accretion on superhydrophobic aluminum surfaces under low-temperature conditions. *Cold Reg Sci Technol*. 2010; 62(1):29-33.

84. Meuler AJ, McKinley GH, Cohen RE. Exploiting topographical texture to impart icephobicity. *ACS nano*. 2010; 4(12):7048-7052.

85. Meuler AJ, Smith JD, Varanasi KK, Mabry JM, McKinley GH, Cohen RE. Relationships between water wettability and ice adhesion. *ACS Applied Materials & Interfaces.* 2010;2(11):3100-3110.

86. Richard D, Quéré D. Bouncing water drops. *EPL (Europhysics Letters)*. 2000;50(6):769.

87. Abràmoff MD, Magalhães PJ, Ram SJ. Image processing with ImageJ. *Biophoton Int.* 2004; 11(7):36-42.

88. Duguid H, Stampfer Jr J. The evaporation rates of small, freely falling water drops. *J Atmos Sci*. 1971; 28(7):1233-1243.

89. Luxford G. Experimental and modelling investigation of the deformation, drag and break-up of drizzle droplets subjected to strong aerodynamics forces in relation to SLD aircraft icing. 2005.

90. Speedy RJ. Thermodynamic properties of supercooled water at 1 atm. *J Phys Chem.* 1987; 91(12):3354-3358.

91. Hacker PT. Experimental values of the surface tension of supercooled water. 1951.

92. Hallett J. The temperature dependence of the viscosity of supercooled water. P*roceedings of the Physical Society*. 1963;82(6):1046.

93. Glycerine Producers' Association. Physical properties of glycerine and its solutions. *Glycerine Producers' Association*; 1963.

94. Vadillo D. Caractérisation des phénomènes hydrodynamiques lors de l'impact de gouttes sur différents types de substrats. 2007. *PhD dissertation.*

95. Hocking L, Rivers A. The spreading of a drop by capillary action. *J Fluid Mech*. 1982; 121:425-442.

96. Duvivier D, Seveno D, Rioboo R, Blake T, De Coninck J. Experimental evidence of the role of viscosity in the molecular kinetic theory of dynamic wetting. *Langmuir*. 2011; 27(21):13015-13021.

97. Seeley LH. Heterogeneous nucleation of ice from supercooled water.; 2001. *PhD dissertation.*

98. Pruppacher HR, Klett JD, Wang PK. Microphysics of clouds and precipitation. 1998.

99. Hsieh JS. Principles of thermodynamics. McGraw-Hill Washington; 1975.

100. Worster MG. Solidification of fluids. Lent term. 2009-2010.

101. Tarshis L, Walker J, Gigliotti M. Solidification. *Annual Review of Materials Science.* 1972;2(1):181-216.

102. Jung S, Dorrestijn M, Raps D, Das A, Megaridis CM, Poulikakos D. Are superhydrophobic surfaces best for icephobicity? *Langmuir.* 2011; 27(6):3059-3066.

103. Zobrist B, Koop T, Luo B, Marcolli C, Peter T. Heterogeneous ice nucleation rate coefficient of water droplets coated by a nonadecanol monolayer. *The Journal of Physical Chemistry C.* 2007; 111(5):2149-2155.

104. Yang G, Guo K, Li N. Freezing mechanism of supercooled water droplet impinging on metal surfaces. *Int J Refrig.* 2011;34(8):2007-2017.

105. Feng L, Li S, Li Y, et al. Super-hydrophobic surfaces: From natural to artificial. *Adv Mater.* 2002;14(24):1857-1860.

106. Kroger DG and Branfield GR. Evaporation-from a water surface: Theory and experiment. *R& D journal.* 2007; 23(3):5-11.

107. Mohammadi M, Attarzadeh M, Tembely M, Dolatabadi A. Dynamic of water droplet impacting on a hydrophilic surface accompanied with stagnation flow. *4ᵗʰ joint US-European fluids engineering division summer meeting.* 2014: FEDSM2014-21760.V01AT05A010.

108. Mohammadi M, Moghtadernejad S, Graham PJ, Dolatabadi A. Dynamic impact behavior of water droplet on a superhydrophobic surface in the presence of stagnation flow. *Journal of applied mechanics and material.* 2012;232:267-272.

109. Antonini C, Bernagozzi I, Jung S, Poulikakos D, Marengo M. Water drops dancing on ice: How sublimation leads to drop rebound. *Phys Rev Lett*. 2013; 111(1):014501.

110. Wachters L, Westerling N. The heat transfer from a hot wall to impinging water drops in the spheroidal state. *Chemical Engineering Science.* 1966; 21(11):1047-1056.

111. Chandra S, Avedisian C. On the collision of a droplet with a solid surface. *Proceeding of royal society of a mathematical, physical and engineering sciences.* 1991; 432(1884):13.41.

112. Levi-Hevroni D, Levy A, Borde I. Mathematical modeling of drying of liquid/solid slurries in steady state one-dimensional flow. *Drying Technol*. 1995; 13(5-7):1187-1201.

113. Touloukian Y, Saxena S, Hestermans P. Thermophysical Properties of Matter-the TPRC Data Series.Volume 11.Viscosity. 1975.

114. McQuillan F, Culham J, Yovanovich M. Properties of dry air at one atmosphere. University of Waterloo-Microelectronics Heat Transfer Laboratory Report UW MHTL. 1984;8406.

115. Eddi A, Winkels KG, Snoeijer JH. Short time dynamics of viscous drop spreading. *Physics of Fluids (1994.present)*. 2013;25(1):013102.

116. Duvivier D, Seveno D, Rioboo R, Blake T, De Coninck J. Experimental evidence of the role of viscosity in the molecular kinetic theory of dynamic wetting. *Langmuir*. 2011;27(21):13015-13021.

117. Pasandideh-Fard M, Bhola R, Chandra S, Mostaghimi J. Deposition of tin droplets on a steel plate: Simulations and experiments. *Int J Heat Mass Transfer*. 1998; 41(19):2929-2945.

118. Maali A, Bhushan B. Measurement of slip length on superhydrophobic surfaces. *Philos Trans A Math Phys Eng Sci*. 2012; 370(1967):2304.2320.

119. Choi C, Ulmanella U, Kim J, Ho C, Kim C. Effective slip and friction reduction in nanograted superhydrophobic microchannels. *Physics of Fluids (1994.present)*. 2006;18(8):087105.

120. Sastry S. Water: Ins and outs of ice nucleation. *Nature*. 2005;438(7069):746-747.

121. Brown PP, Lawler DF. Sphere drag and settling velocity revisited. J Environ Eng. 2003; 129(3):222.231.

122. Kobus C, Shumway G. An experimental investigation into impinging forced convection heat transfer from stationary isothermal circular disks. *Int J Heat Mass Transfer*. 2006;49(1):411-414.

123. Gao J, Szoszkiewicz R, Landman U, Riedo E. Structured and viscous water in subnanometer gaps. *Physical Review B*. 2007; 75(11):115415.

Appendices

Appendix A

Drag force analysis of moving liquid droplet through airflow

Understanding the net effect of air flow on an impacting water droplet is carried out by having same droplet impact velocity with and without air flow. In analysis of the stagnation flow it was shown that droplet before impact is imposed to the normal force of incoming air flow which might vary droplet impinging velocity. Therefore, appropriate experimental test set up strategies were taken into considerations. Associated drag force of moving liquid droplet through air flow is approximated by the equation (A.1) which assumes spherical shape of droplet is maintained through entire domain. Calculation of the drag force is important as droplet impact velocity with and without air flow should be equal in order to have a same droplet Weber and Reynolds numbers. These two aforementioned dimensionless numbers are used for calculation of the maximum spreading diameter. For spherical particle exposed to air flow drag force coefficient is presented by equation (A.1).[121]

$$C_D = \frac{24}{Re}(1 + 0.150Re^{0.681}) + \frac{0.407}{1+\frac{8710}{Re}} \qquad\qquad Re < 2 \times 10^5 \qquad\qquad (A.1)$$

Analysis of droplet moving through air shows that if relative Weber number (i.e. $\frac{\rho_{air}\,(U_g - U_d)\,D_d}{\gamma_{lv}}$) become less than 3. Droplet shape is almost spherical. However, it was confirmed that drag coefficient is increased about 15 % to that of pure spherical solid object.[89] Therefore, for air velocity up to 10 m/s at room temperature condition, drag force coefficient is 0.42. Consequently, associated drag force due to the imposed air flow is illustrated by equation (A.2):

$$F_{Drag} = \frac{1}{2}\rho_{air}(U_{air} - U_d)^2 \; 1.15C_D \frac{\pi D_d^2}{4} \qquad\qquad (A.2)$$

Calculated amount of imposed drag force for the worst case scenario (i.e. the largest droplet size and relative velocity between air and droplet) at room temperature condition becomes 1.2 e-4. Therefore, increased velocity is about 0.07 m/s for water droplet size as large as 2.6 mm at room temperature condition having velocity up to 1.2 m/s for 5.5 ms exposure time to airflow. In the following, mechanism of releasing water droplet exposed to air flow is explained.

As demonstrated in figure (A.1), a small pipe was attached to the needle which was long enough to be reached almost 1 mm above nozzle throat. It is clear that droplet dynamics is not much affected by the air flow at domain 1.
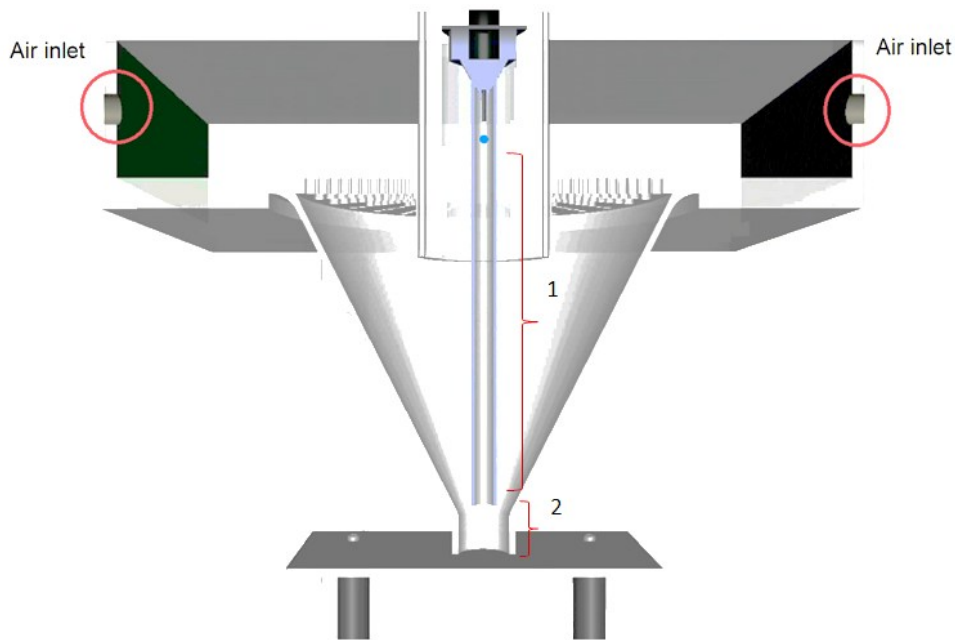

Figure A.1: Schematic of experimental set up for injection of droplet in the stagnation point.

In experimental test, the measured impact velocity was based on the few sequential images of moving droplet above the substrate which was recorded with high speed camera. It showed that imposed drag force between domain 1 and 2 cancel each other and droplet impact velocity was almost identical and even in the lower range of impact velocity compare to still air case. This topic is elaborated in detail in the following discussion.

181

By using particles equation of motions, the accessioned increased velocity by incoming air flow in domain 2 was almost 0.07 m/s for 5.5 ms air-droplet exposure time. This small increase in velocity results in a slight increase in the droplet Weber number (from 88 to 95 for droplet size and impact velocity up to 2.6 mm and 1.6 m/s, respectively). However, carefully measurement of droplet impact velocity accompanied with air flow with high speed imaging experiment shows that impinging droplet velocity is almost identical or even slightly smaller with that of still air. This phenomenon can be referred to the effect of very small air suction through the small pipe connected to the droplet generator system. It can be more argued that based on the results of numerical simulation reverse velocity was also observed and it was small (see appendix B). In presence of small suction velocity almost impinging velocity become similar with that of still air having a good agreement with experimental results. To this end, all aforementioned calculations were performed for highest air velocity up to 10 m/s. Indeed, where incoming air velocity becomes lower, deviation of the impinging droplet velocity with that of still air is insignificant (i.e. completely locates in the precision error of experiment).

Appendix B

Numerical simulation of stagnation flow

Characterization of air profile of stagnation air flow at the nozzle exit was carried out by numerical simulation of one-phase air flow. Modeling of the geometry was accomplished with ICEM CFD with almost 400000 tetrahedral meshes, as demonstrated in figure (B.1). Mesh resolution in the vicinity of nozzle throat was 500 μm in order to capture air profile precisely. The numerical simulation was carried out by non-commercially use of ANSYS-FLUENT 14 software. Different

turbulent models were evaluated through available options in the software. Here, results of standard k–ε model are presented. Numerical simulation results has shown good agreements with that of experimental measurements around the core of nozzle exit which is a matter of interest in the current study. As shown in figure (B.2), uniform air velocity up to 10 m/s was observed which is used for quantitative evaluation of droplet wetting dynamics in the current study.
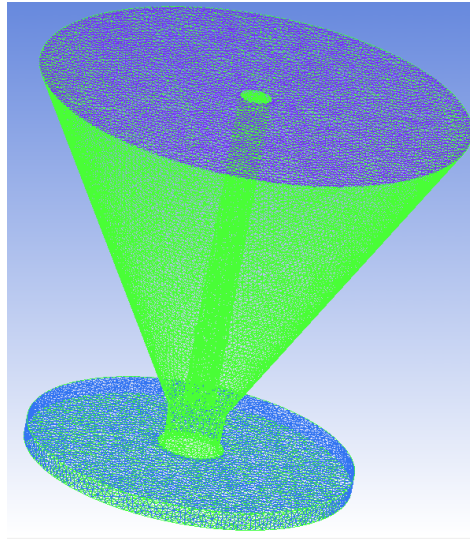

Figure B.1: Mesh generation using ICEM CFD 14. Almost 400000 tetrahedral meshes have been used for proper capturing of air jet velocity profile.

Contours of Velocity Magnitude (m/s)   Velocity Vectors Colored By Velocity Magnitude (m/s)
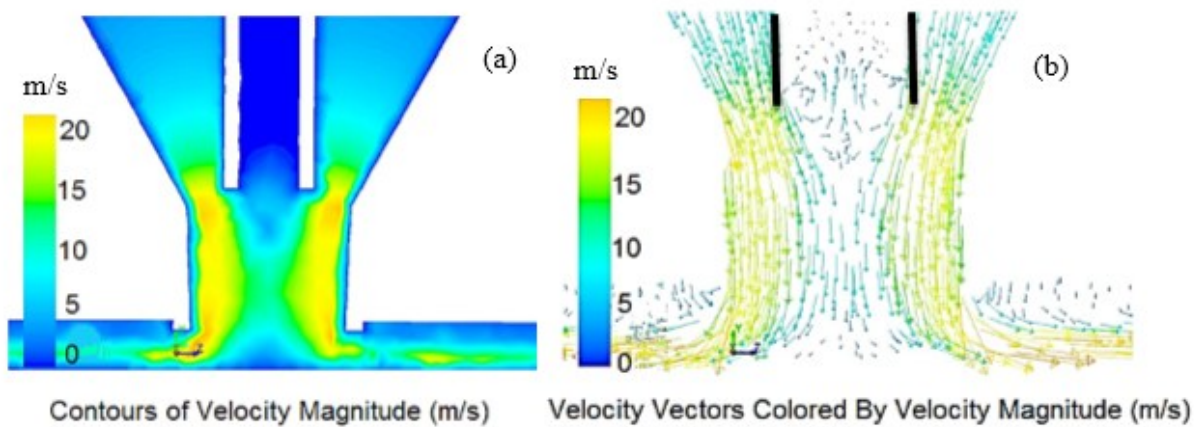
Figure B.2: Numerical simulation of stagnation air flow of present experimental set up. a) Contours of velocity magnitude, b) velocity vectors showed by velocity magnitude.

Appendix C

C.1 Solid-liquid interface temperature, analytical solution

Solid-liquid interface temperature is obtained by transient solution of conduction equations within droplet to substrate, as demonstrated in equations (C.1) and (C.2). Therefore, appropriate boundary and initial conditions are required in order to obtain the solution.

$$\frac{\partial T_{pa}(x,t_c)}{\partial t_c} = \alpha_{pa} \frac{\partial^2 T_{pa}(x,t_c)}{\partial x^2} \text{, for region between } 0 < x < h. \tag{C.1}$$

$$\frac{\partial T_w(x,t_c)}{\partial t_c} = \alpha_w \frac{\partial^2 T_w(x,t_c)}{\partial x^2}, \text{ for region between } x > h. \tag{C.2}$$

The boundary and initial conditions for water droplet and semi post-air domain are presented in the following. As highlighted in the main context of the current study, two boundaries and one initial conditions are needed for each domain.[2]

Boundary and initial conditions for semi post-air domain are like the following:

First boundary condition: $T_{pa}(0,t) = T_{substrate}$, $x = 0$ (C.3)

Second boundary condition: $T_{pa}(h,t) = T_w(h,t)$, $x = h$ (C.4)

First initial condition: $T_{pa}(x < h, 0) = T_{substrate}$, $t = 0$ (C.5)

Boundary and initial conditions for water domain are like following:

First boundary condition: $T_w(h,t) = T_{pa}(h,t)$, $x = h$ (C.6)

Second boundary condition: $T_w(\infty,t) = T_{droplet}$, $x = infinity$ (C.7)

First initial condition: $T_w(x > h, 0) = T_{droplet}$, $t = 0$ (C.8)

It is clear that subsequent solution of two transient conduction equations become similar at the interface, as demonstrated in the boundary conditions (C.4) and (C.6) which are the same. The following equations can be defined in order to reduce the order of equation.

$$\theta_{pa}(x,t) = T_{pa}(x,t) - T_{drop} \tag{C.9}$$

$$\theta_w(x,t) = T_w(x,t) - T_{drop} \qquad (C.10)$$

Due to the fact that there are infinity boundary conditions, the best way for solving partial differential equation is defining the similarity variable which make PDE to ODE like below:

$$\eta_{pa} = \frac{x}{2\sqrt{\alpha_{pa}t_c}}, \eta_w = \frac{x}{2\sqrt{\alpha_w t_c}} \qquad (C.11)$$

Inserting equations (C.9), (C.10) and (C.11) to equations (C.1) and (C.2) and by definition of chain derivatives following second order ODE are obtained.

$$\frac{d^2\theta_{pa}}{d\eta_{pa}^2} + 2\eta_{ns}\frac{d\theta_{pa}}{d\eta_{pa}} = 0 \qquad (C.12)$$

$$\frac{d^2\theta_w}{d\eta_w^2} + 2\eta_w\frac{d\theta_w}{d\eta_w} = 0 \qquad (C.13)$$

Equations (C.12) and (C.13) can be solved by defining variable S like below:

$$\frac{d\theta_{pa}}{d\eta_{pa}} = S_{pa}, \frac{d\theta_w}{d\eta_w} = S_w \qquad (C.14)$$

These substitutions make second order equation in to the first order equation which can be solved analytically by method of separation of variables, as demonstrated in equations (C.15) and (C.16).

$$\frac{dS_{pa}}{d\eta_{pa}} + 2\eta_{pa}S_{pa} = 0 \qquad (C.15)$$

$$\frac{dS_w}{d\eta_w} + 2\eta_w S_w = 0 \qquad (C.16)$$

$$S_{pa} = \frac{d\theta_{pa}}{d\eta_{pa}} = C_{pa}\exp(-\eta_{pa}^2) \qquad (C.17)$$

$$S_w = \frac{d\theta_w}{d\eta_w} = C_w\exp(-\eta_w^2) \qquad (C.18)$$

Therefore, solution of equation (C.17) is defined based on the error function shown in equations (C.19) and (C.20).

$$\theta_{pa}(\eta) - \theta_{pa}(0) = \int_0^\eta C_{pa}\exp(-\eta_{pa}^2)\,d\eta \qquad (C.19)$$

$$\theta_{pa}(\eta) - \theta_{pa}(0) = a_{ps}erf(\eta_{pa}) \qquad (C.20)$$

Which, a_{pa}, is new integral constant defined by applying associated boundary conditions.

By substitution of equation (C. 9) to (C.20), following equation is presented.

$$T_{pa}(\eta) - T_{pa}(0) = a_{pa}erf(\eta_{pa}) \tag{C.21}$$

However, equations (C.4) and (C.6) are the same at x=h and t=0.

$T_{pa}(\eta) = T_{drop}$ and $T_{pa}(0) = T_{substrate}$, therefore, the following equation is derived:

$$T_d - T_{sub} = a_{pa}erf(\infty) \xrightarrow{yields} a_{pa} = T_d - T_{sub} \tag{C.22}$$

Transient temperature profile in the semi post-air domain is presented by equation (C.23) by recalling equation (C.21) and knowing $T_{pa}(0) = T_{substrate}$

$$T_{pa}(\eta) - T_{pa}(0) = T_d - T_d + a_{pa}erf(\eta_{pa}) \tag{C.23}$$

Therefore, by substitution equations (C.22) in (C.23), Transient conduction equation for semi post-air domain is derived, as demonstrated in equation (C.26) which, $erfc(\eta)$, is a complementary error function.

$$T_{pa}(\eta) = T_d + T_{sub} - T_d + (T_d - T_{sub})erf(\eta_{pa}) \tag{C.24}$$

$$T_{pa}(\eta) = T_d + (T_{sub} - T_d)(1 - erf(\eta_{pa})) \tag{C.25}$$

$$T_{pa}(\eta) = T_d + (T_{sub} - T_d)erfc(\eta_{pa}) \tag{C.26}$$

Same as aforementioned procedure for solving transient conduction equation in semi post-air domain, solution of equation (C.18) is also defined based on the error function. Transient conduction equation in water domain can be presented by integrant splitting in equation (C.27).

$$\theta_w(\eta) - \theta_w(h) = \int_h^\eta C_w \exp(-\eta_w^2)\, d\eta \tag{C.27}$$

$$\theta_w(\eta) - \theta_w(h) = \int_h^0 C_w \exp(-\eta_w^2)\, d\eta + \int_0^\eta C_w \exp(-\eta_w^2)\, d\eta \tag{C.28}$$

$$\theta_w(\eta) - \theta_w(h) = -a_w\, erf(h_w) + a_w\, erf(\eta_w) \tag{C.29}$$

Which, a_w, is new integral constant defined by applying associated boundary conditions.

From equation (C.7) , $x \to \infty, \eta \to \infty$, $T_w(\infty) = T_{drop}$, and also from equation (C.10), following

equation is presented,

$$\theta_w(\infty) = T_{drop} - T_{drop} = 0 \qquad\qquad (C.30)$$

It is worth stressing that after defining similarity variable in equation (C.11), variables in equation

(C.10) (i.e. x and t) are substituted with one variable defined η.

Furthermore, from equation (C.10), water temperature at $\eta = h$, is presented like following:

$$\theta_w(h) = (T_w(h) - T_{drop}) \qquad\qquad (C.31)$$

Inserting equations (C.30) and (C.31) into (C.29), following useful equation is derived.

$$- (T_w(h) - T_{drop}) = -a_w \operatorname{erf}(h) + a_w = a_w[1 - \operatorname{erf}(h)] = a_w erfc(h_w) \qquad (C.32)$$

Form boundary conditions (C.7) or (C.6) temperatures at interface of two boundaries are similar;

$T_w(h) = T_{pa}(h)$. Therefore, by recalling equation (C.26), following equation is emerged.

$$T_w(h) = T_d + (T_{sub} - T_d)erfc(h_{pa}) \qquad\qquad (C.33)$$

$$T_w(h) - T_d = (T_{sub} - T_d)erfc(h_{pa}) \qquad\qquad (C.34)$$

Recalling equation (C.32) and using equation (C.34) following formula are derived.

$$- [(T_{sub} - T_d)erfc(h_{pa})] = a_w erfc(h_w) \qquad\qquad (C.35)$$

$$a_w = - [(T_{sub} - T_d)]\frac{erfc(h_{pa})}{erfc(h_w)} \qquad\qquad (C.36)$$

Recalling equation (C.29) and using equation (C.10), following equation is presented.

$$T_w(\eta) - T_w(h) = -a_w \, erf(h_w) + a_w \, erf(\eta_w) \qquad\qquad (C.37)$$

On the other hand from equation (C.32), (i.e. $T_w(h) = T_{drop} - a_w erfc(h_w)$), and substitution

into equation (C.37), equation (C.38) is illustrated.

$$T_w(\eta) = T_{drop} - a_w[erfc(h_w) + erf(h_w) - erf(\eta_w)] = T_{drop} - a_w[1 - erf(\eta_w)] = T_{drop} -$$

$$a_w[erfc(\eta_w)] \qquad\qquad (C.38)$$

$$T_w(\eta) = T_{drop} + [(T_{sub} - T_d)] \frac{erfc(h_{pa})}{erfc(h_w)} . erfc(\eta_w) \tag{C.39}$$

Therefore, interface temperature can be obtained by choosing $\eta = h$ in equation (C.39), as demonstrated in equation (C.40).

Therefore, transient temperature distribution within water droplet is also presented in equation (C.41).

$$T_{w-interface}(h, t_c) = T_{drop} + [(T_{sub} - T_d)] erfc\left(\frac{h_{pa}}{2\sqrt{\alpha_{pa}t_c}}\right) \tag{C.40}$$

$$T_w(x_w, t_c) = T_{drop} + [(T_{sub} - T_d)] \frac{erfc\left(\frac{h_{pa}}{2\sqrt{\alpha_{pa}t_c}}\right)}{erfc\left(\frac{h_w}{2\sqrt{\alpha_w t_c}}\right)} . erfc\left(\frac{x_w > h}{2\sqrt{\alpha_w t_c}}\right) \tag{C.41}$$

C.2 Gas-liquid interface temperature

In the following, more explanation of derived predictive model of gas-liquid interface temperature is presented. As illustrated in equation (C.42), the final form of aforementioned predictive model are incorporated with some variables needed to be discussed here. These variables are mass flux ($\dot{m}_{f,eva}$), maximum spreading diameter (D_{max}), and convective heat transfer coefficient for stagnation flow (h_g), respectively.

$$T_{g-w,interface} = \left(h_g T_g + 1.5 \frac{k_w D_{max}^2 T_{s-w,interface}}{D^3} - \Delta H_v \dot{m}_{f,eva}\right) / \left(h_g + 1.5 \frac{k_w D_{max}^2}{D^3}\right) \tag{C.42}$$

The first variable is related to the mass flux illustrated in equation (C.43) which involves variables namely density of saturated air at water interface (ρ_{s-aw}), specific heat of water vapor for supercooled droplet (c_{pwa}), radial air velocity (V_{air}), vapor pressure at gas-water interface (P_{vo}), vapor pressure in the air (P_{vi}) and average surface temperature of water and ambient gas (T_{oi}).

$$\dot{m}_{f,eva} \approx [0.0093/\rho_{s-aw}c_{pwa} + 6.7 \times 10^{-6} V_{air}] \frac{(P_{vo} - P_{vi})}{T_{oi}} \tag{C.43}$$

Information regarding T_{oi}, c_{pwa}, P_{vo} and P_{vi} can be found in the main context of the current study.

Density of saturated air at water interface is demonstrated by equation (C.44).[106]

$$\rho_{s-aw} = (1 + W_o).\left[1 - \frac{W_o}{W_o + 0.622}\right].P_{atm}/(287.08T_o) \tag{C.44}$$

Where, W_o , is humidity ratio of water vapor at interface of water and it is shown by equation (C.45).

$$W_o = 0.622P_{vo}/(P_{atm} - P_{vo}) \tag{C.45}$$

In equation (C.44) and (C.45) P_{atm}, P_{vo} are vapor pressure at the interface and atmospheric pressure, respectively. Water vapor pressure at water interface is represented by surface temperature of water by equation (C.46).

$$P_{vo} \approx 2.368745 \times 10^{11} \exp(-\frac{5406.1915}{T_o}) \tag{C.46}$$

Where,(T_o) is the surface temperature of water at interface which is temperature of droplet. In the next step, air radial velocity (i.e. V_{air}) is elaborated in the following.

It was confirmed that air flow enhances the evaporation rate.[36] In equation (C.43), the effect of air velocity was added in equation in order to distinguish pure diffusive evaporation with that of forced convective evaporation. As demonstrated in figure (C.1), radial air velocity must be taken into account due to the fact that incoming stagnation flow is exposed to the cylindrical flattened shape of spread droplet. Therefore, an average value of radial velocity in the viscous layer (i.e. boundary layer, $f'(\eta) = 0.7$) was taken into account, as demonstrated in equation (C.47).

$$V_{air} = V_{r@D_{max}} = 0.7a\frac{D_{max}}{2} \tag{C.47}$$

Coefficient of a is obtained from the numerical simulation of impinging air flow. For air velocity up to 10 m/s this coefficient is extracted from figure (C.1) by linear growth approximation which is around 1700 (1/s).[107]

Having discussed about variables in the mass flux equation, elaboration on the maximum spreading diameter and convective heat transfer coefficient are presented in the following.
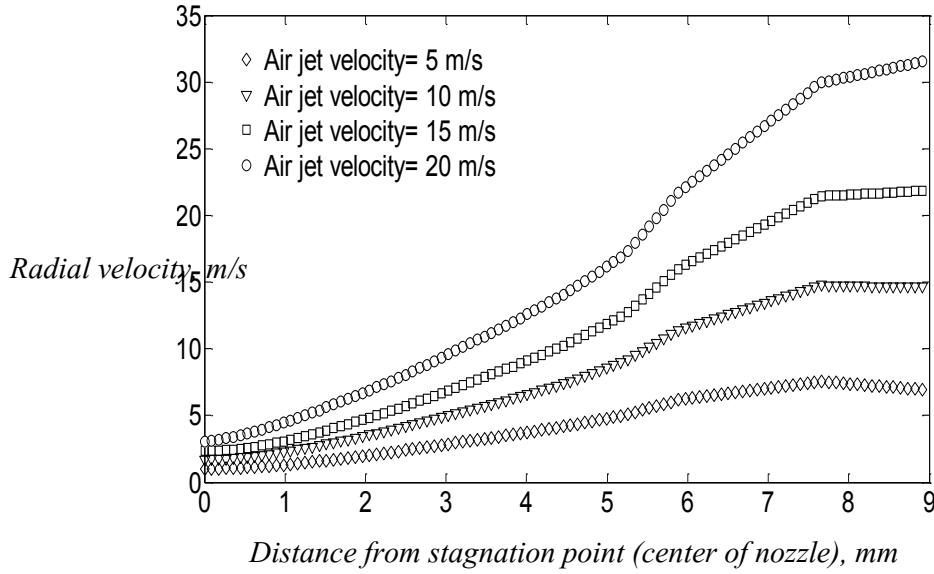

Figure C.1: Variation of radial velocity against distance from stagnation point as a function of air jet velocity.[107]

Maximum spreading diameter of an impacting water droplet can be inserted in equation (C.42) by energy based model of Passandideh-Fard et al.[41] for hydrophilic and hydrophobic surfaces, as shown in equation (C.48). While for superhydrophobic surface proposed correlation of Clanet et al.[44] is used, as demonstrated in equation (C.49).

$$D_{max} = D\sqrt{\frac{We+12}{3(1-cos\theta_{adv})+4\frac{We}{\sqrt{Re}}}}$$
(C.48)

$$D_{max} = 0.9D\,We^{0.25}$$
(C.49)

The only remaining parameter which has not been discussed yet is convective heat transfer coefficient of incoming stagnation flow. In order to properly obtain gas-water interface temperature, convective heat transfer coefficient of an impinging gas flow is required to be determined. New correlation of convective heat transfer coefficient of an impinging air flow for

190

wide range of Reynolds number from 10 to 100000 (Pr=0.72) was experimentally determined.[122] , The Reynolds number is calculated based on the impinging disk diameter (i.e. from 5.2 mm to 19.9 mm) which is demonstrated by equation (C.50). In fact, the aforementioned experimental study covered variety of length scale (i.e. disk diameter) which is in the range of the maximum spreading diameter of an impacting water droplet (from 7.2 mm for SHS to 8.8 mm for the aluminum surface). The following correlation of Nusselt number is obtained based on the dimensionless Reynolds and Prandtl numbers, as demonstrated in equations (C.50) to (C.53).

$$Re = \frac{\rho_g \, D_{max} \, U_{g,jet}}{\mu_g} \qquad\qquad (C.50)$$

$$Pr = \frac{\mu_g \, c_{p,g}}{k_g} \qquad\qquad (C.51)$$

$$Nu = 0.966 \, Re^{0.46} \, Pr^{\frac{1}{3}} \qquad\qquad (C.52)$$

$$h_g = \frac{Nu.k_g}{D_{max}} \qquad\qquad (C.53)$$

C.3 Droplet wetting dynamics model with effect of the heterogeneous ice nucleation mechansim

Heterogeneous ice nucleation phenomenon is occurred on superhydrophobic surfaces if surface temperature maintained below the critical temperature of ice nucleation for bouncing droplets (i.e. -24 °C). Bahaduer et al.[2] showed that wetting dynamics of an impacting supercooled water droplet on superhydrophobic surfaces is changed through the variation of surface-water contact angle. Indeed, by propagation of ice nuclei underneath of supercooled water and substrate, superhydrophobicity breakdown is happened and surface-water contact angle became as-low as hydrophilic surfaces.

By consideration of variation of contact angle with temperature, [2] the final form of the droplet wetting dynamics considering the effect of heterogeneous ice nucleation is presented by equation (C.54).

$$\frac{d^2R}{dt^2} + \left[1 - C\phi_o t_c^2 \exp\left(f(T_{interface})\right)\right]R = 0 \qquad \text{(C.54)}$$

Where C, ϕ_o, t_c are empirical and theoretical term regarding ice propagation in supercooled water droplet[65], ratio of wet area to base area of substrate and total contact time of an impacting water droplet, respectively.

Additionally, the function $f(T_{interface})$ is approximated by the relation (C.55).[65]

$$f(T_{interface}) \approx \frac{-T_m^2}{((T_m - T_{s-l})^2 T_{s-l})} \qquad \text{(C.55)}$$

The theoretical value of coefficient, C, which is originated from the classical nucleation theory is presented by equation (C.56).[2]

$$C = \pi K(T)U^2 \qquad \text{(C.56)}$$

Where U is the speed of freezing front propagated through water, demonstrated in equation (C.57).[66] $K(T)$ is the kinematic prefactor (i.e. kinematic rate) of ice nucleation phenomenon. For small degree of supercooling water droplet (for the current study above -5.5 °C) it is assumed to be constant $10^{-24} m^{-2}s^{-1}$.[2]

$$U = \left(4\alpha_{ice}\frac{C_{p-ice}}{2H_{f,l}}(T_m - T_{sub})\left[1 + \frac{k_w}{k_{ice}}\sqrt{\frac{\alpha_w}{\alpha_{ice}}}\frac{(T_m - T_{droplet})}{(T_m - T_{sub})}\right]\right)^{1/2} \qquad \text{(C.57)}$$

In equation (C.57) , α_{ice}, is the thermal diffusivity of ice, α_w, is the thermal diffusivity of supercooled water, C_{p-ice}, is the specific heat of ice, $H_{f,l}$, is the latent heat of fusion, T_m, is the melting point temperature of water, T_{sub}, is the substrate temperature, k_{ice}, is the thermal conductivity of ice and k_w, is the thermal conductivity of supercooled water at the specific temperature.

In addition, it was assumed that formed ice nuclei is propagated as an hemispherical cluster. Therefore, transient $\emptyset$ ratio with expanding ice cap with radius, r, is presented in equation (C.58).[2]

$$\emptyset(t) = 2\pi\emptyset_o \int_0^t J(t)[r(t)]^2 dt \qquad (C.58)$$

Where ice cap radius is a production of speed of freezing front to the solidification time as demonstrated in equation (C.59).[2]

$$r(t_c - \hat{t}) = U(T_{sub}, T_{droplet}, T_m)\sqrt{(t_c - \hat{t})} \qquad (C.59)$$

As it was experimentally observed,[65] due to rapid process of spreading phase, droplet pinning is not happened but might face freezing process at retraction phase if solid-liquid interface temperature is below the critical temperature of heterogeneous ice nucleation for the bouncing droplets.[1] Therefore, equation (C.54) is used for an impacting droplet in the retraction phase.

It is worth stressing that theory of classical ice nucleation rate is not well established yet due to the fact that experimental detection of ice growth rate is referred to the macroscopic level while at this time ice nuclei has already been grown.[74] On the other hand, after formation of macroscopic level of ice-water interface, solidification time was shown to be substantially slower than to that of classical nucleation theory. This discrepancy originates form ice-water molecular diffusivity and also release of latent heat of fusion during phase change which systematically changes nucleation rate in comparison with theoretical model. In fact, variation in the hydrogen structure close to substrate[123] along with aforementioned parameters results in qualitatively usage of this theory rather than quantitative one which needs a modification on the kinetic coefficient prefactor.[65,102] Therefore, it can be anticipated that same issue is present for homogeneous ice nucleation mechanism where air flow is present.

Appendix D

D.1 Isothermal droplet impact dynamics exposed to airflow on hydrophilic and hydrophobic surfaces

Phenomenology of droplet impact on solid substrates in still air condition was profoundly elaborated in previous studies. Here, effect of the stagnation air flow on an impacting water droplet on aluminum and Teflon substrate is presented. When air flow is presents dynamics of spreading and retraction might be systematically changed. More elaboration of stagnation air flow can help us to quantitatively explain different behavior of retraction phases especially for aluminum substrate which has a lowest retraction capillary force compare with other substrates (i.e. Teflon, sanded Teflon and coated superhydrophobic surface).

As discussed in chapter 4, for large droplet impact velocity up to 2.5 m/s which has a large maximum spreading diameter, non-recoiling phase was observed for aluminum substrate where air velocity is increased up to 10 m/s. However, the effect of stagnation air flow for small droplet impact velocity having different droplet sizes from 1.65 to 2.6 mm has not been elaborated yet which is discussed in the following. Further evaluation of droplet wetting behavior which is directly correlated by droplet Weber and Reynolds numbers can be accomplished by experimentation of various droplet sizes and droplet impact velocity up to 1.2 m/s. Different droplet sizes ranging from 1.65 to 2.6 mm were chosen to demonstrate the importance of maximum spreading diameter on the recoiling behavior of an impacting droplet where air flow is present. As demonstrated in figure (D.1), due to the smaller maximum spreading diameter compare to transitional cases (i.e. non-recoiling phases) resultants shear and normal forces of airflow cannot change the wetting behavior of an impacting water droplet. In fact, the resultant shear force is not well developed at the small maximum spreading diameters, as shear force of airflow is increased based on the radial distance from the stagnation point. After discussion regarding wetting behavior

of an impacting water droplet on hydrophilic surface, the effect of stagnation air flow on a

hydrophobic surface (i.e. Teflon substrate) is discussed in the following.
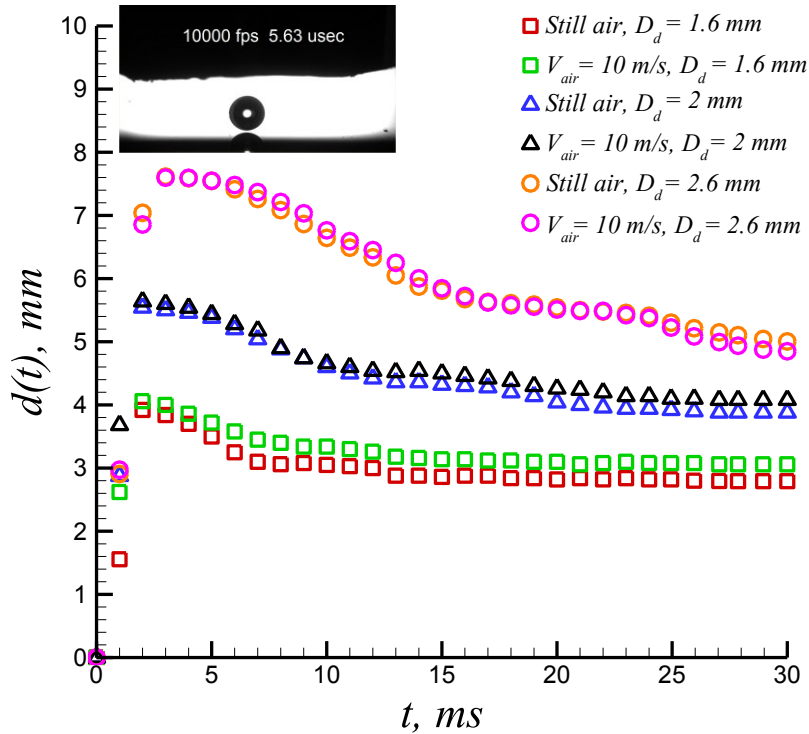

Figure D.1: Temporal evolution of an impacting water droplet on aluminum substrate at various droplet sizes ranging from 1.65 to 2.6 mm at impact velocity up to 1.2 m/s. Corresponding Weber and Reynolds numbers are 30 to 50 and 1980 to 3120, respectively.

It is appreciated to see droplet impact behavior exposed to air flow where hydrophobicity of

surface is increased. Therefore, similar experiments to that of aluminum one were carried out for

Teflon, surface. In this section analysis of water droplet impacting on Teflon substrate is presented

for low droplet impact velocity having various droplet sizes.

Figure (D.2) shows the sequential image of an isothermal impacting water droplet on Teflon

substrate at the room temperature condition. Droplet size and impact velocity were 2.6 mm and

1.6 m/s, respectively. Similar to what was mentioned for the aluminum substrate, analysis of

droplet impact behavior can be carried out by temporal analysis of the droplet wetting (spreading) diameter and height which is exposed to various air speeds from 0 (still air) to 10 m/s.
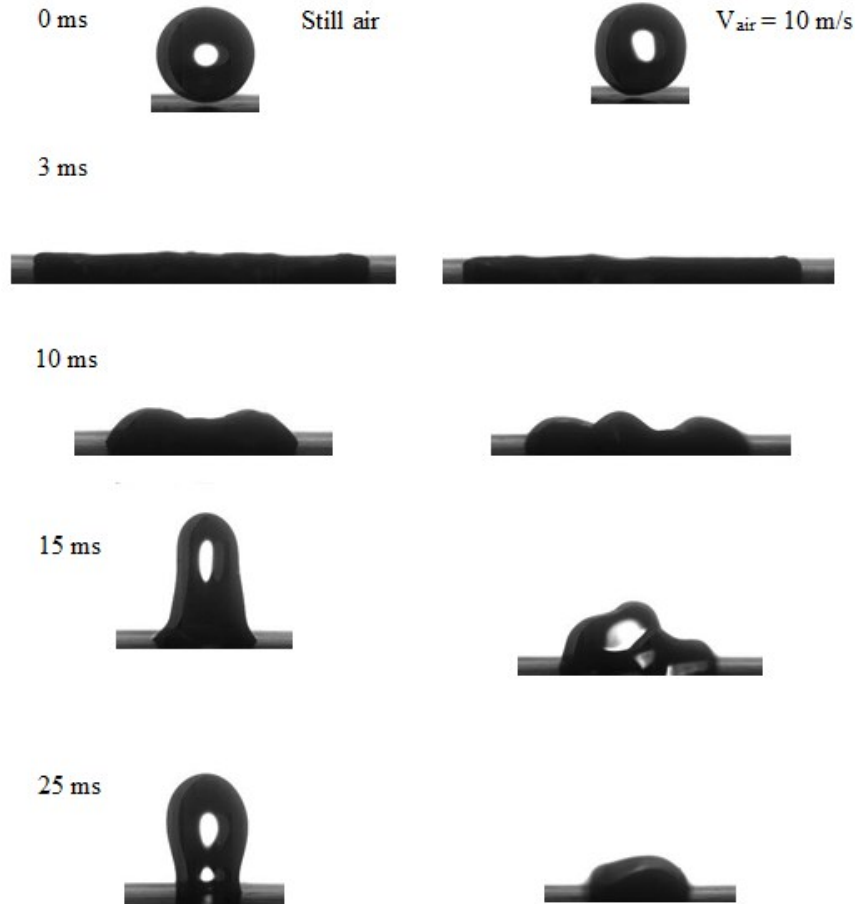
Figure D.2: Sequential images of water droplet impacting on the Teflon substrate at room temperature condition. Droplet size and impact velocity are 2.6 mm and 1.6 m/s, respectively. It is exposed to different air velocities from 0 to 10 m/s.

As illustrated in figure (D.2), spreading phase lasts 3 ms without any measurable changes in the maximum spreading diameter with and without airflow. However, droplet recoiling phase was affected by the presence of air flow. Quantitative evaluation of temporal height of impacting water droplet on the Teflon substrate is demonstrated in figure (D.3). the effect of normal force (stagnation pressure) can clearly influences the dynamics of recoiling phase. Droplet reaches to the maximum height up to 3.8 mm at 20 ms in the still air while it significantly suppressed by the

stagnation flow pressure force where air velocity is increased. By increasing air speed up to 10 m/s which results in higher stagnation pressure force, droplet maximum height dramatically decreases up to 50% at 15 ms. Additionally, droplet oscillation' amplitude was decreased by increasing air speeds. Droplet starts shedding at 20 ms due to fact that axisymmetrical behavior of spread droplet is no longer present. In the following, the effect of stagnation air flow on the high inertia droplet impact velocity up to 2.5 m/s is elaborated.
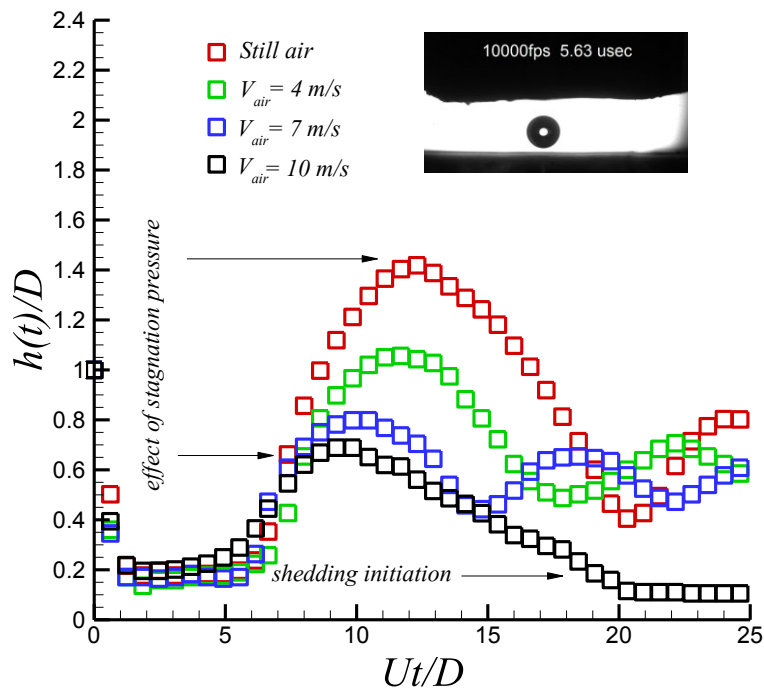
Figure D.3: Temporal height evolution of an impacting water droplet on the Teflon surface at room temperature condition. Droplet size and impact velocity are 2.6 mm and 1.6 m/s, respectively. It is exposed to different air speeds from 0 to 10 m/s.

The effect of incoming air flow on larger maximum spreading diameter is evaluated by impacts of water droplet size as large as 2.6 mm having 2.5 m/s impact velocity. Corresponding Weber and Reynolds number are around 220, 6500, respectively. Sequential images of an impacting water droplet with and without air flow is illustrated in figure (D.4). As shown, physics of spreading and

retraction is almost similar to what was elaborated for moderate impact velocity on the Teflon substrate (i.e. 1.6 m/s). Such a high inertia water droplet impacting on the Teflon substrate results in the largest maximum spreading diameter about (10.3.10.6) mm which is almost identical to that of aluminum substrate (i.e. 10.5-10.8 mm). However, behavior of retraction phase is fundamentally different. As demonstrated in figure (D.4), droplet edges start pulling back with slightly decrease in retraction velocity due to the imposed shear and normal force of incoming air flow. In fact, it becomes clear that the effect of receding contact angle (see figure(4.5)) is the main reason of systematic difference between hydrophilic and hydrophobic surfaces, as receding velocity is about 2 folds higher than aluminum surface arise from differences in retraction force, $\pi \gamma D_{max}(1 - cos\theta_{rec})$. Detailed quantitative evaluation of this phenomenon was illustrated in the main context of the current study (i.e. chapter 4).

As shown in figure (D.5), normal force of incoming airflow significantly suppresses droplets height at the highest droplet Weber number around 220. In fact, the combination of large resultant shear force of incoming air flow which reduces receding velocity and consequent imposing normal force cause droplet height dramatically reduces up to 62% to that of still air case. In the following, the effect of stagnation air flow on small droplet wetting spreading diameter is elaborated.
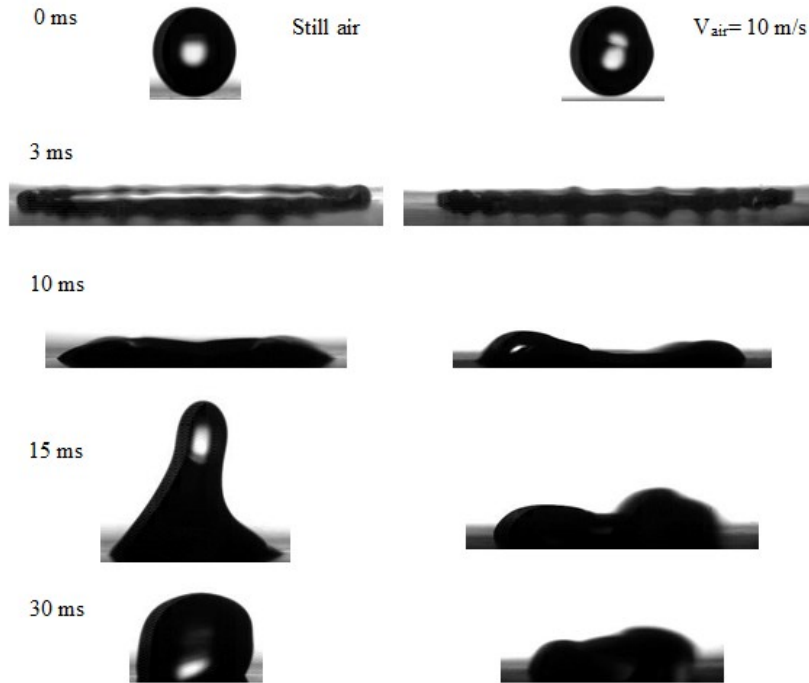
Figure D.4: Sequential images of water droplet impacting on the Teflon substrate. Droplet impact velocity is 2.5 m/s imposed to different air velocities from 0 to 10 m/s.
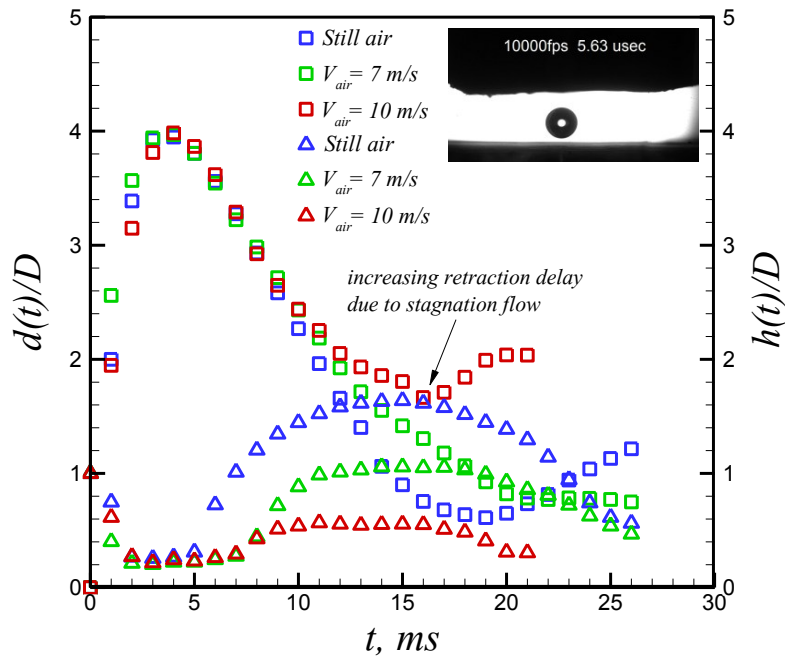

Figure D.5: Quantitative evaluation of temporal spreading diameter and height of an impacting water droplet on the Teflon substrate. Droplet size and impact velocity are 2.6 mm and 2.5 m/s, respectively.

In order to having small maximum spreading diameter smaller droplet size experimentations were carried out on the Teflon substrate similar to that of aluminum surface. As demonstrated in figure (D.6), it is clear that lower resultant shear flow of incoming air flow due to the small maximum spreading diameter compare with aforementioned cases combined with relatively strong retraction force results in almost insignificant changes on the dynamics of spreading water droplet having Weber numbers from 30 to 50.
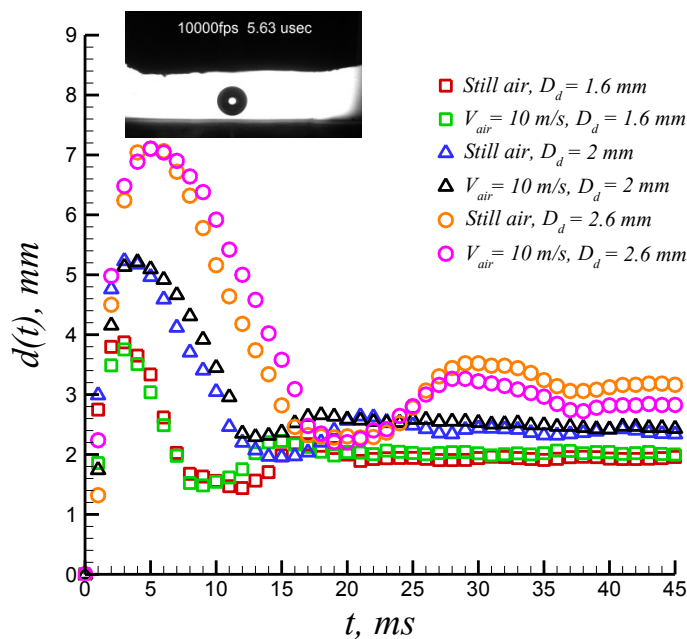
Figure D.6: Temporal evolution of an impacting water droplet on the Teflon substrate at various droplet impact sizes from 1.65 to 2.6 mm at impact velocity up to 1.2 m/s. Corresponding Weber and Reynolds numbers are 30 to 50 and 1980 to 3120, respectively.

D.2 Isothermal droplet impact dynamics exposed to airflow on a superhydrophobic surface

Sequential images of an impacting water droplet on the superhydrophobic substrate is presented in figure (D.7). Droplet reaches to the maximum spreading diameter at 3 ms without significant breaks up. However, due to large instability generated at the rim periphery due to the sudden

acceleration-deceleration phenomenon, recoiling phase is faced sever break up at 7 ms. However, at this phase, it is accompanied with subsequent satellite droplet merging. It results in further decrease in recoiling velocity which results in an increase in droplet contact time up to 16 ms.
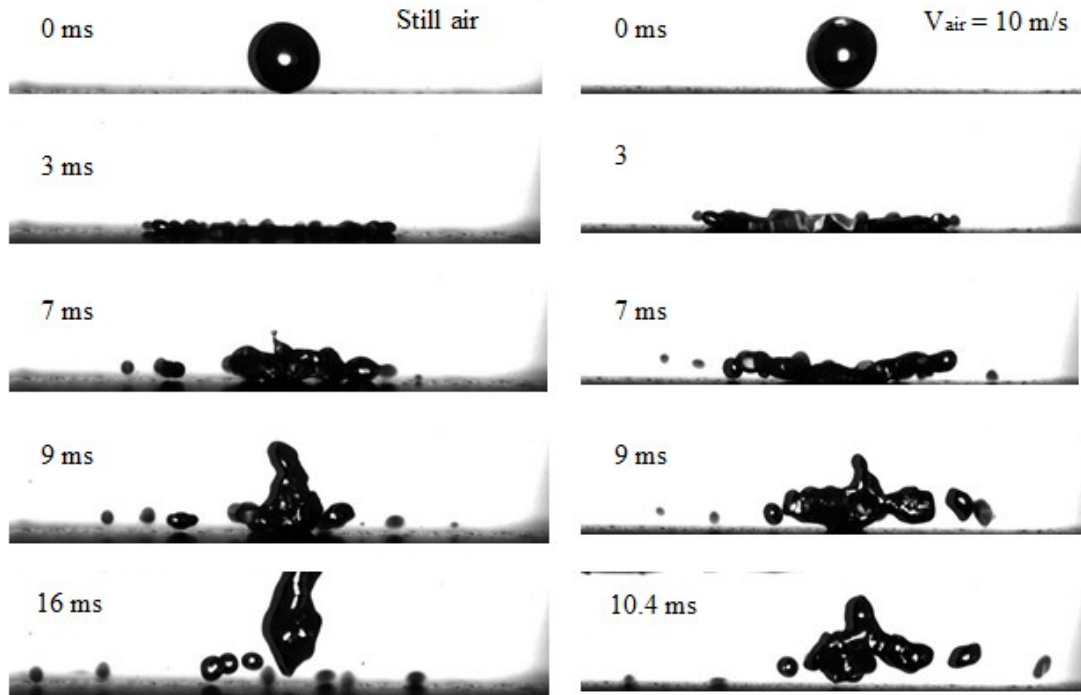

Figure D.7: Sequential images of water droplet impacting on the superhydrophobic surface. Droplet size and droplet impact velocity are 2.6 mm and 2 m/s, respectively. Corresponding Weber and Reynolds numbers are around 140 and 5200, respectively.

On the other hand, the effect of stagnation air flow on an impacting water droplet with large maximum spreading diameter is shown to be substantially different to that of still air condition. As illustrated in figure (D.7), Droplet is pulling back spread edges at 3ms. Droplet rim periphery is slightly lifted up from substrate at 7 ms which is accompanied with subsequent droplet breaks up. Finally, it detaches from the substrate at conseiderably smaller time to that of still air condition up to 10.4 ms shows a reduction as large as 35%.

As it was highlighted in the main context of the current study in chapter 4, normal force of stagnation air flow has a clear effect on the droplet wetting dynamics which is elaborated in detail

here. Normal pressure (i.e. stagnation pressure force) can be profoundly evaluated by temporal height variation of an impacting water droplet, as illustrated in figure (D.8), droplet height reaches to 4 mm at 10.7 ms (corresponding dimensionless time up to 6.6) while by increasing air speed up to 10 m/s droplet height reaches to 1.9 mm at the same time (i.e. 52% height reduction). As can be deducted from the influence of both shear and normal forces of incoming stagnation flow, droplet impact behavior in non-isothermal condition (e.g. low temperature condition) results in larger solidified wetting diameter due to the smaller retraction force which is suppressed by the incoming air flow. This phenomenon is described in detail in chapter 4.
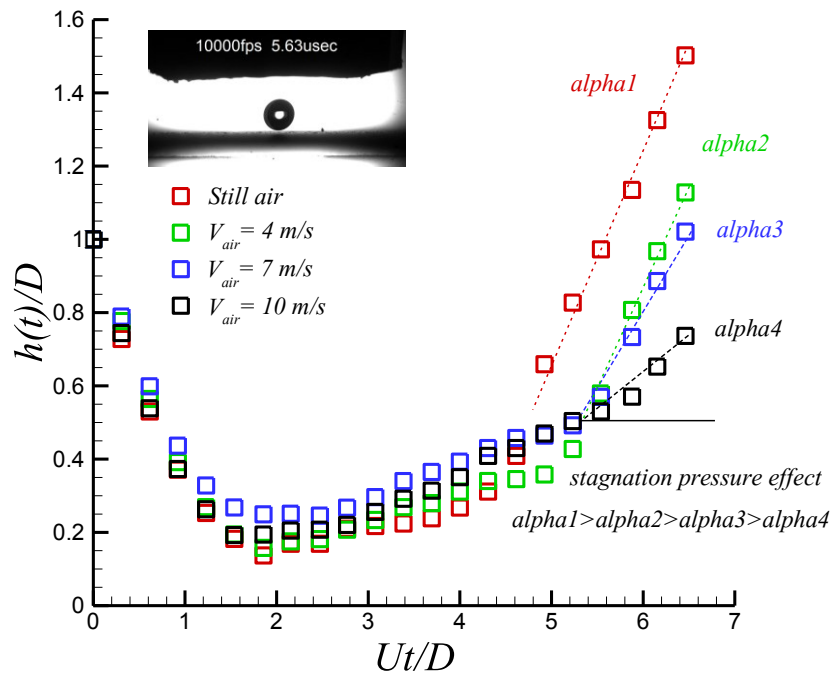
Figure D.8: Temporal height evolution of an impacting water droplet on the superhydrophobic surface at room temperature condition. Droplet size and impact velocity are 2.6 mm and 1.6 m/s, respectively. It is accompanied with different air speeds from 0 to 10 m/s.

D.3 Comparison of maximum spreading diameter with various theoretical models

Figure (D.9) shows comparison of two predictive models of the maximum spreading diameter with experimental results of aluminum substrate. Both energy based model and analytical

hydrodynamic model agree very well with experimental results. As demonstrated in figure (D.9) associated errors for energy based model becomes slightly larger than analytical hydrodynamic model at low Weber number droplet impact condition (i.e. We = 50) with the mean value deviations up to 3.3% and 1%, respectively. While by increasing droplet Weber number up to around 220 the mean value deviations become almost below 1% and 2% for energy based and analytical hydrodynamic models, respectively.
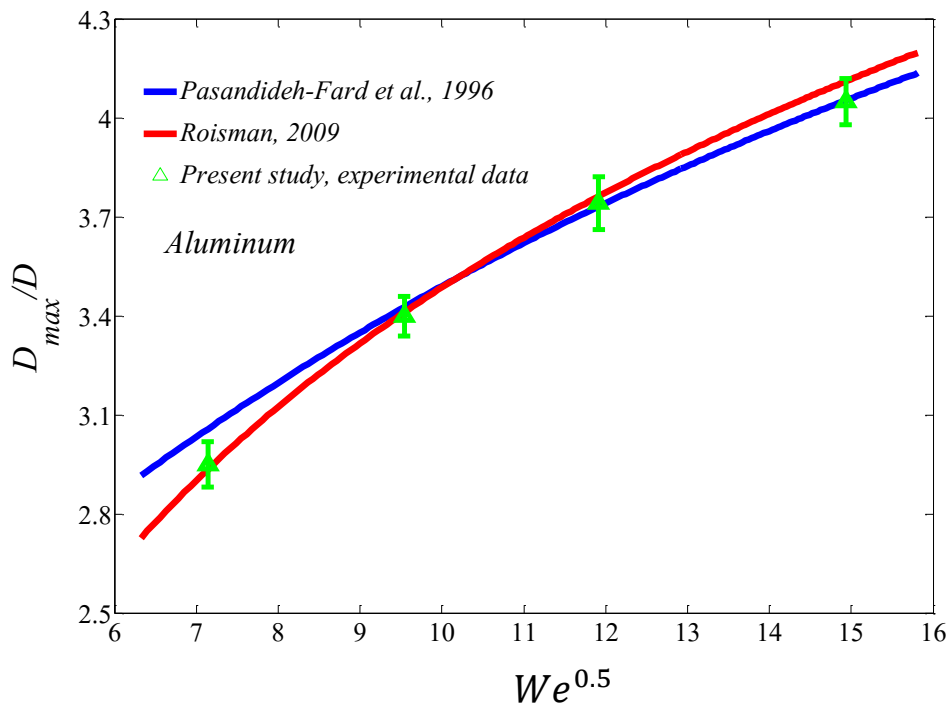

Figure D.9: Comparison of experimental data with two predictive models of maximum spreading diameter for aluminum substrate. Droplet Weber numbers vary from 50 to 220.

Same procedure is carried out for Teflon substrate. As illustrated in figure (D.10), both energy based and analytical hydrodynamic models agree well with experimental results but it is slightly in favor of energy based model. For low Weber number water droplet impact condition up to 50 associated mean value deviations for energy based and analytical hydrodynamic models become

3.65% and 7.7%, respectively. However, the mean value deviation becomes almost similar up to 2.5% for both models at high Weber number droplet impact up to around 220.
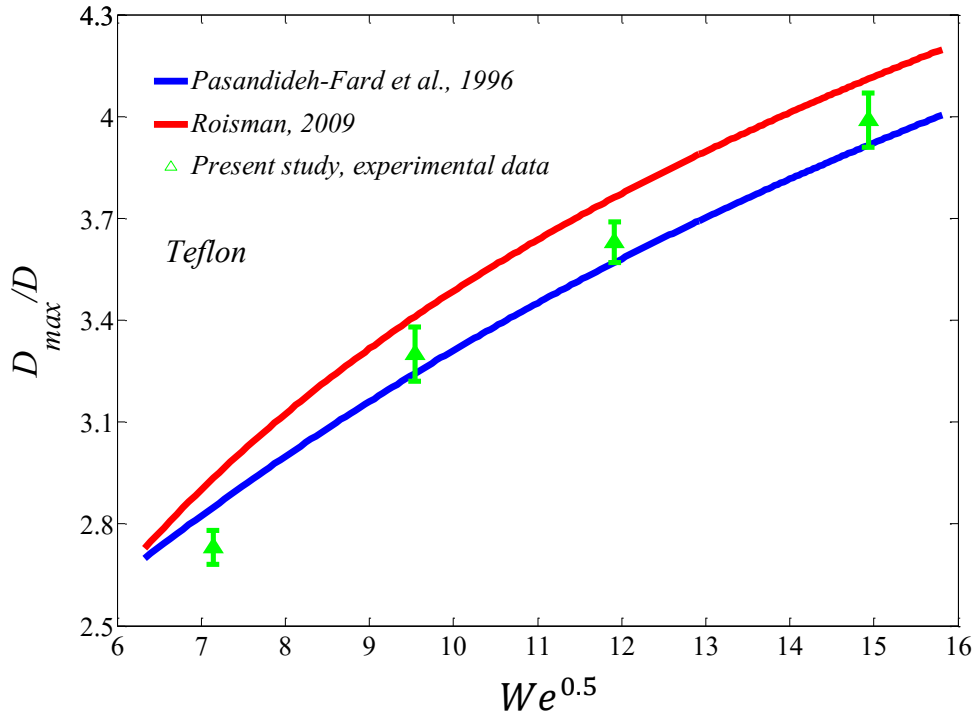

Figure D.10: Comparison of experimental data with two predictive models of maximum spreading diameter for the Teflon substrate. Droplet Weber numbers vary from 50 to 220.

Comparison of aforementioned models is also carried out for the sanded Teflon substrate. As it was explained in chapter 2, regarding surface characterization, this surface have large both static contact angle close to superhydrophobic surfaces (i.e. 135º) and contact angle hysteresis similar to the aluminum substrate (i.e. 40º). As illustrated in figure (D.11), energy based model predicts well the experimental data but predicted value based on the analytical hydrodynamic model becomes slightly larger to that of hydrophilic and hydrophobic substrates. The mean value deviation for the low Weber number droplet impact condition (i.e. We = 50) become 3.4% and 13% for energy based and analytical hydrodynamic models, respectively. While for highest droplet Weber number

around 220, the mean value deviations become 2% and 7.5% for energy based and analytical hydrodynamic models, respectively.
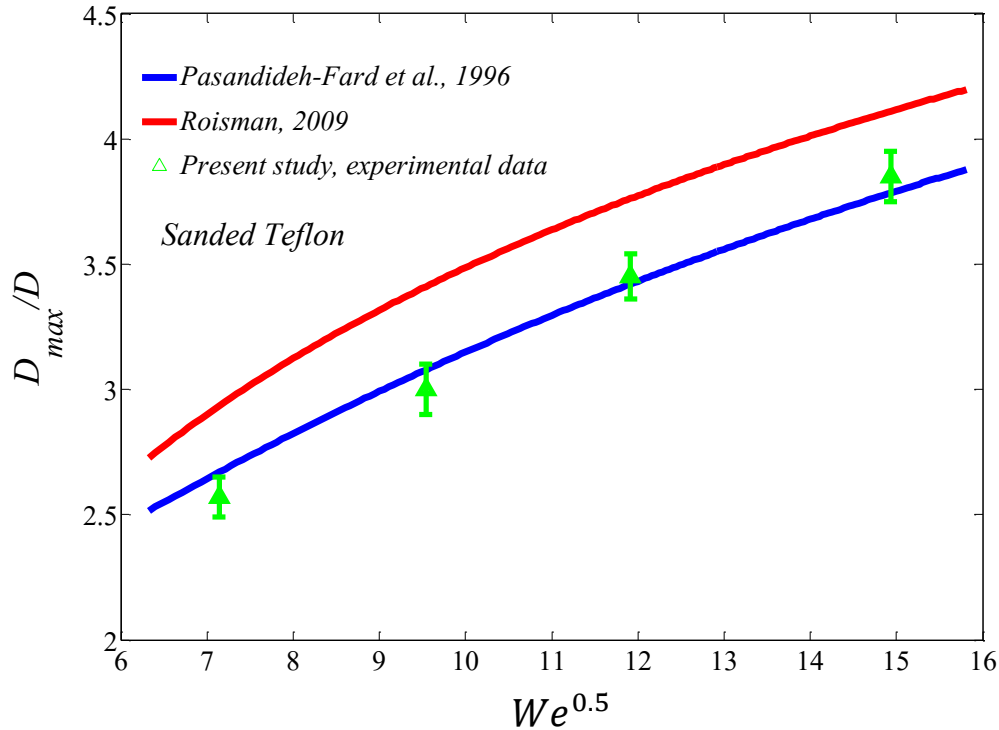

Figure D.11: Comparison of experimental date with two predictive models of maximum spreading diameter for sanded Teflon substrate. Droplet Weber numbers vary from 50 to 220.

Appendix E

Thermal transport analysis of cold target substrates

After heat transfer analysis of moving droplet through cold air, which was described in the main context of the current study, thermal transport analysis of substrates are become necessary. Calculation of Biot numbers of substrates contacting with cold air flow are carried out by the usage of the forced convective heat transfer coefficient of impinging air flow based on the modified correlation of Nusselt number.[122] In this correlation, Reynolds number is calculated based on the impinging air jet velocity and diameter of impinging area. Therefore, maximum spreading

diameter for each surface has been used as a characteristic length for calculation of Reynolds number. Figure (E.1), shows the schematic of contacting cold air flow on the substrate.
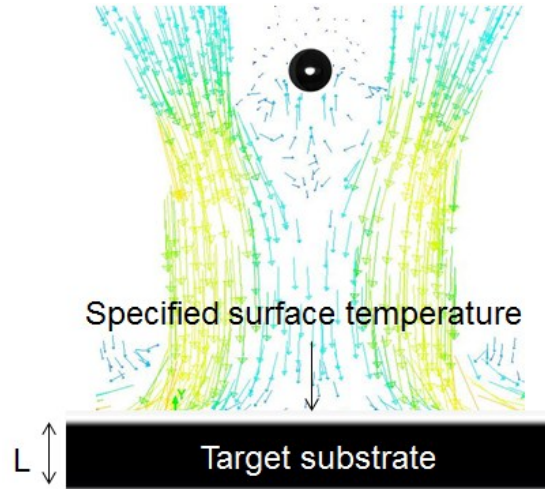

Figure E.1: Schematic of impinging air flow on different target substrates.

Calculation of convective heat transfer coefficient was based on the maximum air jet velocity in order to investigate the worst case scenario. Therefore, for aluminum substrate with thermal conductivity of 148 (*w/m.K*), maximum spreading diameter about 8.5 mm and thickness of 2.1 mm (thickness of aluminum plate) Biot number becomes as low as 0.002. This calculation was carried out by equations (E.1) to (E.5).

$$Re = \frac{\rho_g \, D_{max} \, U_{g,jet}}{\mu_g} \tag{E.1}$$

$$Pr = \frac{\mu_g \, c_{p,g}}{k_g} \tag{E.2}$$

$$Nu = 0.966 \, Re^{0.46} \, Pr^{\frac{1}{3}} \tag{E.3}$$

$$h_g = \frac{Nu.k_g}{D_{max}} \tag{E.4}$$

$$Bi = \frac{h_g l_c}{k_{substrate}} \qquad\qquad\qquad\qquad (E.5)$$

For the Teflon substrate, due to the low thermal conductivity, Biot number becomes slightly larger than critical value up to 0.47. Therefore, we need to calculate Fourier number for the flat surface $(i.e.\, \tau = \frac{\alpha t}{L_c^2})$. For the maximum period of 100 ms, which is sufficient time for evaluation of spreading and retraction phases and thickness of Teflon plate up to 1 mm, it becomes as small as 0.016. Therefore, refereeing to Heisler charts, core temperature of substrate becomes almost equal to the surface temperature. (i.e. 0.98 substrate temperature). Same procedure for the superhydrophobic surface is carried out which shows Biot number (i.e. 0.075, thickness of coating is 0.2 mm) smaller than critical Biot number (i.e. 0.1).

Appendix F

F.1 Non-isothermal condition, hydrophilic and hydrophobic substrates

The effect of stagnation flow on an impacting supercooled water droplet is deeply elaborated by the analysis of Homann flow.[3] Resulting shear and normal forces might lead to an important changes in the wetting dynamics of an impacting water droplet. Furthermore, it significantly changes thermal transport properties of air-liquid interface by evaporation cooling. In the analysis of Homann flow radial velocity is varied by the distance from centerline of nozzle. It means that the higher droplet spreading diameter the more effective resultant shear force presents. The normal force of air flow will push droplet towards substrate and act as an extra dashpot (i.e. along with viscous dissipation through bulk and contact line of an impacting droplet) on recoiling stage which changes droplet recoiling behavior. However, quantitative analysis of an impacting supercooled water droplet on the cold substrate at all scenarios (i.e. -10 ºC, -20 ºC and -30 ºC) did not show

significant differences between with and without air flow due to the higher viscosity of supercooled water droplet and smaller spreading diameter which results in smaller or weaker imposed shear force on the spread ligament of water droplet.

Furthermore, the effect of capillary ridge become important when exposed shear flow on thin film of supercooled water is contacted with substrate. [64] On the other hand, due the fact that both homogeneous nucleation which weaken surface tension and heterogeneous nucleation which results in increasing in hydrophilicity of substrate by changing the contact angle[65] capillary force become smaller on the polished aluminum surface. Consequently, resulting normal and shear forces of stagnation air flow cannot overcome this capillary ridge, $\pi \gamma D_{max}(1 - cos\theta_{rec})$.

Figure (F.1), shows sequential images of an impinging supercooled water droplet with mean temperature of -3.5 ºC which impacts on the cold polished aluminum substrate. It maintained at temperature as low as -20 ºC. Corresponding droplet diameter, droplet impact velocity, Weber, Reynolds, Stefan, and Prandtl number are 2.6 mm, 1.6 m/s, 88, 2077, 0.26, 15.93, respectively. It is exposed to various air velocities ranging from 0 to 10 m/s. As shown in both figure (F.1) and (F.2), almost instantaneous freezing is initiated at the end of relaxation phase where droplet edge start pulling back. It can be seen that this phenomenon is happened at 8 ms after impact of supercooled water droplet. Droplet edges are stopped at this moment highlighting the event of heterogeneous ice nucleation between underneath of an impacting water droplet and substrate. After this time, further decrease in the capillary force, (capillary force governed by surface tension and surface contact angle) is initiated due to the forced convective heat transfer and evaporation cooling.
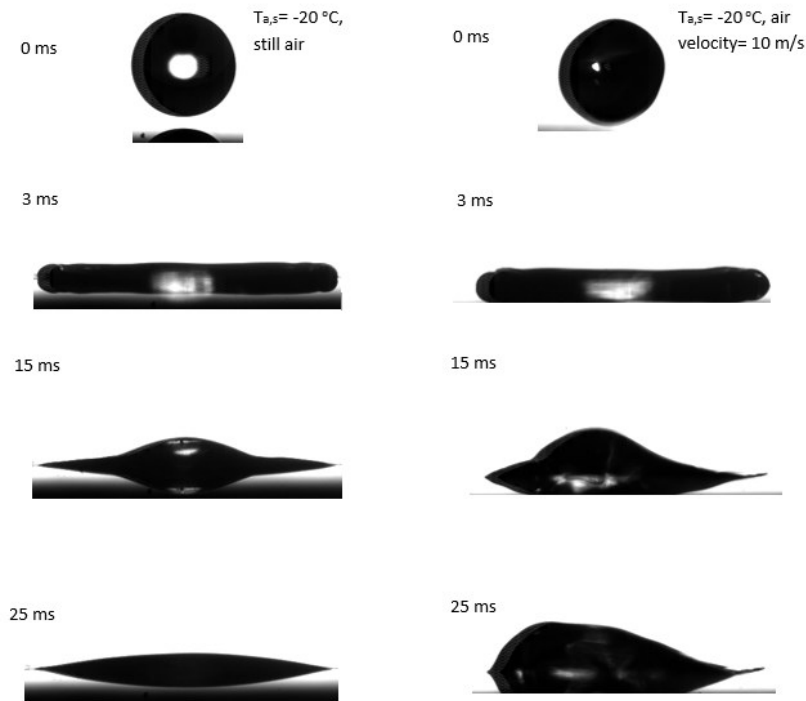
Figure F.1: Sequential images of supercooled water droplet impacting on the aluminum substrate exposed to different air velocities.
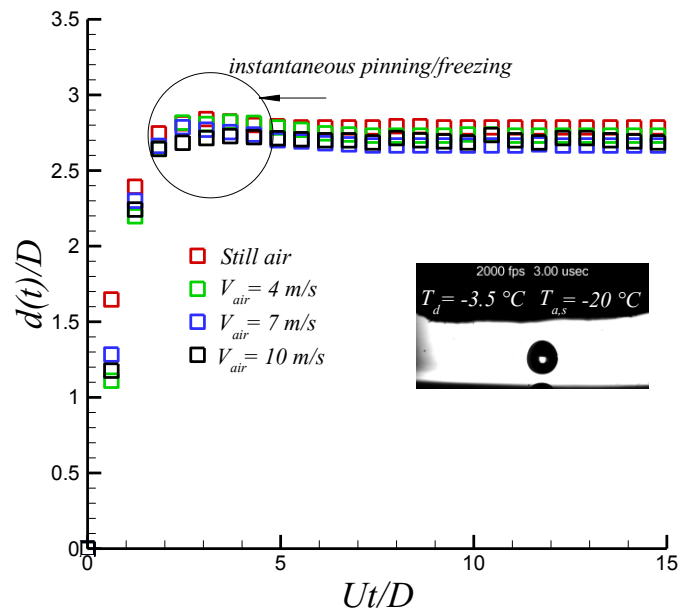

Figure F.2: Temporal evolution of spreading diameter of an impacting supercooled water droplet on aluminum substrate maintained at -20 ºC.

Figure (F.3), Shows sequential images of an impinging supercooled water droplet on cold polished aluminum with temperature maintained at -30 ºC. The mean value temperature of droplet was as

low as -5.5 ⁰C. Corresponding droplet diameter, droplet impact velocity, Weber, Reynolds, Stefan, and Prandtl number are 2.6 mm, 1.6 m/s, 88, 1890, 0.40, 17.51, respectively. Combination of an increase in viscosity and having higher relaxation time compare to the previous cases results in an increase in the heat transfer cooling rate causing an instantaneous pinning when droplet reaches to the maximum spreading diameter at 3 ms. As discussed earlier, classical nucleation theory emphasis that nucleation rate is a function of Gibbs free surface energy. By lowering the surface temperature, energy barrier regarding phase change is further decreased which is led to an immediate freezing at the maximum spreading diameter, as it illustrated in figure (F.4). In terms of wetting dynamics, cooled air flow does not show observable changes in an impacting supercooled water droplet. After this phase, droplet start freezing and it shape becomes more blurry up to 25 ms.
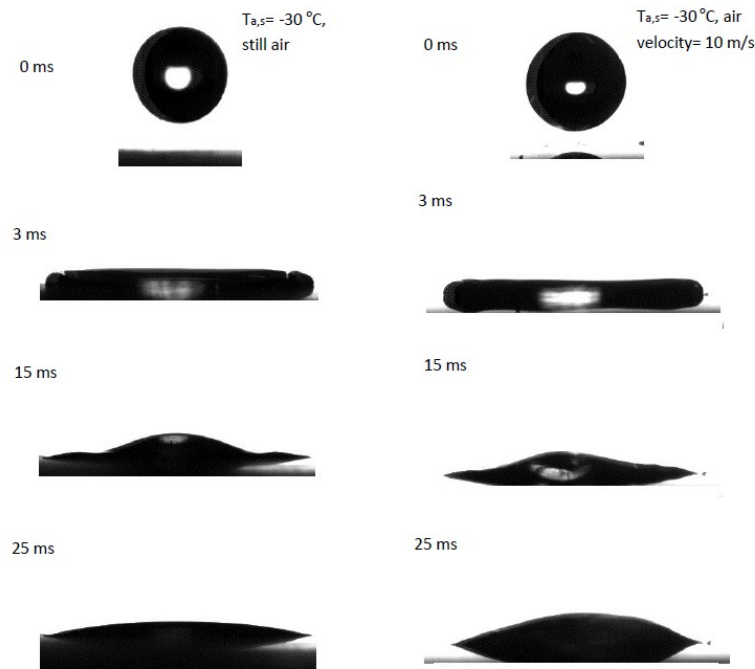
Figure F.3: Sequential images of supercooled water droplet impacting on the aluminum substrate maintained at -30 ⁰C.
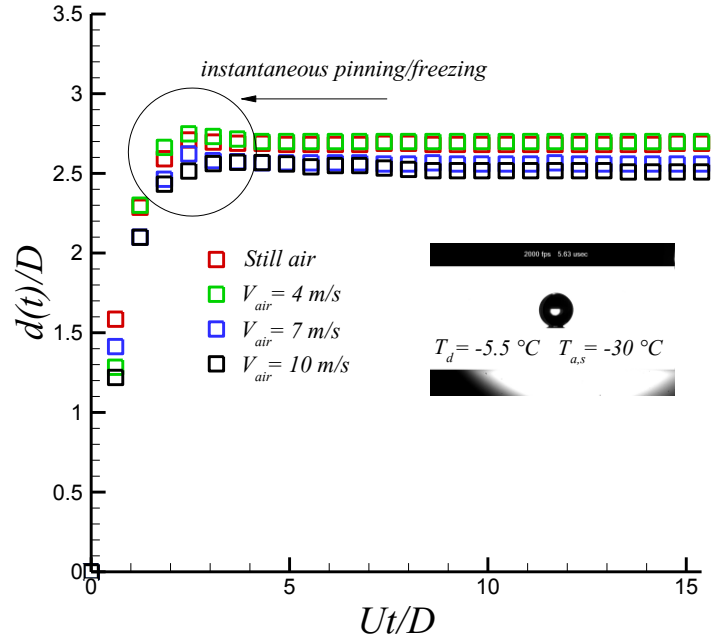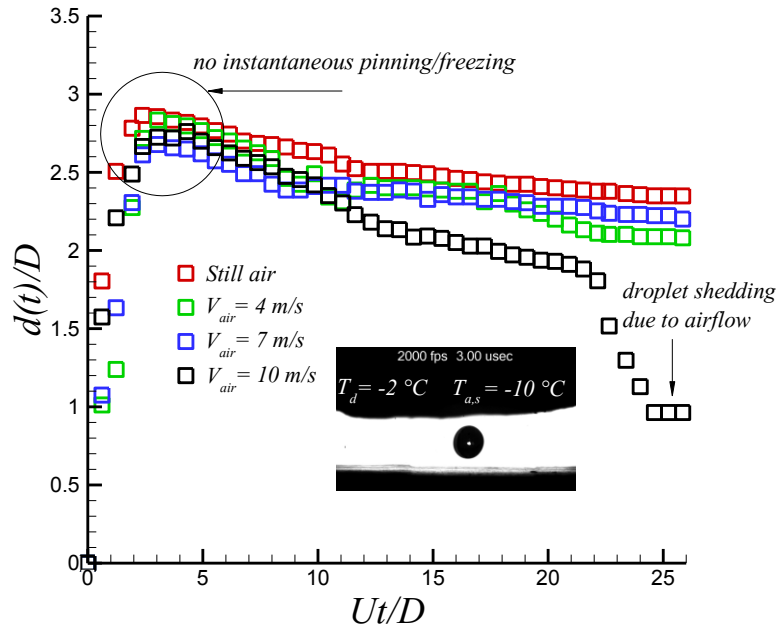
210

Figure F.4: Temporal evolution of an impacting supercooled water droplet on the cold aluminum substrate. Droplet and substrate temperatures are -5.5 and -30 ⁰C, respectively.

Figure (F.5), shows sequential images of an impacting supercooled water on Teflon substrate as a hydrophobic surface. As illustrated, droplet impact dynamics is similart to that of aluminum substrate with and with out air flow. This behavior was also observed by reducring surface temperature from -10 ºC to -30 ºC which can be explanied with similar to previous cases.. However, when air flow is incresed up to 10 m/s, wetting behavior is slighty changed.

211
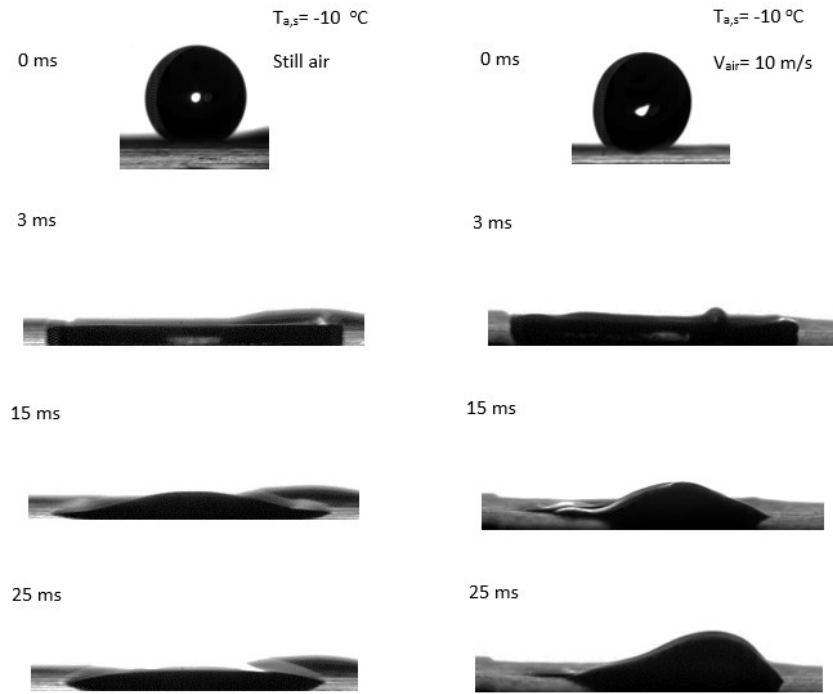
Figure F.5: Sequential images of supercooled water droplet impacting on the Teflon substrate maintained at -10 ºC.

At the recoiling stage, due to probable slight deviation from the stagnation point, by increasing air speed droplet is no longer in axisymmetrical condition. Resultant shear and normal forces cause droplet moves slightly from the stagnant point. Consequently, it is accompanied by shedding, as demonstrated in figure (F.6). For lower air speed, stagnation flow cannot overcome capillary ridge produced by both homogeneous ice nucleation (forced convective heat transfer and evaporation cooling) and heterogeneous ice nucleation (due to presence of external agent (i.e. substrate) contacting with supercooled liquid). Droplet finally reaches to the pinning condition at 40 ms.

Figure F.6: Temporal evolution of an impacting supercooled water droplet on the cold Teflon substrate. Droplet and substrate temperatures are -2 and -10 ºC, respectively.

Same scenario was also observed for the lower temperature condition (i.e. -20 ºC), as demonstrated in figures (F.7) and (F.8).
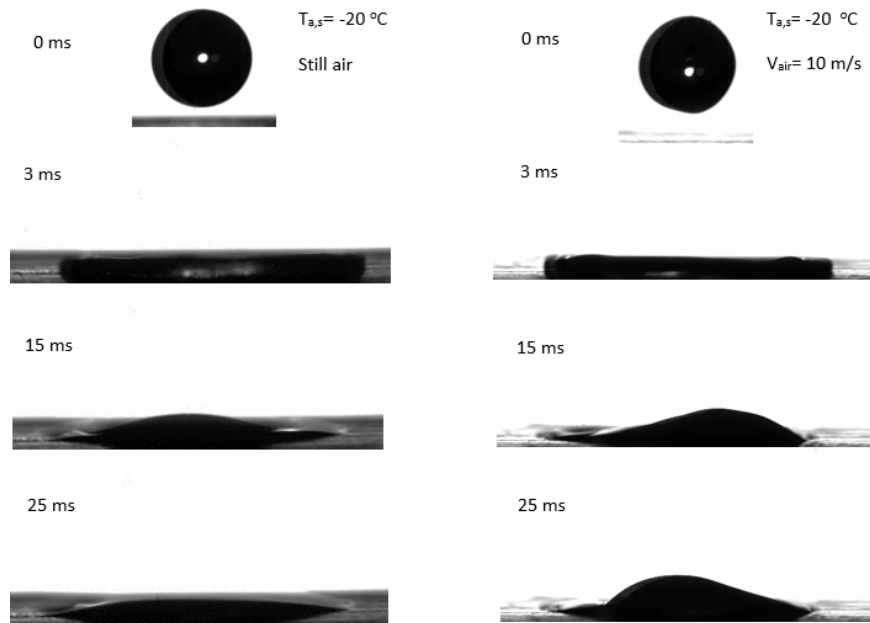

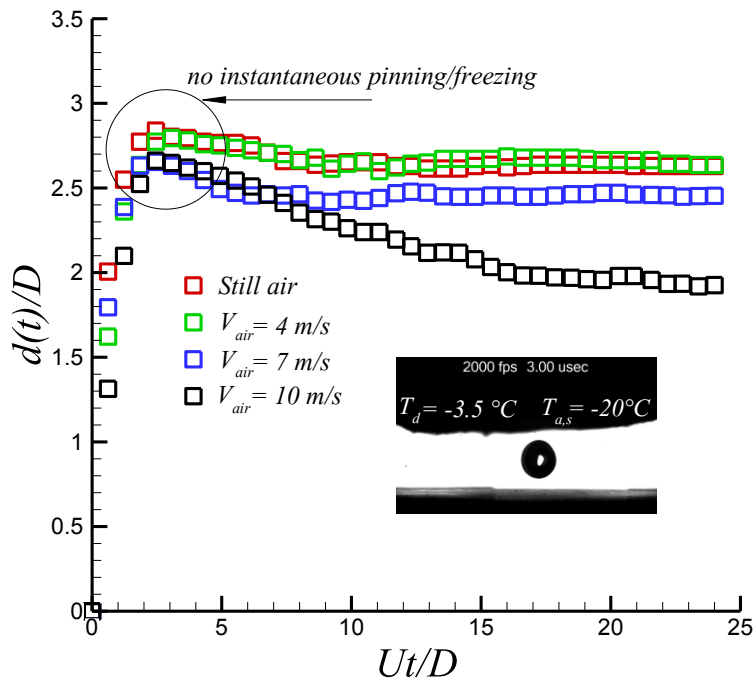**Figure F.7 Sequential images of supercooled water droplet impacting on the Teflon substrate maintained at -20 ºC.**

213

Figure F.8: Temporal evolution of an impacting supercooled water droplet on the cold Teflon substrate. Droplet and substrate temperatures are -3.5 and -20 ºC, respectively.

Figure (F.9) shows sequential images of an impinging supercooled water droplet with mean value temperature up to -5.5 ºC impacting on cold Teflon substrate with temperature maintained at -30 ºC. Corresponding droplet diameter, droplet impact velocity, Weber, Reynolds, Stefan, and Prandtl number are 2.6 mm, 1.6 m/s 88, 1890, 0.40, 17.51. It is exposed to various air velocities ranging from 0 to 10 m/s.
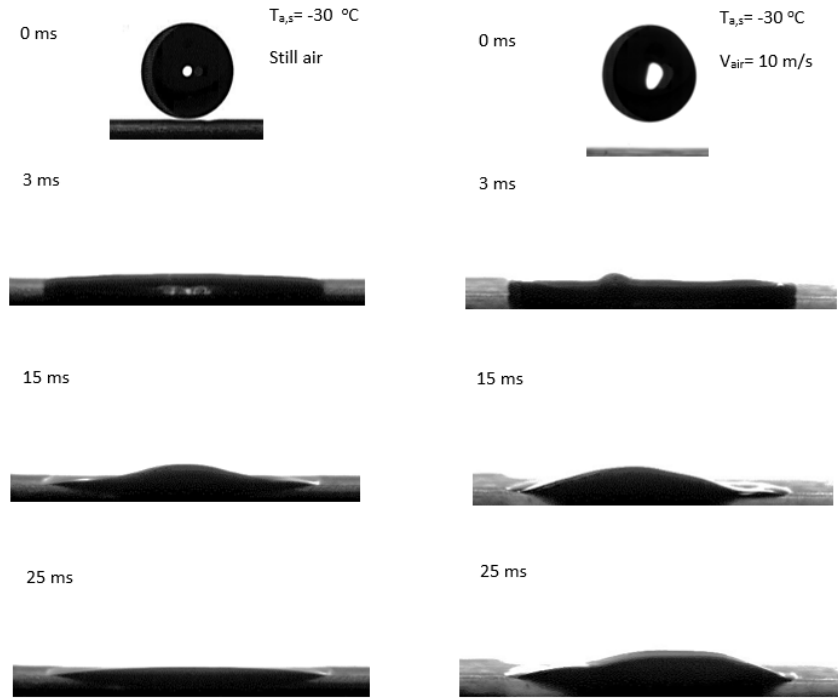
Figure F.9: Sequential images of supercooled water droplet impacting on the Teflon substrate maintained at -30 ºC.

Viscous force both internal and line are dramatically increased proposing harsher viscous dissipation at the maximum spreading diameter. In terms of thermal transport phenomenon, larger cooling rate increases the probability of phase change at this moment. Quantitative evaluation of temporal spreading diameter, which is illustrated in figure (F.10), shows that instantaneous pinning or freezing is happened at 3 ms and retraction phase completely eliminated.
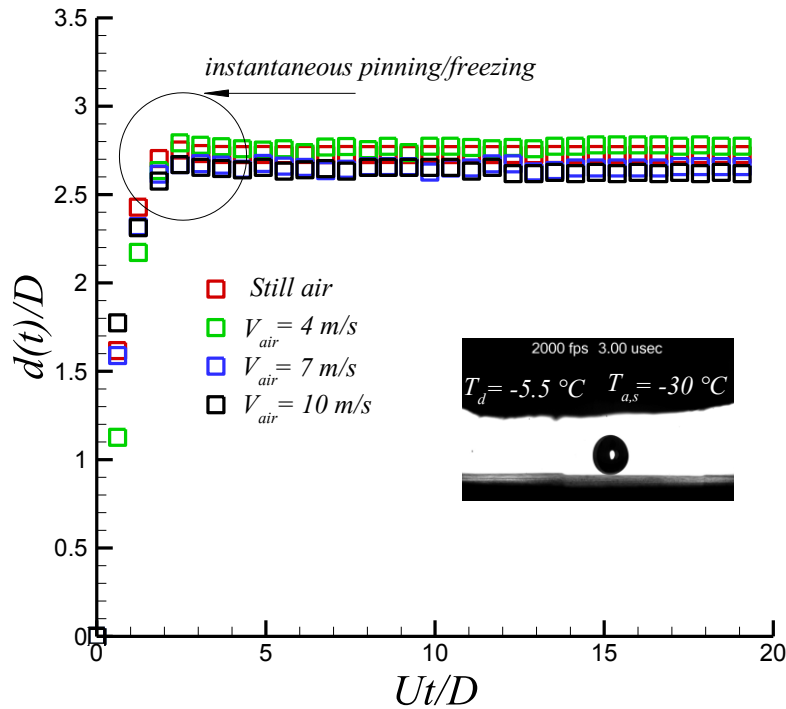
Figure F.10: Temporal evolution of an impacting supercooled water droplet on the cold Teflon substrate. Droplet and substrate temperatures are -5.5 and -30 ºC, respectively.

F.2 Non-isothermal condition, superhydrophobic substrate

Figure (F.11), shows sequential images of an impinging supercooled water droplet on the coated superhydrophobic surface maintained at substrate as low as -20 ºC. Corresponding droplet diameter, droplet impact velocity, Weber, Reynolds, Stefan, and Prandtl number are 2.6 mm, 1.6 m/s, 88, 2077, 0.26, 15.93, respectively. It is exposed to various air velocities ranging from 0 to 10 m/s. It has a same wetting dynamics to that of supercooled water droplet at -2 ºC. In spite of the fact that droplet temperature is almost 2 times lower than the previous case on the superhydrophobic substrate (i.e. droplet and substrate temperatures are -2 ºC and -10 ºC, respectively), an increase in the surface tension of an impacting supercooled droplet is almost negligible. It shows the capillary force is not changing significantly with droplet degree of

supercooling. Comparing with that of room temperature property, it shows an increase just up to 4.6 % which falls in the experimental precision errors. On the other hand, viscous force become more dominant as droplet viscosity increases 2 folds higher than room temperature water droplet. It highlights that contact line velocity is affected by liquid internal viscosity and contact line viscosity. As demonstrated in figure (F.12), viscosity effect results in an increase in droplet contact time about 11% in comparison with room temperature water droplet.
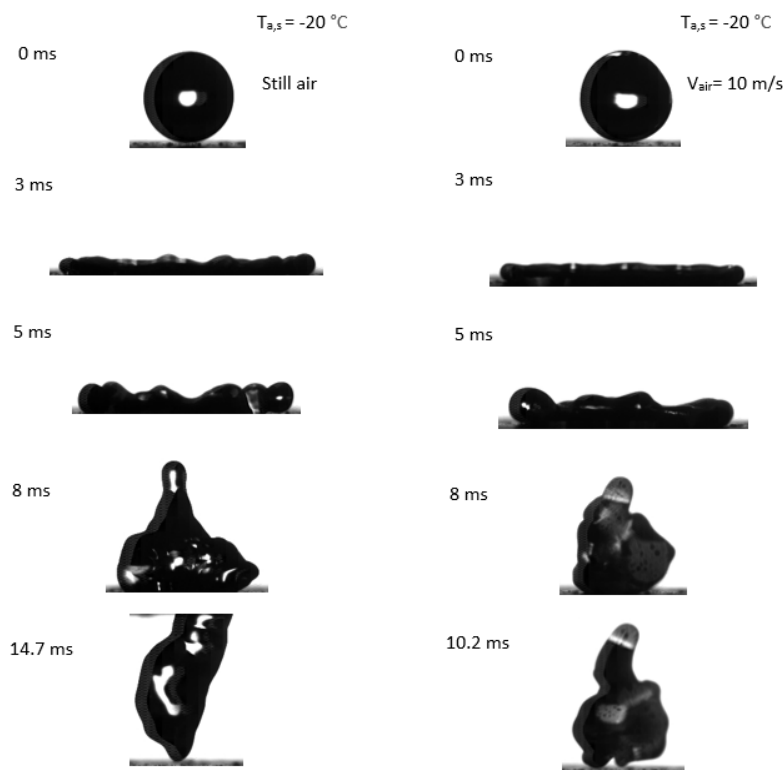

Figure F.11: Sequential images of supercooled water droplet impacting on the superhydrophobic substrate maintained at -20 ºC.
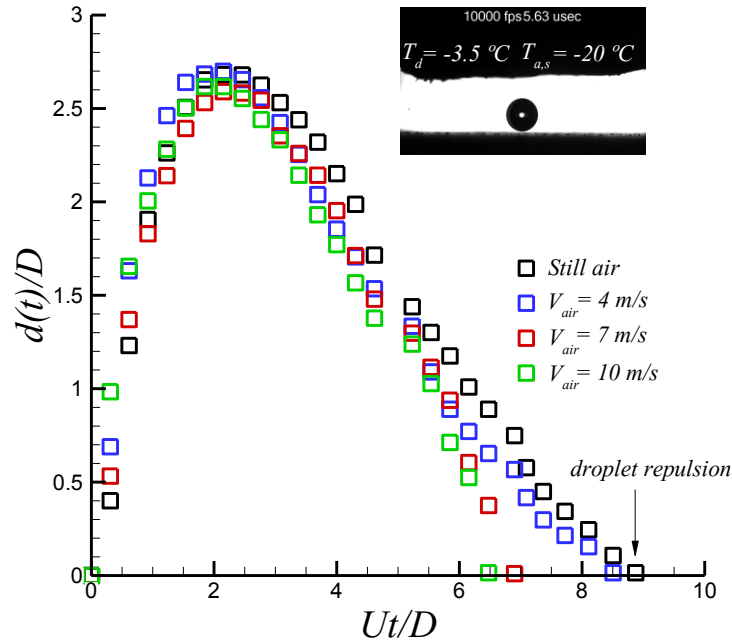
Figure F.12: Temporal evolution of an impacting supercooled water droplet on the cold superhydrophobic substrate. Droplet and substrate temperatures are -3.5 and -20 ºC, respectively.

F.3 Comparison of maximum spreading diameter with various theoretical models

In figures (F.13), (F.14) and (F.15) comparison of the maximum spreading diameter were carried out by three different models namely energy based mode, analytical hydrodynamics model and a correlation based on the scaling law analysis which was described in detail in chapter 1. As demonstrated in figure (F.13), for supercooling condition, scaling law (P_s factor varies from 0.11 to 0.21), Predicts very well with that of supercooled water droplet at -2 ºC. However, it overestimates the maximum spreading diameter for the lowest temperature condition of water droplet (i.e. -5.5 ºC) with the mean value deviation up 3%. The best agreement was observed for the energy based model at the supercooling condition. This model fits very well with the experimental data with the mean value deviation up to 1%. However, analytical hydrodynamic model predicts relatively well with the mean value deviation up to 14% for supercooled water

droplet at -5.5 °C. In addition to supercooled water droplet experiments, droplet impact behavior of water-glycerol solution with various viscosities ranging from 1.9 (corresponding supercooled water at -2 °C) to 2.2 (corresponding −5.5 °C supercooled water) were carried out to mimic an increased viscosity in the supercooled water due to the temperature reduction. The results show a very well agreement with that of supercooled condition.
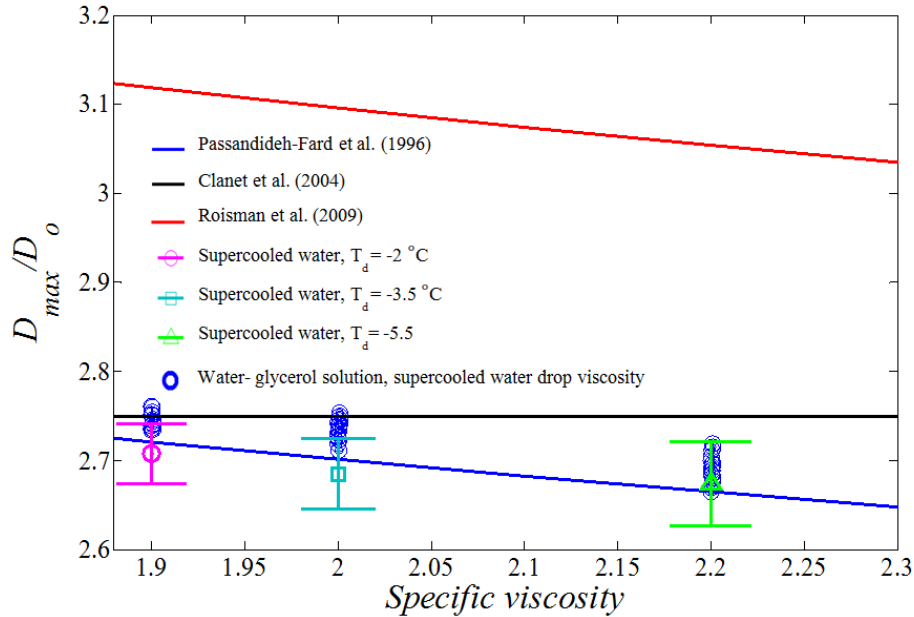

Figure F.13: Comparison of the maximum spreading diameter with energy based model (blue line), hydrodynamic analytical model (red line), scaling law analysis (black line) and water-glycerol solution with same viscosity of supercooled water (dark blue circle).

Same comparisons were carried for aluminum and Teflon substrates, as demonstrated in figure (F.14) and (F.15). Both energy based and hydrodynamic models agree very well with experimental results. As demonstrated in figure (F.14) and (F.15), associated error for energy based model becomes slightly larger than hydrodynamic model for room temperature condition on the aluminum substrate with the mean value deviation up to 4.6% and 3.5%, respectively. Same results were found for Teflon substrate for both models with almost same mean value deviation up to 8% for room temperature condition. However, when viscosity is increased the difference between

experimental results and two aforementioned models become larger. For higher water droplet degree of subcooling (i.e. -5.5 °C), the mean value deviation for energy based and hydrodynamic models become 12% and 15% for aluminum substrate and 10% and 14% for Teflon substrate, respectively. The difference between experimental results with that of aforementioned models stem from supercooled water droplet interface temperature which moves through cold air. Thermal transport analysis, as explained in chapter 4, shows that Biot number becomes larger than 0.1 and Fourier number becomes as small as 0.0045. Therefore, an interfacial temperature change can be expected. Calculation of heat penetration lengths [67], $\delta_h \approx (\alpha_w t_c)^{\frac{1}{2}}$, shows that this length varies up to 0.1 mm ($\alpha_w = 0.13\ 10 - 6\left(\frac{m^2}{s}\right)$ and $t_c \approx 85$ ms). It is evident that interface temperature of an impacting supercooled water becomes as cold as air temperature (i.e. -30 °C) . Consequently, there is a viscosity jump up to 8 and 3.6 folds higher than to that of room temperature and water droplet temperature at -5.5 °C, respectively.[76] Therefore, viscous dissipation should be represented by the combination of internal bulk of an impacting water droplet and that of interface one.

 Further justification is carried out by the usage of different water-glycerol solution having same viscosity to that of an impacting supercooled water droplet. In all experimental results, the mean value of maximum spreading diameter of supercooled water were smaller than water-glycerol mixture having same bulk viscosity which can be observed in figures (F.13), (F.14) and (F.15) for all target substrates.
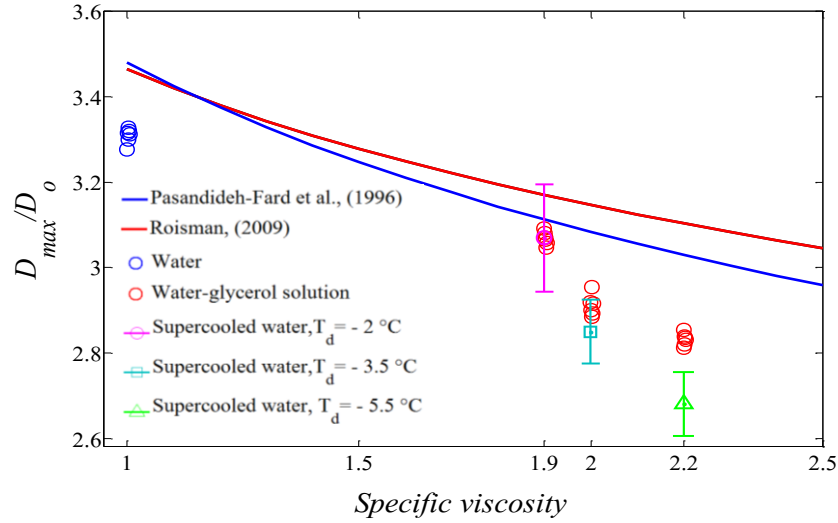
Figure F.14: Comparison of the maximum spreading diameter on aluminum substrate with energy based model (blue line), hydrodynamic analytical model (red line), and water-glycerol solution with same viscosity of supercooled water (red circle).
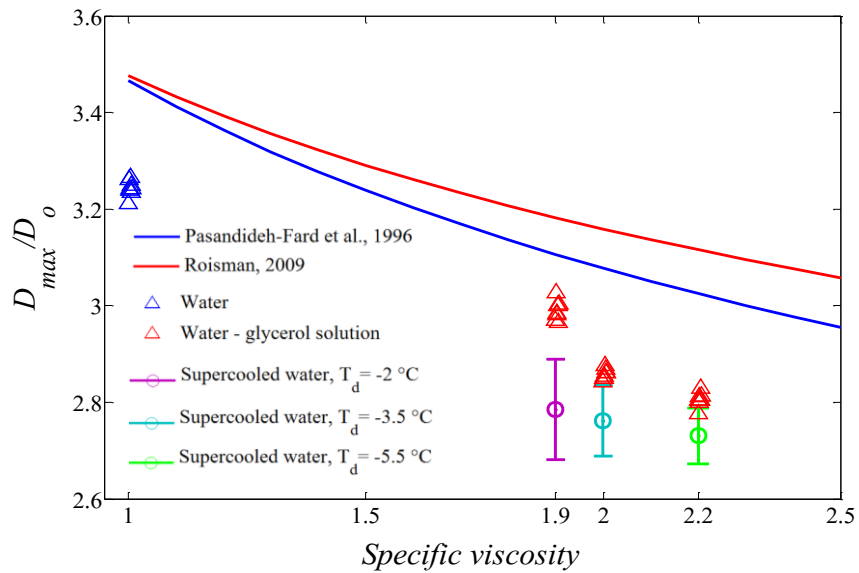

Figure F.15: Comparison of the maximum spreading diameter on Teflon substrate with energy based model (blue line), hydrodynamic analytical model (red line), and water-glycerol solution with same viscosity of supercooled water (red triangle).